Universitat de les Illes Balears

Doctoral Thesis
2021

SURFACE WAVE DYNAMICS EFFECTS AT MULTIPLE SCALES IN THE MEDITERRANEAN SEA

Verónica Morales Márquez

Universitat de les Illes Balears

Doctoral Thesis
2021

Doctoral programme of Physics

SURFACE WAVE DYNAMICS EFFECTS AT MULTIPLE SCALES IN THE MEDITERRANEAN SEA

Verónica Morales Márquez

Thesis Supervisor: Alejandro Orfila Förster
Thesis Supervisor: Gonzalo Simarro Grande
Thesis Supervisor: Ismael Hernández Carrasco
Thesis Tutor: Damià Gomis Bosch

Doctor by the University of Balearic Islands

Universitat
de les Illes Balears

This thesis has been written by Verónica Morales Márquez under the supervision of Dr. Alejandro Orfila Förster, Dr. Gonzalo Simarro Grande and Dr. Ismael Hernández Carrasco.

Palma de Mallorca, May, 2021

Supervisors: **PhD student:**

LIST OF PUBLICATIONS ASSOCIATED WITH THE DOCTORAL THESIS:

Morales-Márquez, V., Orfila, A., Simarro, G., Gómez-Pujol, L., Álvarez-Ellacuría, A., Conti, D., Galán, Á., Osorio, A., and Marcos, M. (2018). Numerical and remote techniques for operational beach management under storm group forcing. *Natural Hazards and Earth System Sciences*, 18(12): 3211-3223. doi: https://doi.org/10.5194/nhess-18-3211-2018.

Morales-Márquez, V., Orfila, A., Simarro, G., and Marcos, M. (2020). Extreme waves and climatic patterns of variability in the eastern North Atlantic and Mediterranean basins. *Ocean Sciences*, 16(6): 1385-1398. doi: https://doi.org/10.5194/os-16-1385-2020.

Morales-Márquez, V., Hernández-Carrasco, I., Simarro, G., Rossi, V., and Orfila, A. (2020). Regionalizing the impacts of wind and wave-induced currents on surface ocean dynamics: a long-term variability analysis in the Mediterranean Sea. Under review in *Journal Geophysical Research: Oceans*. doi: https://doi.org/10.1002/essoar.10505583.1.

Morales-Márquez, V., Hernández-Carrasco, I., and Orfila, A. (2021). Ageostrophic contribution by the wind and waves induced flow to the lateral stirring in the Mediterranean Sea. Submitted to *Journal of Physical Oceanography*.

Universitat de les Illes Balears

Dr. Alejandro Orfila Förster, of Mediterranean Institute of Advanced Studies (IMEDEA)

I DECLARE:

That the thesis titled “Surface wave dynamics effects at multiple scales in the Mediterranean Sea”, presented by Verónica Morales Márquez to obtain a doctoral degree, has been completed under my supervision and meets the requirements to opt for an International Doctorate.

For all intents and purposes, I hereby sign this document.

Signature

Palma de Mallorca, May, 2021.

Universitat de les Illes Balears

Dr. Gonzalo Simarro Grande, of Institute of Marine Sciences (ICM)

I DECLARE:

That the thesis titled “Surface wave dynamics effects at multiple scales in the Mediterranean Sea”, presented by Verónica Morales Márquez to obtain a doctoral degree, has been completed under my supervision and meets the requirements to opt for an International Doctorate.

For all intents and purposes, I hereby sign this document.

Signature

Palma de Mallorca, May, 2021.

Universitat de les Illes Balears

Dr. Ismael Hernández Carrasco, of Mediterranean Institute of Advanced Studies (IMEDEA)

I DECLARE:

That the thesis titled “Surface wave dynamics effects at multiple scales in the Mediterranean Sea”, presented by Verónica Morales Márquez to obtain a doctoral degree, has been completed under my supervision and meets the requirements to opt for an International Doctorate.

For all intents and purposes, I hereby sign this document.

Signature

Palma de Mallorca, May, 2021.

A mi familia, por ser la colchoneta que te proteje en la escalada.

Agradecimientos

Hasta aquí hemos llegado. Aquí termina esta etapa, este túnel que empecé a hacer con sólo una cuchara como herramienta. Porque sí, para mí empezar a hacer una tesis es plantearte construir un túnel (por algún lado tenía que salir la ingeniera de caminos), con la esperanza de llegar a un lugar de ensueño, pero sólo con una cuchara en la mano. Menos mal, que por el camino llegan refuerzos. A ellos les debo que este "túnel" me haya llevado a una realidad que ha superado las expectativas.

Como no puede ser de otra manera, mi primer agradecimiento va para Jano. GRACIAS (así, en mayúsculas) por la oportunidad que me diste de emprender esta aventura a tu lado. He crecido una barbaridad no solo profesionalmente, sino también personalmente. Gracias por empujarme a salir de mi zona de confort, expandiéndola y haciéndola más segura con tu apoyo, por marcarme nuevas metas y guiarme para conseguirlas. Gracias por aprender conmigo y por enseñarme a disfrutar de la ciencia, a cuestionarme todo y creer en mí. Esto es tanto mío como tuyo.

Gracias Ismael, por tu paciencia y empatía. Por ese entusiasmo que le pones a todo, es contagioso. Por estar dispuesto a enseñarme todo lo que sabes y aprender aquello que aún no conocemos. Gracias por invertir tu tiempo en este proyecto, ha sido un placer.

Me gustaría también agradecer a Marta, Gonzalo, Lluís y Amaya por su colaboración en esta tesis, gracias por vuestros comentarios y sugerencias tan acertadas.

Agradezco a Juanma, Pau Luque y Esther por su ayuda, su apoyo y por nuestras conversaciones. Os admiro chicos y me siento afortunada de haber formado parte del mismo grupo científico que vosotros.

One of the most beautiful things of this period was undoubtedly the stays abroad. Thank you very much to Prof. Leo Oey for the opportunity to work with his group in the National Central University of Taiwan. Thanks Lin and Yoyo for your help. Allí tuve la suerte de coincidir con los chicos más bonitos con los que podría haberlo

hecho. Gracias Héctor, Amadeo y Jose. Llegasteis en el momento oportuno. Fue un punto de inflexión para esta tesis y un hito en mi vida, gracias por vivirlo conmigo. My second stay was in the Mediterranean Institute of Oceanology of Marseille, thanks to Dr. Vincent Rossi, it was a pleasure to be twice and I would have liked to spend more time there. Thanks for showing me how you and your group work, I love your way of doing science. Thanks Katixa, Térence and Madiop for your support and your time.

Gracias a mis refuerzos personales, a Albert por todo el cariño y cuidado con el que me has tratado estos 4 años. A Javi, siempre serás mi patata preferida. A Carlota, Raquel y Laura, sois amor chicas, qué suerte la mía. A Julia y Melo, por ese despacho de las guapas que me ha hecho la recta final mucho más amena. A Júlia, Álex, Inma, Manu, Àngels, Miguel, Tim, Xisca, Noe, Guille y una larga lista de gente que sin ellas mi estancia en Mallorca no habría sido lo mismo. Estas líneas se quedan cortas con todo lo que me gustaría agradeceros, de cada uno de vosotros saldría al menos un párrafo entero. Habéis conseguido que me sienta en casa con vosotros. Gracias de todo corazón. Os quiero.

Gracias Marina por darme esa paz, es extraño como alguien te puede hacer sentir tanta calma. Esta etapa acaba para mí, pero sé que nos vemos en la siguiente, te llevo siempre conmigo.

Gracias por el cariño que me han dado mi abuela y mi madrina durante esta tesis.

Gracias a mi familia, Ana, Pepa, Rafa y Rafael (quería que en mi tesis apareciera cada uno de vuestros nombres, igual que aparece el mío), qué suerte contar con vosotros en mi vida. Esta tesis lleva mucho vuestro, desde la portada hasta el último punto y final. Gracias y mil veces gracias. Por apoyarme e intentar comprenderme, por ser esa cuerda salvavidas que hace que la caída sea más leve cuando las fuerzas flaquean. Os quiero. Gracias mamá por la portada tan maravillosa que encabeza este trabajo, sin duda la tesis ha subido de nivel con ella.

Todo este trabajo no habría sido posible sin la financiación recibida desde el Ministerio de Economía y Competividad a través del contrato FPI2016 (BES-2016-076323) asociada al proyecto MORFINTRA/MUSA (CTM2015-66225-C2-2-P). Gracias al IMEDEA por el espacio ofrecido para realizar este trabajo.

Abstract

Wind generated waves are crucial to transfer energy and momentum from the atmosphere to the sea surface, redistributing and transporting such energy to remote areas of the ocean. Waves induce ventilation in the ocean upper layer, enhancing vertical mixing and producing vertical transport of biogeochemical tracers. When waves reach coastal areas they dissipate energy through viscous damping at the bottom and eventually by breaking, resulting in morphological changes of the bathymetry, sediment transport and erosion.

The general objective of this Thesis is to perform a characterization of spatio-temporal variability of surface ocean waves, and to study their effect on the dynamics at the upper layers and at a coastal system. In particular, we analyze the large scale variability of the extreme wave climate in the Mediterranean Sea and the North Atlantic Ocean. We compute the monthly extreme waves analyzing their inter-annual variability. Then, at regional scale, we study the regional impact of the wind and wave induced velocity on the total surface dynamics at different sub-regions of the Mediterranean Sea from the Eulerian and Lagrangian standpoints. Finally, at coastal scale, the effects of extreme waves from storm groups on the sediment transport is assessed based on a multi-system approach combining remote and *in situ* data with numerical techniques.

Seasonal signal accounts for 50% of the extreme wave height variability in the North Atlantic Ocean and up to 70% in some areas of the Mediterranean Sea. For the winter season, the North Atlantic Oscillation and the Scandinavian modes are the dominant large-scale atmospheric modes of variability that modulate extreme waves in the North Atlantic Ocean; and to a lesser extent, the East Atlantic Oscillation also controls extreme waves in the central part of the basin. In the Mediterranean Sea, the negative phase of East Atlantic Oscillation dominates the variability of extreme waves during winter season.

At regional scale, ageostrophic currents substantially modulates the total mesoscale dynamics by two non-exclusive mechanisms; by providing a vigorous input of momentum (e.g. where regional winds are stronger) and/or by opposing momentum to the main direction of the geostrophic component. To properly characterize the spatio-temporal variability of the mesoscale dynamics induced by wind and wave, we propose a regionalization of the Mediterranean Sea based on the homogeneous variability of the coupled geostrophic and agesotrophic velocity components, combining self-organizing maps (SOM) and wavelet coherence analyses.

We study the impact of the wind and waves induced motions on the mixing and transport properties of the surface marine flow. Transport pathways unveiled by the geostrophic Lagrangian coherent structures are significantly modified by the ageostrophic currents, often leading to a decrease of the retention capacity of the eddies. The ageostrophic component induces an increase in mixing activity up to 36% in some regions of the Mediterranean basin, finding the largest values during autumn and winter seasons. The study of the anisotropy in the separation scales between pairs of trajectories reveals that the zonal component of the flow plays an important role, determining the properties of the relative dispersion.

The characterization of time scales evolution of sandy coasts has been a topic of wide interest over the past decades, since sandy beaches and dune systems are the first natural lines of coastal defense against floods and erosion hazards. The results of this work show that sandy systems have two characteristic time scales: the eroding process associated with the extreme waves generated by the storm is of the order of hours, while the time scale of the transition to the equilibrium is of the order of months. This different behavior provides the basis for a more efficient beach management strategy.

Resumen

El oleaje generado por el viento es crucial a la hora de transferir energía y momento desde la atmósfera a la superficie marina, redistribuyendo y transportando esta energía a zonas lejanas. Además, favorece la ventilación en las capas superficiales del océano, mejorando así la mezcla y provocando un transporte efectivo de trazadores biogeoquímicos a lo largo de la columna de agua. Cuando el oleaje llega a la costa, su energía es disipada por efecto de la viscosidad en el fondo y por la rotura de las olas, lo que da lugar a cambios morfológicos en la batimetría por el transporte de sedimentos y la erosión.

El objetivo general de esta Tesis es caracterizar la variabilidad del oleaje y estudiar su efecto sobre la dinámica superficial del océano. En particular, se analiza el clima marítimo extremal en el mar Mediterráneo y en el Atlántico Norte. Se estudian los valores mensuales de oleaje extremo analizando su variabilidad interanual. Posteriormente, a escala regional, se evalúa el impacto regional de la velocidad inducida por el viento y el oleaje en la dinámica superficial de las diferentes subcuencas del mar Mediterráneo desde una perspectiva euleriana y lagrangiana. Finalmente, a escala costera, se analizan los efectos del oleaje extremo asociado a grupos de tormentas en el transporte de sedimentos desarrollando una herramienta multi-plataforma que combina datos remotos e *in situ* junto con modelos numéricos.

La estacionalidad representa un $50\,\%$ de la variabilidad de la altura de ola extrema en el Norte del Océano Atlántico, y hasta un $70\,\%$ en algunas zonas del mar Mediterráneo. Durante el invierno, la Oscilación del Atlántico Norte y el Índice Escandinavo dominan los forzamientos atmosféricos a larga escala que modulan el oleaje extremal en el Atlántico Norte; y en menor medida, la Oscilación del Atlántico Este también controla el oleaje extremo en la parte central de la cuenca. En el mar Mediterráneo, la fase negativa de la Oscilación del Atlántico Este domina la variabilidad del oleaje extremal

durante el invierno.

A escala regional, las corrientes inducidas de Ekman y Stokes modulan sustancialmente la dinámica total de mesoescala mediante dos mecanismos no excluyentes: proporcionando una gran cantidad de momento (por ejemplo, en zonas donde los vientos son más intensos) y/o por oposición a la dirección principal de momento de la componente geostrófica. Para caracterizar adecuadamente la variabilidad espacial y temporal de la dinámica de mesoescala, se propone una regionalización del mar Mediterráneo basada en la variabilidad homogénea del acomplamiento de las componentes geostrófica y ageotrófica de la velocidad, combinando mapas autoorganizados (SOM) y análisis de "wavelets".

Continuando con el análisis a escala regional del Mediterráneo, se estudia el impacto de los movimientos inducidos por el viento y las olas en las propiedades de mezcla y transporte del flujo oceánico superficial. Las líneas de transporte desveladas por las estructuras coherentes lagrangianas geostróficas son modificadas significativamente por las corrientes ageostróficas, lo que a menudo conduce a una disminución de la capacidad de retención de los remolinos. La componente ageostrófica induce un aumento de la actividad de mezcla de hasta el $36\,\%$ en algunas regiones de la cuenca mediterránea, encontrando los valores más altos durante las estaciones de otoño e invierno. El estudio de la anisotropía en las escalas de separación entre pares de trayectorias revela que la componente zonal del flujo juega un papel importante en la determinación de las propiedades de la dispersión relativa.

La evolución de las playas de arena a diferentes escalas temporales ha sido un tema de gran interés durante las últimas décadas, ya que estas playas y los sistemas dunares son las primeras líneas naturales de defensa costera contra los peligros de las inundaciones y la erosión. Los resultados de este trabajo muestran que los sistemas costeros de arena responden a los forzamientos del oleaje en dos escalas temporales características: el proceso de erosión asociado al oleaje extremo generado por las tormentas corresponde a una escala temporal con un orden de magnitud horario, mientras que la escala de la transición al equilibrio es del orden de meses. Este comportamiento tan diferente proporciona una base para estrategias eficientes en la gestión costera.

Resum

L'onatge generat pel vent és cabdal a l'hora de transferir energia i moment des de l'atmosfera a la superfície marina, ja que redistribueix i transporta aquesta energia a zones allunyades. A més a més, afavoreix la ventilació en les capes superficials de l'oceà i millora la mescla de masses d'aigua, el que acaba provocant un transport vertical dels traçadors biogeoquímics. Quan l'onatge arriba a la costa, la seva energia es dissipa per efecte de la viscositat en el fons i pel trencament de les onades. Tot plegat es tradueix en canvis morfològics en la batimetria, així com en el transport de sediments i en l'erosió.

L'objectiu general d'aquesta Tesi és caracteritzar la variabilitat de l'onatge i estudiar el seu efecte sobre la dinàmica superficial de l'oceà. En particular, s'analitza el clima marítim extremal a la mar Mediterrània i a l'Atlàntic Nord. S'estudien els valors mensuals d'onatge extrem i s'analitza la seva variabilitat interanual. Després, a escala regional, s'avalua l'impacte regional de la velocitat induïda pel vent i l'onatge en la dinàmica superficial de les diferents subconques de la mar Mediterrània des d'una perspectiva euleriana i lagrangiana. Per acabar, a escala costanera, s'analitza els efectes de l'onatge extrem dels grups de tempestes en el transport de sediments, tot desenvolupant una eina multi-sistema que combina dades remotes i dades in situ amb models numèrics.

L'estacionalitat representa un 50% de la variabilitat de l'alçària d'ona de l'onatge extrem al Nord de l'oceà Atlàntic, i fins a un 70% en algunes zones de la mar Mediterrània. Durant l'hivern, l'Oscil·lació de l'Atlàntic Nord i l'Índex Escandinau dominen els forçaments atmosfèrics a llarga escala que modulen l'onatge extremal a l'Atlàntic Nord; i en menor mesura, l'Oscil·lació de l'Atlàntic Est també controla l'onatge extrem a la part central de la conca. A la mar Mediterrània, la fase negativa de l'Oscil·lació de l'Atlàntic Est domina la variabilitat de l'onatge extrem durant l'hivern.

A escala regional, els corrents induïts d'Ekman i Stokes (component ageostròfica) modulen substancialment la dinàmica total de mesoescala mitjançant dos mecanismes no excloents: d'una banda indueixen una gran aportació de moment (per exemple allà on els vents regionals són més forts), i per altra banda, modulen la dinàmica per l'oposició a la direcció principal de moment de la component geostròfica. Per caracteritzar de forma escaient la variabilitat espacial i temporal de la dinàmica a mesoescala, es proposa una regionalització del mar Mediterrània basada en la variabilitat homogènia de l'acoblament de les components geostròfica i ageostròfica de la velocitat, tot combinant mapes auto-organitzats (SOM) i anàlisi de coherència d'ones.

S'estudia l'impacte dels moviments induïts pel vent i les onades a les propietats de mescla i transport del flux oceànic superficial. Les línies de transport revelades per les estructures coherents lagrangianes geostròfiques són modificades significativament pels corrents ageostròfics, el que tot sovint condueix a una disminució de la capacitat de retenció dels remolins. La component ageostròfica indueix un augment de l'activitat de mescla de fins el 36% en algunes regions de la conca mediterrània, els valors més alts es donen durant els períodes de tardor i hivern. L'estudi de l'anisotropia en les escales de separació entre parells de trajectòries revela que la component zonal del flux juga un paper important en la determinació de les propietats de la dispersió relativa.

L'evolució de les platges de sorrad'arena a diferents escales temporals ha estat un tema de gran interès durant les últimes dècades, ja que aquestes les platges i els sistemes dunars són les primeres línies naturals de defensa costanera contra front ael risc de s perills de lles inundacions i l'erosió. Els resultats d'aquest treball mostren que els sistemes costaners de sorraarenosos presenten responen als forçament de l'onatge en dues escales temporals característiques: el procés d'erosió associat a l'onatge extrem generat per les tempestes està en l'ordre d'horescorrespon a una escala temporal amb un ordre de magnitud horari, mentre que l'escala de la transició a l'equilibri és de l'ordre de mesos. Aquest comportament tan diferent proporciona una base per implementar estratègies més eficients de gestió costanera.

Contents

1 Introduction **1**

1.1 Ocean surface waves 1

1.2 Wind-generated Ocean Waves 2

1.3 Waves-generated Ocean Currents 5

1.4 Spatiotemporal scales of wave variability 7

1.4.1 Large scale 8

1.4.2 Regional and seasonal scale 10

1.4.3 Coastal scale 13

1.5 Plan of Thesis 13

2 Data and methods **15**

2.1 *In-situ* measurements 15

2.2 Remote sensing measurements 16

2.3 Numerical models 17

2.4 Analysis methods 18

3 Extreme waves and climatic patterns of variability in the eastern North Atlantic and Mediterranean basins **21**

3.1 Introduction 21

3.2 Data and extreme wave values 23

3.2.1 Waves and atmospheric data 23

3.2.2 Extreme wave climate 24

3.3 Spatiotemporal patterns of extreme waves 28

3.3.1 Correlations between winter extreme waves and climatic modes of variability 29

3.3.2 Synoptic atmospheric composites associated with extreme wave patterns 33

3.4 Summary and conclusions 38

4 Regionalizing the impacts of wind and wave-induced currents on surface ocean dynamics: a long-term variability analysis in the Mediterranean Sea 41

4.1 Introduction 42
4.2 Sea Surface Currents 44
4.2.1 Geostrophic currents 44
4.2.2 Ageostrophic currents: wind and wave driven components 44
4.3 Data 47
4.3.1 Wave and atmospheric data 47
4.3.2 Geostrophic velocity field 49
4.4 Statistical Methods 49
4.4.1 Self Organizing Maps 49
4.4.2 Wavelet power spectral method 50
4.4.3 Combined SOM-Wavelet coherence analysis 51
4.5 Results and discussion 51
4.5.1 Regionalizing the impacts of wind and waves on the total surface kinetic energy 54
4.5.2 Regional assessment of the temporal variability 57
4.6 Conclusions 62

5 Ageostrophic contribution by the wind and waves induced flow to the lateral stirring in the Mediterranean Sea 69

5.1 Introduction 69
5.2 Data 71
5.2.1 Velocity fields 71
5.2.2 Lagrangian drifter data 72
5.2.3 Dynamical regions of the Mediterranean Sea 73
5.3 Lagrangian dynamics 73
5.3.1 Relative dispersion statistics 74
5.3.2 Lagrangian Coherent Structures 76
5.4 Results and discussion 77

5.4.1 Ageostrophic induced leakage across mesoscale LCS 77
5.4.2 Horizontal stirring variability 80
5.4.3 Dispersion properties 83
5.4.4 Anisotropy of the Mediterranean Sea flow 88
5.5 Conclusions 92

6 Numerical and remote techniques for operational beach management under storm group forcing 101
6.1 Introduction 102
6.2 Study area 103
6.3 Data and Methods 106
6.3.1 Wave conditions 107
6.3.2 Beach Morphology 108
6.3.3 Sediment characteristics 109
6.3.4 Video monitoring 109
6.3.5 Numerical modelling 110
6.4 Results and Discussion 111
6.4.1 Bathymetry extraction from model and video images 111
6.4.2 Beach morphological response to storms and recovery 113
6.5 Conclusions 116

7 Conclusions 119

List of Figures 138

List of Tables 149

List of Terms and Abbreviations 151

Chapter 1

Introduction

Research on physical oceanography began at the end of the XIX century with occasional measurements in multidisciplinary surveys mainly focused on bathymetry. In 1905 the pioneering work of Ekman established the basis of the theoretical oceanography (Ekman, 1905). Since then, the role of the ocean as one of the key actors of the Earth's system has been established thanks to the advance in theoretical, observational and numerical approaches. While the first studies in oceanography were addressed for military purposes, today society is aware of the importance of understanding the ocean processes in regulating the climate and in maintaining the global biodiversity and thus, research in the ocean system is one of the priorities in Earth sciences.

Dynamical oceanography studies the response of the ocean to external and internal forces (Stokes, 1880). The former act on ocean boundaries (surface, bottom and continents), while the latter are developed in its core. At the surface, the forces are of meteorological origin: the atmospheric pressure, the wind stress and the density gradient as a result of precipitation, radiation and evaporation. At the bottom and continental margins, friction, viscous damping and Earth's rotation generate small-amplitude and low-frequency dynamics. At the ocean interior, the main forcing is due to the Earth's rotation and gravity, the tides and some non-conservative forces such as the turbulence stress. Most of these forces generate dynamical perturbations known as waves.

This Thesis is focused on ocean surface dynamics, since the atmosphere-ocean interaction induces vigorous physical phenomena which affect the dynamics of the entire water column, impacting in the biogeochemical processes (e.g. Hernández-Carrasco et al., 2014), biodiversity (Buesseler, 1998), climate variability (Jones et al., 2015) and all human activities (Sayol et al., 2014).

1.1 Ocean surface waves

Surface waves cover a wide range of periods (Toffoli and Bitner-Gregersen, 2017), as shown in Fig. 1.1. Waves characterized with longer periods are the planetary waves which are large-scale systems with slow drifting (Massel, 2017). Then, there are the long-period gravity waves, such as tides or waves produced by earthquakes or moving atmospheric pressure systems and wind surges (LeBlond and Mysak, 1981). At shorter periods, there is a broad range of wind-induced gravity waves followed by capillary waves, caused by the sea surface tension (Kinsman, 1984). As shown in Fig. 1.1, wind generated waves contain the largest part of the spectrum, thus providing the largest input of energy into the ocean.

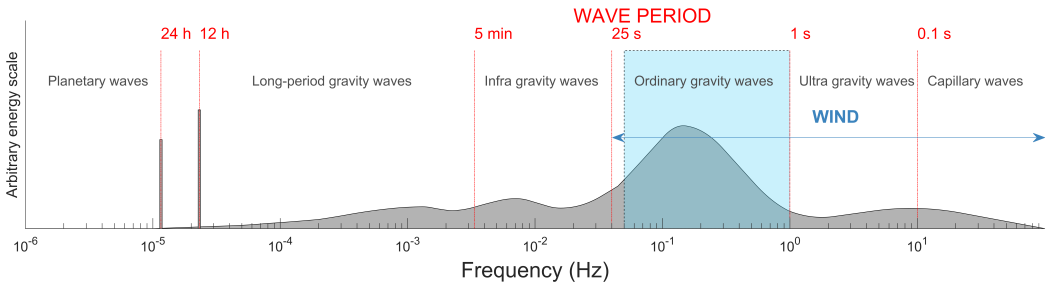

Figure 1.1 *Frequency and period ranges of ocean waves. The order of magnitude of the relative energy power is indicated by the curve (adapted from Munk, 1950). The shaded area represents the range of wave periods in which this Thesis focuses.*

Here, we will focus on the wind-generated surface ocean waves analyzing their variability and their effects on the ocean dynamics at several spatial and temporal scales. An accurate analysis and evaluation of their features provide crucial information to:

i design and operate marine systems and structures, such as offshore platforms, pipelines, mooring systems, renewable energy installations, port activities and shipping (LeBlond and Mysak, 1981; Faltinsen, 1990; Tsinker, 2004) through long-term statistics and extreme-value theory;

ii better understand physical, biological and chemical properties of the marine environment (Babanin, 2011) due to the impact of waves on the mixing activity at the ocean surface through the turbulent processes (Babanin, 2006; Babanin et al., 2009);

iii manage coastal areas, evaluating the coastal morphodynamics and its effects on population and biodiversity (Eichentopf et al., 2019, 2020).

1.2 Wind-generated Ocean Waves

Wind waves are ocean surface waves originated by the friction of wind blowing over the sea. The area where waves are generated is known as fetch, although, this term is often applied to the maximum distance in this area (see Fig. 1.2). Throughout the fetch, one can assume that wind blows with a nearly constant direction during a period of time. This duration is essential for the waves to be generated, since waves not only need a distance where wind acts, but also they require time in order to develop and reach large periods and heights (Ardhuin and Orfila, 2018). Under the effect of a local wind, the first generated waves are the capillary waves, with different wave periods, directions and phases. The ripples of capillary waves are restored by surface tension (Kinsman, 1984). A uniform wind gust over a large fetch is able to force capillary waves to become longer than the threshold wave period of 1 second, where the waves can be classified as gravity waves (see Fig. 1.1). Here, gravity becomes the main restoring mechanism. Capillary waves are rapidly damped along the sea surface if wind stops, while gravity waves remain propagating until they loss their energy by breaking or through dissipation at the bottom boundary layer in shallow waters (Hasselmann et al., 1973). Within the fetch, the resulting gravity waves generate an irregular pattern known as “wind sea”, which retains the chaotic features that capillary waves have in terms of periods, directions and phases (Fig. 1.2). Waves of different characteristics couple with each

others resulting in a height and length increase within a changing overlapped pattern. They start growing in both height and length, until they reach a threshold height, from which they only evolve in wavelength (Toffoli and Bitner-Gregersen, 2017). In deep waters, where the depth is much larger than the wavelength, larger wavelengths propagate faster (Holthuijsen, 2007). In this way, larger waves with larger wavelengths are able to travel beyond the generating area faster than shorter ones, and they evolve into swell (Fig. 1.2). Swell propagates without the influence of wind being less steep than the sea waves and presenting longer periods and larger wavelengths in a narrow range of frequencies, which directly implies a more regular ocean surface pattern. In addition, swell waves have smaller heights than wind sea waves due to the combination of different waves, and as a consequence, the energy dissipated in swell waves is smaller (Toffoli and Bitner-Gregersen, 2017).

Usually, the period of wind-generated surface gravity waves (wind sea and swell) ranges between 1 and 25 seconds, although in this Thesis we only deal with periods smaller than 20 seconds.

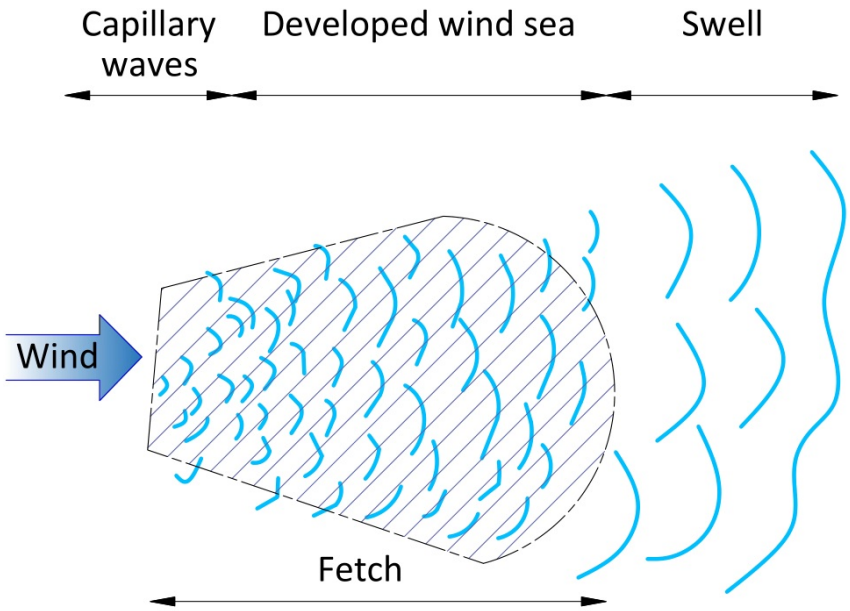

Figure 1.2 *Scheme of wind-driven surface waves generation.*

Once wind-generated surface gravity waves (hereinafter *waves*) are outside the fetch, the surface tension may be neglected, and they are propagated across the ocean as an irrotational flow. Waves can be represented as a superposition of monochromatic sinusoidal progressive trains propagating in any horizontal direction and with any frequency within the frequency range shown in Fig. 1.1, where the free surface elevation (η) and its potential flow (Φ) can be described as (Phillips, 1966),

$$\eta(x, y, t) = a \ \cos\left(k_x \ x + k_y \ y - \sigma t + \varphi\right), \tag{1.1}$$

$$\Phi(x, y, z, t) = \frac{\sigma a}{k} \frac{\cosh\left[k \left(h + z\right)\right]}{\sinh\left(kh\right)} \sin\left(k_x \ x + k_y \ y - \sigma t\right), \tag{1.2}$$

where (x, y) is the spatial location, t the time, a the wave amplitude, $k = (k_x, k_y)$ the wavenumber associated with the wavelength (λ) as $\lambda = \frac{2\pi}{k}$, σ the radian wave frequency

related to the wave period (T) as $\sigma = \frac{2\pi}{\mathrm{T}}$, φ the wave phase, h the local water depth and z the vertical coordinate pointing downwards (with $z = 0$ at the mean sea level). Introducing Eq. (1.1) and Eq. (1.2), and using the kinematic free surface boundary conditions, one obtains the dispersion relation, that relates k, σ and h (Laplace, 1776) as follows,

$$\sigma^2 = gk \tanh(kh). \tag{1.3}$$

The celerity of the wave $\mathrm{c} = \sigma/\mathrm{k}$ and the group celerity $\mathrm{c_g} = \partial\sigma/\partial\mathrm{k}$, which is the speed of the wave energy (Ardhuin and Orfila, 2018) can be readily obtained from the dispersion equation (Eq. (1.3)). It should be noted, that Eq. (1.3) can be simplified for deep waters (when $kh \gg 1$) as $\sigma^2 = gk$ (i.e. $c = 2c_g = \sqrt{g/k}$, dispersive waves) and for shallow waters (when $kh \ll 1$) as $\sigma^2 = gk^2h$ (i.e. $c = c_g = \sqrt{gh}$, non-dispersive waves).

Since the wave profile has a large spatiotemporal variability, the waves features cannot be easily characterized on a wave-by-wave basis (phase description). On the contrary, waves are often described through their statistical attributes during the periods of time where their characteristics can be assumed steady (phase averaging). The description of waves during a certain period is referred to as *sea state*. The sea state is described by a two-dimensional power spectral density $E(f, \theta)$ of the surface elevation, which provides the distribution of surface elevation variance over the range of frequencies f and directions θ. The evolution of the power spectral density considering a flat ocean bottom is given by:

$$\frac{\partial E(f,\theta)}{\partial t} + c_g \cdot \nabla E(f,\theta) = S(f,\theta), \tag{1.4}$$

where $S(f, \theta)$ contains the source and the dissipation terms (Ardhuin and Orfila, 2018).

Wave action modelling (Eq. (1.4)) aims to represent the random sea surface elevation into generalizing the sea state through Fourier spectrum, considering its slow time and space evolution (Priestley, 1965). Some available spectral models are able to include the wave phase information, especially relevant in shallow waters (Herbers and Burton, 1997). An idealized spectrum for wind waves was proposed by Priestley (1965), who constructed frequency spectra of wind waves for constant wind speeds in the absence of swell. However, during the Joint North Sea Wave Project experiment (Hasselmann et al., 1973), it was shown that the spectral representation by Priestley (1965) for developed waves in a limited fetch under strong winds tended to be characterized by sharp peaks. In this context, Hasselmann et al. (1973) modified the Pierson-Moskowitz spectrum through an artificial extension of the spectral density around the peak, resulting in the JONSWAP spectrum formulation:

$$E_{\mathrm{JONSWAP}}(f) = \beta_J \mathrm{SWH}^2 \mathrm{T_p}^{-4} \mathrm{f}^{-5} \exp\left[-1.25\left(\mathrm{T_p f}\right)^{-4}\right] \gamma^{\exp\left[\frac{-(\mathrm{T_p f}-1)^2}{2\sigma^2}\right]}, \tag{1.5}$$

$$\beta_J \approx \frac{0.06238}{0.23 + 0.0336\gamma - 0.185\left(1.9+\gamma\right)^{-1}} \left[1.094 - 0.01915 \ln\gamma\right], \tag{1.6}$$

$$\sigma = \begin{cases} 0.07 & : \quad f \leq f_p \\ \\ 0.09 & : \quad f > f_p \end{cases}, \tag{1.7}$$

with γ the "peak enhancement" factor, the significant wave height (SWH) defined as the average of the highest $1/3$ waves, and the peak period ($\mathrm{T_p}$) defined as the wave period associated with the most energetic waves.

Some of the most common statistical parameters used to describe a sea state are the SWH, T_p and the root mean square wave height, $\mathrm{WH_{RMS}} = \sqrt{\overline{\mathrm{WH}^2}}$, which can be approximated as $\mathrm{SWH}/\sqrt{(2)}$. It is usual to work with the one-dimensional power spectral density ($E(f) = \int E(f,\theta)\, d\theta$) that only depends on the frequency range.

Nowadays, the main physical processes driving the waves spectra evolution are well known, including non-linear interactions, dissipation, whitecapping and wave breaking (Ardhuin et al., 2009). However, these processes involve complex and turbulent air-sea interactions and numerical models based on empirical parametrizations are presently under development (Ardhuin et al., 2010; Ardhuin and Orfila, 2018).

1.3 Waves-generated Ocean Currents

Oceanic circulation results from movements of fluid in response to internal forces and external forces. At the ocean surface, total currents velocities can be assessed by the mathematical description of the time-dependent ocean surface in the rotating Earth (LeBlond and Mysak, 1981). However, depending on the process of interest, it is common to apply some approximations. One of them is the Boussinesq approximation which assumes that the ocean motions can be described by an isentropic state of reference where the salinity and the entropy are constant, $i.e.$, ignoring density differences except when they are multiplied by g, as well as the potential density and the potential temperature. In addition, it considers that the fluid is at rest relative to the Earth's rotation. The Boussinesq approximation is reasonable for layers very near to the free surface because the entropy of a given fluid element varies only as a result of molecular diffusion and of radiative transfer (Phillips, 1966). Under this assumption, the governing equations for the fluid are given by the mass and momentum conservation equations in terms of velocity, $\mathbf{U}$, pressure, p and density, ρ, as:

$$\nabla \cdot \mathbf{U} = 0 \tag{1.8}$$

and

$$\rho \frac{D\mathbf{U}}{Dt} + \rho\, 2\, \mathbf{\Omega} \times \mathbf{U} + \nabla p - \rho \mathbf{g} = \mathbf{F}, \tag{1.9}$$

where in Eq. (1.9), the first term on the left hand represents the mass-acceleration, the second, the Coriolis force, which is related to the Earth's angular velocity $\mathbf{\Omega}$, the third term is the pressure gradient and the last one the density in the vertical. The right hand side term is the resultant of all the frictional forces acting on a unit volume of the fluid, being the most important the molecular viscosity (Phillips, 1966). Moreover Eq. (1.8) is obtained assuming incompressibility of water. When the viscous effect is significant, and assuming the ocean fluid as isotropic, incompressible and Newtonian, the frictional force per unit volume can be approximated as,

$$\mathbf{F} = \mu \nabla^2 \mathbf{U}, \tag{1.10}$$

with $\mu = \rho A_z$, being the dynamic molecular viscosity and being A_z the kinematic viscosity. These kind of viscous forces are normally relevant in very small-scale of

motions where the changes in the velocity are limited to distances of the order of $\mu/\rho\mathbf{U}$ (Phillips, 1966).

Since waves are irrotational, there exists a velocity potential Φ (Eq. (1.2)) so that $\mathbf{U} = \nabla\Phi$ and thus the mass conservation (Eq. (1.8)) reduces to the Laplace equation:

$$\nabla^2\Phi = 0, \tag{1.11}$$

expressed from the Eulerian point of view. However, it is possible to develop a further description from a Lagrangian point of view which expresses the dynamical equations following the fluid a parcel motion. For that, the dynamical problem can be solved from the beginning in Lagrangian terms or deriving the Lagrangian properties of flow from the Eulerian solution used in the Thesis.

Denoting the Lagrangian velocity of a fluid element $\mathbf{U_L}(\zeta(\mathbf{t}), \mathbf{t})$ at the trajectory $\zeta(\zeta_\mathbf{0}, t)$ defined as:

$$\zeta(\zeta_\mathbf{0}, t) = \zeta_\mathbf{0} + \int_0^t \mathbf{U}_L(\zeta(t'), t')\, dt'. \tag{1.12}$$

The trajectory $\zeta(\zeta_\mathbf{0}, t)$, defined in Eq. (1.12), depends on the initial position $\zeta_\mathbf{0}$ at time $t = 0$ and the Lagrangian velocity $\mathbf{U_L}(\zeta(t), t)$.

According to the linear theory taking into account the propagation direction ($\mathbf{x}$) and the depth (z), the displacement of a water parcel under the wave integrated in a wave period (T) is zero. However, comparing the Eulerian ($\overline{\mathbf{U}(\mathbf{x}, t)}$) and the Lagrangian $\overline{\mathbf{U_L}(\zeta(t), t)}$ velocities at location $\mathbf{x}$ for a time t there is a difference:

$$\mathbf{U_s}(\mathbf{x}, t) = \overline{\mathbf{U_L}(\zeta(t), t)} - \overline{\mathbf{U}(\mathbf{x}, t)} = \overline{\mathbf{U}(\mathbf{x}, t) + (\zeta - \mathbf{x}) \cdot \nabla_\mathbf{x}\mathbf{U}(\mathbf{x}, t) + \cdots} - \overline{\mathbf{U}(\mathbf{x}, t)}, \tag{1.13}$$

which is related to the Stokes drift (Stokes, 1880) and has been obtained by approximating the Lagrangian velocity through a first order Taylor expansion around the position $\zeta_0 = x$. The first order term is taken into account since its ratio with $\mathbf{U}(\mathbf{x}, t)$ has the same order of magnitude than the wave slope (Phillips, 1966). Focusing on the first term, the Eulerian and Lagrangian velocities are identical, being derived from Eq. (1.2), and take the following expression,

$$\left.\begin{array}{ll} x) & u(\mathbf{x}, t) = \frac{\partial\phi}{\partial x} = \frac{\sigma a \cosh[k(z+h)]}{\sinh(kh)} \cos(kx - \sigma t) \\ z) & w(\mathbf{x}, t) = \frac{\partial\phi}{\partial z} = \frac{\sigma a \sinh[k(z+h)]}{\sinh(kh)} \sin(kx - \sigma t) \end{array}\right\}, \tag{1.14}$$

which is equivalent to the solution of the Laplace equation (Eq. (1.11)) after applying the kinematic and dynamic free surface condition and the bottom boundary condition.

Taking the x-axis along the propagation direction and integrating the Eq. (1.14) in time, the fluid element describes an elliptic orbit, where the magnitude of its semi-axes is defined as,

$$\left.\begin{array}{ll} x) & \zeta_x = \int_0^t u(\mathbf{x}, t)dt = -a\frac{\cosh[k(z+h)]}{\sinh(kh)} \sin(kx - \sigma t) \\ z) & \zeta_z = \int_0^t w(\mathbf{x}, t)dt = a\frac{\sinh[k(z+h)]}{\sinh(kh)} \cos(kx - \sigma t) \end{array}\right\}. \tag{1.15}$$

In this way, the mean value during a wave period of the first-order term of the Eq. (1.13) is,

$$\left.\begin{array}{ll} x) & \overline{u_s(\mathbf{x},t)} = \frac{\sigma k a^2 \cosh\left[2k(z+h)\right]}{2\sinh^2(kh)} \\ z) & \overline{w_s(\mathbf{x},t)} = 0 \end{array}\right\}. \tag{1.16}$$

From Eq. (1.16), it is clear that the motion of the particle is not exactly a closed ellipse (Fig. 1.3), but there is a mean drift along the direction of the wave propagation. This is a second-order velocity, firstly identified by Stokes (1880). It is usually defined as the difference between the Eulerian and the Lagrangian wave averaged motion for a particle located below the waves.

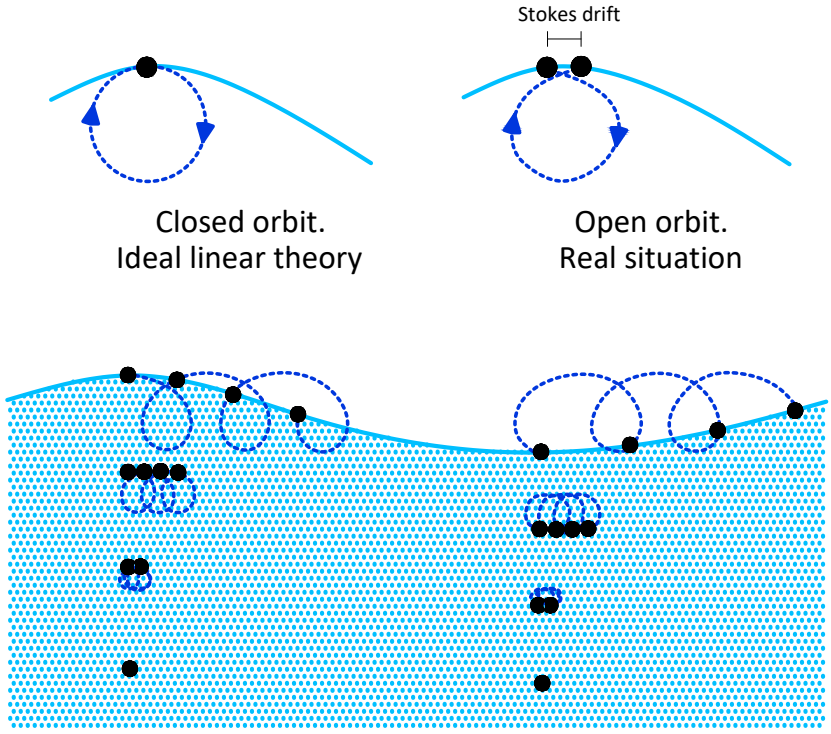

Figure 1.3 *Scheme of Stokes drift.*

The Stokes drift introduces a displacement of the fluid parcels that has to be considered in the surface ocean dynamics.

1.4 Spatiotemporal scales of wave variability

According to the temporal and spatial scales of interest, in this Thesis, we distinguish waves at different scales: large scale (characteristics periods of decades and spatial scales of thousand of km) where climatic phenomena can be analyzed; regional open ocean scale (seasonal scales and hundreds of km) where the basin and sub-basin wave variability is analyzed, and coastal scale (scales of hours-days and km(s)) where a vast amount of energy dissipates, producing large modifications at the shore.

1.4.1 Large scale

This scale covers characteristic time periods of decades, with a large oceanic spatial domain. The wave conditions are characterized through long-term statistics (usually the SWH, the return period related to its value and its long-term distribution), which requires long time periods of observation over large areas. The extreme-value theory provides a fundamental support for the analysis and interpretation of such scales.

To estimate the long-term extreme values of the SWH, three different approaches are usually applied: 1) the initial-distribution; 2) the peak-over-threshold; and 3) the annual-maximum methods. Through them, we can evaluate the probability of exceedance and the return period of a specific event (Holthuijsen, 2007). These approaches should fulfill some theoretical restrictions, being the most important one that the extreme values have to be independent while they have to be identically distributed. Sometimes, this restriction can involve a challenge since the most extreme values of waves heights usually belong to the same event and they are strongly correlated. This is especially notable when using data with time resolution smaller than one day.

At large scales, the atmospheric circulation presents a well-defined variability. This variability displays circulation systems and weather patterns, which can be defined through climatic phenomena that affect not only the regions of the ocean where they directly act, but also remote areas through "teleconnections" (Wallace and Gutzler, 1981). The use of teleconnections to study the large scale waves, allows us to gain an extensive knowledge about their temporal (interannual and interdecadal) and spatial (ocean basins and even planetary-scale) variability, facilitating the assessment of the extreme waves dynamics (Martínez-Asensio et al., 2016).

According to the National Weather Service of Climate Prediction Center of the National Oceanic and Atmospheric Administration (NOAA), the main four climatic modes of variability in the Northern Hemisphere are represented by the North Atlantic Oscillation (NAO), the East Atlantic (EA), the East Atlantic-Western Russian (EA/WR) and the Scandinavian (SCAND) indices (Barnston and Livezey, 1987). These indices are constructed using a method based on the Rotated Principal Component Analysis (RPCA) implemented by Barnston and Livezey (1987). The RPCA is applied to monthly mean standardized 500-mb height anomalies from January 1950 to December 2000 in order to define the primary leading un-rotated modes (Barnston and Livezey, 1987). The most notable teleconnection pattern is the NAO, which is defined by a north-south dipole of mean standardized 500-mb height anomalies with one center located in Iceland (Low) and the other one in Azores (High) (Hurrell et al., 2003). NAO is connected with the atmospheric mass redistribution between these two centers. The positive phase of NAO indicates below-normal 500-mb geopotential heights and sea level pressure in high latitudes of the North Atlantic and above-normal geopotential heights and sea level pressure over the central North Atlantic, the eastern North America and western Europe (see the positive phase of NAO in Fig. 1.4). The phase variations on the NAO index cause large effect on the wind speed and direction, usually blowing from eastern North America to western Europe, and dramatically influencing on the number of storms and their intensity, trajectories and weather over the Atlantic Ocean (Van Loon and Rogers, 1978; Hurrell, 1995; Marshall et al., 2001). This mode of teleconnection presents a strong interseasonal and interannual variability, in addition to a significant multi-decadal variability during winter (Chelliah and Bell, 2004).

The EA index is the second prominent mode describing the low-frequency variabil-

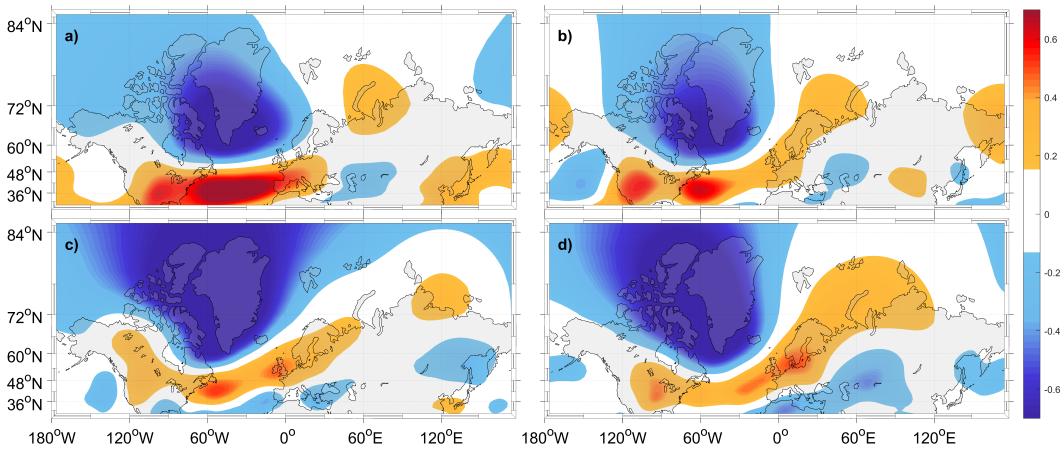

Figure 1.4 *Temporal correlation between monthly NAO index values and the monthly standardized* 500*-mb geopotential height anomalies from* 1950 *to* 2020 *for a) January, b) April, c) July and d) October.*

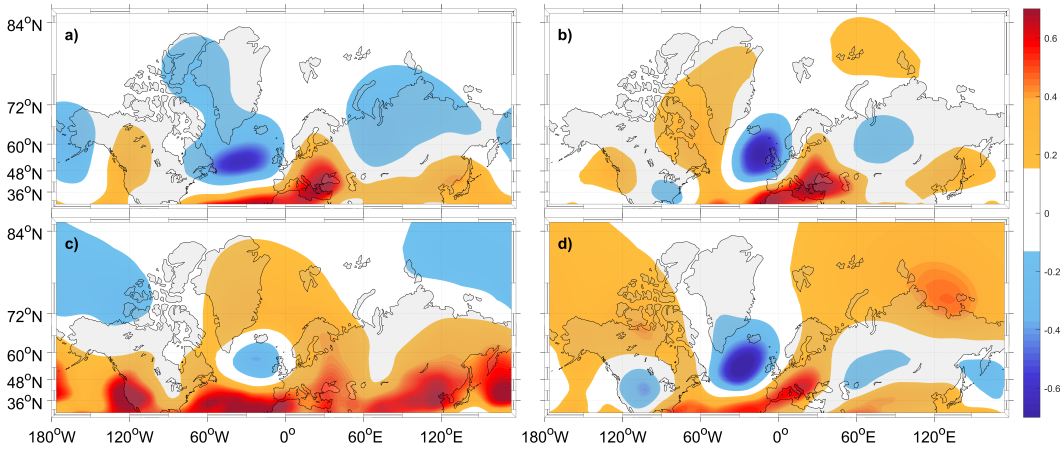

Figure 1.5 *Temporal correlation between the monthly EA index values and the monthly standardized* 500*-mb geopotential height anomalies from* 1950 *to* 2020 *for a) January, b) April, c) July and d) October.*

ity over the North Atlantic Ocean. It is also represented as the 500-mb geopotential height anomaly of a north-south dipole over the North Atlantic Ocean, but unlike NAO, the centers are located further south than in the NAO dipole. It should be noted that, the lower-latitude center is related to the modulations in the subtropical ridge intensity and location. The positive phase of EA is associated with above-normal 500-mb geopotential heights and pressure in Europe and below-normal heights and pressure at the southeast side of Greenland (see the positive phase of EA in Fig. 1.5) that, depending on the season, are closer. The EA mode presents a strong multidecadal variability.

The third mode over the North Atlantic Ocean is the EA/WR, that consists of four main anomaly centers. Its positive phase is associated with positive standardized geopotential height anomalies at 500-mb located over Europe and negative anomalies over the central North Atlantic (see Fig. 1.6). This mode displays a variability of 5 years although not as clear as the other phenomena.

Finally, the SCAND mode is defined by a primary circulation center over Scandinavia, with weaker centers of opposite sign over western Europe and eastern Russia/

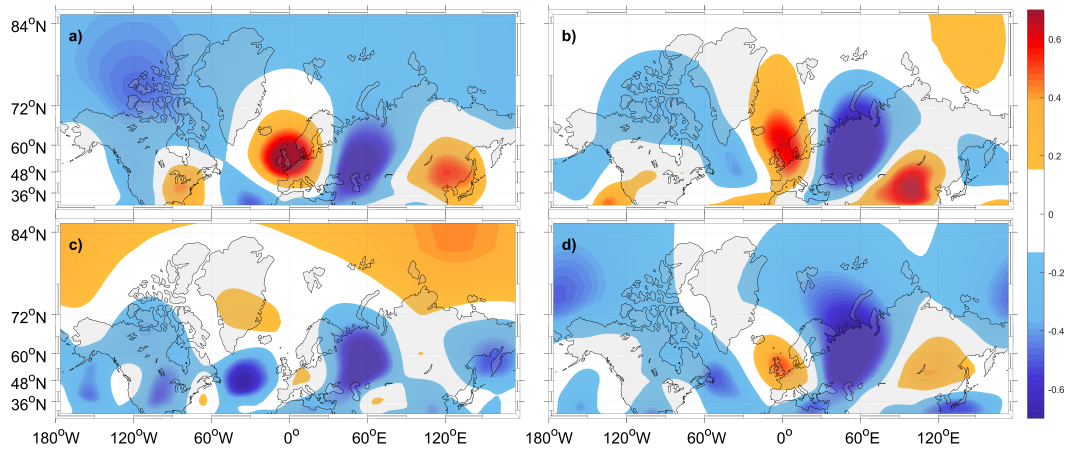

Figure 1.6 *Temporal correlation between the monthly EA/WR index values and the monthly standardized* 500*-mb geopotential height anomalies from* 1950 *to* 2020 *for a) January, b) April, c) July and d) October.*

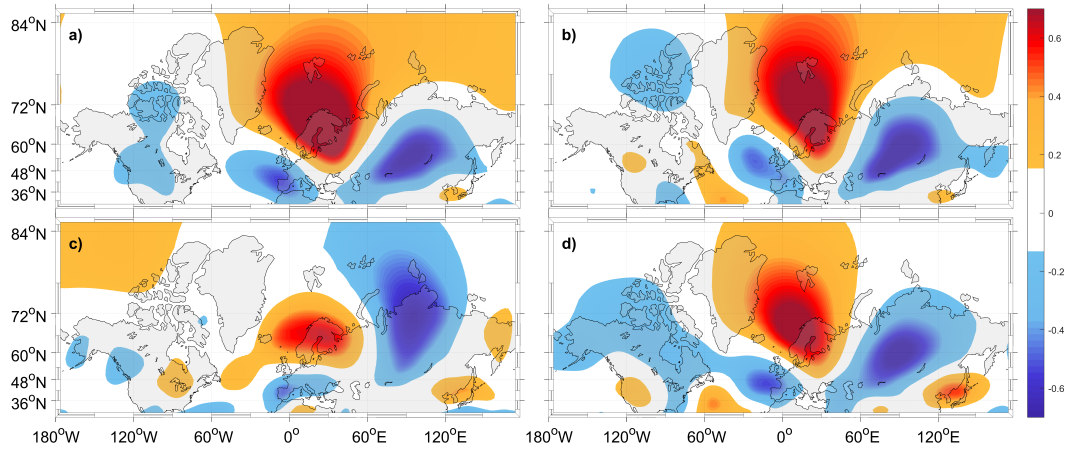

Figure 1.7 *Temporal correlation between the monthly SCAND index values and the monthly standardized* 500*-mb geopotential height anomalies from* 1950 *to* 2020 *for a) January, b) April, c) July and d) October.*

western Mongolia (see the positive phase of SCAND in Fig. 1.7). The positive phase of the SCAND index is associated with below-average 500-mb geopotential height anomalies across central Russia and also over western Europe; and with above-average geopotential height anomalies over Scandinavian peninsula. The SCAND mode shows a strong multidecadal variability.

1.4.2 Regional and seasonal scale

This scale refers to the seasonal wave variability at the basin or sub-basin domains, such as the Mediterranean Sea.

The Mediterranean Sea is a large semi-enclosed basin located between 30°N and 45°N and, 6°W and 37°E (Fig. 1.8). The Mediterranean basin presents a strong anthropogenic pressure (Lionello et al., 2006) with large impacts on the marine ecosystem functioning (Hulme et al., 1999). In addition, it is one of the most selected touristic destinations, increasing the concentration of people along the coastal areas during summer period (UNWTO 2019).

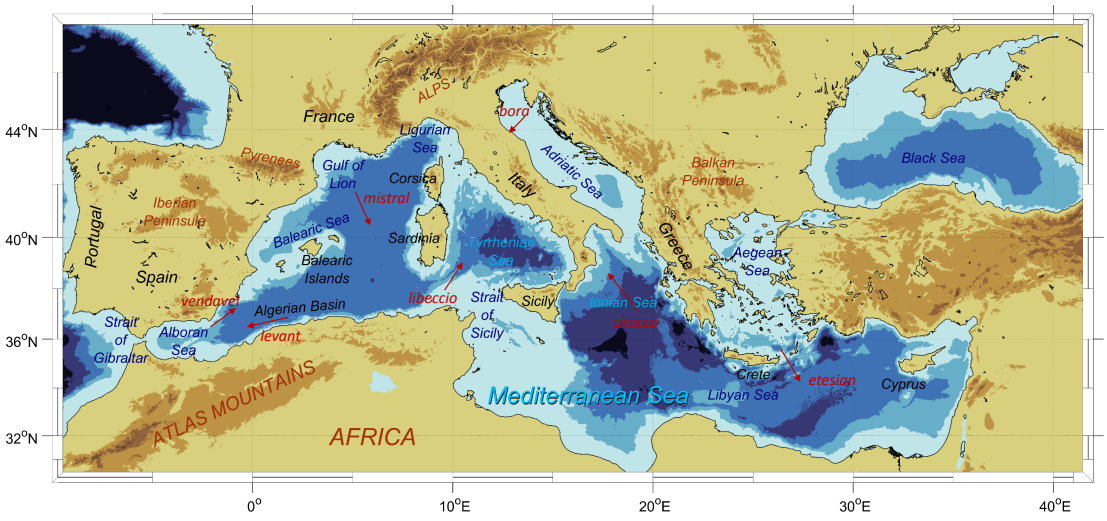

Figure 1.8 *Mediterranean Sea. Color indicates the bathymetry from deep (dark) to shallow (light) blue. Red arrows represent the main wind directions.*

The Mediterranean Sea has an average depth of 1500 m and an area of 2.5 million km^2. It can be divided into two parts by the Strait of Sicily, the eastern and western sub-basins. The Sicily channel, with 145 km length and a maximum depth of 316 meters constrains the flow from one side to the other one and the dynamics within each sub-basin. At the west, the Mediterranean is connected with the Atlantic Ocean through the Strait of Gibraltar with a length of 14.3 km and variable depths between 300 to 900 meters. The mean inflow of Atlantic waters through the Gibraltar Strait is 0.81 ± 0.06 Sv (Soto-Navarro et al., 2010).

The surface circulation in the Mediterranean Sea is the result of a wide range of processes interacting at several spatial and temporal scales (Robinson et al., 2001). The dynamics is conditioned by a complex topography, with the presence of high submarine mountains, canyons, peninsulas, capes and numerous islands resulting in a intricate bathymetry. The large scale circulation is driven by a thermohaline gradients (Malanotte-Rizzoli et al., 2014) governed at the west by the inflow of Atlantic waters flowing eastwards and returning to the Atlantic as intermediate waters after gaining *in-situ* densification by air-sea interaction as they travel throughout the entire basin (Cacho et al., 2000). The general circulation forms two large cyclonic paths delimited by the Sicily Strait. Many permanent and intermittent mesoscale features such as eddies, gyres and fronts emerge in the two sub-basins as the result of the geostrophic balance (Poulain et al., 2012) (Fig. 1.9). At smaller scales, there is a rich spectrum of submesoscale dynamics that is presently as the subject of many studies.

Weather in the Mediterranean is largely controlled by the passage of cyclonic systems and their associated fronts, whose occurrence and frequency is to a large extent determined by the distributions of the high mountains, the temperature gradient at the sea surface and the orientation of baroclinic zones (Ulbrich et al., 2012). These processes are responsible for the intensification of strong regional winds locally known as “mistral”, “tramontane”, “libeccio”,“vendavel”, “levant”, “bora”, “sirocco” and “etesian” (Zecchetto and De Biasio, 2007; Herrmann et al., 2011) (Fig. 1.8). The Mediter-

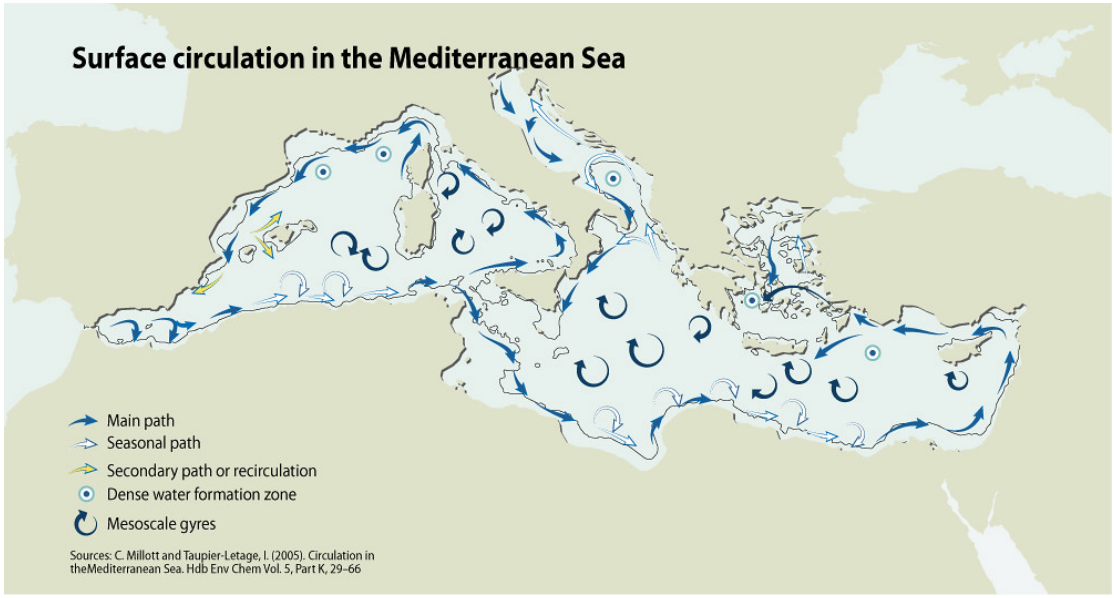

Figure 1.9 *Surface circulation scheme at the Mediterranean Sea. Source: GRID Arendal www.grida.no/resources/5915.*

ranean wind patterns are characterized by a clear North-South direction. The most intense winds in the western sub-basin are found offshore of the Gulf of Lion and focusing on the eastern Mediterranean, in the central Aegean Sea; both during winter seasons (Soukissian et al., 2018) although in the eastern sub-basin there is also strong winds during summer. The regional winds in the Mediterranean Sea have shorter lifetimes than in the Atlantic Ocean and they develop and evolve within a range of spatial and temporal scales smaller and shallower than in other oceanic systems (Trigo et al., 1999). However, they are able to induce extreme waves in the basin, especially when they act over large fetch areas, such as those produced by the "mistral" and "tramontane" blowing southwards the Gulf of Lion (Zecchetto and De Biasio, 2007; Obermann et al., 2018).

The climate variability in the Mediterranean Sea is dominated by intense north-south storms in winters and by the Azores anticyclone in summers, achieving intermediate conditions during spring an autumn with surface cyclogenesis usually enhancing eastwards storms coming from Atlantic Ocean (Trigo et al., 2002).

Regarding the temporal variability of the more severe sea states at the Mediterranean Sea, the maximum values of the SWH are found during winter seasons (December-January-February-March) with monthly averaged SWH values around 6.5 m in the western sub-basin and around $4 - 4.5$ m in the eastern and central Mediterranean Sea (Sartini et al., 2017). In the western sub-basin, the most severe sea states conditions reach SWH values close to 10 m, which are associated with strong meteorological perturbations, particularly, at the surroundings of the Gulf of Lion, as a consequence of intense winds and close to the Algerian basin thanks to the long wind fetches (Sartini et al., 2017). In the eastern Mediterranean Sea, the sea states achieve strong values into the Aegean Sea as a result of intense "etesian" winds. In addition, high values of SWH in the Ionian and Libyan Sea are connected to some located cyclogenesis systems (Trigo et al., 1999). It should be noted that, although the sea states are usually weaker during summer, there are some situations where waves with SWH values up to 3 m are found in the Levantine sub-basin (Lionello et al., 2008).

1.4.3 Coastal scale

At coastal scales, the spatial and temporal scales of interest are below kilometers and between hours and days. At these scales, waves can be analyzed using both, phase averaged or phase resolving approaches.

Coastal areas are environments where waves suffer the majority of processes from shoaling, breaking, diffraction and refraction either by bottom or morphological features. Processes of wave-current interactions are also intensified (Holthuijsen, 2007). Shoaling phenomenon changes the wave height along its direction of propagation from energy conservation. In shallow waters, waves become less dispersive, the wavelength decreases when feeling the bottom and the wave height increases. In addition, wave direction changes along the ray propagation due to the depth-induced variations in the phase speed along the wave crest in the lateral direction by refraction process. The crest moves faster in deeper water (moving a larger distance) than in shallow water. The effect is that waves always turn towards the region with lower propagation speed (Snell law). Normally, these processes tend to change the wave amplitude and direction slowly. Finally, the most relevant nonlinear process of waves in coastal areas is depth-induced breaking. It occurs when the horizontal velocity of the particles located at the wave crest is higher than the speed of the wave, waves become sharper and the vertical acceleration of the wave exceeds the value of gravity.

The above described depth-induced processes produce a large input of energy in coastal areas that is dissipated through boundaries, inducing large morphological changes and sediment transport.

1.5 Plan of Thesis

This PhD thesis is structured in seven chapters. After this general introduction, **Chapter 2** briefly describes the data and the methodology used, including the relevant tools and concepts which will be explained in more detail within each chapter.

The following chapters analyze the effects of ocean surface waves on the Mediterranean Sea dynamics from the large scale towards the regional and coastal scales.

Chapter 3 presents an assessment of extreme waves in the Mediterranean Sea and their relation with several climatic patterns of variability acting in the Northern Hemisphere. The methodology has been validated in the North Atlantic Ocean, since extreme waves and the atmospheric variability are well-known in this region.

Chapter 4 analyzes the temporal and spatial variability at regional scale of the surface dynamics at the Mediterranean Sea. Surface velocity currents are computed for the geostrophic and the ageostrophic components (wind- and wave-induced flow). We identify the areas where ageostrophy has a large impact on the surface dynamics through on objective regionalization of the basin according to the relative contributions of the geostrophic, and the wind- and waves-induced surface velocities.

Chapter 5 addresses a regional assessment of the impact of the ageostrophic velocity components on the transport and mixing properties. We analyze the anisotropy of the flow based on the relative dispersion statistics.

Chapter 6 analyzes the effects of extreme waves in a coastal system. In this chapter, the morphodynamical behavior of a semi enclosed beach is studied during and after a storm group highlighting the impact of extreme waves on the sediment transport at small temporal scales.

Finally, in **Chapter 7** the main conclusions of this Thesis are presented.

Chapter 2

Data and methods

In order to properly characterize the wave variability, a wide range of spatial and temporal scales needs to be analyzed. In this Thesis, we use complementary methodological approaches combining a suite of datasets at different spatiotemporal scales in the Mediterranean Sea, ranging from decades to hours, and from the whole basin to coastal scale. In this Chapter we summarize the different datasets and methods applied, explaining what they are used for and in what way.

2.1 *In-situ* measurements

- **Wave buoys:** The dataset of wave buoys from Copernicus Marine environment monitoring service (CMEMS, https://marine.copernicus.eu/, last access: $02/07/2020$ at $15{:}41$) is collected in Chapter 3 of this Thesis for validating the *WAVEWATCH III 30-year Hindcast Phase 2* dataset. For that purpose, data of 13 buoys for the North West Atlantic and 11 for the Mediterranean Sea were assembled (see the location of the buoys in Fig. 3.1)

- **Climate data**: In Chapter 3, the large-scale relationship between main atmospheric patterns variability and the extreme waves is studied in the North Atlantic Ocean and in the Mediterranean Sea through the climatic indices obtained from National Oceanic and Atmospheric Administration Climate Prediction Centre (https://www.cpc.ncep.noaa.gov/data/teledoc/telecontents.shtml, last access: $27/02/2020$ at $13{:}34$). The dataset consists of monthly mean values of North Atlantic Oscillation (NAO), East Atlantic (EA), East Atlantic-Western Russian (EA/WR) and Scandinavia (SCAND) indices, since these teleconnections control the major atmospheric circulations close to European coasts (Barnston and Livezey, 1987). The procedure followed to calculate the teleconnection indices is based on the Rotated Principal Component Analysis (RPCA) applied to monthly mean standardized 500-mb height anomalies obtained from the Climate Data Assimilation System (NCEP/NCAR).

- **Lagrangian drifters**: An available dataset of 1632 Lagrangian drifter covering the Mediterranean Sea from 1986 to 2006 is provided by the Italian National Institute of Oceanography and Experimental Geophysics (OGS). This dataset is a compilation of the drifter trajectories deployed by different institutions. Most of them belong to three types: Surface Velocity Program (SVP), Coastal Ocean Dynamics Experiment (CODE) system and Compact Meteorological and Oceano-

graphic Drifter (CMOD). SVP drifters consist of a surface buoy that is tethered to a holey-sock drogue, centered at a nominal depth (0, 1, 12.5, 15, 30, 45, 50 and 75 m) (Sybrandy, 1991). CODE drifters are made up of a vertical slender 1-m-long negatively buoyant tube with four drag producing vanes extended radially from it over its entire length and four small spherical surface floats attached to the upper extremities of the vanes to provide buoyancy (Davis, 1985). And finally, CMOD drifters are sonobuoys with a 100-m-long drogue, which consist of a 60-cm-long aluminum cylindrical hull with a flotation collar (Matteoda and Glenn, 1996). In Chapter 5, data of 690 1-m drogue drifters trajectories database (Menna et al., 2017) have been used in several Lagrangian analyses of the sea surface dynamics. A total of 15 SVP and 675 CODE drifter trajectories have been analyzed during 1994 - 2005.

- **AWACs**: The hydrodynamical data of Cala Millor beach were collected with wave recorders (acoustic wave and current meter, AWAC) moored at different depths. In Chapter 6, only the data moored at $25\,\mathrm{m}$ depth is employed. The provided wave data are Significant Wave Height (SWH), peak period and mean wave direction with a temporal resolution of 1 hour (http://www.socib.es; last access on: 24 October 2018).

- **High resolution bathymetries**: The morphodynamic analysis of the Cala Millor beach performed in Chapter 6, is carried out with data from the periodic beach monitoring program of Balearic Islands Coastal Observing and Forecasting System, SOCIB (12 June 2014) and the RiskBeach campaign (17 March 2014) performed by the SOCIB, the Mediterranean Institute for Advanced Studies (IMEDEA) and the Institute of Marine Sciences (ICM-CSIC). A DGPS–RTK with submetrical resolution (having a horizontal accuracy of around $8\,\mathrm{mm}$ and a vertical accuracy of around $15\,\mathrm{mm}$) is used in order to collect the bathymetry data (Tintoré et al., 2013). The topographic surveys of RiskBeach campaign consisted of nine daily bathymetric profiles (see their locations in Fig. 6.1) from 17 to 26 March 2014.

- **Sediment**: Sediment samples of Cala Millor beach were picked up along a central section of the beach (see locations Fig. 6.1) from 17 to 26 March 2014.

2.2 Remote sensing measurements

- **Sea Level Anomaly**: Through the combination of multi-satellite missions available (Jason-3, Sentinel-3A, HY-2A, Saral/AltiKa, Cryosat-2, Jason-2, Jason-1, T/P, ENVISAT, GFO, ERS1/2), CMEMS provides the Sea Level Anomaly (SLA) fields that are used in Chapter 4 and Chapter 5 of this Thesis in order to calculate the geostrophic velocity fields in the Mediterranean Sea. SLA data are processed by the DUACS multimission altimeter data processing system (for more details of this method see Dibarboure et al., 2008) providing a regional L4 gridded product of absolute geostrophic velocities (https://resources.marine.copernicus.eu/?option=com_csw&view=details&product_id=SEALEVEL_MED_PHY_L4_REP_OBSERVATIONS_008_051; last access on: 7 February 2019). This dataset has a spatial resolution of 0.125° with a daily temporal resolution.

- **Video-images**: The SIRENA/Ulises system (Nieto et al., 2010; Simarro et al., 2017) is operating since 2009 in Cala Millor. The system is composed of five charge-coupled device (CCD) cameras (Gómez-Pujol et al., 2013) connected to a server acquiring images at 7.5 Hz during the first 10 min of each hour, and providing three hourly products (snapshot, mean, variance and time-stack images). The five cameras cover an alongshore distance of around 1.7 km. In Chapter 6 the time-stack images are used in order to estimate the bathymetric profile of the beach.

2.3 Numerical models

- **Waves**: The wave model used in Chapter 3 is the *WAVEWATCH III 30-year Hindcast Phase 2*, a third generation wind-wave model from National Center for Environmental Prediction (NCEP) (Chawla et al., 2012). It solves the spectral action density balance equation with random phase for wavenumber-direction spectra. This model is forced with 10-m height wind fields from the NCEP Climate Forecast System Reanalysis and Reforecast (CFSRR). This hindcast provides data each 3 hours from 1979 to 2009 with a spatial resolution for the North West Atlantic Ocean of 0.5° and for the Mediterranean Sea of 0.167°. In Chapter 4 and Chapter 5, the reanalysis implemented is ERA-Interim. It obtains the wave fields running the WAM wave model (Group, 1988) with the assimilation of available measurements of ERS1 satellite wave height data (Janssen et al., 1997). This global climate reanalysis covers the period since 1979 until 2019 with a temporal resolution of 6 hours and a spatial resolution of 0.125° in the Mediterranean Sea. Finally, in Chapter 6, the offshore wave conditions at 50 m in depth (significant wave height, peak period and mean wave direction) are obtained from a reanalysis of a 60-years wave model output produced by the Spanish Harbor Authority. The temporal resolution of the data is 3 hours (http://www.puertos.es/es-es/oceanografia/Paginas/portus.aspx, last access: 29 November 2018).

- **Wind and Sea Level Pressure**: In Chapter 3, the 10-m height wind and sea level pressure (SLP) considered fields are obtained from NCEP-CFSRR. This model represents the global ocean-atmosphere interaction through a coupled atmosphere-ocean-land surface-sea ice system over the period from January 1979 to March 2011, extending as an operational real-time product (Saha et al., 2010). This atmospheric model delivers wind velocity data each 3 hours with a spatial resolution of 0.167° and hourly SLP data in a regular grid of 0.5°. In Chapter 4 and Chapter 5, 10 -m above the sea surface wind velocities are provided by the ERA-Interim reanalysis (Dee et al., 2011) through local GRIB code of the European Centre for Medium-Range Weather Forecasts (ECMWF) covering the period between 1979 and 2019 with a temporal resolution of 6 hours and a spatial resolution of 0.125° in the Mediterranean Sea (Berrisford et al., 2011).

- **Beach morphodynamic**: Morphological beach evolution analyzed in Chapter 6 is carried out using the XBeach (eXtreme Beach behavior) model (Roelvink et al., 2009). This numerical model solves the action balance equation (Eq. (1.4)) equation in 2D for short waves, long waves and mean flow. In addition, this model calculates the sediment transport and the morphological changes of the nearshore area, beaches, dunes and backbarrier during storms. XBeach has a

hydrostatic and a non-hydrostatic mode. In Chapter 6, the hydrostatic mode is used, where the short wave amplitude variation is solved separately from the long waves, currents and morphological change. The main advantage of this mode is its shorter computational time, since it does not simulate the phase of the short waves.

2.4 Analysis methods

- **Tools to analyze the spatiotemporal variability**
  - **Empirical Orthogonal Functions**: EOFs algorithm decomposes efficiently a signal into representative modes through the empirical identification of the eigenfunctions that best describe the variance of the data (Weare and Nasstrom, 1982; Thomson and Emery, 2014). This technique is called empirical because it finds the optimum decomposition with none assumptions on either spatial or temporal behavior, formulating an eigenvalue problem involving the two-point spatial covariance matrix. The EOF eigenmodes are uncorrelated each other, and they are ordered according to the percentage of the total variance described. This technique allows to characterize a significant part of the total variance collecting only the first few modes, which means less storage space. In addition, EOF enables to isolate the phenomena associated with each mode differing spatial/temporal scales (Kaihatu et al., 1998). In Chapter 3, EOFs are used in order to evaluate the spatiotemporal variability of the extreme wave height in winter seasons.
  - **Self-Organizing Maps**: SOMs is a statistical method based on an unsupervised machine learning algorithm applied to an artificial neuronal network (Kohonen, 1982). This technique reduces large input datasets to a lower dimensional network of units (neurons), implementing a nonlinear mapping method. The input dataset is introduced in a neural network that is modified along an iterative procedure where at the end, the probability density function of the input sample is approximated relating each neuron with a reference pattern (Liu et al., 2006). One of the assets of SOMs is the dataset topology conservation, improving the display of the patterns. This tool can be applied in both spatial and temporal domains, depending on the features to be analyzed. Temporal SOMs is deployed in Chapter 4 in order to disclose a regionalization of the Mediterranean Sea according to the temporal variability of each component of the oceanic currents velocity.
- **Sea surface circulation governing equations**: Chapter 4 presents the ocean surface dynamics equations as the sum of geostrophic and ageostrophic velocities. The geostrophic component represents the equilibrium between the Coriolis force and the pressure gradients, while the ageostrophic velocity is obtained from the solution of the momentum equation in the steady state with the interaction of wind-stress, Coriolis force and waves which produce a mean momentum in waves propagation direction. In Chapter 4, 25 years of 6-hourly data of ocean surface velocities are analyzed for the Mediterranean Sea at the resolution of $0.125°$. Chapter 5 also uses these velocity fields to perform a Lagrangian analysis of the surface dynamics in the Mediterranean Sea.

- **Wavelet transform**: This method allows to define the dominant modes of variability of an input dataset and how they change along the time, extracting the local-frequency information (Torrence and Compo, 1998). This tool implements a Fourier transform approach on a sliding temporal series segment returning frequencies at each time step (Kaiser, 1994), allowing the study of time series that contain non-stationary power at many different frequencies (Daubechies, 1990). We evaluate the cross-correlation between two time series through the wavelet coherence analysis. This method is based on the square wavelet cross-spectrum between two variables normalized by the individual cross-spectrum, allowing the identification of the frequency and time periods at which two signals are correlated. In Chapter 4, the wavelet transform and wavelet coherence analysis techniques are used in order to evaluate the dominant frequencies of the different components of oceanic currents and the relationships between climate indices and velocity patterns in the Mediterranean Sea.

- **Finite Size Lyapunov Exponents (FSLE)**: Transport and mixing properties in the sea surface flow are analyzed in Chapter 5 using FSLE (d'Ovidio et al., 2004; Hernández-Carrasco et al., 2011). FSLE was originally developed to describe the separation rate between two particle trajectories over any scale of motion following the definition (Aurell et al., 1997),

$$\lambda(\delta) = \left\langle \frac{1}{\tau(\delta, \alpha\delta)} \right\rangle \ln \alpha, \tag{2.1}$$

  where δ is the initial spatial separation of two particles, α is the amplification rate of separation and $\tau(\delta, \alpha\delta)$ the time required for the two particles to separate from δ to $\alpha\delta$. In this way, an analysis of the physical mechanism of the relative dispersion can be carried out computing the averaged scale dependence of $\lambda(\delta)$ curves over all the pairs of particle trajectories for each initial separation (δ) (Lacorata et al., 2001) in two-dimensions (horizontal) flows.

  Additionally, the characteristic scales in the Lagrangian dispersion can be analyzed independently for longitudinal and latitudinal directions splitting the FSLE into the zonal and meridional components as,

$$\lambda_x(\delta_x, \alpha) = \left\langle \frac{1}{\tau(\delta_x, \alpha\delta_x)} \right\rangle \ln \alpha \tag{2.2}$$

  and

$$\lambda_y(\delta_y, \alpha) = \left\langle \frac{1}{\tau(\delta_y, \alpha\delta_y)} \right\rangle \ln \alpha, \tag{2.3}$$

  respectively, denoting with δ_x and δ_y the initial distance between a pair of particles separated in the longitudinal or in the latitudinal direction. The final distance in both definitions, $\alpha\delta_x$ and $\alpha\delta_y$, is evaluated along one direction: longitudinal and latitudinal, respectively.

  Furthermore, the analysis of the flow structures organizing the flow transport can be obtained from the non-averaged λ values and using a rate of separation $\alpha \gg 2$. This provides an expression of the FSLE field that depends on the position and time as

$$FSLE(\mathbf{r}, t, \delta, \alpha) = \frac{1}{\tau} \ln \left(\frac{\delta_f}{\delta} \right), \tag{2.4}$$

being **r** the 2D position vector (x,y) and δ_f the final distance between the pair of particles ($\alpha\delta$).

Ridges of the FSLE field are heuristically considered as hyperbolic Lagrangian Coherent Structures (LCSs) (Haller and Yuan, 2000; Shadden et al., 2005). Ridges of forward FSLE identify the repelling LCS (stable manifold) and ridges of backward FSLE the attracting LCS (unstable manifold).

In Chapter 5, this technique is applied to evaluate the contribution to the geostrophic and ageostrophic induced currents to the horizontal transport and mixing properties in the Mediterranean Sea surface.

- **Lagrangian Anisotropy Index (LAI)**: The anisotropy in the dispersion process studied in Chapter 5 is computed with the LAI, defined as, (Espa et al., 2014),

$$LAI = \frac{\lambda_x(\delta_x) - \lambda_y(\delta_y)}{\lambda_x(\delta_x) + \lambda_y(\delta_y)}, \tag{2.5}$$

through the difference between the zonal and meridional dispersion rates ($\lambda_x(\delta_x)$ and $\lambda_y(\delta_y)$, respectively) at a given scale ($\delta_x = \delta_y = \delta$). This index is dimensionless and varies between -1 and 1, depending on whether the dispersion is dominated by latitudinal or longitudinal flows, respectively. The perfect isotropy is thus represented with the zero value.

Additionally, the spatial variability of the effect of the flow anisotropy on the LCS estimated in Chapter 5 is carried out through the Lagrangian Coherent Structure Anisotropy (LCSA), defined as:

$$LCSA(\mathbf{r}, t, \delta, \alpha) = \frac{FSLE_x(\mathbf{r}, t, \delta_x, \alpha) - FSLE_y(\mathbf{r}, t, \delta_y, \alpha)}{FSLE_x(\mathbf{r}, t, \delta_x, \alpha) + FSLE_y(\mathbf{r}, t, \delta_y, \alpha)}, \tag{2.6}$$

where FSLE_x (FSLE_y) is the finite size Lyapunov exponent obtained evaluating the pair separation only along the longitudinal, δ_x, (latitudinal, δ_y) direction. Depending on whether LCSA is positive or negative, the LCS is given by a higher contribution of the longitudinal or latitudinal stretching, respectively.

- **Bathymetry inversion through images**: In Chapter 6, the time-stack product from SIRENA/Ulises system (Nieto et al., 2010; Simarro et al., 2017) is used in order to infer the beach profile from the inversion of the wave dispersion relationship. Time-stack is defined as a pseudo-image built with all pixel observations taken in a period of time at predefined cross-shore transect. Thus, one of the dimensions of the time-stack image is the distance from the coastal line (space) and the other one is the number of frames (related to the time because SIRENA/Ulises system provides images at $7.5\,\text{Hz}$). Through the capture of the visible signature of the waves propagation at consecutive snapshots, the estimation of the bathymetry can be made, taking into account the linear wave theory for progressive waves along the observed cross-shore transect (Stockdon and Holman, 2000).

Chapter 3

Extreme waves and climatic patterns of variability in the eastern North Atlantic and Mediterranean basins

This chapter has been published as:

Morales-Márquez, V., Orfila, A., Simarro, G., and Marcos, M. (2020). Extreme waves and climatic patterns of variability in the eastern North Atlantic and Mediterranean basins. *Ocean Sciences*, 16(6): 1385-1398. doi: https://doi.org/10.5194/os-16-1385-2020.

Abstract

The spatial and temporal variability of extreme wave climate in the North Atlantic Ocean and the Mediterranean Sea is assessed using a 31-year wave model hindcast. Seasonality accounts for 50% of the extreme wave height variability in North Atlantic Ocean and up to 70% in some areas of the Mediterranean Sea. Once seasonality is filtered out, the North Atlantic Oscillation and the Scandinavian index are the dominant large-scale atmospheric patterns that control the interannual variability of extreme waves during winters in the North Atlantic Ocean; to a lesser extent, the East Atlantic Oscillation also modulates extreme waves in the central part of the basin. In the Mediterranean Sea, the dominant modes are the East Atlantic and East Atlantic/Western Russia modes which act strongly during their negative phases. A new methodology for analyzing the atmospheric signature associated with extreme waves is proposed. The method obtains the composites of significant wave height (SWH), mean sea level pressure (MSLP) and 10 m-height wind velocity (U_{10}) using the instant when specific climatic indices have a stronger correlation with extreme waves.

3.1 Introduction

The accurate assessment of extreme wind-wave conditions is essential for human activities e.g., maritime traffic and wave energy generation and is a major source of coastal hazards. Extreme waves influence the upper ocean by enhancing vertical mixing through the Stokes layer (Polton et al., 2005). Extreme waves reaching port areas also determine the design and operation of coastal and offshore infrastructures; they are also responsible for coastal flooding at intra-annual scales (Orejarena-Rondón et al., 2019).

Waves are the ocean surface response to the wind stress acting over it and therefore there is a direct connection between surface atmospheric circulation and waves (Lin et al., 2019).

The study of extreme waves at different temporal scales has been extensively addressed in several works (Wang and Swail, 2001, 2002; Caires et al., 2006; Méndez et al., 2006; Menéndez et al., 2008, 2009; Izaguirre et al., 2010, 2012; Young et al., 2012; Weiss et al., 2014; Sartini et al., 2017). Most of these studies focused on the spatiotemporal distribution of extreme waves rather than on the atmospheric conditions producing them.

Over the North Atlantic Ocean and the Mediterranean Sea, atmospheric circulation is driven by the temperature gradient between the North Pole and the Equator that organizes a three-cell system associated with the Equatorial-Low, the subtropical Azores-High, the Icelandic-Low and the North Pole-High pressure centers (Martínez-Asensio et al., 2016). Atmospheric circulation can be characterized by specific modes of variability with defined characteristics that may also have effects over a region or remote area through atmospheric teleconnections (Wallace and Gutzler, 1981). The main patterns of atmospheric variability in the North Atlantic and Europe are the North Atlantic Oscillation (NAO), the East Atlantic pattern (EA), the Scandinavian pattern (SCAND) and the East Atlantic/Western Russia (EA/WR) pattern (Barnston and Livezey, 1987). NAO is the leading mode of variability in the North Atlantic and is often defined as the sea level pressure difference between the Icelandic Low and the Azores High (Hurrell et al., 2003). NAO controls the strength and direction of westerly winds reaching the European coasts and the location of the storm tracks across the North Atlantic (Marshall et al., 2001). The EA is the second predominant mode of low-frequency variability in the North Atlantic area. It consists of a north-south dipole of anomaly over the North Atlantic, with a strong multidecadal variability. The SCAND pattern consists of a primary circulation center over Scandinavia, with weaker centers of opposite sign over western Europe. The EA/WR pattern consists of four main anomaly centers; its positive phase is associated with positive wave height anomalies located over Europe and negative wave height anomalies over the central North Atlantic (https://www.cpc.ncep.noaa.gov/data/teledoc/telecontents.shtml, last access: $27/02/2020$ at 13:34).

There have been a number of studies that have tried to unravel the relation between wave climate and large-scale atmospheric patterns. Woolf et al. (2002) found a strong connection between interannual wave climate variability in the North Atlantic Ocean and the NAO, as well as with the EA index to a lesser degree. Castelle et al. (2018) examined the relation between winter mean wave height, detailing a high correlation with the NAO index and with the Western Europe Pressure Anomaly (WEPA) index; this is a new definition of a climatic pattern based on the sea level pressure gradient between the stations Valentia (Ireland) and Santa Cruz de Tenerife (Canary Islands). Izaguirre et al. (2010) detected a relation between the NAO and EA indices with the extreme wave climate in the northeast Atlantic Ocean. Izaguirre et al. (2012) evaluated the synoptic atmospheric patterns associated with the extreme significant wave height (SWH) finding a higher interannual variability of the extreme SWH in the northern part of the Atlantic Ocean. In the Mediterranean Sea, clear relations between extreme waves and the negative phases of EA and the EA/WR indices have been also reported (Izaguirre et al., 2010).

In this Chapter, we extend earlier studies, by analyzing the short- and long-term

variability of extreme waves in the North Atlantic Ocean and in the Mediterranean Sea, not only for diagnostic purposes but also to be able to provide statistical prognostics of extremes waves associated with the most important climatic indices. The Chapter is structured as follows. In Section 3.2, the data used and the description of the extreme waves are presented. In Section 3.3, we present the spatial and temporal distribution of the extreme waves and the relation between the four patterns of climatic variability and the spatial distribution of extreme waves during winter. Finally, Section 3.4 concludes the work.

3.2 Data and extreme wave values

3.2.1 Waves and atmospheric data

Wave data are obtained from a high-resolution global hindcast from the National Center for Environmental Prediction (NCEP) with a temporal sampling of 1 hour and different spatial resolutions. This dataset (i.e.,WAVEWATCH III 30-year Hindcast Phase 2, (Chawla et al., 2012)) has been generated by forcing the "state-of-the-art" wave model WAVEWATCH III (Tolman, 2009) with 10-m height high-resolution wind fields from the NCEP Climate Forecast System Reanalysis and Reforecast (CFSRR) a 30-year homogeneous dataset of hourly $1/2^{\circ}$ spatial resolution winds.

The wave model consists of global and regional nested grids, developed by the presence of currents and bathymetry (Amante and Eakins, 2009), taking into account the conservation of action density (Janssen, 2008). In addition, the dissipation and physical term parameterization formulated in Ardhuin et al. (2010) is used in this work.

The hindcast has been validated using the National Data Buoy Center of National Oceanic and Atmospheric Administration (NDBC-NOAA) and with the altimeter database provided by the Institut Français de Recherche pour l'Exploitation de la Mer (IFREMER) (Chawla et al., 2011, 2012, 2013).

The simulation spans a time period of 31 years from 1979 to 2009 with hourly outputs, although since we assume that wave climate is constant for 3 hours, we only use one data point for this period with a spatial resolution varying according to the study area. In all the grids, the full-resolution ETOPO1 bathymetry is used in regular spherical grids. The North Atlantic domain spans from 20°N to 70°N in latitude and 60°W to 10°E in longitude at 0.5° resolution (Fig. 3.1, a). The Mediterranean Sea covers 30°N to 48°N in latitude and 7°W to 43°E in longitude with a spatial resolution of 0.167° (see Fig. 3.1, b). Sea level pressure and wind velocity at 10 m-height are provided by the NCEP-CFSR forcing with a resolution of 0.5° for the same period (Saha, 2009).

The hindcast is validated at the two basins with available buoys following the methodology described in Morales-Márquez et al. (2018). For 13 buoys in the Atlantic and 11 in the Mediterranean Sea, we compute the correlation coefficient (R^2), scatter index (SCI) and relative bias (RB) as:

$$R^2 = \frac{\mathrm{Cov(b,m)}}{\sigma_{\mathrm{b}}\sigma_{\mathrm{m}}}, \tag{3.1}$$

$$SCI = \frac{\mathrm{rms_{m-b}}}{\max(\mathrm{rms_b}, |\langle \mathrm{b} \rangle|)}, \tag{3.2}$$

Table 3.1 *Statistical comparison between SWH data from WAVEWATCH III 30-year Hindcast Phase 2 and CMEMS buoys.*

Basin	$R^2(\%)$	SCI	Relative bias
Mediterranean Sea	73.09 ± 0.17	0.39 ± 0.00	-0.13 ± 0.00
North Atlantic	72.67 ± 0.96	0.33 ± 0.02	0.16 ± 0.02

$$RB = \frac{\langle \mathrm{m} - \mathrm{b} \rangle}{\max(\mathrm{rms_b}, |\langle \mathrm{b} \rangle|)}, \tag{3.3}$$

with m representing modeled dataset by WAVEWATCH III 30-year Hindcast Phase 2 and b the *in situ* buoy dataset.

Table 3.1 shows the comparison between the WAVEWATCH III 30-year Hindcast Phase 2 and the buoys from the Copernicus Marine Environment Monitoring Service (CMEMS, https://marine.copernicus.eu/, last access: $02/07/2020$ at $15{:}41$). See Fig. 3.1 for buoy locations.

Leading climatic modes of variability, namely NAO, EA, EA/WR and SCAND (see the Section 3.1 for a description of these modes) have been downloaded from the NOAA Climate Prediction Center. Indices are constructed through a rotated principal component analysis of the monthly mean standardized 500-mb height anomalies in the Northern Hemisphere, ensuring independence between modes at a monthly scale due to orthogonality (Barnston and Livezey, 1987).

3.2.2 Extreme wave climate

Extreme wave climate is defined here in terms of the monthly 99^{th} percentile of SWH (hereinafter $\mathrm{SWH_{99}}$). Over the North Atlantic, maximum values of $\mathrm{SWH_{99}}$ during the whole period of time analyzed (1979-2009), are observed at mid to high latitudes with values reaching 13 m (see Fig. 3.2, a). This situation is very similar to results obtained in Vinoth and Young (2011), wherein there are higher values of SWH in the northern part of the study area. These maximum values occur predominantly during winter (DJFM), with an 81.2% occurrence (Fig. 3.2, c). Over the Mediterranean Sea, maximum values of $\mathrm{SWH_{99}}$ are at most 8 m (Fig. 3.2, b) with a 91.06% occurrence during winter (DJFM) (Fig. 3.2, d).

Seasonality is assessed by fitting a cosine function to the monthly $\mathrm{SWH_{99}}$ series through a least-squares adjustment (Menéndez et al., 2009):

$$f(t) = \sum_{i=1}^{2} A_i \cos\left(\frac{2\pi}{T_i}(t - \phi_i)\right), \tag{3.4}$$

where $i = 1, 2$ represents the annual and semiannual cycle, A_i the amplitude, ϕ_i the phase, $T_{1,2} = 365.25$ and 182.63 and t time in days. The monthly $\mathrm{SWH_{99}}$ for the location with the largest variance reduction in the North Atlantic (point 1, Fig. 3.3, a), is shown in black in the top panel of Fig. 3.3 (the same for the Mediterranean Sea, point 2 in Fig. 3.3 b), while the time series after removing seasonality by fitting Eq. (3.4) are shown in blue. Seasonality in the North Atlantic accounts on average for a 50% of the variance in the signal (Fig. 3.3, a). It means that half of the extreme wave signal is explained by the annual and semiannual cycle. In the Mediterranean Sea, there are

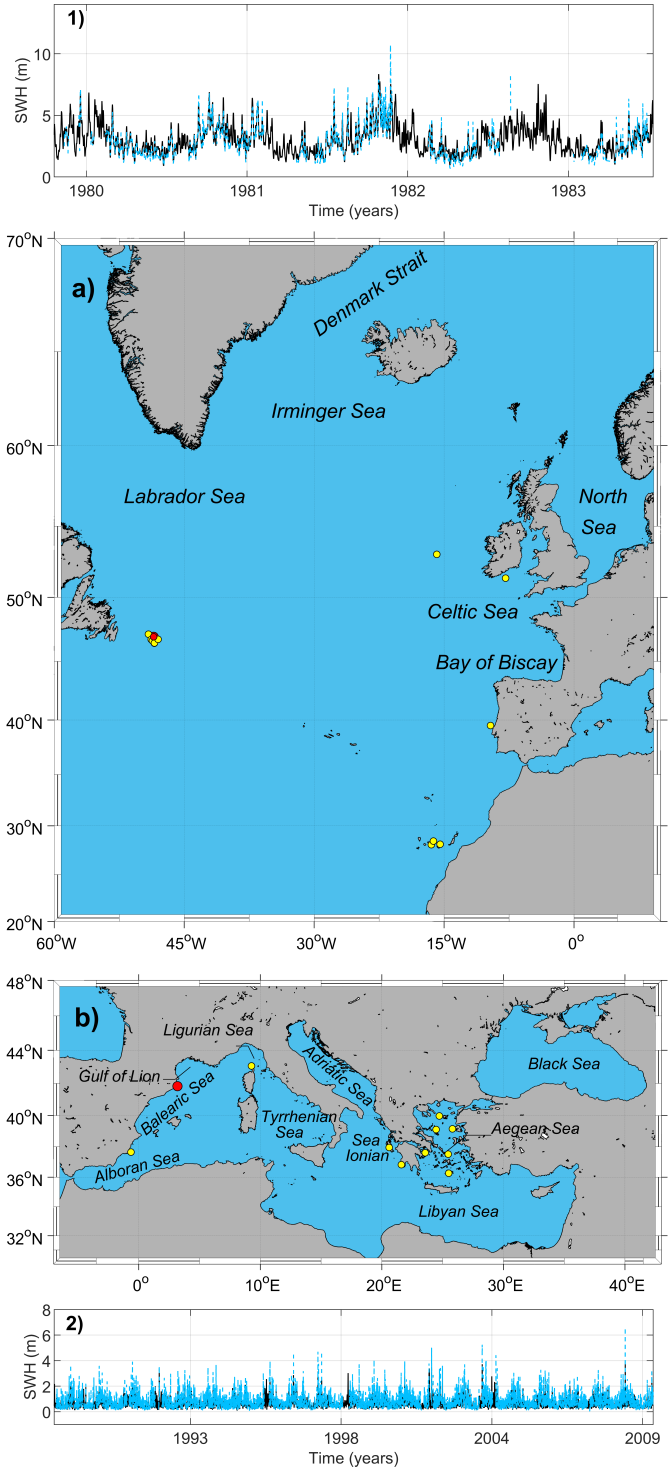

Figure 3.1 *Location of the study zones. a) Eastern North Atlantic Ocean. b) Mediterranean Sea. The yellow points are the locations of the buoys used in the comparison with the modeled data by WAVEWATCH III 30-year Hindcast Phase 2. Panels 1 and 2: SWH series of hindcast (black line) and a representative buoy (dashed blue line) for the North Atlantic Ocean and Mediterranean Sea, respectively. The red points are the locations of the representative buoys.*

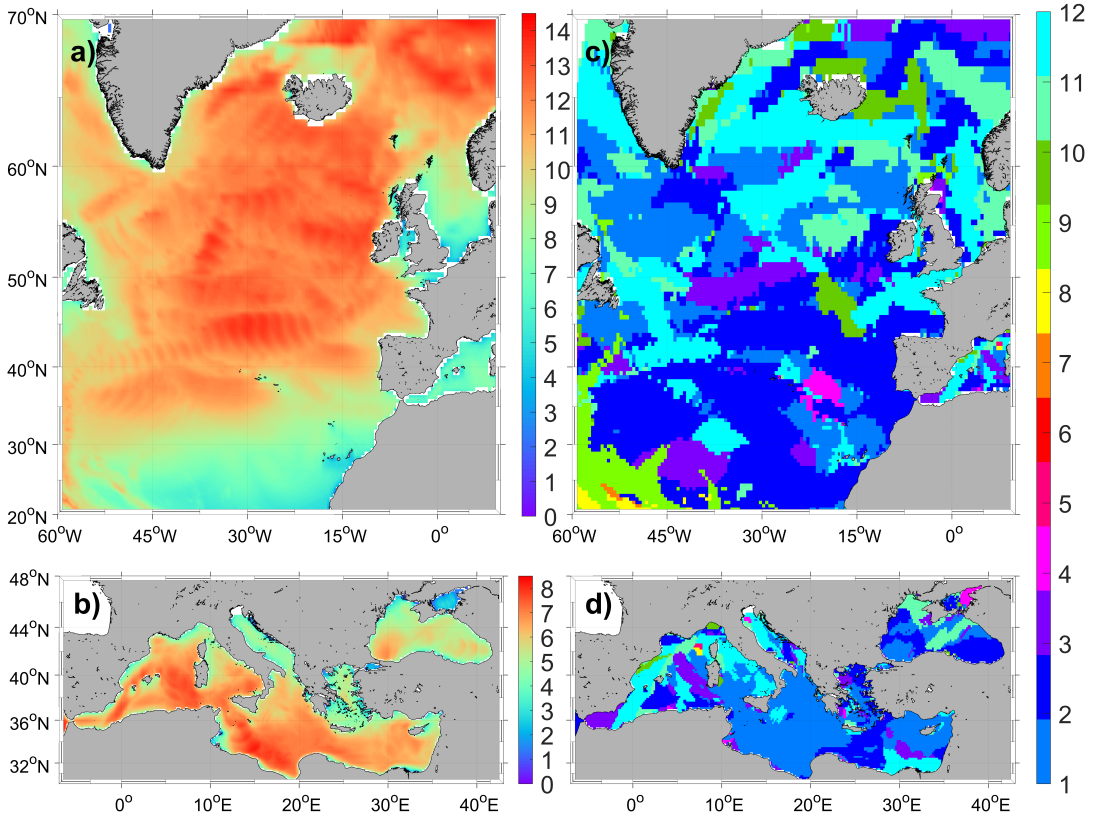

Figure 3.2 *Maximum value of monthly* 99^{th} *percentile SWH in meters for a) the North Atlantic Ocean and b) Mediterranean Sea, as well as the month of the year [from January* (1) *to December* (12)*] when there is the maximum value of the* 99^{th} *percentile SWH for c) the North Atlantic Ocean and d) Mediterranean Sea.*

two different areas in terms of seasonality. One is located in the central basin where seasonality explains up to 70% of extreme waves and the other is located in the Gulf of Genoa and the Alboran Sea, where seasonality explains less than 10% of the signal (Fig. 3.3, b). These areas are very active in terms of cyclogenetic activity (Trigo et al., 2002) and thus the seasonal signal is relatively less important here.

To analyze the long-term trend of SWH_{99} during winter months (DJFM) when most extreme waves occur, the temporal series is fitted by a linear regression in time at the 90% confidence level at each spatial point (see Fig. 3.4). Locations where the trend is not significant are represented with a dot. The 31-year trend in the North Atlantic (Fig. 3.4, a) displays an area with significant positive values (up to 2.5 cm/year) from the Portuguese coast to Canada. The rest of the basin presents a negative value tendency, with maximum values around 3.5 cm/year in the Bay of Biscay, Labrador Sea, and between the United Kingdom and Iceland. This aligns with the obtained results in Gallagher et al. (2016), wherein the future projections of mean surface wind show an average decrease over the North Atlantic Ocean for winter, so the extreme waves likely continue with the same pattern in terms of long-term variability. In the Mediterranean Sea, the values of SWH_{99} tendency during winter months (DJFM) are substantially smaller (see Fig. 3.4, b). Only the center part, north of Cyprus (with negative values up to 2.4 cm/year and 1 cm/year, respectively) and the Aegean Sea (with positive values for the trend of around 1 cm/year), presents a trend that is statistically significant. These

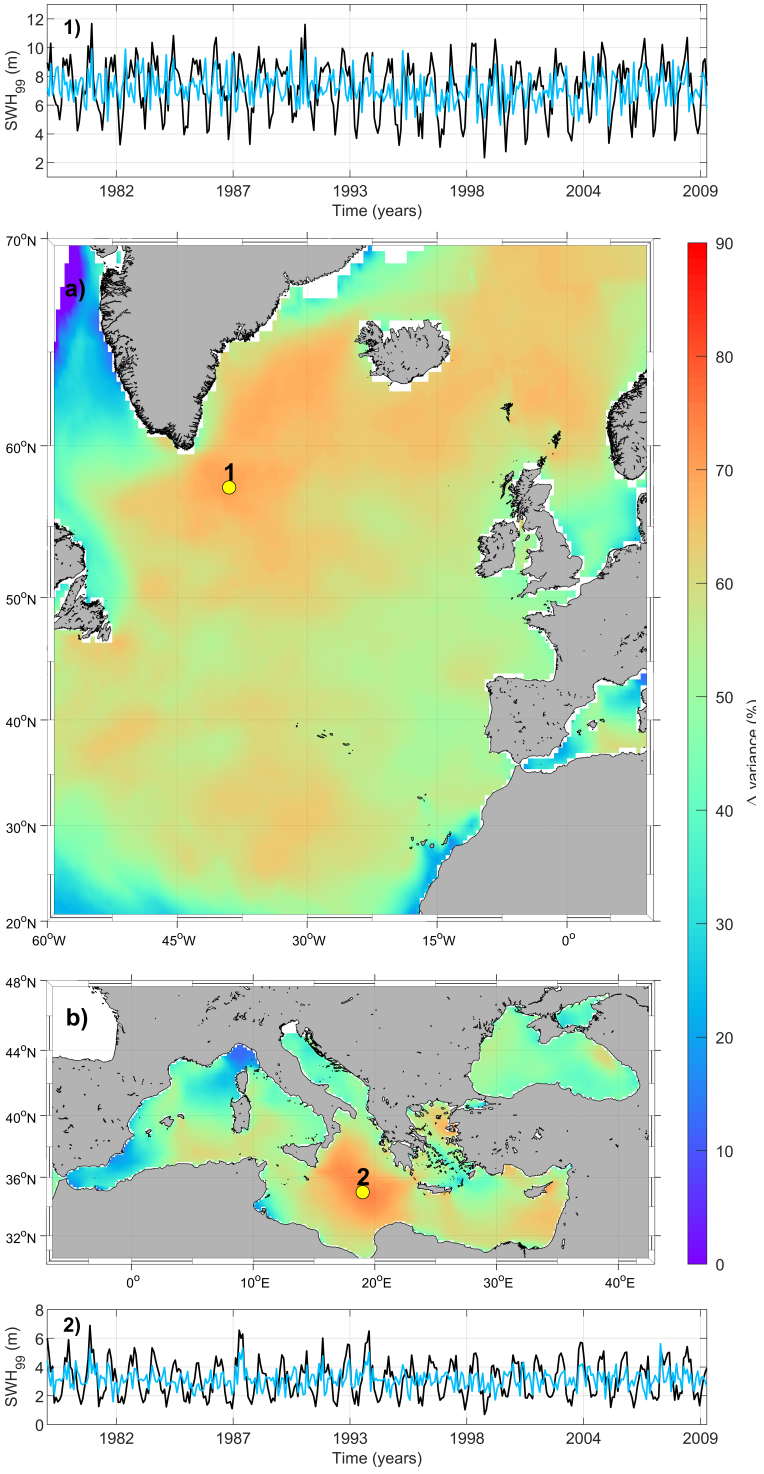

Figure 3.3 *Variance reduction in percentage if the seasonality is removed from the monthly 99^{th} percentile SWH series for the a) North Atlantic Ocean and b) Mediterranean Sea. Panels 1 and 2: monthly 99^{th} percentile SWH series (black line) and monthly 99^{th} percentile SWH series without seasonality (blue line) for a point in the North Atlantic Ocean and Mediterranean Sea, respectively.*

calculations are restricted to the time period corresponding to the atmospheric forcing of the WAVEWATCH III 30-year Hindcast Phase 2, and different patterns could be

obtained for different periods.

These results differ from the trend calculated in Young et al. (2011), since in that study they considered all the months of the year in order to calculate the monthly SWH_{99}'s trend, and in this work, we analyze the tendency of the monthly SWH_{99} only during winter (DJFM). We have verified that there is a positive trend of SWH_{99} during the summer season (it is not shown in this study); however, the values in this season are considerably lower than those found during winters.

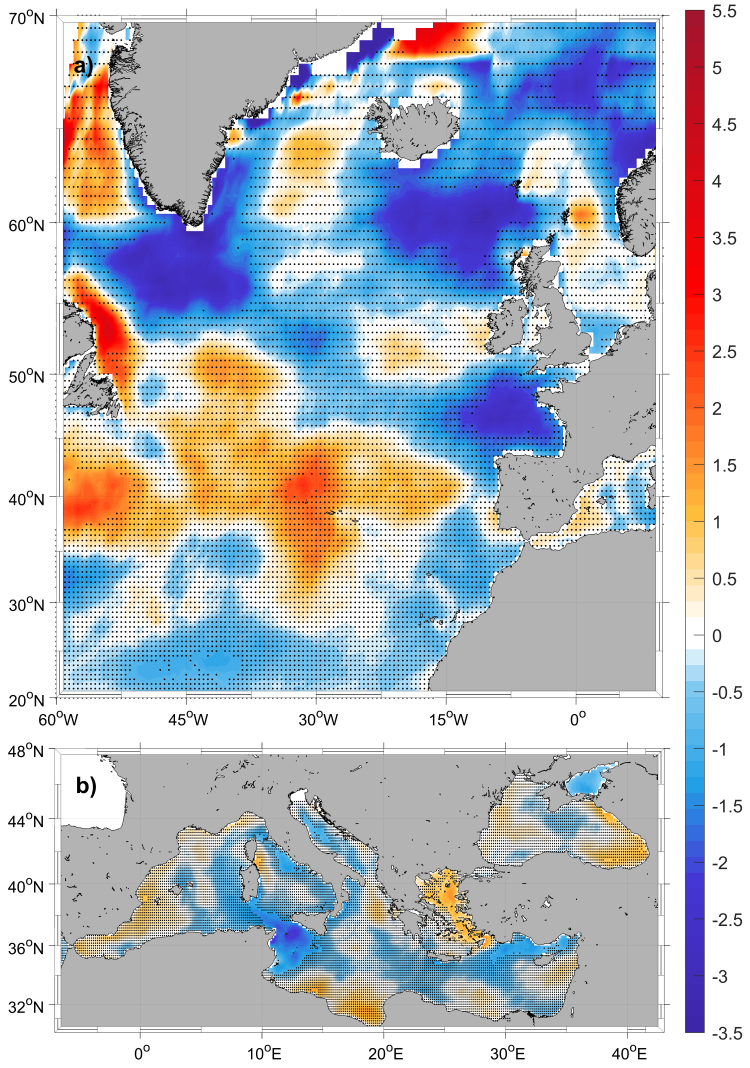

Figure 3.4 *Trend of the monthly* 99^{th} *percentile SWH during winters (DJFM) in centimeters per year. Dotting indicates no significant values at the* 90% *confidence interval.*

In this Chapter the winter extreme wave climate is studied in order to remove the seasonality because maximum values of SWH_{99} take place during the winter season.

3.3 Spatiotemporal patterns of extreme waves

The spatiotemporal variability of SWH_{99} is assessed by computing empirical orthogonal functions (EOFs) of the winter (DJFM) fields. Prior to the computation of the

EOFs, the spatial mean winter SWH_{99} was removed and the analyses were performed on anomalies with respect to the mean values (Ponce de León et al., 2016). Mean fields are mapped in Fig. 3.5, a and 3.6, a.

The first three EOFs for the North Atlantic are shown in Fig. 3.5 (b, c and d) and their principal components (PCs) together with their explained variance in Fig. 3.5 (1, 2 and 3). The first EOF, which explains 28.5% of the winter SWH_{99}, presents a periodicity in its PC of around 5 years (calculated through a FFT analysis in Fig. 3.5, panel 1). This first mode shows a spatial dipole with opposite values in the north and south of the basin. The second mode, which explains 15.5% of the winter variability shows an area in the central basin separating two zones at the north and south with different sign (Fig. 3.5, c). Values for the central part are 3 times larger than the ones obtained for the northern and southern sides, indicating that the contribution of this EOF is to increase (decrease) the winter extremes in the central Atlantic when its PC is negative (positive). The third EOF, which explains 8.3% of the winter variability also displays three different zones with a central area shifted to the east-west direction extending from the Bay of Biscay to the Celtic Sea and at the north and at the south zones displaying an opposite sign during winter (Fig. 3.5, d).

For the Mediterranean Sea, the first three EOF modes for winter are shown in Fig. 3.6 (b, c and d) and their PCs in Fig. 3.6 (1, 2 and 3). The first EOF, explaining 38.0% of the total variance, represents a spatially coherent increase (decrease) of SWH_{99} over the entire basin. The second EOF, explaining 15.1% of the variance, shows differences between the eastern and western basins. The contribution of this mode is to increase (decrease) SWH_{99} in the western Mediterranean with a simultaneous decrease (increase) in the eastern Mediterranean according to the amplitude of the PC. Finally, the third EOF, explaining a 7.3% of the variance displays two zones; the Tyrrhenian Sea and the southern part of the Gulf of Lion with the same sign and the rest of the basin with opposite behavior.

The relationship between extreme waves and the climatic modes of variability in the North Atlantic Ocean and Mediterranean Sea is explored and quantified as follows. Winter averages of climate indices are first correlated with the corresponding PCs described above for each basin. The significance level is set at 90% with a t-value adjusted as

$$t = |\mathrm{c}| \sqrt{\frac{N-2}{1-\mathrm{c}^2}}, \tag{3.5}$$

where c is the correlation coefficient and N, the length of the time series. If t is equal to or higher than the t-value of a Student's t-distribution of $N-2$ degrees of freedom, then the correlation is assumed to be statistically significant at the predefined 90% confidence level. These significance values are particular for this study since they depend on the data used and the analyzed time period.

3.3.1 Correlations between winter extreme waves and climatic modes of variability

The correlation between the four climate indices and the first three SWH_{99} PCs are shown in Table 3.2 where (and hereinafter) bold indicates statistically significant correlations at the 90% confidence level. The major correlation in the North Atlantic is obtained with the NAO and the SCAND through the PC1 (correlation of 82.6% and -63.3%, respectively). This is not surprising, as winter NAO and SCAND indices are

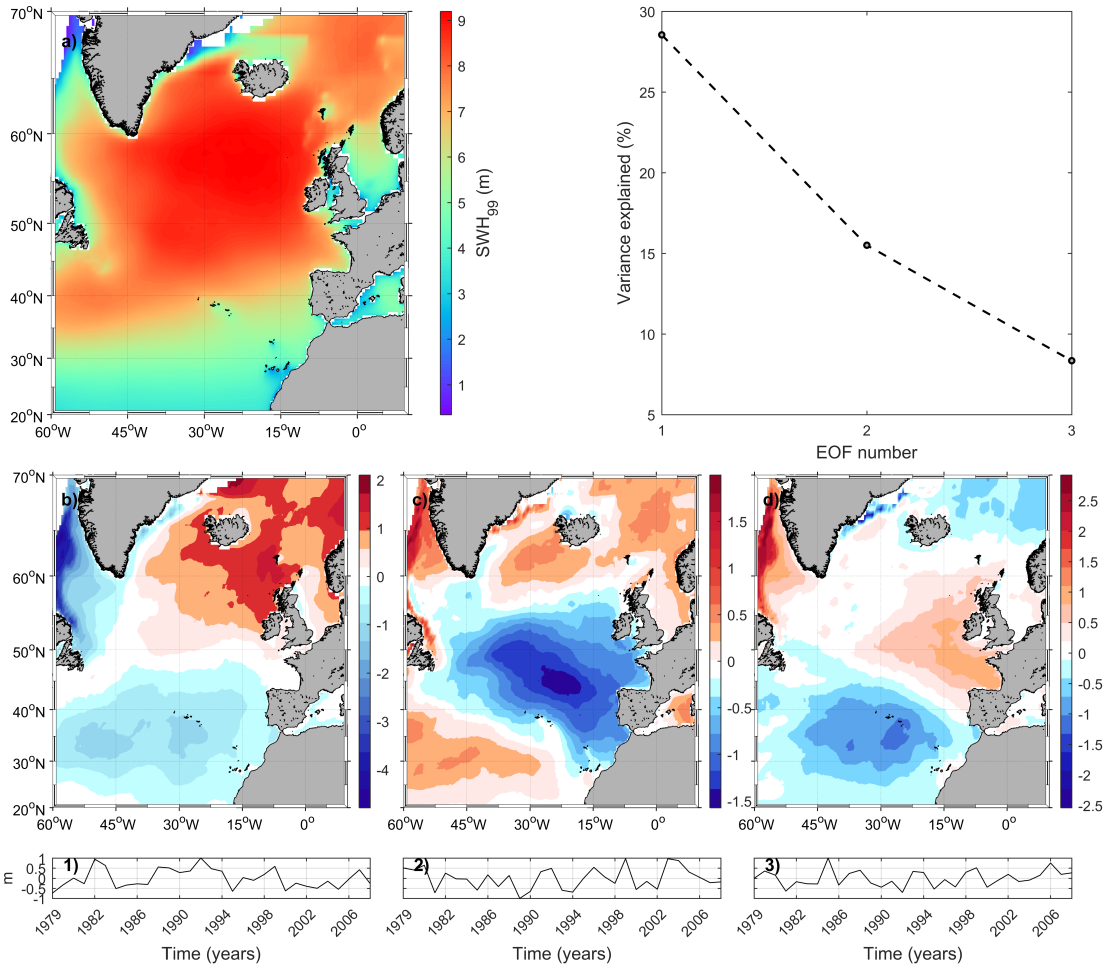

Figure 3.5 *a) Mean field of winter SWH* 99^{th} *percentile in meters over the North Atlantic. EOF analysis of* SWH_{99} *anomalies, showing the explained variance of the first three EOFs, b-d) spatial patterns of EOFs 1-3, and 1-3) principal components of the EOFs above.*

correlated themselves (note that, although monthly indices are orthogonal, this does not necessarily hold for seasonal or yearly averages). The NAO teleconnection not only dominates the extreme values of SWH during winter; but also the mean SWH, wave period and peak wave direction magnitudes for wintertime in this region (Gallagher et al., 2014). To a lesser extent, EA is correlated with the second PC (explaining around 16% of the winter variability). These results are in accordance with those obtained by Izaguirre et al. (2010) and Gleeson et al. (2019), who show that extreme waves in the North Atlantic are related to the positive phase of NAO and the negative of EA and SCAND. For the Mediterranean Sea, both the NAO and the EA are correlated with the winter SWH_{99} through the first PC and some of the variability is correlated with the negative phases of EA and EA/WR through the second PC. However, the values of the correlations in the Mediterranean Sea are significantly lower than those in the North Atlantic because the main climatic patterns consist of some strong poles located in the Atlantic Ocean, which drive zonal flows toward Europe. These climatic situations generate a weak circulation into the Mediterranean Sea, which is not as related to the higher values of waves. In addition, wave climate depends on wind regimes and on land-

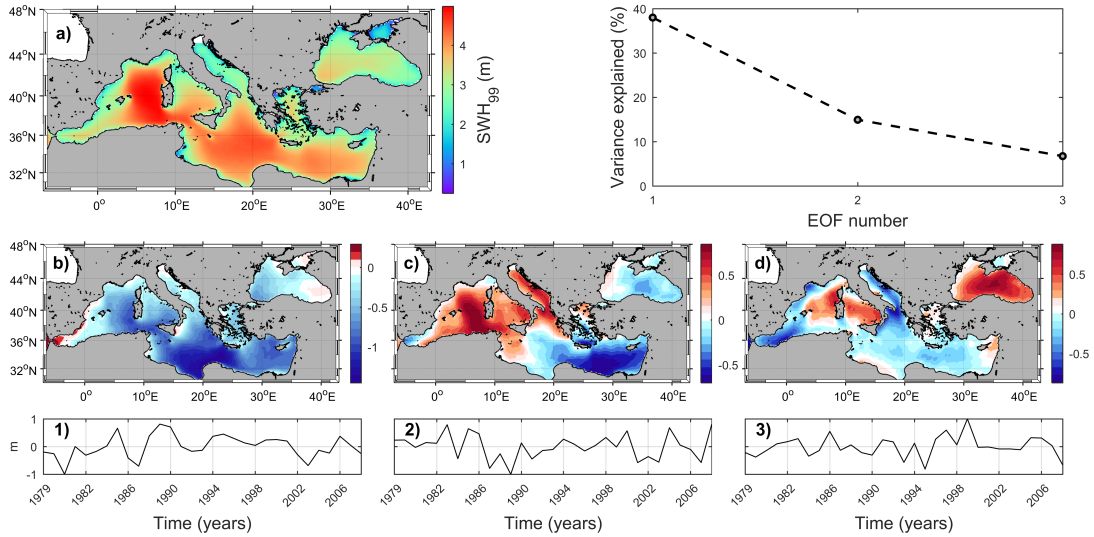

Figure 3.6 *a) Mean field of winter SWH* 99^{th} *percentile in meters over the Mediterranean Sea. EOF analysis of* SWH_{99} *anomalies, showing the explained variance of the first three EOFs, b-d) spatial patterns of the EOFs 1-3, and 1-3) principal components of the EOFs above.*

Table 3.2 *Correlation between main climate indices and the amplitudes of the first three modes of the average monthly* SWH_{99} *series for the North Atlantic Ocean and the Mediterranean Sea in winter.*

	North Atlantic Ocean			Mediterranean Sea		
	PC1	PC2	PC3	PC1	PC2	PC3
NAO	**0.826**	−0.138	**0.323**	**0.242**	−0.193	**0.297**
EA	−0.120	**-0.459**	−0.042	**0.298**	**-0.361**	0.026
EA/WR	0.057	0.171	−0.127	0.093	**-0.342**	**0.366**
SCAND	**-0.633**	−0.126	−0.165	−0.091	**0.347**	**-0.390**

sea distribution. In other words, waves need fetch to develop, and in the Mediterranean Sea, the available distance is more restricted (Lionello and Sanna, 2005).

Atlantic Ocean

Correlation maps for winter SWH_{99} in the North Atlantic and the four climate indices are displayed in Fig. 3.7. Some of these spatial correlations present similarities to the EOF patterns shown in Fig. 3.5. In particular, the correlation map between NAO and SWH_{99} (Fig. 3.7, a) mimics the first SWH_{99} EOF for winter (Fig. 3.5, b), with correlation values consistent with the one obtained using PC1 (see Table 3.2). The correlation between EA and SWH_{99} (Fig. 3.7, b) shows large similarities to the second SWH_{99}-EOF for winter extreme waves (see Fig. 3.5, c) but with the opposite sign. Finally, the correlation between SCAND and SWH_{99} (Fig. 3.7, d) shows similarities to the first SWH_{99} EOF (Fig. 3.5, b). During winter, the northern part of North Atlantic Ocean has a positive correlation with the NAO and a negative correlation at the south with maximum values close to 0.8 (Fig. 3.7, a). The correlation map for the EA index shows positive correlations with maximum values close to 0.75 in the central part of the

basin and negative at the north and south with maximum values of 0.47 (Fig. 3.7, b). Correlation map for the EA/WR displays an area of negative correlation extending from the Bay of Biscay to Greenland and also near the west coast of Africa. At the northern and central basin there appear to be two zones with a positive correlation, with maximum values around 0.55 (Fig. 3.7, c). Finally, the correlation map between SCAND and SWH_{99} shows negative correlations in the north-central Atlantic, with maximum values of 0.74, and positive correlations in the south-central Atlantic with a maximum value of 0.60 (Fig. 3.7, d).

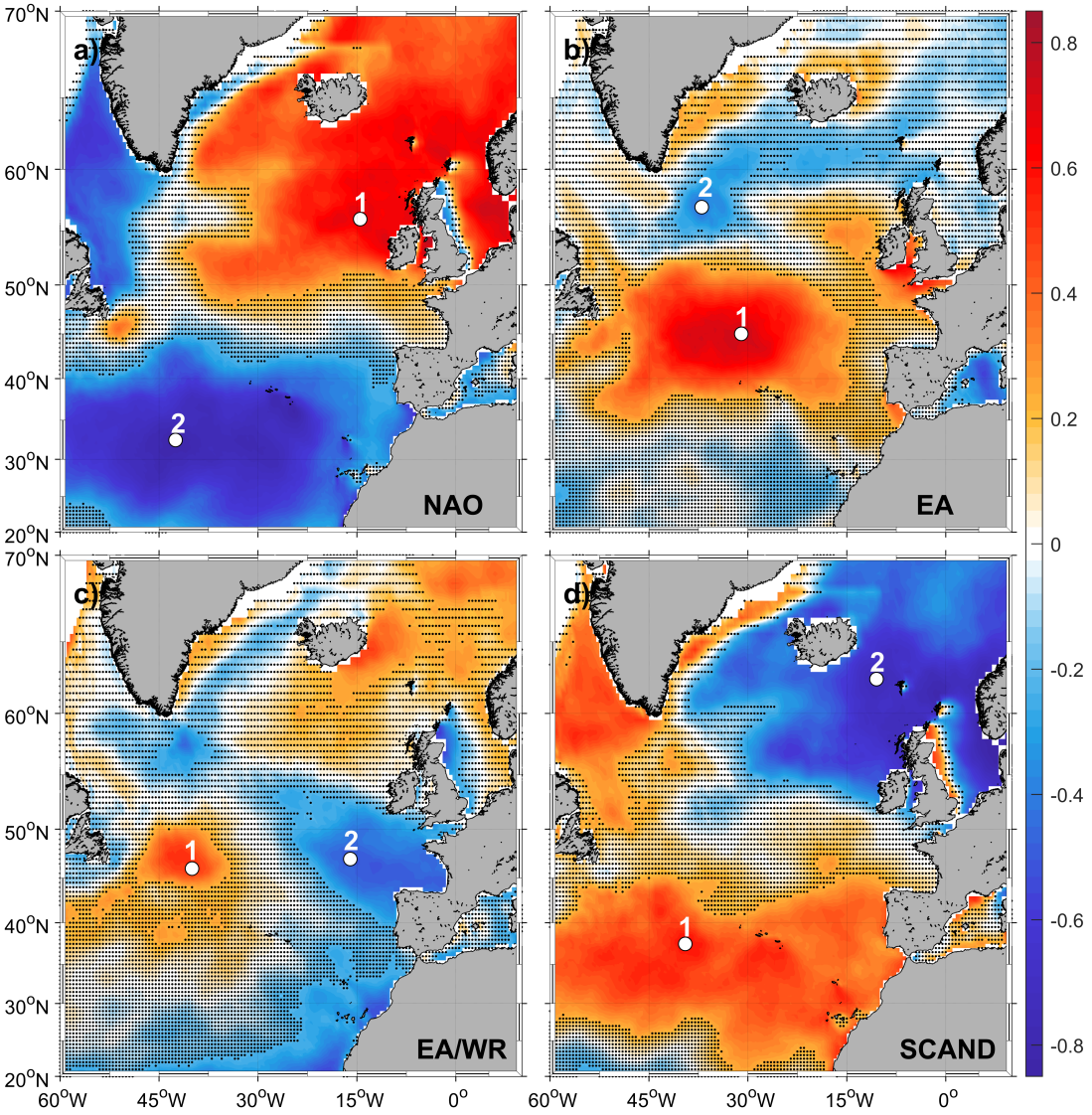

Figure 3.7 *Pearson correlation coefficient of winter mean 99^{th} percentile SWH North Atlantic series and a) NAO, b) EA, c) EA-WR and d) SCAND winter mean indices. Dotting indicates no significant values at the 90% confidence interval. The white points show $1)$ the maximum positive and $2)$ the maximum negative value of the correlation coefficient.*

Mediterranean Sea

Correlation maps between winter SWH_{99} in the Mediterranean Sea and the four climatic indices are shown in Fig. 3.8. Contrary to what is found in the North Atlantic, maps of correlations between extreme waves and climate modes are not clearly linked with the EOF patterns of the wave field. The NAO index presents negative correlation in the whole Mediterranean basin (Fig. 3.8, a). The eastern side of the domain, the Adriatic and Aegean Sea, presents maximum correlations with values around 0.50. The correlation is positive only in the Ligurian Sea, with a value around 0.30. The EA index also displays a negative correlation in the whole domain (Fig. 3.8, b) with larger values over the west with a correlation around 0.60. The correlation map between EA/WR and SWH_{99} shows negative correlations in the Tyrrhenian Sea, the Adriatic Sea and the Ionian Sea with a maximum correlation of 0.40 (Fig. 3.8, c). A positive correlation is obtained in the Aegean Sea with maximum values around 0.60. Finally, the correlation map between SCAND and SWH_{99} shows large positive correlations in the Gulf of Lion, in the southern and central Mediterranean Sea and in the Adriatic Sea with values of around 0.50.

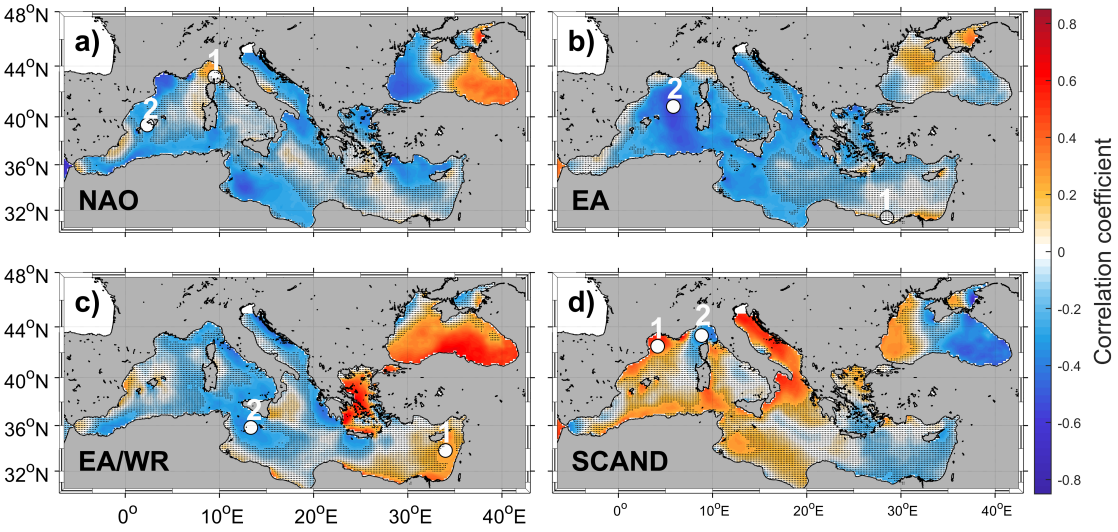

Figure 3.8 *Pearson correlation coefficient of winter mean* 99^{th} *percentile SWH Mediterranean Sea series and a) NAO, b) EA, c) EA-WR and d) SCAND winter mean indices. Dotting indicates no significant values at the* 90% *confidence interval. The white points show* 1*) the maximum positive and* 2*) the maximum negative value of the correlation coefficient.*

3.3.2 Synoptic atmospheric composites associated with extreme wave patterns

The analysis of the atmospheric signature associated with extreme SWH is performed by computing the composites of extreme SWH, atmospheric mean sea level pressure (MSLP) and 10 m wind velocity (U_{10}). The objective is to find the atmospheric pattern that is associated with extreme winter waves. The procedure to build the composites is as follows.

- First, we select the locations with the highest correlations between SWH_{99} and each of the atmospheric indices (points labeled as no. 1 for maximum positive

correlation and as no. 2 for maximum negative correlation in Fig. 3.7 and Fig. 3.8 for the North Atlantic and Mediterranean Sea, respectively).

- We select the time steps for which the original 3-hourly SWH time series at points no. 1 and no. 2 exceed SWH_{99} (two values each month are selected because the monthly number of data points is 224-248 depending on the month of the year).
- Finally, we compute the composites for SWH, U_{10} and MSLP over the whole domain for all selected dates.

Note that the locations labeled no. 1 and no. 2 in each map represent the largest positive and negative correlations with the corresponding index. The composite maps are thus interpreted as the synoptic patterns associated with positive and negative phases (respectively) of the climate index leading to extreme waves.

Atlantic Ocean

The composite for U_{10} and MSLP built using location no. 1 (positive correlation between SWH_{99} and NAO) (Fig. 3.9, a) shows the typical configuration associated with the positive NAO phase that is characterized by low pressures across high latitudes in the North Atlantic and high pressures over the central North Atlantic, the eastern United States and western Europe. This composite is characterized by a strong westerly wind stream crossing the central North Atlantic whose fetch generates large waves at the western part of the British Islands and south of Iceland ($\mathrm{SWH} > 9$ m). A similar relationship was demonstrated dynamically by Wolf and Woolf (2006). By contrast, in the south of the North Atlantic Ocean, in the Azores region, a positive NAO phase results in low SWH_{99} values ($\mathrm{SWH} \approx 4$ m). This pattern corresponds to the first EOF (Fig. 3.5, a and Fig. 3.5, point 1, for the spatial mode and its amplitude, respectively) when, for positive values of the PC, positive anomalies are presented in the north part of the basin and negative anomalies in the central part (the opposite for negative values of the PC). The composite for the positive phase of EA shows a similar structure as the one obtained for the positive phase of NAO, but with the North Atlantic cyclone shifted southwards and with the high pressures covering the entire Atlantic at 30° N (Fig. 3.9, b). Maximum waves associated with the positive phase of EA are obtained in the central Atlantic as a result of the southward winds blowing from Greenland. This pattern corresponds to the second EOF (Fig. 3.5, c and Fig. 3.5, point 2). The composite for the EA/WR positive phase shows the low-pressure system at 40° W, with the maximum extreme waves located to the east of Newfoundland (Fig. 3.9, c). Finally, the atmospheric composite for the positive SCAND phase shows a cyclone (at 40° N) generating extreme waves smaller than obtained with the previous three composites, with values of SWH below $7\mathrm{m}$ (Fig. 3.9, d). This pattern is associated with the first EOF when its amplitude takes negative values (see Fig. 3.5, b and Fig. 3.5, point 1), also corresponding to the atmospheric situation related to the negative phase of NAO (see Fig. 3.10, a). For the negative EA phase, the cyclone is located between Greenland and Iceland, generating a strong wind jet from the coast of Canada to Ireland (Fig. 3.10, b). At this point, we want to remark that since we are analyzing the negative correlations, the values displayed in Table 3.2 have to be changed in sign. The second EOF (Fig. 3.5, c) according to Table 3.2 is related to the composite built for the maximum negative correlation between SWH_{99} and the EA index (Fig. 3.10, b). Composites for the negative phase of EA/WR, are characterized by a western shift of the Icelandic low that

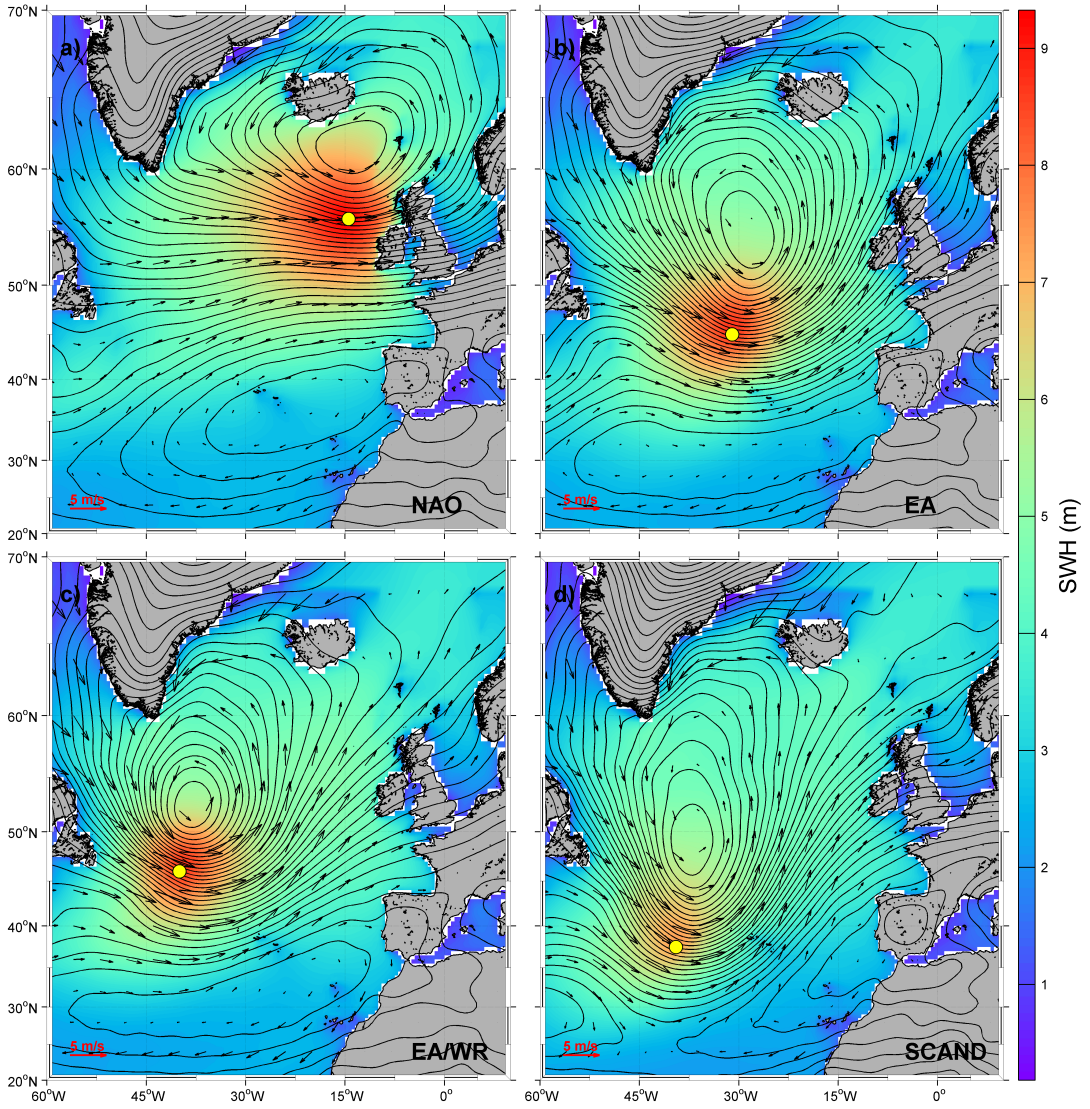

Figure 3.9 *Winter atmospheric situations for the positive phase of a) NAO, b) EA, c) EA-WR and d) SCAND indices in the North Atlantic Ocean. The vectors represent the 10 m wind speed in meters per second; the contours represent the sea level pressure (Pa) and the color range is the mean value of SWH in meters. The red left bottom arrow represents the wind scale.*

generates strong zonal winds between 50°N and 60°N with maximum extreme waves located between the south of Ireland and north of Spain (Fig. 3.10, c). The Icelandic Low for the negative SCAND phase is shifted northeast of Iceland with winds blowing southwestwards and extreme waves located between Iceland and Great Britain (Fig. 3.10, d). This composite is associated with the first EOF (Fig. 3.5, b), thus having a correlation with the positive NAO phase (see also Fig. 3.9, a for comparison).

Mediterranean Sea

In the Mediterranean Sea, for the positive correlations between indices and extreme waves, we choose locations near the coast since negative correlations dominate the en-

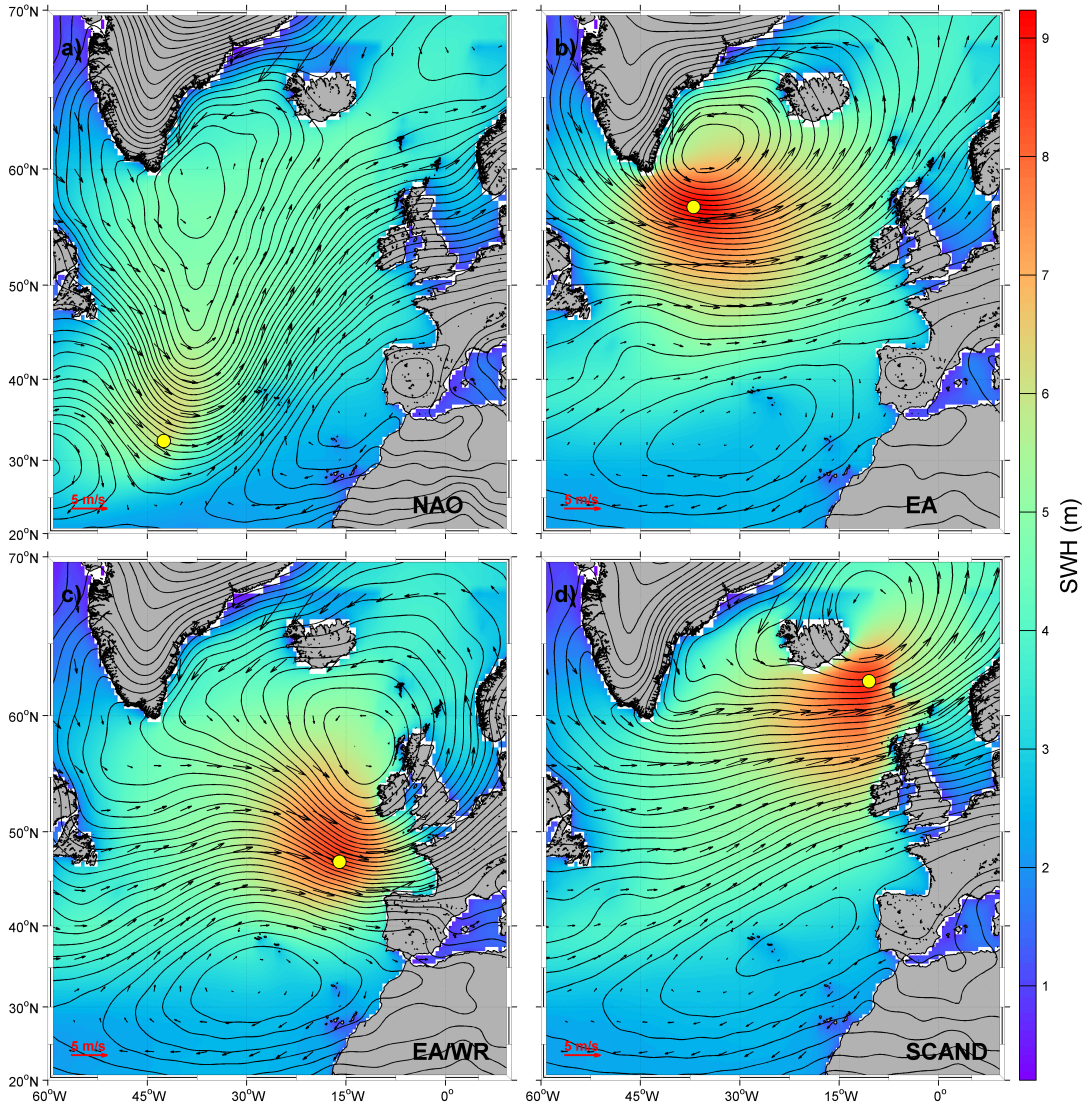

Figure 3.10 *Winter atmospheric situations for the negative phase of a) NAO, b) EA, c) EA-WR and d) SCAND indices in the North Atlantic Ocean. The vectors represent the 10 m wind speed in meters per second; the contours represent the sea level pressure (Pa) and the color range is the mean value of SWH in meters. The red left bottom arrow represents the wind scale.*

tire basin (Fig. 3.8). The atmospheric composite for the positive NAO phase displays a low-pressure system in the north of Italy with associated eastward winds in the western and central basins (Fig. 3.11, a). These conditions are strongly associated with the atmospheric situations discussed in Trigo et al. (1999) for the cyclogenetic activity during winters. This composite is related to the distribution of extreme waves shown by the third EOF (Fig. 3.6, d). Note that the amplitude of this mode is positively correlated with NAO according to Table 3.2. The composite for the positive EA phase shows intense cyclogenetic activity in the eastern Mediterranean Sea with its center of action over Cyprus which generates strong winds and waves north of Egypt (Fig. 3.11, b). This index, as shown in Table 3.2, is negatively correlated with the amplitude of the second EOF whose pattern presents large values for the extreme wave anomalies over

the eastern Mediterranean Sea (Fig. 3.6, c); in other words, a positive EA results in larger SWH_{99} in the eastern basin as displayed in Fig. 3.11, b. Regarding the positive EA/WR phase, the resulting composite presents a very similar pattern for surface pressure, winds and waves as the one obtained for the positive EA phase (see Fig. 3.11, b and Fig. 3.11, c). The EA/WR index is also negatively correlated with the amplitude of the second EOF (Table 3.2) resulting in the same distribution of extreme waves as previously explained regarding the EA. Finally, the composite for the positive SCAND index displays a cyclonic structure in the northwestern part of the Mediterranean Sea -between Corsica and Sardinia- with winds blowing southwards at the Gulf of Lion (Fig. 3.11, d). The SCAND index is positively correlated with the amplitude of the second EOF (Table 3.2), indicating larger (smaller) SWH_{99} in the western (eastern) Mediterranean during its positive phase.

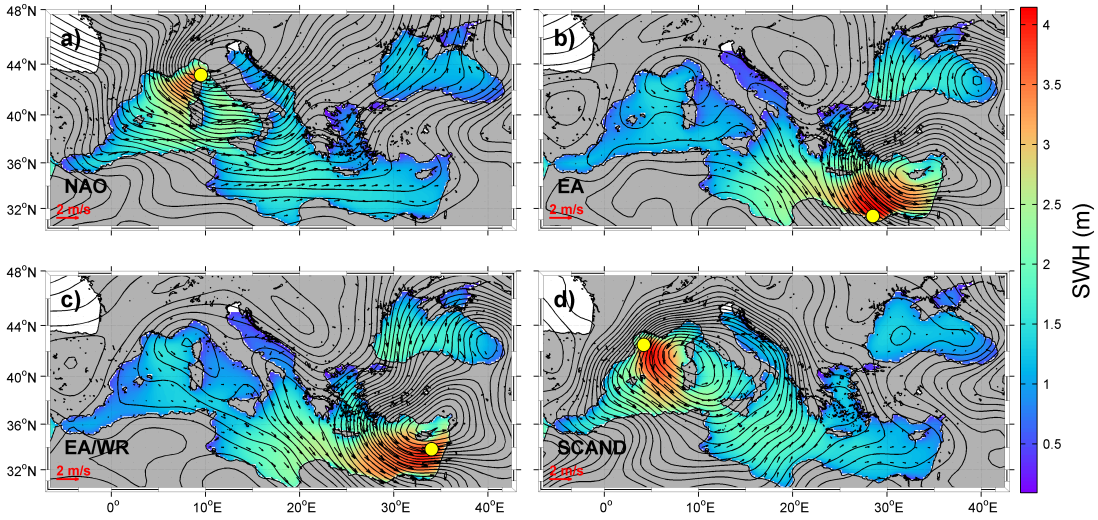

Figure 3.11 *Winter atmospheric situations for the positive phase of a) NAO, b) EA, c) EA-WR and d) SCAND indices in the Mediterranean Sea. The vectors represent the 10 m wind speed in meters per second; the contours represent the sea level pressure (Pa) and the color range is the mean value of SWH in meters. The red left bottom arrow represents the wind scale.*

For the negative phases during winters, the composite for the NAO displays a weak cyclone over the Ligurian Sea (Fig. 3.12, a). In this situation, however, the pressure gradient is weaker and due to the small fetch the resulting extreme waves are small (below $3.5\mathrm{m}$ in SWH). Regarding the negative phase of the EA index, the composite shows a strong cyclone centered over Italy with a large pressure gradient over the northwestern Mediterranean Sea. This situation generates strong winds between the Balearic Islands and Corsica and Sardinia, generating large waves in this area. The EA index is negatively correlated with the amplitude of the second EOF (see Fig. 3.6, c). For the negative phase of EA/WR, composite shows a low-pressure system over the Ionian Sea with a strong pressure gradient between Sicily and Tunisia, resulting in large extreme waves in this passage (Fig. 3.12, c). This index is negatively correlated with the amplitude of the second EOF (Table 3.2), suggesting that for positive anomalies of SWH_{99} (see Fig. 3.6, c) a negative phase of the EA/WR index results in an increase in extreme waves. Finally, the composite for the negative phase of the SCAND index displays a

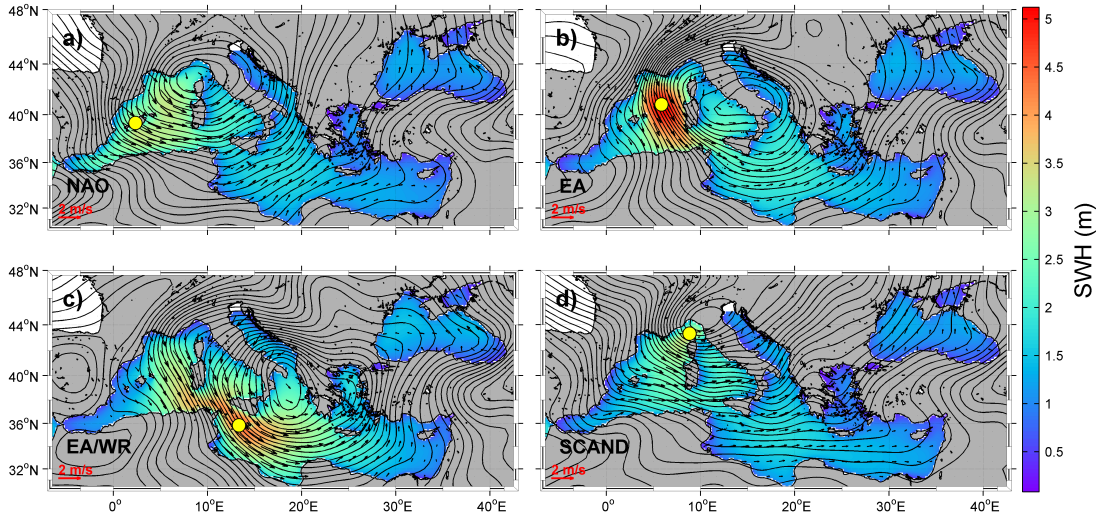

Figure 3.12 *Winter atmospheric situations for the negative phase of a) NAO, b) EA, c) EA-WR and d) SCAND indices in the Mediterranean Sea. The vectors represent the 10 m wind speed in meters per second; the contours represent the sea level pressure (Pa) and the color range is the mean value of SWH in meters. The red left bottom arrow represents the wind scale.*

low-pressure system over north of Italy. Although the pressure gradient associated with this low system is intense north of Corsica, the small fetch encourages the formation of extreme waves (Fig. 3.12, d).

3.4 Summary and conclusions

This work presents a new methodology to study extreme wave climate and the atmospheric synoptic conditions responsible for extreme waves. Winds and pressure are obtained by computing the composites corresponding to the monthly values of the 99^{th} percentile of the significant wave height. As a result, it is possible to infer changes in the location and intensity of extreme waves through an understanding of the variability of climatic patterns (widely studied). This approach could be of interest for all the activities related to the prognosis of extreme waves, such as, the design of offshore structures, among others.

The study is focused on the North Atlantic Ocean and the Mediterranean Sea, although the methodology can be extrapolated to any region in order to get a deeper insight into the seasonal and interannual variability of extreme wave climate. In the present work, the interannual variability has been analyzed using empirical orthogonal functions, which have been correlated against the four main climate indices of variability in the area, i.e., NAO, EA, EA/WR and SCAND. Finally, the most reliable atmospheric situation associated with each climatic pattern is discussed using the described methodology.

The extreme waves climate has a large seasonal signal in both in the North Atlantic Ocean and the Mediterranean Sea. Our results also indicate a large intra-annual variability in the central part of the Mediterranean Sea and lower variability in the Alboran and Ligurian sub-basins, in agreement with Sartini et al. (2017) wherein they exhibited

different degrees of seasonality depending on the main mesoscale meteorological features of the locations analyzed. Concerning the long-term trend of extreme waves, it is predominantly negative, although there are some areas, such as in the center of the North Atlantic Ocean and in the Aegean Sea, where the value of the tendency is positive. These results are not in line with the studies of Young et al. (2011) and Young and Ribal (2019) because here we assess only the extreme wave values during the winter season, when most of the maximum SWHs occur.

Regarding climatic modes of variability, we found that the NAO and the SCAND indices are the leading modes of climatic variability affecting extreme waves in the North Atlantic Ocean during winters. The positive NAO phase increases extreme waves in the northern North Atlantic while the negative NAO phase results in an increase in extreme waves in the southern North Atlantic, in accordance with Hurrell et al. (2003). By contrast, a positive SCAND index increases extreme waves in the southern North Atlantic while a negative SCAND index increases extreme waves in the north part of the North Atlantic Ocean, as Martínez-Asensio et al. (2016) also pointed out. To a lesser extent, the EA also influences extreme waves in the North Atlantic Ocean, as Izaguirre et al. (2010) also concluded. While the positive EA phase drives extreme wave climate in the central North Atlantic, the negative phase controls extreme wave climate at higher and lower latitudes (see Fig. 3.7, b). For future studies, a wavelet coherence analysis (Torrence and Compo, 1998) between the main climatic indices and extreme waves will provide additional information on the dominant modes of variability and how they vary in time.

The interannual variability of extreme waves during winters in the Mediterranean Sea is dominated, to a large extent, by the negative phase of EA, with a larger effect in the western basin. A positive NAO phase also has an influence on extreme waves although they are smaller in the whole Mediterranean Sea.

Caires et al. (2006) reported that the wave climate is expected to change by a small amount in response to climate change (below 5% between 1990 and 2080). The results presented here could be used to project climate and to develop appropriate studies for coastal protection, improving numerical models and defining long-term wave energy conversion strategies; the climatic patterns of the NAO will dominate the extreme wave climate in the North Atlantic Ocean in future scenarios according to Gleeson et al. (2017).

Chapter 4

Regionalizing the impacts of wind and wave-induced currents on surface ocean dynamics: a long-term variability analysis in the Mediterranean Sea

This chapter is under review as:

Morales-Márquez, V., Hernández-Carrasco, I., Simarro, G., Rossi, V., and Orfila, A. (2020). Regionalizing the impacts of wind and wave-induced currents on surface ocean dynamics: a long-term variability analysis in the Mediterranean Sea. *Journal Geophysical Research: Oceans*. doi: https://doi.org/10.1002/essoar.10505583.1.

Abstract

Effects of wind and waves on the surface dynamics of the Mediterranean Sea are assessed using a modified Ekman model including a Stokes-Coriolis force in the momentum equation. Using 25 years of observations, we documented intermittent but recurrent episodes during which Ekman and Stokes currents substantially modulate the total mesoscale dynamics by two non-exclusive mechanisms: (i) by providing a vigorous input of momentum (e.g. where regional winds are stronger) and/or (ii) by opposing forces to the main direction of the geostrophic component. To properly characterize the occurrence and variability of these dynamical regimes, we perform an objective classification combining self-organizing maps (SOM) and wavelet coherence analyses. It allows proposing a new regional classification of the Mediterranean Sea based on the respective contributions of wind, wave and geostrophic components to the total mesoscale surface dynamics. We found that the effects of wind and waves are more prominent in the northwestern Mediterranean, while the southwestern and eastern basins are mainly dominated by the geostrophic component. The resulting temporal variability patterns show a strong seasonal signal and cycles of 5 - 6 years in the total kinetic energy arising from both geostrophic and ageostrophic components. Moreover, the whole basin, specially the regions characterized by strong wind- and wave- induced currents, shows a characteristic period of variability at 5 years. That can be related with climate modes of variability. Regional trends in the geostrophic and ageostrophic currents shows an intensification of $0.058 \pm(1.43 \cdot 10^{-5})$ $\mathrm{cm/s}$ per year.

4.1 Introduction

Ocean currents are of crucial importance for the transport of physical, chemical and biological variables across the world oceans. They are the main responsible for the horizontal redistribution of energy, salt and heat, playing an important role in the climate system (Covey and Barron, 1988). In particular, the sea surface is a key transitional layer where most biological and biogeochemical activities concentrate and tightly interact with vigorous physical features (e.g. Hernández-Carrasco et al., 2014) ultimately affecting marine biodiversity patterns (e.g. Villarino et al., 2018) and atmosphere-ocean coupled processes (e.g. Bronselaer and Zanna, 2020). Hence, a precise knowledge of the circulation in the upper oceanic boundary layer and of its variability is key to many issues of broad scientific and practical importance, ranging from ecosystem and fisheries management (e.g. Dubois et al., 2016; Futch and Allen, 2019), the tracking of marine pollution including microplastic (e.g. Van Sebille et al., 2015) to marine safety such as search and rescue operations (e.g. Sayol et al., 2014).

Oceanic circulation results from movements of fluid in response to internal forces (pressure gradients and Coriolis forces) and external forces (gravity and frictional forces, such as wind stress and waves at the surface, and drag at the bottom and lateral boundary layers). At the ocean surface, total currents result from several energy inputs from diverse sources occurring at multiple scales. In particular, wind and waves interact with the ocean general circulation, giving rise to a highly variable multi-scale environment. During the last decade or so, mesoscale surface currents have traditionally been interpreted as dominated by the geostrophy. This simplifying assumption, together with the advances in satellite altimetry, have led the oceanographic community to estimate surface horizontal currents from the balance between the pressure gradient and the Coriolis forces. However, although geostrophy provides a reasonable view of the low frequency/large-scale motion of the ocean, it has limitations. As such, previous studies aimed at expressing total currents as a sum of both geostrophic and Ekman components (Sudre et al., 2013; Rio et al., 2014). Despite relative improvements, our description of the upper oceanic layer dynamics is still incomplete as it is also necessary to account for the high frequency and ageostrophic motions caused by both wind- and wave-driven currents. Indeed, there is growing evidence that the mesoscale ageostrophic flow plays an important role in the transport and mixing processes, affecting the distribution patterns of transported materials (Dobler et al., 2019) such as, the fate of marine debris (Onink et al., 2019). Moreover, Fraser et al. (2018) have shown that wave-induced currents enhance ocean connectivity around Antarctica, potentially affecting the local ecosystems.

Although great advances have been made in the last decades for measuring geostrophy at meso and larger scales or wind stress over the ocean surface, such as satellite scatterometers like QuikSCAT or ASCAT (Bourassa et al., 2019), wave and wind-wave combined measurements are still limited to specific sites (mooring, stations and buoys) or interpolated from radar radiometers (Ardhuin et al., 2018). However, the availability of global forecasting systems both for wave and surface winds, allows the inclusion of these high frequency velocities in recently developed models of the ocean circulation, by merging the different sources to obtain improved velocity products (Breivik et al., 2016; Onink et al., 2019).

The wind-driven currents at the sea surface were initially studied by Ekman's seminal work (Ekman, 1905). He proposed that the momentum balance between the turbu-

lence stress caused by the wind and Coriolis force can be modeled as a classical diffusion problem but with a kinematic viscosity. Besides, gravity waves have an associated current, the Stokes velocity resulting from the non-linearity of the wave orbital velocities (Stokes, 1880). From the Eulerian standpoint, the Stokes-drift-induced-current component acts as an additive term that interacts with the mean ageostrophic current, appearing in the momentum equations as an external force such as, a vortex force or as the Coriolis-Stokes force (McWilliams and Restrepo, 1999; Polton et al., 2005). The low and high frequency velocities can be of the same order of magnitude depending on the intensity of the local wind and wave fields (Polton et al., 2005; Breivik et al., 2016; Fraser et al., 2018).

Despite substantial efforts in studying the effects of wind and waves on surface currents around the world (Kaiser, 1994; Polton et al., 2005; Ardhuin et al., 2009; Hui and Xu, 2016; Onink et al., 2019), our knowledge of these ageostrophic currents and of their impacts on the upper layer dynamics of the Mediterranean Sea is still poor. The Mediterranean Sea is a semi-enclosed basin with large spatial and seasonal variability of both winds and wave fields, making it an excellent laboratory to study the effects of the interaction of the wind and wave induced currents in the general circulation. Sayol et al. (2016) studied the energy and mass fluxes generated by wind-wave interactions in the western part of the Mediterranean Sea and showed that the induced surface transport has a seasonal character, peaking during winter seasons. Recently, Morales-Márquez et al. (2020b) showed that this variability is largely controlled by large-scale climatic patterns. The atmospheric circulation over the Mediterranean Sea can be indeed characterized by specific modes of variability related to atmospheric teleconnections (Wallace and Gutzler, 1981). The main climatic patterns influencing the Mediterranean dynamics are the North Atlantic Oscillation (NAO), the East Atlantic pattern (EA), the Scandinavia pattern (SCAND) and the East Atlantic/Western Russia (EA/WR) (Barnston and Livezey, 1987; Morales-Márquez et al., 2020b).

In this Chapter, we first derive analytical expressions to estimate the total oceanic surface currents as a sum of a geostrophic term and another ageostrophic one, taking into account wind and waves forcing. We then apply our expressions to altimetric and re-analyses datasets in order to compute surface currents over the whole Mediterranean Sea for the last 25 years. It allows investigating the relative contributions, which vary in space and time, of both geostrophic and ageostrophic components to the total kinetic energy. In order to identify the regions where the Ekman- and Stokes-induced flows affect substantially the upper ocean dynamics, we perform an objective regionalization of the Mediterranean Sea. Homogeneous dynamical regions are unveiled using a machine-learning algorithm applied to an artificial neural network. Previous studies have proposed diverse objective regionalizations of the Mediterranean Sea (Ayata et al., 2018), using different statistical techniques, and based on different oceanic variables, e.g. climatological averages of temperature, salinity, nutrients concentrations (Reygondeau et al., 2017), transport properties of surface waters (Rossi et al., 2014) or phytoplankton variability (d'Ortenzio and d'Alcalà, 2009; Nieblas et al., 2014). By doing so, we analyze the regional variability of the dynamical impacts of both winds and waves on the surface circulation in the Mediterranean Sea. In each homogeneous dynamical region, we further extract the dominant temporal scales and study their relationships with the main climatic modes to assess the interannual variability of the currents field.

4.2 Sea Surface Currents

Total current at the sea surface ($\mathbf{U_T}$) can be expressed, in complex notation, as the sum of the geostrophy, $\mathbf{U_g} = u_g + iv_g$, and an ageostrophic velocity, $\mathbf{U_a} = u_a + iv_a$ which is associated with the wind and non linear wave-induced momentum along their direction of propagation:

$$\mathbf{U_t} = \mathbf{U_g} + \mathbf{U_a}. \tag{4.1}$$

4.2.1 Geostrophic currents

Considering a steady and Boussinesq flow, the geostrophic term can be obtained from the equilibrium between Coriolis and pressure gradient forces in the momentum equation:

$$\mathrm{i}f\mathbf{U_g} = -\frac{1}{\rho_w}\nabla P, \tag{4.2}$$

where $\nabla = \frac{\partial}{\partial x} + i\frac{\partial}{\partial y}$ and P is the pressure. Using the hydrostatic balance in homogeneous ocean, an expression of the geostrophic velocities can readily be obtained from the Sea Surface Height (SSH) as:

$$u_g = -\frac{g}{f}\frac{\partial(\mathrm{SSH})}{\partial y}, \quad v_g = \frac{g}{f}\frac{\partial(\mathrm{SSH})}{\partial x}, \tag{4.3}$$

where g is the acceleration of gravity and $f = 2\Omega sin\phi$ is the Coriolis parameter with Ω the angular Earth velocity and ϕ the latitude.

4.2.2 Ageostrophic currents: wind and wave driven components

The wind- and wave-induced ageostrophic currents in the upper boundary layer are obtained from the horizontal Ekman-wave induced momentum equation for a steady and Boussinesq flow (Lewis and Belcher, 2004; Huang, 1979; Polton et al., 2005):

$$\mathrm{i}f\mathbf{U_a} = \frac{\partial}{\partial z}\left(\mathrm{A}_z\frac{\partial \mathbf{U_a}}{\partial z}\right) - \mathrm{i}f\mathbf{U_s}, \tag{4.4}$$

where $\mathbf{U_a} = u_a + iv_a$ denotes the horizontal ageostrophic velocity in complex notation, $\mathbf{U_s} = u_s + iv_s$ is the wave-induced Stokes velocity, resulting $if\mathbf{U_s}$ the term from the Coriolis-Stokes force (rotation acting on the Stokes drift), and A_z is the vertical eddy viscosity of sea water. Previous works (Huang, 1979; Polton et al., 2005) have shown that the flow is significantly modified by the Coriolis–Stokes force not only at the near-surface layer, but throughout the entire Ekman layer. We assume that the vertical viscosity is constant and equal to $A_z = 1.0710^{-2}\mathrm{m}^2\,\mathrm{s}^{-1}$ (McWilliams et al., 1997). While other approaches considered a vertical parametrization of A_z (Polton et al., 2005; Wenegrat and McPhaden, 2016), we use a constant value since: (i) it would only affect the estimation at the surface boundary condition and, (ii) the wave-induced circulation changes are independent of the vertical mixing parametrization when the typical depth scale of the waves effect is smaller than the typical Ekman layer.

Assuming a monochromatic wave field propagating in deep water with a wavenumber $\mathbf{k} = (k_x, k_y)$, the Stokes drift velocity, $\mathbf{U_s} = U_s\widehat{\mathbf{k}}$, is related to the wave as (Phillips,

1966):

$$U_s = a^2 \omega k e^{2kz}, \tag{4.5}$$

being a the wave amplitude, $\omega = \sqrt{gk}$ the wave frequency at deep waters, $k = |\mathbf{k}|$ and the wave number unit vector:

$$\widehat{\mathbf{k}} = \cos\left(\theta_{\mathrm{w}}\right) + \mathrm{i}\sin\left(\theta_{\mathrm{w}}\right), \tag{4.6}$$

with θ_w the mean direction of propagation waves, which is not necessarily parallel to the wind stress. We compute the Stokes drift including the sea and swell components of the wave. Thus, the combined effect of wind and waves are not only provided in the generation area but also while waves propagate across their swell.

Both boundary conditions required by the second-order ordinary differential equation (Eq. (4.4)) are given at the free surface and at the vanishing boundary as:

$$\mathrm{A}_z \frac{\partial \mathbf{U_a}}{\partial z} = \frac{1}{\rho_w}\left(\boldsymbol{\tau} + \frac{\partial \boldsymbol{S}}{\partial \boldsymbol{X}}\right), \qquad \text{at} \qquad z = 0, \tag{4.7}$$

$$\mathbf{U_a} \to 0, \qquad \text{as} \qquad z \to -\infty, \tag{4.8}$$

where ρ_w is the sea water density and $\boldsymbol{\tau}$ is the wind stress at the sea surface, $\boldsymbol{\tau} = \rho_a C_D u_{10} \mathbf{u_{10}}$, where ρ_a is the air density (1.2 $\mathrm{kg/m^3}$, u_{10} is the 10-m wind speed and C_D is the neutral drag coefficient taken as, $C_D = (2.7/u_{10} + 0.142 + 0.0764 u_{10})/1000$ following Large et al. (1994). S_{ij} are the components of the radiation stress provided at the surface by:

$$\frac{\partial \boldsymbol{S}}{\partial \boldsymbol{X}} = \left(\frac{\partial S_{xx}}{\partial x} + \frac{\partial S_{yx}}{\partial y}\right) + i\left(\frac{\partial S_{xy}}{\partial x} + \frac{\partial S_{yy}}{\partial y}\right),$$

$$S_{xx} = \frac{E}{2}\cos^2\theta_{\mathrm{w}}, \quad S_{xy} = S_{yx} = \frac{E}{2}\sin\theta_{\mathrm{w}}\cos\theta_{\mathrm{w}}, \quad S_{yy} = \frac{E}{2}\sin^2\theta_{\mathrm{w}},$$

with $E = \rho_w g a^2/2$.

The steady-state solution of Eq. (4.4) subjected to boundary conditions (Eq. (4.7) and (4.8)) is:

$$\mathbf{U_a}(z) = \frac{\boldsymbol{\tau}}{\rho_w \mathrm{A}_z m} e^{mz} + \frac{\frac{\partial \boldsymbol{S}}{\partial \boldsymbol{X}}}{\rho_w \mathrm{A}_z m} e^{mz} + \frac{m^2 \mathbf{U_{s0}}}{4k^2 - m^2} e^{2kz} - \frac{2km\mathbf{U_{s0}}}{4k^2 - m^2} e^{mz}, \tag{4.9}$$

with $\mathbf{U_{s0}} = \mathbf{U_{s(z=0)}}$, $m = \sqrt{\mathrm{i}f/\mathrm{A}_z} = (1+\mathrm{i})\,\lambda$ and $\lambda = \sqrt{f/(2\mathrm{A}_z)}$. The characteristic depth of the Ekman layer is defined as $\delta_e = 1/m$ and the characteristic Stokes depth scale as $\delta_s = 1/2k$.

To clarify the importance Coriolis-Stokes interaction, Eq. (4.9) is rewritten as,

$$\mathbf{U_a}(z) = \mathbf{U_E}(z) + \mathbf{U}_{\tau_{\mathbf{w}}}(z) + \mathbf{U_S}(z) + \mathbf{U_{ES}}(z). \tag{4.10}$$

Each term constituting Eq. (4.10) corresponds to the different components of the ageostrophic velocity. $\mathbf{U_E}(z)$ represents the classical Ekman component. $\mathbf{U}_{\tau_{\mathbf{w}}}(z)$ accounts for the surface current induced by the wave radiation stress, which will not be analyzed separately in the following sections because its value is small compared to the other components, $\mathbf{U_S}(z)$ is the Stokes component, that decreases over the Stokes depth scale, being much shallower than the Ekman layer ($\delta_s \ll \delta_e$). The latter component

is correlated with the dynamical response to the Coriolis–Stokes force, being different than the Lagrangian Stokes drift U_s given by Eq. (5.3). The last term, $\mathbf{U_{ES}}(z)$ is the Ekman-Stokes component that accounts for the non-linear interaction between wind and waves acting over the entire Ekman layer with a similar value than Stokes component on the surface (Polton et al., 2005).

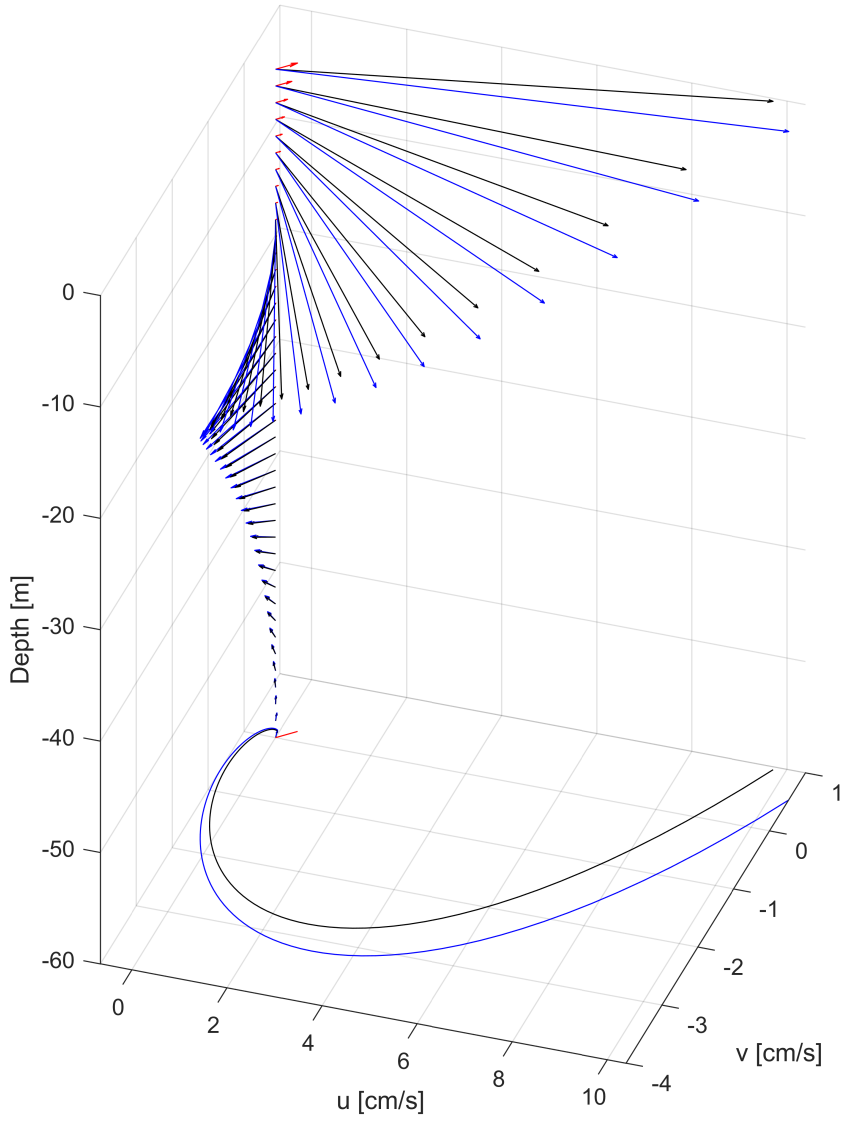

Figure 4.1 *Ekman (blue arrows), Stokes (red arrows) and ageostrophic (black arrows) velocity profiles (in cm/s) at spatial point 6ºE, 38.5ºN corresponding to the* 5^{th} *of February* 2014 *at* $6{:}00$ *UTC.*

Here, $\mathbf{U_a}$ is integrated over 1 meter depth since the mean Stokes layer depth is generally smaller than 2m in the Mediterranean Sea (Sayol et al., 2016). Fig. 4.1 displays an example of the vertical distribution of the Stokes (red arrows), Ekman (blue arrows) and ageostrophic (black arrows) velocity components along the water column in the

Mediterranean Sea. It clearly shows that the Stokes component has a smaller influence (only a few meters near sea surface), while the Ekman component has a significant effect at deeper depths. Also, it is important to note how the Stokes component modifies the vertical distribution of the ageostrophic velocities in spite of its relative small value as compared to the Ekman velocity (see the difference between blue and black arrows).

The velocity fields obtained with this formulation have been validated with the drifters-database provided by the National Institute of Oceanography and Experimental Geophysics Institute (OGS) of Italy. This data encompasses drifters in the Mediterranean Sea from 1986 to 2016. The averaged separation distance between the real and the virtual drifter trajectories averaged over all the hourly initializations is smaller (up to 15 km smaller after 72 hours of integration, not shown) when the virtual drifter trajectory is computed using the total velocity field as compared to the geostrophic velocities. Besides, we found that the variance of the difference between the virtual and the real drifters is also smaller when we advect the drifters in the total velocity field, showing that errors in $\mathbf{U_T}$ are significantly reduced as compared to $\mathbf{U_g}$.

Further modifications of the Ekman model have been considered in the last years, such as including an additional ageostrophic component caused by the geostrophic stress (McWilliams et al., 2015; Wenegrat and McPhaden, 2016). The global comparison between the different ageostrophic components performed in Wenegrat and McPhaden (2016) shows that this term has a higher influence at low latitudes while the Coriolis-Stokes stress dominates at higher latitudes, as in the case of the Mediterranean Sea. Additionally, in the very surface layers of the ocean this component (geostrophic stress) has not a significant value on the effective stress profile, and a relative value respect to the surface wind stress smaller than 3% in spring and summer and smaller than 8% in winter and autumn over the Mediterranean Sea, as shown in Figure 9 of Wenegrat and McPhaden (2016). They also found that the contribution of Coriolis-Stokes stress is 5 times greater than the geostrophic stress in the Mediterranean Sea, with a seasonal variability significantly larger in the Coriolis-Ekman induced currents. This small contribution suggests that the results obtained in this study will not be substantially modified if the geostrophic stress is considered in the Mediterranean basin.

4.3 Data

4.3.1 Wave and atmospheric data

Gridded wave and sea surface wind data can be obtained from remote sensing equipped with scatterometer (Bourassa et al., 2019) and from model outputs. However, while satellites collect indirect observations of wind and waves (Ardhuin et al., 2018), data are acquired along tracks, generating maps with an effective resolution of approximately 40-50km and one week. Since the wave field changes at high frequency, that is for periods spanning a few hours, remote-sensed winds are not the most suitable dataset in order to study the wave effect on surface circulation. Concurrently, there exist nowadays consistent and global database about the wave field, also providing high-resolution wind velocities, that are generated by model reanalyses. Such model reanalyses have been extensively validated with different *in-situ* observations (Berrisford et al., 2011) and have already been used to study transport in the ocean (Breivik et al., 2016).

Surface waves and 10 -m above the sea surface wind velocities are provided by the ERA-Interim reanalysis (Dee et al., 2011). Wave fields are obtained using the WAM

wave model with the assimilation of available global measurements of ERS1 wave height data (Janssen et al., 1997). These reanalysis data are provided by local GRIB code of the European Centre for Medium-Range Weather Forecasts (ECMWF) covering the period between 1979 and 2019 with a temporal resolution of 6 hours and a spatial resolution of $0.125°$ both in latitude and longitude in the Mediterranean Sea (Fig. 4.2). For a detailed description of these products the reader is referred to Berrisford et al. (2011).

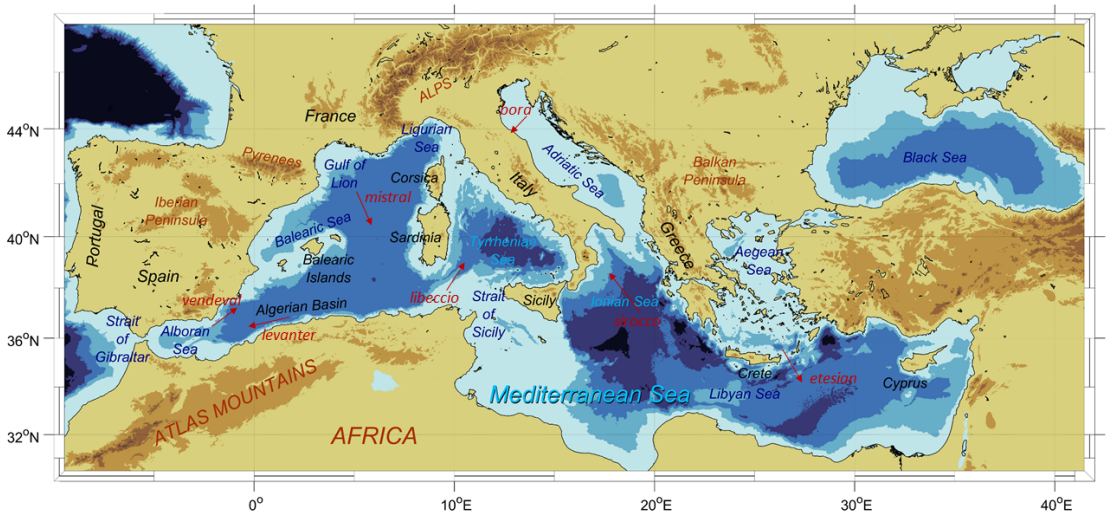

Figure 4.2 *Topography of the Mediterranean basin and naming convention of the main geographical locations used in the Chapter.*

While new wind and wave reanalysis are currently available in the Mediterranean Sea, we use ERA Interim since it provides wind and wave fields at a spatial resolution consistent with the geostrophic velocity field; i.e. $0.125°$ in the Mediterranean Sea against $0.25°$ of winds provided by ERA5, and even coarser for the wave field ($0.5°$ against $0.125°$ of ERA-Interim). Furthermore, we have compared both products and we have found a high correlation and low values of Scatter index and Relative bias between both reanalysis data, as shown in Table 4.1 (Roelvink et al., 2009).

Table 4.1 *Statistical comparison between the ERA-Interim and ERA5 dataset.*

Variable	R^2	SCI	RB
SWH	0.96	0.20	-0.04
U_{10}	0.90	0.42	-0.01
V_{10}	0.89	0.44	-0.05

The leading climatic modes of variability in the Mediterranean Sea, NAO, EA, EA/WR and SCAND have been downloaded from the NOAA Climate Prediction Centre (https://www.cpc.ncep.noaa.gov/data/teledoc/telecontents.shtml; last access on: 27 February 2020). NAO is usually defined as the sea level pressure difference between the Iceland Low and the Azores High (Hurrell et al., 2003). The EA index consists of a north-south dipole of anomaly over the North Atlantic, with a strong multidecadal

variability. The EA/WR is represented with four main anomaly centers; positive phase is associated with positive wave height anomalies located over Europe and negative wave height anomalies over the central North Atlantic. Finally the SCAND pattern is composed with a primary circulation center over Scandinavia, with weaker centers of opposite sign over western Europe. Climate indices are constructed through a rotated principal component analysis of the monthly mean standardized 500-mb height anomalies in the Northern Hemisphere, ensuring the independence between modes at a monthly scale due to orthogonality (Barnston and Livezey, 1987).

4.3.2 Geostrophic velocity field

Geostrophic currents are derived from the Sea Level Anomaly (SLA) provided by the Copernicus Marine Environment Monitoring Service (CMEMS) through the product *Mediterranean Sea Gridded L4 Sea Surface Heights and derived variables reprocessed (1993-ongoing)* (https://resources.marine.copernicus.eu/?option=com_csw&view=details&product_id=SEALEVEL_MED_PHY_L4_REP_OBSERVATIONS_008_051; last access on: 7 February 2019). This product merges the different altimeter missions available (Jason-3, Sentinel-3A, Haiyang-2A, Saral/AltiKa, Cryosat-2, Jason-2, Jason-1, TOPEX/Poseidon, ENVISAT, GFO, ERS1/2). SLA data are homogenized by the DUACS multimission altimeter data processing system in order to generate gridded L4 absolute geostrophic velocities and optimal reprocessed products for long-term analysis, including the robust estimation of regional mean sea levels trends (Pujol et al., 2016). This data set has a daily temporal resolution and is provided over a regular mesh of $0.125°$ over the entire Mediterranean Sea.

Velocity fields $\mathbf{U_g}$ and $\mathbf{U_a}$ are computed every 6 hours for 25 years from 1993 to 2018. For the geostrophic component, daily data are linearly interpolated to 6-hourly time step, while for the ageostrofic component each of the terms are computed for each model output.

4.4 Statistical Methods

4.4.1 Self Organizing Maps

Self-Organizing Maps (SOM) is a statistical method using unsupervised learning neuronal network which is especially suited to extract patterns in large datasets (Kohonen, 1982). SOM is a nonlinear mapping tool that reduces the high-dimensional feature space of the input data to a lower dimensional (usually 2D) network of units called neurons. Through the machine learning algorithm, SOMs are able to compress the information contained in large and complex dataset into a single set of patterns. Similar neurons are mapped adjacent on the network, since SOM preserves topology. This helps to improve the visualization of the patterns, being one of the advantages of this technique.

SOM learning process algorithm inserts the input velocity fields into a neural network which is modified along an iterative procedure. Each neuron is represented by a weight vector containing as many components as the dimension of the input sample data. At each iteration, the neuron whose weight vector is closest (as measured by minimum Eulerian distance) to input data vector is retrofitted together with its topological neighbors towards the input sample according to a neighborhood relationship specified

with a given mathematical function. At the end of the training process, SOM approximates the probability density function of the input data associating each neuron with a reference pattern.

The SOM technique is able to be applied both in the spatial and temporal domains. Since we are interested in classifying the regions in the Mediterranean Sea according to the temporal variability of each of the velocity components, we implement SOM analysis in the time domain. The input dataset is constituted not only by the total velocity time-series ($\mathbf{U_T}$) at each grid point, but also by coupling the geostrophic ($\mathbf{U_g}$), Ekman ($\mathbf{U_E}$) and Stokes ($\mathbf{U_S}$) velocities at the same grid point; as such, it allows analyzing the simultaneous variations of these terms. The resulting time-series are normalized before starting the learning process. At its completion, each neuron will correspond to a specific velocity temporal pattern for $\mathbf{U_T}$, $\mathbf{U_g}$,$\mathbf{U_E}$ and $\mathbf{U_S}$. Then, the time-series of the velocity components at each grid point are classified in accordance with the SOM temporal patterns, providing a map of different sub-regions characterized with a particular temporal variability. To compromise the levels of the regionalization and its interpretability, we retain 6 neurons (2x3 SOM) for the temporal analysis. Preliminary tests using larger numbers of neurons returned more detailed temporal patterns for numerous sub-regions which are, however, difficult to clearly distinguish by their dynamical behaviors (see the supplementary material Fig. S.4.13, Fig. S.4.14 and Hernández-Carrasco and Orfila, 2018). We use a hexagonal map lattice in order to have equidistant neighbors and do not introduce artificial anisotropy. We opted for a linear mode for the initialization, a batch algorithm for the training process, and an 'ep' type of neighborhood function since this parameter configuration produces lower quantitative and topological errors and a minimized computational cost (Liu et al., 2006).

4.4.2 Wavelet power spectral method

Wavelet transform of a time-series $\mathrm{x_n}$ ($W^X(s)$) performs a time-frequency domain decomposition of the time-series by varying the wavelet scale s and by estimating its spectral characteristics as a function of time (Torrence and Compo, 1998). Wavelet is able to extract local-frequency information from a temporal signal in order to extract the dominant modes of variability and detect changes over time (Torrence and Compo, 1998). Wavelet uses a Fourier transform approach on a sliding temporal window returning frequencies at each time step, therefore being well suited for identifying periodic phenomena with changing spectra (Kaiser, 1994). This tool facilitates the study of time-series that contain non-stationary power at many different frequencies (Daubechies, 1990), as is the case here. We used a Morlet wavelet transform, which is a plane wave of wavevector ω_0 modulated by a Gaussian of unit width with an adimensional frequency ω_0=6 (i.e. it contains 6 complete cycles of the temporal scale that is being analyzed). This wavelet base function is adequate to be localized in both time and frequency spaces and therefore to properly assess changes in the wavelet amplitude over time (Torrence and Compo, 1998). To distinguish the signal from the underlying noise, a threshold above the 95% confidence interval of a red-noise spectrum was used. The ability of wavelets to extract significant frequencies in localized time periods provides a powerful tool to characterize the patterns resulting from the previously-described SOMs analysis in the time domain.

4.4.3 Combined SOM-Wavelet coherence analysis

To assess the response of the sub-regions identified by the SOMs to large-scale forcing, we use an approach based on the Wavelet Coherence Analysis (WCA) between two time-series (Grinsted et al., 2004). WCA characterizes cross-correlations by identifying the main frequencies, phase differences and time periods over which the relationships between the variability of the currents components (geostrophy, Ekman and Stokes) and the main relevant large-scale forcing (e.g. NAO, EA, EA/WR and SCAND indices) are tight in each region. To do so, we first analyze the variability in both frequency and time of each velocity components characteristic time and the time series of the climate indices, using the continuous wavelet transform.

Using the cross-Wavelet Transform (XWT), we determine the cyclic changes of the velocity components and their relationship with the climatic indices described above, in each of the sub-regions. The XWT of two time-series x_n and y_n indicates common power and relative phase in the frequency-time domain, given by $W^{XY}(s) = W^X(s)W^{Y^*}(s)$, where $*$ represents the complex conjugate. $|W^{XY}(s)|$ is the cross-wavelet power and the complex argument arg($W^{XY}(s)$) is the relative phase between both time-series (shown in the Fig. 4.10 as arrows).

Finally the degree of coherence of the XWT at each time point is obtained by computing the coefficient R^2 given by the squared absolute value of the smoothed cross-wavelet spectrum, normalized by the product of the smoothed wavelet squared individual spectra, for each scale (Torrence and Compo, 1998; Grinsted et al., 2004), as:

$$R_n^2 = \frac{|S(s^{-1}W_n^{XY}(s))|^2}{S(s^{-1}|W_n^X(s)|^2)S(s^{-1}|W_n^Y(s)|^2)}, \tag{4.11}$$

whose values range from 0 (no correlation) to 1 (perfect correlation) and where S denotes the smoothing operator along the wavelet scale axis and along time. R_n^2 can be interpreted as a localized correlation coefficient in the frequency-time domain. It should be noted that, while cross-wavelet analysis does not establish causative relationships, still allows identifying possible linkages between variables through the synchrony of their time-series.

Last but not least, wavelet coherent analysis is particularly suited to unveil regional relationships between global forcing (climate modes of variability) and the temporal velocity patterns obtained from the SOM given its ability to extract the frequencies and time periods when two time-series are correlated.

4.5 Results and discussion

The overall picture of the mesoscale dynamics at the upper layer is mainly dominated by the geostrophic component for most space and time windows considered (not shown). However, we found time periods where the ageostrophic velocities associated with wind and waves effects largely govern the main circulation over different regions of the Mediterranean Sea. As an example, Fig. 4.3 shows the total surface current and its respective components for the 19^{th} of January 2005 at $12{:}00$ UTC. It exemplifies a dynamical situation characterized by the net prevalence of Stokes and Ekman-induced velocities compared to the geostrophic component. At the geographical coordinate N38° E7°, 37′, 30″ (i.e. central location of the south-western Mediterranean basin), the maximum value of Stokes velocity reaches 15cm/s, being the Ekman velocity of

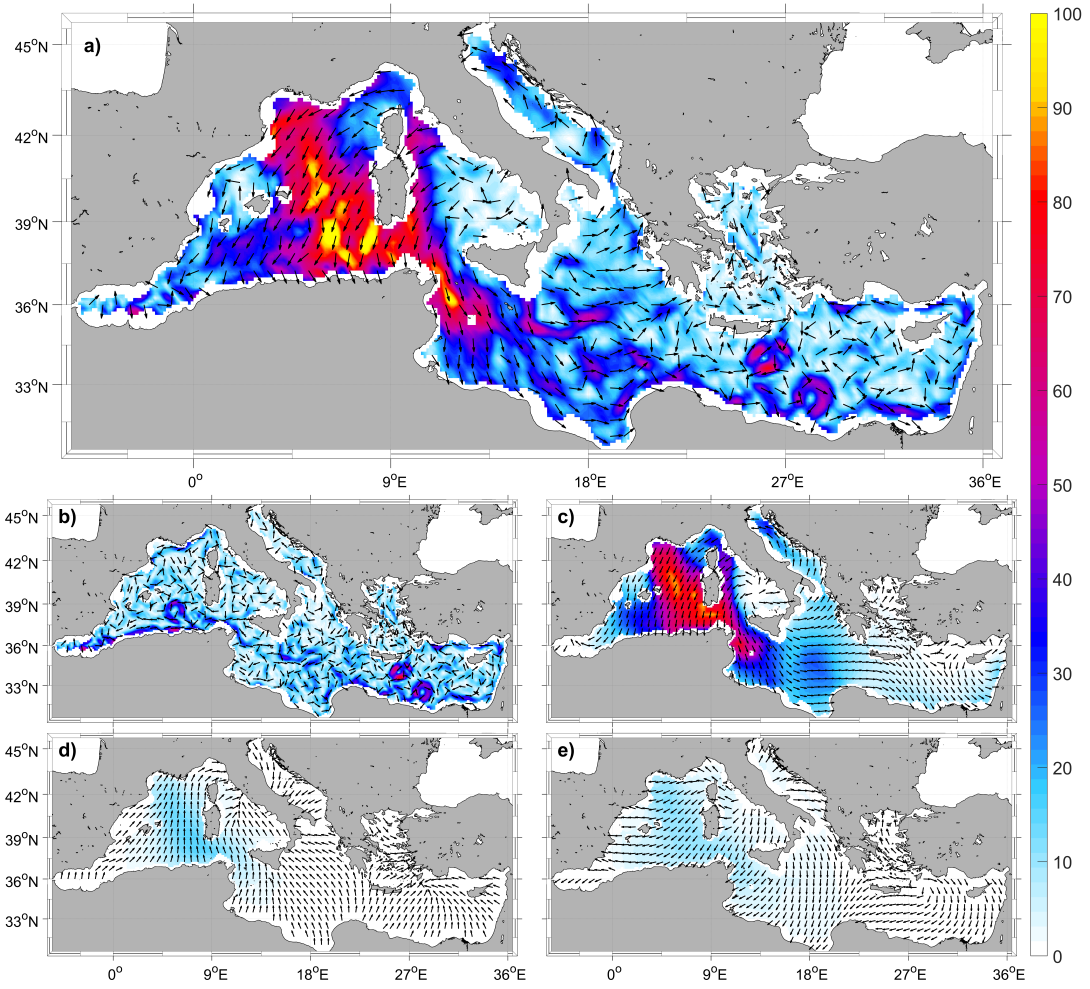

Figure 4.3 *a) Total, b) Geostrophic, c) Ekman, d) Stokes and e) Ekman-Stokes velocity fields for January,* 19^{th} *of* 2005 *at* 12:00 *UTC. The magnitudes (module, in cm/s) of each velocity component are displayed as background colors according to the color-scale. The black arrows represent the direction of the velocity fields. Only 1 of each 5 data points have been plotted for clarity.*

78cm/s which is largely exceeding the geostrophic velocity of 18cm/s. The contributions of $\mathbf{U_S}$ and $\mathbf{U_E}$ to the total velocity at this location for that particular date are 16.7% and 85.18%, respectively. As shown in Fig. 4.3, the spatial distributions of the ageostrophic velocities between the eastern and western basins clearly differ. While in the western Mediterranean, the total velocity is mainly governed by the Ekman component (i.e. intense winds blowing in the Gulf of Lion towards the center of the basin and modifying the Northern Current), the eastern Mediterranean basin is mainly governed by geostrophy (see Fig. 4.2 for the distinct hydrodynamical features).

The relevance of both Ekman and Stokes components on the total current is not only restricted to the situations where they reach maximum values, as shown by the previous exemplary case (Fig. 4.3), since they can also have a noticeable impact on the dynamics with relatively small values. Indeed, the relative differences of direction between the wind stress and wave propagation on one hand, and the geostrophic component on the other hand, affect the total surface circulation. Fig. 4.4 displays an example corre-

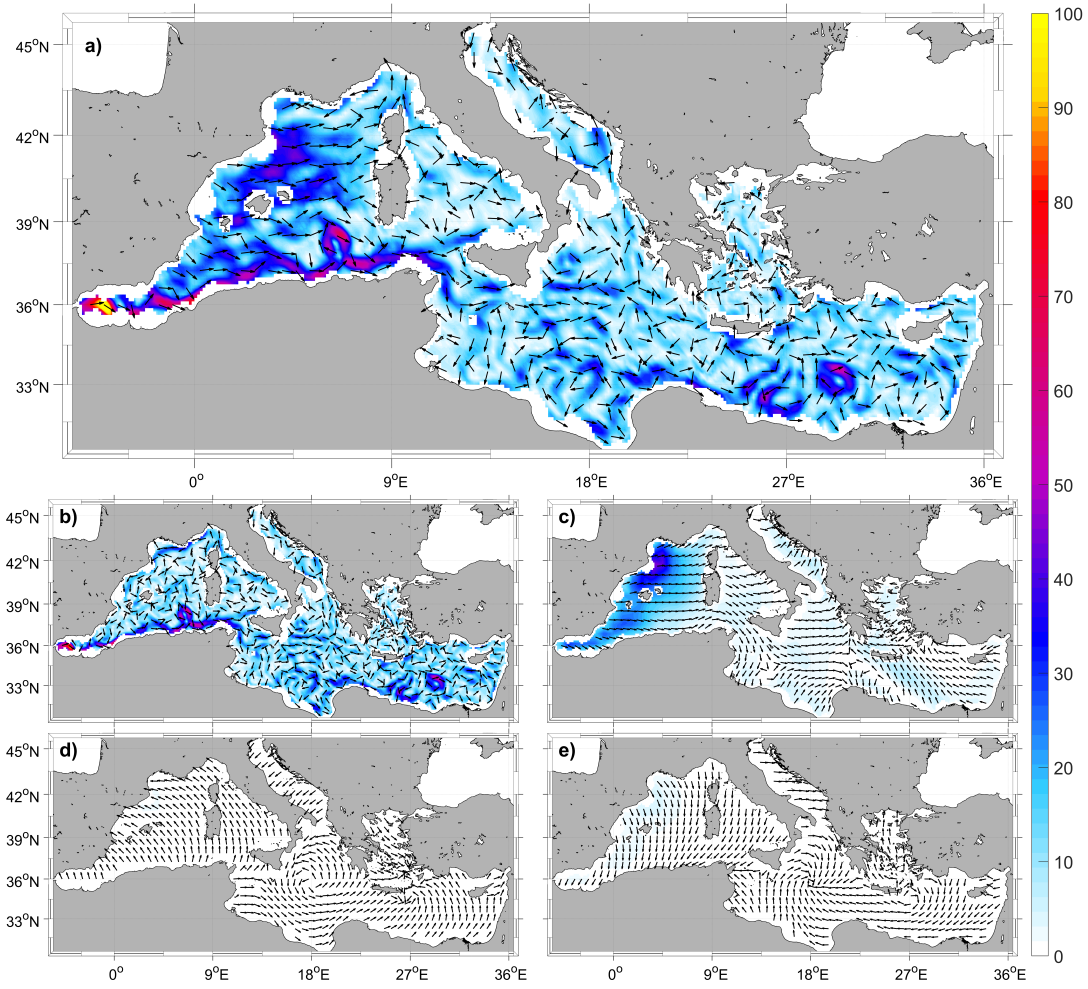

Figure 4.4 *a) Total, b) Geostrophic, c) Ekman, d) Stokes and e) Ekman-Stokes velocity fields for February the* 5^{th} *of* 2014 *at* $6{:}00$ *UTC. The magnitudes (module, in cm/s) of each velocity component are displayed as background colors according to the color-scale. The black arrows represent the direction of the velocity fields. Only 1 of each 5 data points have been plotted for clarity.*

sponding to the 5^{th} of February 2014 at $6{:}00$ UTC where, even though the geostrophy represents the main contribution on the total velocity, both Ekman and Stokes components suppress the Liguro-Provençal Current (Fig. 4.5). This suppressor effect of the Ekman component is not caused by its intensity, ($|\mathbf{U_E}|$ is similar to $|\mathbf{U_g}|$), but because its direction is opposite to the geostrophic current direction.

It is worth noting that $\mathbf{U}_{ES}$ ensures that the total velocity satisfies the wind stress boundary condition at the sea surface. Thus, it removes the sea surface stress caused by the Stokes component ($\mathbf{U}_S$) (Polton et al., 2005; Pearson, 2018). For this reason, $\mathbf{U}_S$ and $\mathbf{U}_{ES}$ usually have opposite direction with the same order of magnitude, with a minor impacts on the total current. This is particularly appreciable when the Ekman layer is deeper than the Coriolis-Stokes depth ($\delta_s \ll \delta_e$), i.e. under short wave periods, where the effect on the current profile resembles the traditional pure Ekman solution (Polton et al., 2005).

These dynamical conditions associated with a large contribution of the wind and

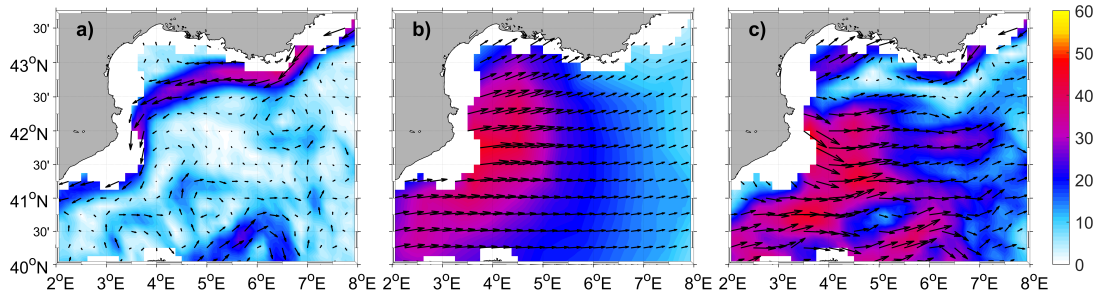

Figure 4.5 *Zoom at the Liguro-Provençal current for a) Geostrophic, b) Ekman and c) Total velocity fields for February the* 5^{th} *of* 2014 *at* $6{:}00$ *UTC. The magnitudes (module, in cm/s) of each velocity component are displayed as background colors according to the color-scale. The black arrows represent the direction of the velocity fields.*

waves induced currents are not isolated cases since these ageostrophic circulation patterns occur frequently over different Mediterranean regions.

4.5.1 Regionalizing the impacts of wind and waves on the total surface kinetic energy

To further characterize the regions and time periods for which the total surface dynamics are governed by the Ekman and Stokes components, we perform a coupled SOMs analysis between the absolute value of $\mathbf{U}_T$, $\mathbf{U}_g$, $\mathbf{U_E}$ and $\mathbf{U_S}$. Note that, these magnitudes are closely related to the root-squared Kinetic Energy (henceforth referred as to KE) given by KE=$(u^2 + v^2)^{1/2}$. We first apply the SOM algorithm to the 6-hour velocities for 2005, since this year presents maximum averaged values for the ageostrophic velocities and the areas influenced by each velocity component can be more clearly delimited.

The different temporal patterns extracted from the SOM analysis using a 2x3 neural network in the time domain are shown in Fig. 4.6 for each of the velocity components. As expected, geostrophy dominates the low frequency variations while the Ekman and Stokes components modulate the high frequency signal of the total velocity, including the sub-daily variability (Onink et al., 2019). This high frequency signal shows the highly variable response of the upper layer dynamics to the rapidly evolving waves and wind forcing. In general, $\mathbf{U_g}$ is of the same order of magnitude as $\mathbf{U_T}$, whereas $\mathbf{U_E}$ is about half (or smaller) of $\mathbf{U_T}$'s intensity while $\mathbf{U_S}$ is one order of magnitude smaller than $\mathbf{U_T}$. As observed in Fig. 4.6, due to the preservation of the topology, the SOM method organizes the patterns in the neural network according to the similarity in the intensity and variability of each velocity components. Patterns showing high contribution of geostrophy are located around the right top corner of the neuronal network (P2 and P3 in Fig. 4.6), while patterns where the contribution of Ekman and Stokes velocities is large are found at the left-hand side of the neural network (P1 and P4). And between them, there are some intermediary patterns (P5 and P6). As revealed by some patterns, the wind and waves induced currents are more intense during winters, exceeding the value of the geostrophic component in some patterns (i.e. P1, P4 and P5). This suggests a strong seasonal variability in the ageostrophic signal which is further analyzed in section 4.5.2.1.

Fig. 4.7 shows the objective classification of the Mediterranean Sea in sub-regions

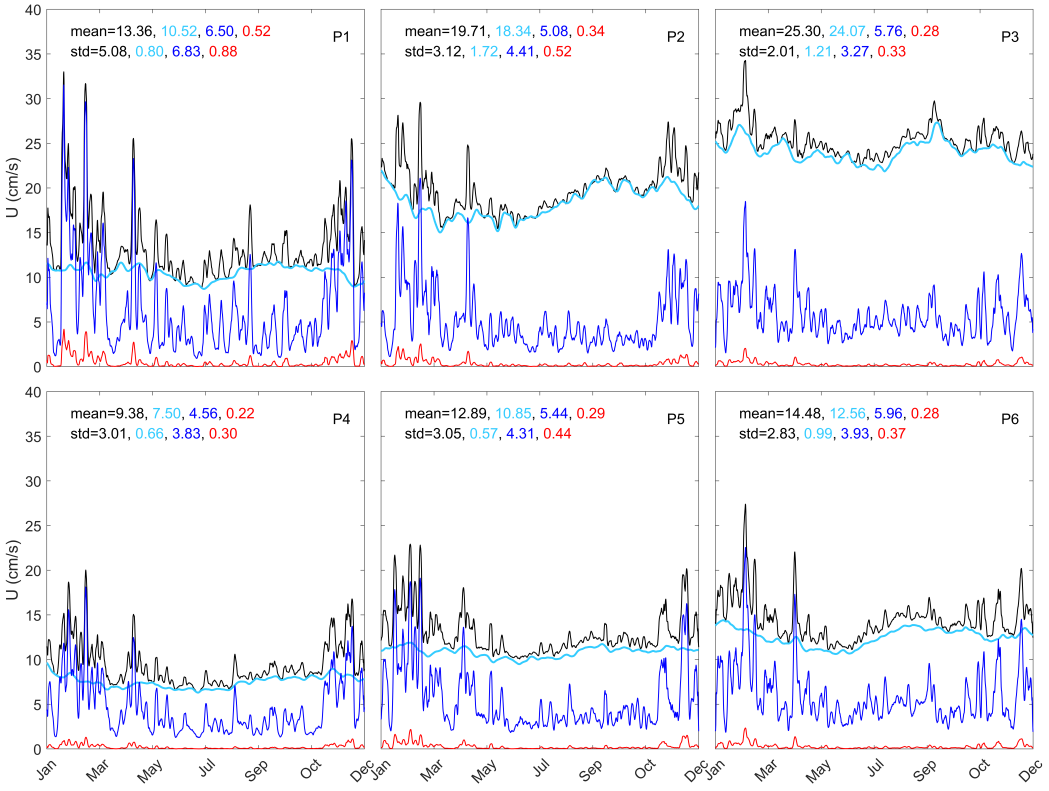

Figure 4.6 *Temporal patterns of the absolute value of the total (black line), geostrophic (cyan line), Ekman (blue line) and Stokes (red line) velocity component fields (in cm/s) extracted from the coupled SOMs technique for* 2005. *Patterns have been smoothed using a moving window of* 3.5 *days in order to facilitate comparison. The means and the standard deviations (in cm/s) of each temporal pattern are reported within each panel.*

based on the combined variability of total, geostrophic, Ekman and Stokes velocity components given by the temporal patterns described previously (Fig. 4.6). The region where the Ekman and Stokes components have the largest values (R1) corresponds to the temporal pattern P1. It identifies the northern and central sub-basins of the western Mediterranean as a region whose surface dynamics is largely affected by the wind and waves induced currents. It is indeed dominated by strong regional winds (i.e. 'mistral' and 'tramontane') blowing southward with the marine origin in the Gulf of Lion (Zecchetto and De Biasio, 2007; Obermann et al., 2018), where waves can be developed through the large fetch (Sayol et al., 2016; Morales-Márquez et al., 2020b). This kind of winds although are stronger with longer duration and more frequent in winter, they also take place in summer (Soukissian et al., 2018). Surprisingly, we found in P1 the events with the larger values of $\mathbf{U_T}$ with velocities up to $40\mathrm{cm/s}$ during the 19^{th} of January, the 14^{th} of February, the 11^{th} of April and the 17^{th} of December (although not easily appreciable in Fig. 4.6 since the original temporal pattern has been smoothed). Regarding the eastern and central parts of the basin, the influence of the Ekman and Stokes components is higher in the regions R4, R5 and R6, characterized by patterns P4, P5 and P6 (see green, yellow and purple regions in Fig. 4.7). These patterns can be associated with local winds such as, etesian and bora (Zecchetto and De Biasio, 2007),

that although they do not have enough distance without any obstacle in order to the waves to be developed, they are able to cause a large Ekman velocity. Comparing the amplitude of Ekman and Stokes components over all the regions, we can observe that western basin is the region most impacted by wind and waves of the Mediterranean Sea, since there is a larger fetch.

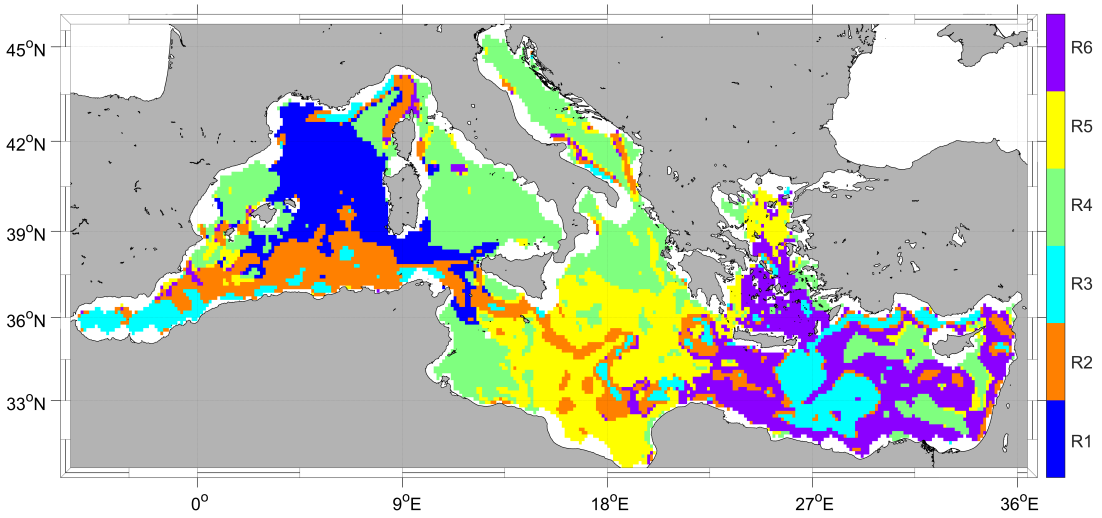

Figure 4.7 *Regions unveiled from the SOM analysis according to the coupled variability of the absolute value of each velocity field component for* 2005. *R1 is dominated by the ageostrophic component; R2/ R3, by the geostrophic one and R4/ R5/ R6 are intermediate patterns.*

Regions where the dynamics is mainly modulated by the geostrophy (low frequency signal) are characterized by P2 and P3 (Fig. 4.6) and shown by R2 and R3 in Fig. 4.7. They identify the well-known geostrophic circulation features in the Mediterranean Sea, including the Alboran gyres, Levantine gyres and the detachment of eddies from the Algerian current through baroclinic instability (R2). Indeed, the Algerian current, which flows along the northern African shelf and then crosses the Strait of Sicily towards the southern Ionian Sea, is clearly identified by R3. It is also remarkable how the main Mediterranean gyres are well characterized within the same region (R2), showing a similar variability in the total kinetic energy of this geostrophic features between the western and eastern basins. These temporal patterns also identify the Liguro-Provençal current that is interrupted in the Gulf of Lions due to the effect of the Ekman and Stokes components (R1). Pattern P3 shows an increase of $\mathbf{U_T}$ during August and September, likely due to the importance of the geostrophic component (in contrast to the weakening of wind and waves). P4 characterizes the regions R4 (green areas in Fig. 4.7) associated with lower total kinetic energy (small values of $\mathbf{U_T}$) and where the Ekman component is relative large, dominating the total velocity during winter season. This pattern identifies broad areas across the western and central parts of the Mediterranean Sea (Thyrrhenian, Adriatic, northern Ionian, Gulf of Gabes and Ebro shelf), as well as, small regions around Cyprus (eastern basin). P5 and P6 are exclusive for the central and eastern Mediterranean, respectively; exhibiting intermediate values of Ekman and Stokes velocities, being higher the contribution of the geostrophy and the total kinetic energy in the eastern region (R6). It is worth mentioning that, the characteristic map of regions shown in Fig. 4.7 is in agreement with the main features of the surface dynamics

in the Mediterranean Sea outlined in Millot (2005).

4.5.2 Regional assessment of the temporal variability

In this Section, we extend the analysis to the 25 years of data to assess the role of wind and waves at the interannual scale. Each velocity component is spatially averaged every 6-h from 1993 to 2018 over each region identified by the previous SOM analysis (Fig. 4.7) to obtain the time-series reported in Fig. 4.8. The time series have been smoothed with a moving window of 45 days to improve readability. The different components exhibit similar variability than previously analysed for 2005, with geostrophy clearly dominating in patterns P2 and P3, and with the wind and wave induced velocities being prominent in pattern P1. The geostrophic component appears as the main contributor describing the large scale variability while Ekman and Stokes components incorporate the high frequency and a clear seasonal signal to the total velocity. Despite the fact that, the values of Ekman and Stokes velocities are high during short time periods, they impact significantly on the total kinetic energy throughout the entire period analyzed. As seen in pattern P1, the Ekman component surpasses the geostrophy during winter. A similar situation occurs in R4, where the P4 presents smaller total kinetic energy with a large impact of the Ekman component in winter. In the central (R5) and eastern (R6) regions, the geostrophic velocities are larger than the Ekman and Stokes components except for a few occasional events, when the two latter are higher than the former. In general, the contribution of the Ekman component to the total velocity is larger in the central part (P5) than in the eastern one (P6). The effect of Ekman and Stokes components at the eastern part, P6, is particularly significant during 2002, 2012 and 2015 winters (see Fig. 4.8).

4.5.2.1 Short-term variability: annual and semiannual cycles

An assessment of the temporal variability (i.e. dominant frequency bands as a function of time) of the different velocity components in each of the SOM regions identified in Fig. 4.7 is here performed applying a wavelet analysis to their corresponding temporal patterns (Fig. 4.9). All the regions show a strong seasonal signal (1 year characteristic period) for all the velocities except for the geostrophic component in R1. This strong intra-annual variability is mainly fueled by the ageostrophic components. While in regions R1, R2, R5 and R6 the annual geostrophic signal is interrupted, the Ekman and Stokes components contribute largely to the short term variability (annual cycle) of the total kinetic energy during these 25 years, as indicated by the marked seasonality of the ageostrophic component for the entire Mediterranean Sea (Fig. 4.8). It should be noted that, $\mathbf{U_T}$ also exhibits an important semi-annual cycle in R6, and in R3 to a lesser extent, during almost all 25 years except 1999. This characteristic period is also present in geostrophy but more discontinued than in the ageostrophic velocity. Note that the semiannual signal in the geostrophic current in R1 from 2000 to 2008 is removed in the total velocity.

4.5.2.2 Long-term variability: relation with climatic modes of variability

Long-term oscillations are found in the total velocity with characteristics periods of around 2, 3 and 5 - 6 years over the whole basin. The long term variability on the

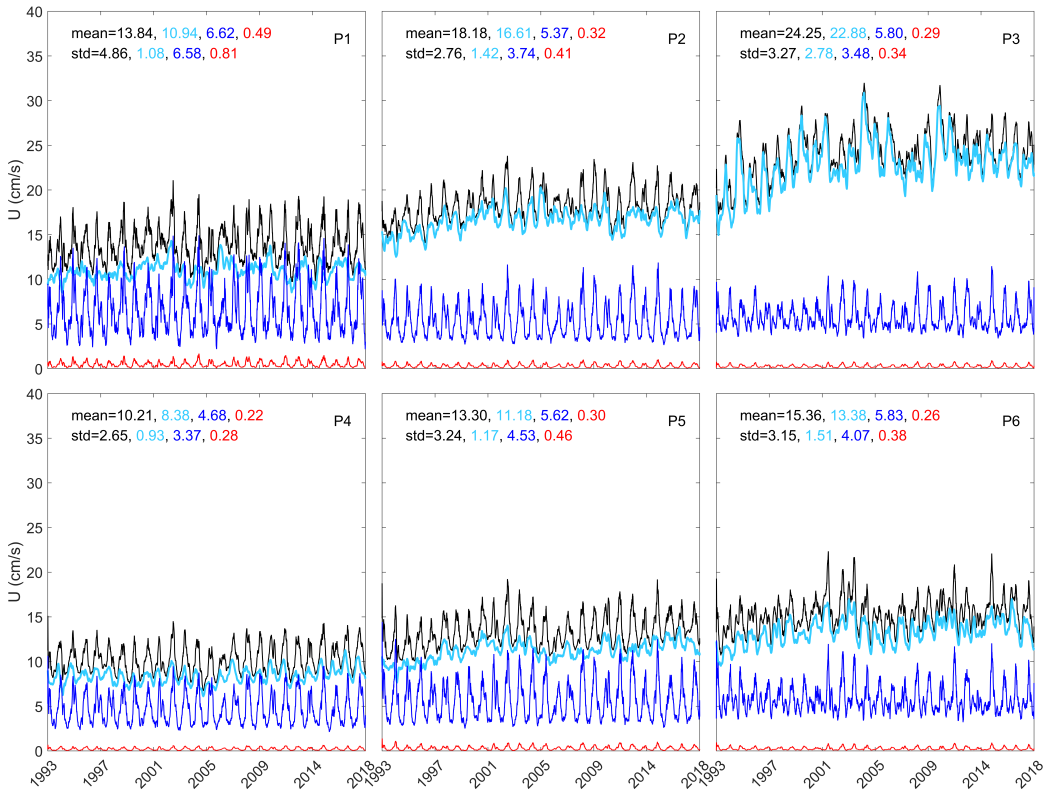

Figure 4.8 *Time series of the spatially-averaged total (black line), geostrophic (cyan line), Ekman (blue line) and Stokes (red line) velocity component module fields (in cm/s) from* 1993 *to* 2018 *in the regions of the temporal SOMs of* 2005.

total velocity field is modulated by the geostrophic component in all the regions. However, Ekman and Stokes components increase the spectrum power of these characteristic periods in some regions. In the western Mediterranean (R1), additional significant periods are identified around 2 and 3 years from 2010 to 2017, from 1999 to 2006 and from 2008 to 2013, respectively, as a result from the combination of the geostrophic and ageostrophic variability. As already suggested in Fig. 4.8, the Ekman component dominates the variability in this region during the 25 years period. In R2, there are significant signals with periods of 1.5 - 2 years and 2 - 4 years over 2013 - 2018 and 2001 - 2015, respectively, also due to the combined influences of the different velocity components. On the other hand, $\mathbf{U_g}$ in R3 is practically the main contributor to the 1.5 - 2 years and 4 - 6 years cycles in the total velocity. Therefore $\mathbf{U_a}$ has poor relevance in explaining the long-term variability in this region. Regions R4 and R5 present a 4 - 6 year-period well defined and a 1.5 years period in some specific years (see Fig. 4.9, R4 and R5). In R5, the annual signal is intermittent in $\mathbf{U_g}$ being present during the 25 years in $\mathbf{U_a}$. Finally, $\mathbf{U_T}$ in R6 registers cycles of 1 - 2.5 years and 1.5 years during 1997 - 2003 and 2013 - 2018, respectively. Periods ranging 5 to 6 years coincide with the characteristic periods of the dominant climatic patterns of variability acting over the Mediterranean Sea (Morales-Márquez et al., 2020b).

In order to get insights about the regional influence of the modes of atmospheric variability on the upper layer dynamics in the Mediterranean Sea, we perform a wavelet coherence analysis between the NAO, EA, EA/WR and SCAND indices and the $\mathbf{U_T}$ in

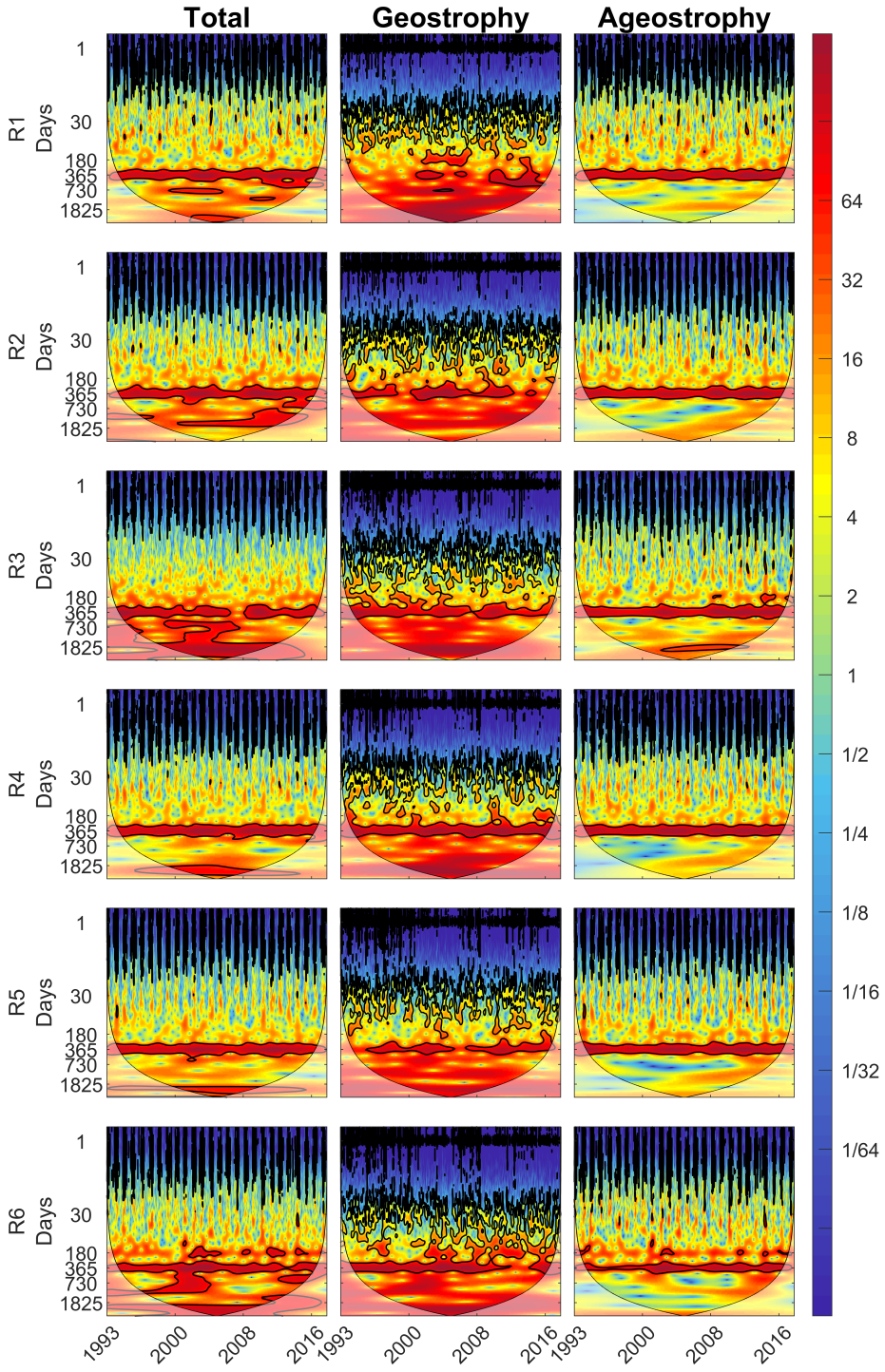

Figure 4.9 *Wavelet power spectrum of the* 6*-hours time series of the spatially-averaged (over the SOM regions shown in Fig. 4.8) Total, Geostrophic and Ageostrophic velocity components from* 1993 *to* 2018*. Contours in black indicates the* 95% *significant levels. Lighter shades show the cone of influence (COI) where the edge effects may distort the Fourier analysis.*

the dynamical regions previously identified (Fig. 4.10). This method allows identifying the frequency bands within which time series of KE for each SOMs region and the large scale atmospheric forcing co-vary.

NAO is correlated with the total velocity with signals of around 1 year during 2014 to 2018 in all the SOM regions (see Fig. 4.10, NAO). For periods spanning 5 - 7 years the total velocity signal is anticorrelated with the NAO in all regions except R1 where the negative correlation is around 2.5 years. Note that, R1 corresponds to the region where wind and waves are most relevant for the modulation of the high frequency variability of the total currents. This is in agreement with the results obtained by Morales-Márquez et al. (2020b), where a strongly significant anticorrelation between extreme waves and the NAO was obtained in the Mediterranean Sea. NAO has a significant influence in R2 with a negative correlation at 2- 5 years during the period of analysis, and in R5 with negative correlation around 2 - 4 years from 1993 to 2002. In addition, NAO has an effect on the semiannual variability in all regions during 1996, 2003 and 2008 being less visible in R3 and R5 (see Fig. 4.10, NAO).

The influence of EA on the variability of the total current in R1 and R4 is associated with 1.5 and 4 - 5 years signals after 2000 (see Fig 4.10, EA). In R1, correlation occurs between 2003 to 2016 with a 4 year-period and for the 25 years period around 7 years (see Fig. 4.10, R1, EA). Similar, but less intense, atmospheric influence is found in R5 and R6. In all regions, a strong anticorrelation is shown around 1 year from 2002 to 2005 and from 2016 to 2018. EA also affects R4 and R5 with a 2 years signal between 2009 to 2012. Note that EA does not affect R3, that is where mesoscale surface dynamics is mainly controlled by the geostrophic component. R6 shows a positive correlation with the EA of 3 year-period from 1993 to 2002.

The signature of the 1 year signal, associated with EA/WR, is clearly seen in all the Mediterranean surface dynamics between 2003 to 2005. The western Mediterranean (R1 and R2) shows an anticorrelation with EA/WR signals at 4 year-period from 2010 to 2018, and around 5-year period in R3 from 1993 to 2007, in agreement with the relationships documented for extreme waves by Morales-Márquez et al. (2020b).

The influence of SCAND index on total surface currents manifests itself with a positive correlation at 1 - 2-year period for the whole basin after 2006. The impact of SCAND climate mode is more intense in eastern Mediterranean, as shown by the negative/positive correlation in the 1.5 - 3 years band between 1993 and 2006 in R3/ R5 and by the strong negative correlation around 3 - 5 year-period during 2000 - 2018 in R6.

4.5.2.3 Trends in the Kinetic Energy

To analyze linear trends in the geostrophic and total velocity modules, the residual of $\mathbf{U_T}$ and $\mathbf{U_g}$ are fitted by a linear regression in time at each spatial point (see Fig. 4.11). We have verified these results with the Theil Sean estimator technique, obtaining similar trend patterns (not shown). The significance level is set at 90% with the Mann Kendall method and with a t-value adjusted of $N-2$ degrees of freedom (Pastor et al., 2018), being the number of points with no-significant values slightly larger using the Mann Kendall method. The estimated global Mediterranean trend of total speed is positive with a value of $0.058 \pm (1.43 \cdot 10^{-5})$ cm/s per year, being the geostrophic one higher with a value of $0.063 \pm (1.20 \cdot 10^{-5})$ cm/s per year (see Fig. 4.11). It suggests that surface velocities, and associated KE, are increasing over this 25 years period.

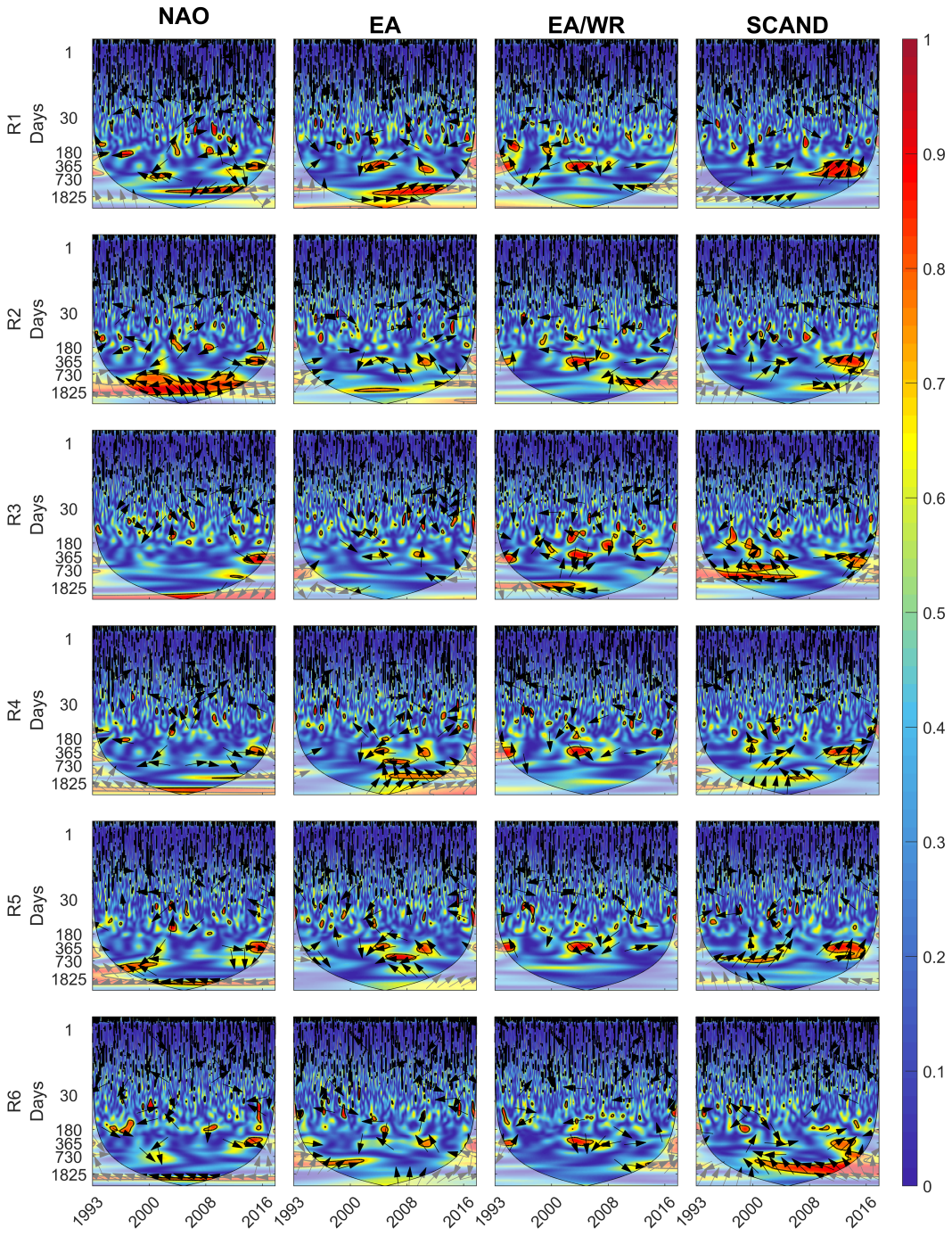

Figure 4.10 *Wavelet coherence between the* 6*-hours time series of the spatially-averaged total velocity module (over the SOM regions shown in Fig. 4.8) and the monthly values of NAO, EA, EA/WR and SCAND climatic indices from* 1993 *to* 2018*. The arrows determine the phase between both series. Arrows pointing to the right represent positive correlation (signals in phase) and when they point to the left, anti-correlation (signals in anti-phase). Contours indicate wavelet squared coherence.*

While regions where the wind- and wave-induced velocities have the largest impacts (R1 and R4) do not exhibit clear and significant trends in the total velocity module, the geostrophic dominated regions (R3 and R2) show positive trends with a shift in 2003 (0.59 $(\pm 8.15 \cdot 10^{-5})$ and 0.37 $\pm(6.56 \cdot 10^{-5})$ $\mathrm{cm/s}$ per year), see Fig. 4.12. These results are consistent with the KE increase presented in Ser-Giacomi et al. (2020), they explain this rise as a potential relation to an increment of a baroclinic instabilities since they show a decrease of the wind stress across the most of the western basin. While such mechanism could also explain the rising trend evidenced here, further analyses are needed to ascertain which mechanism is at play. Note, however, that the clear positive trend from 1993 to 2002 seems to slow down after 2003. It could indicate that this is not a proper trend but rather part of a longer oscillation or an artifact due to the inconsistency in the SLA dataset of 25 years. However, the altimeter product used in this study (see section 4.3) is the result of homogenization procedure among several altimeter satellite observations and is thus considered suitable for trend analysis (Pujol et al., 2016). $\mathbf{U_T}$ and $\mathbf{U_g}$ present similar trends during the 25 years analyzed (see Fig. 4.11, a and b) with an increment in the eastern Mediterranean Sea and a decrease in the western basin. The global trend is generally positive in regions where the geostrophy is dominant, except in the Libyan Sea where both $\mathbf{U_T}$ and $\mathbf{U_g}$ tendencies are negative, in good agreement with Fig. 4.8. The maximum trend of 0.72 $\pm(2.44 \cdot 10^{-5})$ $\mathrm{cm/s}$ per year for $\mathbf{U_T}$ is found in the eastern part of the Mediterranean basin. In contrast, the minimum value in the Libyan Sea is -0.81 $\pm(2.42 \cdot 10^{-5})$ $\mathrm{cm/s}$ per year (Fig.4.11, a). The maximum and minimum trends for $\mathbf{U_g}$ are found in the same regions with slightly smaller values, 0.73 $\pm(2.20 \cdot 10^{-5})$ and -0.77 $\pm(2.85 \cdot 10^{-5})$ $\mathrm{cm/s}$ per year, (Fig.4.11, b). The ageostrophic input on the trend of the total velocity module is evaluated through the difference between both tendencies, $\mathbf{U_T}$ and $\mathbf{U_g}$. Most values are close to zero in the whole Mediterranean (see Fig.4.11, c), except in the region with the minimum trend of $\mathbf{U_T}$, where the difference of trends is $\sim$ 0.2 $\pm(9.89 \cdot 10^{-7})$ $\mathrm{cm/s}$ per year. In the western region, there are some areas with a small positive differences of trend of 0.05 $\pm(6.33 \cdot 10^{-7})$ $\mathrm{cm/s}$ per year, corresponding to R1 of Fig. 4.7 and also to the regions of the main regional winds.

Positive global trends of other oceanic variables have also been observed for the Mediterranean. Pujol and Larnicol (2005) reported a trend in the root squared Eddy Kinetic Energy of 0.7 $\mathrm{cm/s}$ per year, between 1993 and 2003, and Pastor et al. (2018) showed a linear trend for Sea Surface Temperature from 1982 to 2016 of 0.03 ± 0.003 $^{\mathrm{o}}\mathrm{C}$ per year.

4.6 Conclusions

This study analyzes the effect of Ekman and Stokes velocities on the total kinetic energy in the upper layer of Mediterranean Sea. By solving the momentum equation (Eq. (4.4)), we include the interaction between Ekman and Stokes drift on the geostrophic velocity. Total velocity is decomposed into different components: the geostrophic, Ekman, Stokes and the interaction between Ekman and Stokes. The regional relevance of these different components is evaluated through SOM decomposition, and their variability through wavelet analysis.

Once the velocity components are obtained, a dynamical regionalization of the Mediterranean Sea has been performed based on the local impacts of waves and wind on the total velocity variability. Ekman currents account for the short-term variabil-

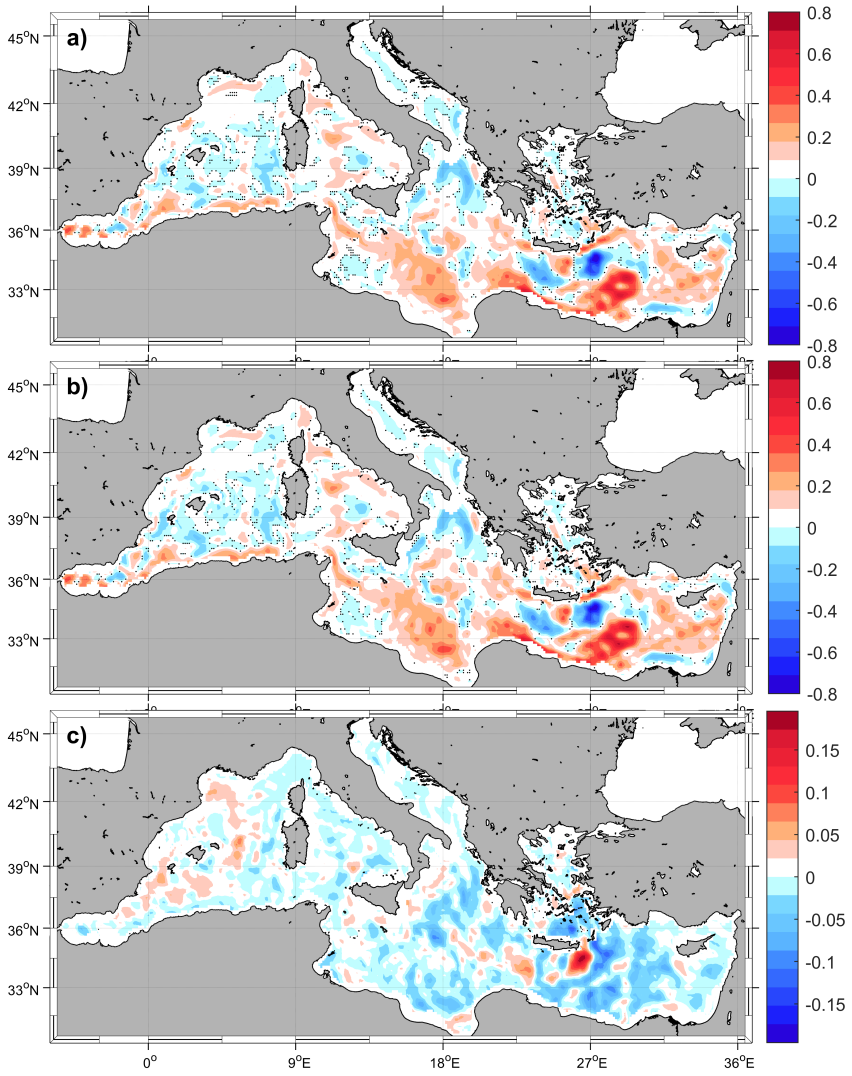

Figure 4.11 *Trend in cm/s per year of the a) Total velocity module and b) Geostrophic component module from* 1993 *to* 2018*. c) Difference between a) and b) in cm/s per year. No significant values at the* 90% *confidence interval are dotted (with Mann Kendall method).*

ity (seasonal, semi-seasonal and smaller time scales) of the surface circulation, especially during winter when the Ekman component occasionally exceeds geostrophy due to strong regional winds. The regionalization shows that the effects of Ekman and Stokes are more marked in the western than in the eastern Mediterranean basin. This is the result of the larger fetch in the western basin, allowing the development of larger swells (Mao and Heron, 2008). Regionalization of velocity components identifies two regions (associated with the main Mediterranean gyres and the Algerian current) where the geostrophy modulates the total kinetic energy variability. These regions are characterized by a positive trend of the module velocity of $0.14 \pm (2.15 \cdot 10^{-5})$ cm/s per year during the 25 years, with stronger increments during $1993 - 2002$. The dominant periods of the total currents in the entire Mediterranean Sea, essentially dominated by geostrophy, are 1 and 5 - 6 years. In regions where the inclusion of both Ekman and Stokes velocities returns a significantly different flow field than the one obtained by

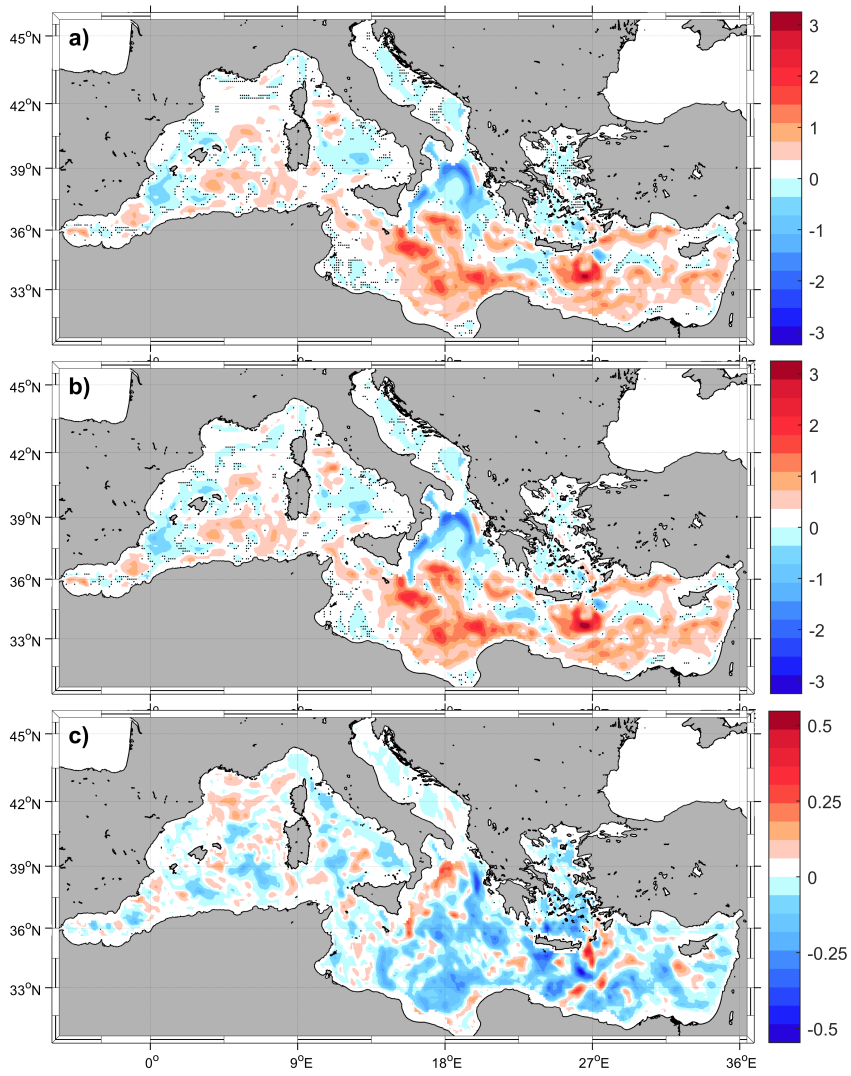

Figure 4.12 *Trend in cm/s per year of the a) Total velocity module and b) Geostrophic component module from* 1993 *to* 2002*. c) Difference between a) and b) in cm/s per year. No significant values at the* 90% *confidence interval are dotted (with Mann Kendall method).*

geostrophic approximation, intermediate periodicity values between 1 and 5 years are found. These signals of variability are related with the principal climatic modes typical of the Mediterranean basin: the NAO, EA EA/WR and SCAND patterns. NAO dominates, with a negative correlation, the large-scale, around 5 - 7 years in the whole basin except in the western Mediterranean, which was already noticed by Morales-Márquez et al. (2020b). Furthermore, NAO is correlated with the annual variability during 2014-2018 and with the semiannual variability at the whole basin, although these connections are weaker for geostrophy-dominated region. The EA index has a positive large-scale correlation in the Mediterranean Sea (4 - 7 years), with the exception of the geostrophic modulated region. The long-term variability effect of EA/WR on the currents velocity is negative and between periods of 4 to 5 years, in particular in the Western Mediterranean. Finally, the SCAND mode of variability has a negative effect in periods of 3 -5 years in the eastern basin.

The methodology presented in this work can be used to better understand the physical, biological and chemical processes occurring at the upper layers of any ocean region using only observations with a low computational cost. In the Mediterranean Sea, there is a need for an improved wave model accounting for the feedback between the Ekman currents on the wave field evolution, and how the Ekman layer evolves due to the non-linear evolution of the wave field, which necessarily contemplates a non-steady Ekman current, as shown in Shrira and Almelah (2020). Next step is devoted to extend this analysis to study transport properties from the Lagrangian point of view. Thus, several applications (e.g. floating debris, oil spill, Search and Rescue, jellyfish tracking, etc.) could benefit from this approach to obtain reliable nowcast.

Supplementary material

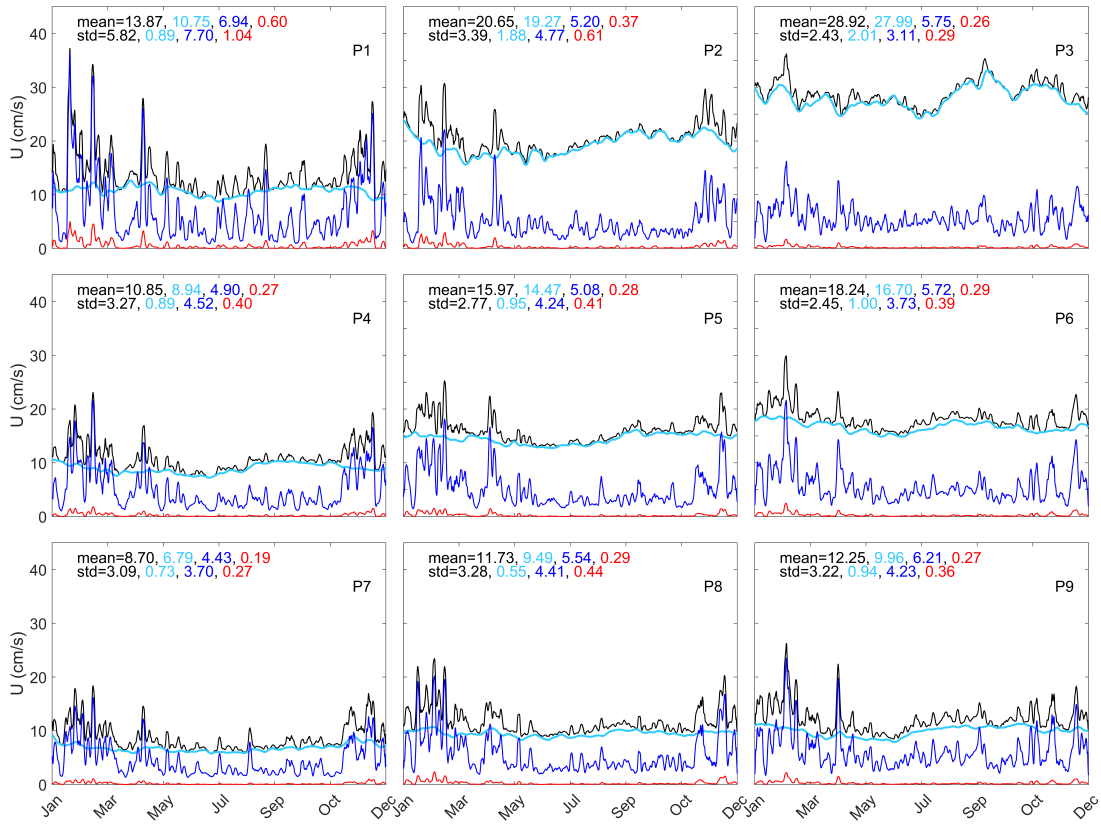

Figure S.4.13 *Temporal patterns of the absolute value of the total (black line), geostrophic (cyan line), Ekman (blue line) and Stokes (red line) velocity component fields (in cm/s) extracted from the coupled SOMs technique for* 2005 *with* 9 *neurons. Patterns have been smoothed using a moving window of* 3.5 *days in order to facilitate comparison. The means and the standard deviations (in cm/s) of each temporal pattern are reported within each panel.*

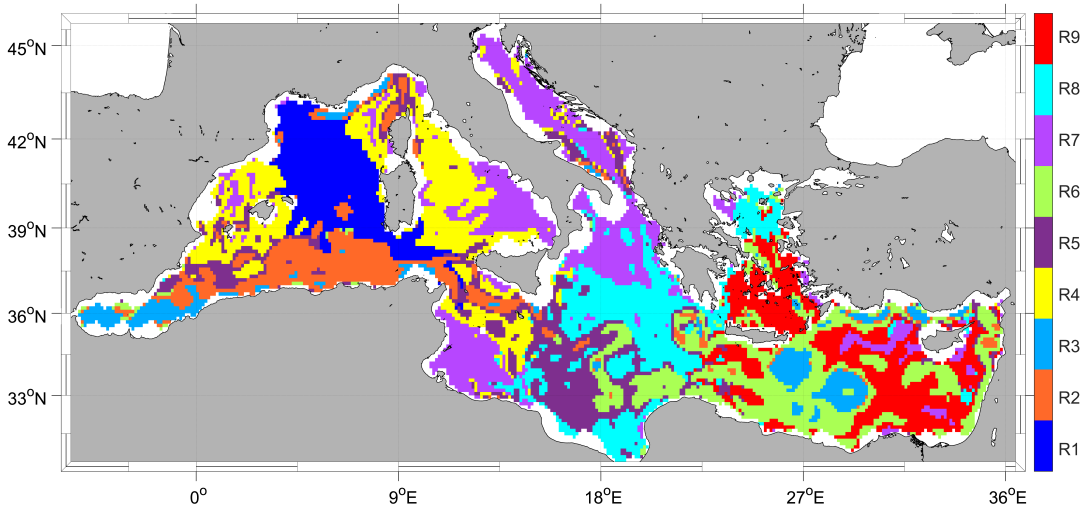

Figure S.4.14 *Regions unveiled from the SOM analysis for* 2005 *with* 9 *neurons, according to the coupled variability of the absolute value of each velocity field component.*

Chapter 5

Ageostrophic contribution by the wind and waves induced flow to the lateral stirring in the Mediterranean Sea

This chapter is under review as:

Morales-Márquez, V., Hernández-Carrasco, I., and Orfila, A. (2021). Ageostrophic contribution by the wind and waves induced flow to the lateral stirring in the Mediterranean Sea. *Journal of Physical Oceanography*.

Abstract

We study the impact of the Ekman currents and Stokes drift on the horizontal mixing and transport properties of the Mediterranean Sea from a Lagrangian perspective. Finite Size Lyapunov Exponents (FSLE) at the ocean surface are computed on the whole basin using 25 years of geostrophic currents derived from SLA, 10-m wind velocity and wave fields. We find that the transport pathways unveiled by the geostrophic Lagrangian coherent structures (LCS) are significantly modified by the ageostrophic currents, often leading to a decrease of the retention capacity of the eddies. An exhaustive assessment of the regional dependence and temporal variability of the FSLE shows an increase of the horizontal mixing activity, due to the ageostrophic component, up to 36% in regions such as the Gulf of Lion or the Aegean Sea, during the seasons where wind and waves are intense and persistent. Positive trends in the total FSLE (up to 1.2% of the value of FSLE per year in some regions) suggest that Mediterranean Sea has experienced a significant increase in mixing activity over the last decades. Ageostrophic features are considered to play a role in determining the properties of the relative dispersion. Through the analysis of the Lagrangian Anisotropy Index (LAI) using virtual and real pairs of drifters, we observe that the particle dispersion is mainly dominated by the zonal flow, and that the ageostrophic currents induce meridional dispersion, particularly in regions where wind and wave are intensified.

5.1 Introduction

Accurate assessment of surface velocities is fundamental for the analysis of the energy budgets at the ocean interface as well as to estimate the transport of mass and momentum with implications in activities, such as the mitigation of oil spills (Abascal

et al., 2009; Sayol et al., 2014), the fate of marine debris (Onink et al., 2019), or to determine the connectivity patterns among different ocean regions (Rossi et al., 2014; Ser-Giacomi et al., 2021), among many others. In particular, transport and mixing properties in the upper layers have profound consequences on the biogeochemical cycles and the dynamics of marine species. The knowledge of such dynamics is therefore crucial to understand the mechanisms regulating marine ecosystems (Lévy et al., 2018; Legrand et al., 2019; Hernández-Carrasco et al., 2020).

Ocean dynamics is mainly driven by the geostrophic currents and, up to a significant extend, modulated by the wind-driven Ekman velocities and the wave-induced Stokes drift (Polton et al., 2005). These components contribute to the variability of the dynamics at the upper ocean layers with different spatial and temporal scales. While geostrophic currents are related to mesoscale and slow processes, the ageostrophy associated with wind and waves, induces high-frequency modifications to the large scale motions (Hui and Xu, 2016; Morales-Márquez et al., 2020a).

Several works have attempted to analyze the role of wind and waves on surface currents (Hui and Xu, 2016; Onink et al., 2019). The first attempt to understand the ageostrophic component at the ocean surface by the wind stress was developed more than a century ago by Ekman (Ekman, 1905). Since then, many works improved the classical Ekman theory modifying the parameterization of the vertical structure of the wind forcing through different eddy viscosity profiles or including the effects of waves (Welander, 1957; Huang, 1979; Price et al., 1987; Polton et al., 2005; McWilliams et al., 2009; Wenegrat and McPhaden, 2016). Previous studies, using an expression for the total surface currents as the sum of both geostrophic and ageostrophic (Ekman and Stokes) components based on available observations, have shown the important role of the wind and wave induced velocities in the global surface dynamics (Sudre et al., 2013; Ardhuin et al., 2009; Sayol et al., 2016; Hui and Xu, 2016). Recently, Morales-Márquez et al. (2020a) by solving the momentum equation in the steady state for wind and waves (Polton et al., 2005), presented a regionalization of the Mediterranean Sea surface dynamics as a function of the relative importance of the geostrophy and ageostrophy components. These authors found a high ageostrophic contribution to the total kinetic energy at the eastern and northwestern basins, while the geostrophy clearly dominates the dynamics in the Alboran, the Algerian and the Ionian sub-basins.

The growing evidence that Ekman and Stokes velocity components have a strong impact on relevant ocean properties ended in a increasing interest in better understanding the effect of these ageostrophic currents on the Lagrangian transport processes (Onink et al., 2019; Dobler et al., 2019). Previous studies have pointed up that Ekman currents play an important role in the accumulation of microplastics in the main subtropical ocean gyres (Onink et al., 2019). Indeed, the wave-induced velocity dramatically affect the direction of the Lagrangian trajectories of marine debris advected by the geostrophic currents in the southern Indian basin (Dobler et al., 2019). However, to date and to the best of our knowledge, the contribution of each velocity component on the lateral stirring and relative dispersion has not been totally assessed. The Lagrangian dynamics of the ocean flow can be readily explored by the Finite Size Lyapunov Exponents (FSLE) (Haller, 2001; d'Ovidio et al., 2004; Hernández-Carrasco et al., 2012). FSLE is an usual method used to analyze the dispersion properties of the turbulent flow as well as to reveal relevant spatial structures, i.e. the Lagrangian Coherent Structures (LCS), which strongly organize the transport in a dynamical fluid system (see Haller, 2015, for a review). The importance of the LCS in the structuring of the biogeochemi-

cal properties and ocean ecosystems has been largely demonstrated in previous studies. For example, the LCS obtained from ridges of FSLE have been correlated with filaments of remote-sensed chlorophyll (Chl *a*) (Lehahn et al., 2007; Hernández-Carrasco et al., 2018, 2020), sea bird foraging behavior (Kai et al., 2009), and with the modelled extension of oxygen minimum zones (Bettencourt et al., 2015).

In this Chapter we analyze the impact of the Ekman and Stokes components on the geostrophic LCS and on dispersion properties at the ocean surface in the Mediterranean Sea. Based on the formulation used in Morales-Márquez et al. (2020a), FSLE are computed for the geostrophic and ageostrophic velocity components using operational available products with the aim to investigate the transport and mixing properties of the different Mediterranean sub-basins.

This Chapter is organized as follows: Section 5.2 describes the used data and contains a brief summary of theoretical equations in order to obtain the velocity field. Section 5.3 exposes the applied methodology to analyze the case study. In Section 5.4, the acquired results in this Chapter are reported and discussed. And, finally, Section 5.5 concludes the work with some highlighted points.

5.2 Data

5.2.1 Velocity fields

Sea surface currents are obtained following the methodology described in Morales-Márquez et al. (2020a). The total velocity field ($\mathbf{U_T}$) can be approximated as the sum of the geostrophic ($\mathbf{U}_g = \mathrm{u}_g + i\mathrm{v}_g$) and the ageostrophic components resulting from wind and waves stress, ($\mathbf{U}_a = \mathrm{u}_a + i\mathrm{v}_a$).

The geostrophic component is obtained from the equilibrium between the Coriolis force and the pressure gradients in the momentum equation for a steady, homogeneous and Boussinesq flow:

$$u_g = -\frac{g}{f}\frac{\partial(\mathrm{SSH})}{\partial y}, \quad v_g = \frac{g}{f}\frac{\partial(\mathrm{SSH})}{\partial x}, \tag{5.1}$$

where SSH is the Sea Surface Height, g the acceleration of gravity and f the Coriolis parameter. These velocity fields are derived from the Sea Level Anomaly (SLA) provided by Copernicus Marine Environment Monitoring Service (CMEMS) through the product *Mediterranean Sea Gridded L4 SSH*. This dataset has a daily temporal resolution, which are interpolated each 6 hours, in accordance with the ageostrophic velocities (see below), to compute the total velocity field in a regular mesh of $1/8^\circ$ over the entire Mediterranean Sea.

The ageostrophic component caused by wind and waves acts on the Ekman-Stokes layer and is obtained solving the horizontal Ekman-wave induced momentum equation for a steady, homogeneous and Boussinesq flow (Huang, 1979; Hui and Xu, 2016):

$$\mathrm{i}f\mathbf{U}_a = \frac{\partial}{\partial z}\left(\mathrm{A}_z\frac{\partial \mathbf{U}_a}{\partial z}\right) - \mathrm{i}f\mathbf{U_s} - \mathbf{T}_{wds}, \tag{5.2}$$

where $\mathbf{U_s}$ is the wave-induced Stokes velocity ($\mathbf{U_s} = U_s\widehat{\mathbf{k}}$), that assuming a monochro-

matic wave field propagating in deep water is related to the wave as (Phillips, 1966):

$$U_s = a^2 \omega k e^{2kz}, \tag{5.3}$$

being a the wave amplitude, $\omega = \sqrt{gk}$ the wave frequency at deep waters, and $k = |\mathbf{k}|$ the wave number unit vector. The wave-induced Stokes velocity results from the Coriolis-Stokes force term, $if\mathbf{U_s}$. In this work, the momentum transfer from waves to the mean flow due to dissipation of wave energy ($\mathbf{T}_{wds}$) is neglected and the vertical viscosity (A_z) is assumed dependent on wind speed with the relation $1.210^{-4}\mathbf{U_{10}}^{\mathbf{2}}\mathrm{m}^2\,\mathrm{s}^{-1}$ (Ekman, 1905; Santiago-Mandujano and Firing, 1990) for the whole basin. According to Polton et al. (2005) and Morales-Márquez et al. (2020a), the momentum equation (Eq. 5.2) can be solved as a two points boundary value problem with the modified Ekman-Stokes condition at the free surface and a vanishing condition at $z = -\infty$ as:

$$\mathbf{U}_a(z) = \frac{\boldsymbol{\tau}}{\rho_w \mathrm{A}_z m} e^{mz} + \frac{\frac{\partial \boldsymbol{S}}{\partial \boldsymbol{X}}}{\rho_w \mathrm{A}_z m} e^{mz} + \frac{m^2 \mathbf{U}_{s0}}{4k^2 - m^2} e^{2kz} - \frac{2km\mathbf{U}_{s0}}{4k^2 - m^2} e^{mz}, \tag{5.4}$$

where τ is the wind stress, ρ_w the water density, $\frac{\partial \boldsymbol{S}}{\partial \boldsymbol{X}}$ the radiation stress due to the waves at the sea surface, k the wavelength, $\mathbf{U}_{s0} = \mathbf{U}_{s(z=0)}$ and $m = \sqrt{\mathrm{i}f/\mathrm{A}_z} = (1+\mathrm{i})\sqrt{f/(2\mathrm{A}_z)}$.

Following the same order of the components in Eq. (5.4), and depending on the physical forcing, the ageostrophic component can be split into:

$$\mathbf{U}_a(z) = \mathbf{U}_E(z) + \mathbf{U}_{\tau_w}(z) + \mathbf{U}_S(z) + \mathbf{U}_{ES}(z), \tag{5.5}$$

where $\mathbf{U}_E(z)$ represents the classical Ekman component, $\mathbf{U}_{\tau_w}(z)$ accounts for the surface current induced by the wave radiation stress, $\mathbf{U}_S(z)$ is the Stokes component, and $\mathbf{U}_{ES}(z)$ is the Ekman-Stokes component that accounts for the interaction between wind and waves acting in the entire Ekman layer (Polton et al., 2005). Here, $\mathbf{U_a}$ is integrated over 1 meter depth since the mean Stokes layer depth is generally smaller than 2 m in the Mediterranean Sea (Sayol et al., 2016).

To obtain this ageostrophic component, we use wave data (SWH and mean period) and 10-m height wind derived from the ERA-Interim reanalysis product, which uses a WAM wave model with the assimilation of available measurements ERS1 satellite wave height data (Janssen et al., 1997). These data are extracted from local GRIB code of the European Centre for Medium-Range Weather Forecasts (ECMWF). This reanalysis product has a temporal resolution of 6 hours from 1979 to 2019 and a spatial resolution of $1/8°$ both in latitude and longitude over the Mediterranean Sea. A detailed description of these products can be found in Berrisford et al. (2011).

5.2.2 Lagrangian drifter data

We use data from a total of 690 (15 SVP (Surface Velocity Program) and 675 CODE (Coastal Ocean Dynamics Experiment)) surface drifters deployed between 1994 and 2005 by several institutions operating in the Mediterranean Sea and collected by the Italian National Institute of Oceanography and Experimental Geophysics (OGS) (Hansen and Poulain, 1996; Menna et al., 2017).

5.2.3 Dynamical regions of the Mediterranean Sea

We evaluate the transport and mixing properties in the six dynamically homogeneous regions of the Mediterranean Sea (shown in Fig. 5.1) reported in Morales-Márquez et al. (2020a). These regions (henceforth SOM-regions: R1, R2, R3, R4, R5 and R6) are unveiled through a Self-Organising Maps (SOM) analysis (machine-learning algorithm applied to an artificial neural network) based on the homogeneous contribution of the geostrophic and Ekman- and Stokes-induced currents to the total kinetic energy. The regions where the mesoscale ageostrophic kinetic energy is significant are identified especially in R1, while the regions where geostrophy dominates the dynamics behavior are defined as R2 and R3. Being R4, R5 and R6 intermediate regions where, in some occasions, the ageostrophic component controls the surface ocean circulation. More details about this regionalization can be found in Morales-Márquez et al. (2020a).

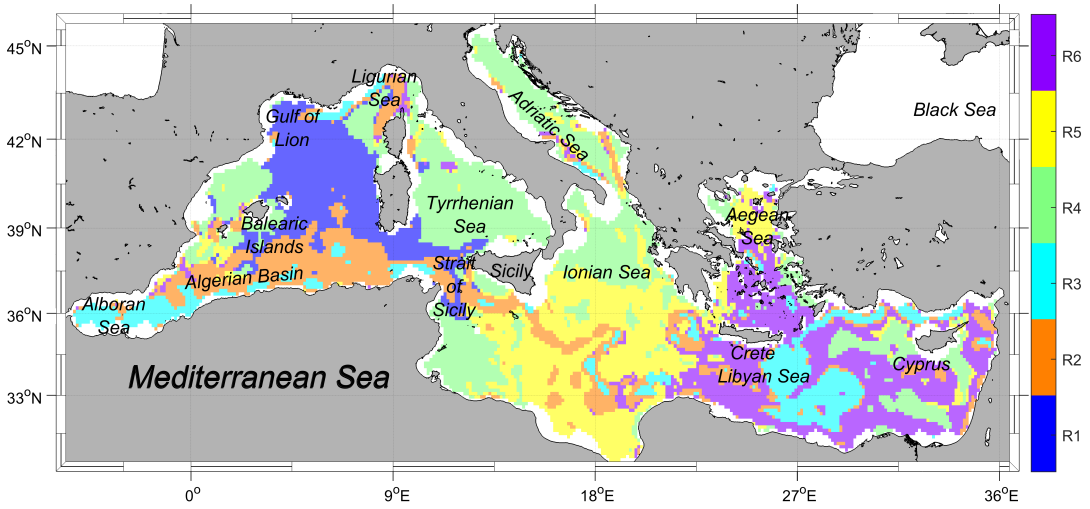

Figure 5.1 *Map of the Mediterranean Sea showing the main oceanographic features and the regions extracted through the SOM analysis applied to the total kinetic energy computed from the coupled geostrophic and ageostrophic (i.e. Ekman and Stokes induced currents) velocity fields. Figure adapted from Morales-Márquez et al. (2020a).*

5.3 Lagrangian dynamics

Neglecting diffusion effects, the trajectory of an infinitesimal and neutrally buoyant particle advected in a Lagrangian flow field $\mathbf{U}(\mathbf{r}, t)$ can be computed integrating the equation of motion

$$\dot{\mathbf{r}}(t) = \mathbf{U}(\mathbf{r}(t), t). \tag{5.6}$$

Here, we only consider two-dimensional fields, i.e. $\mathbf{r}$=(x, y) with x and y the longitudinal and latitudinal coordinates, and where the ageostrophic velocity fields given by Eq. (5.4) are integrated in the vertical dimension, z, over the first meter. The position of the particle between two consecutive times t and $t + \Delta t$ is obtained integrating Eq. 5.6:

$$\mathbf{r}\,(t + \Delta t) \;= \mathbf{r}\,(t) \;+ \int_{t}^{t+\Delta t} \mathbf{U}(\mathbf{r}\,(t)\,, t)dt. \tag{5.7}$$

Owing to the temporal and spatial discretization of the data sets, an interpolation scheme has to be carried out to obtain the flow velocity $\mathbf{U}(\mathbf{r}(t), t)$ at the particle location (see Sayol et al., 2014; Van Sebille et al., 2018, for a comparison on numerical procedures). Trajectories given by Eq. (5.7) are integrated using a fourth-order Runge-Kutta scheme with a bilinear spatial interpolation of the velocity field and an integration time step of 1 hour, thus minimizing the numerical diffusion.

In order to analyze the influence of wind and waves on the total transport at the sea surface, the motion of the particles is computed using both the total and the geostrophic velocitiy fields:

$$\frac{d\mathbf{r}_T(t)}{dt} = \mathbf{U}_T(\mathbf{r}_T(t), t) = \mathbf{U}_g(\mathbf{r}_T(t), t) + \mathbf{U}_a(\mathbf{r}_T(t), t), \tag{5.8}$$

and

$$\frac{d\mathbf{r}_g(t)}{dt} = \mathbf{U}_g(\mathbf{r}_g(t), t). \tag{5.9}$$

5.3.1 Relative dispersion statistics

For the Lagrangian dynamical system, defined in Eq. (5.6), a suitable measure to quantify the mean growth rate of the distance between two trajectories over any scale of motion, is the averaged Finite-Size Lyapunov Exponent (FSLE) (Aurell et al., 1997) defined as:

$$\lambda(\delta, \alpha) = \left\langle \frac{1}{\tau(\delta, \alpha\delta)} \right\rangle \ln \alpha, \tag{5.10}$$

where δ is the initial separation between a pair of particles, α the amplification factor of separation and $\tau(\delta, \alpha\delta)$ the growth time of the distance between two particles from δ to $\alpha\delta$. The bracket $<>$ represents the average of the inverse of the growth time over a large number of realizations (pair of trajectories), sampling a wide range of possible initial separations δ. The scaling laws of FSLE ($\lambda(\delta)$ *vs.* δ) give information about the physical mechanism (e.g. turbulence, chaotic advection, diffusion) and the size of the structures that govern the Lagrangian dispersion processes (Artale et al., 1997; Aurell et al., 1997; Lacorata et al., 2001). The most significant scaling laws ($\lambda \sim C\delta^{\mu}$) associated with the different relative dispersion regimes are (Boffetta et al., 2000; Lacorata et al., 2001; Corrado et al., 2017):

- $\lambda(\delta) \sim$ constant, for exponential separation between particles associated with non-local chaotic advection induced by structures of size larger than the scale of the particle separation (Boffetta et al., 2000);
- $\lambda(\delta) \sim \epsilon^{1/3}\delta^{-2/3}$, corresponding to Richardson's scaling law (μ=-2/3) for ocean turbulence diffusion, usually associated with inverse cascade in the two-dimensions flow approximation, where $\epsilon^{1/3}$ is defined as the mean turbulent dissipation rate (Richardson, 1926; Frisch and Kolmogorov, 1995);
- $\lambda(\delta) \sim \delta^{-1}$, for ballistic or shear dispersion (μ=-1) produced by constant velocities differences associated with particles moving along different currents;
- $\lambda(\delta) \sim \delta^{-2}$, corresponding to standard diffusion (μ=-2) associated with uncorrelated velocities (Taylor, 1921).

To statistically assess the contribution of the different velocity components (geostrophic and ageostrophic) to the total relative dispersion, we compute λ (Eq. (5.10)) and compare the results with the real drifters trajectories. The large number of uniformly distributed pairs of passive particle trajectories considered in the analysis, eliminates a possible bias due to the initial conditions (Artale et al., 1997). A total of 3098 pairs of particles are randomly released in each of regions identified in Morales-Márquez et al. (2020a). The initial position of the particle $\#1$ for each of the pairs of particles is randomly selected inside the regions, as well as, the time when the particle is launched throughout the time period of study. The position of the particle $\#2$ is chosen with a random angle with respect to particle $\#1$ and within a distance $5 \leq \delta \leq 300$ km. In order to analyze the sensitivity of the FSLE spectrum to the orientation of the sampling, we perform an experiment launching pair of drifters separated zonally and meriodinaly (Fig. 5.2). The values of the maximum Lyapunov exponents at small scales are significantly larger for meridional ($\sim$ 0.16 days^{-1}) than for longitudinal ($\sim$ 0.13 days^{-1}) initial separations, Fig. 5.2 (red and blue lines respectively). Indeed, the scaling exponents obtained from the best fit of the FSLE curves at large scales shows a scaling exponent associated with a shear diffusion for meridional (μ = - 1.21) and zonal (μ = - 0.93) separation. Thus, sampling a wide range of directions minimizes possible anisotropic effects due to the direction of the initial separation vector. To resolve the relative dispersion associated with small coherent features and to avoid problems related to the time step of particle advection at small scales, the value of the amplification rate of separation α (Eq.(5.7)) must be smaller than 2 and not too close to 1. Here, we selected a fixed value of α as $\sqrt{2}$ (Lacorata et al., 2001; Haza et al., 2008). The analysis is also applied to the OGS drifters dataset described in section 5.2 with a drogue of 1 meter depth, considering only the pairs of drifters that are inside each region at least during 2 days. Since the Lagrangian model used to compute trajectories considers passive and infinitesimal particles, we neglected possible wind drag and other factors that modify the motion of the real drifter, assuming therefore trajectories of real drifting buoys as the best approximation of passive particle motion in the real ocean flow.

In a two-dimensional surface ocean flow, the characteristic scales in the Lagrangian dispersion can be analyzed independently for longitudinal and latitudinal directions splitting the FSLE into the zonal and meridional components as,

$$\lambda_x(\delta_x, \alpha) = \left\langle \frac{1}{\tau(\delta_x, \alpha\delta_x)} \right\rangle \ln \alpha, \tag{5.11}$$

and

$$\lambda_y(\delta_y, \alpha) = \left\langle \frac{1}{\tau(\delta_y, \alpha\delta_y)} \right\rangle \ln \alpha, \tag{5.12}$$

being δ_x and δ_y the initial distances between pair of particles separated in the longitudinal or in the latitudinal direction. It should be noted that the final distance, in both definitions $\alpha\delta_x$ and $\alpha\delta_y$, is measured specifically along one direction: longitudinal and latitudinal, respectively.

The anisotropy in the dispersion process can be measured computing the difference between the zonal and meridional dispersion rates at a given scale (δ), through the Lagrangian anisotropy index (LAI) defined in Espa et al. (2014) as,

$$LAI = \frac{\lambda_x(\delta_x) - \lambda_y(\delta_y)}{\lambda_x(\delta_x) + \lambda_y(\delta_y)}, \tag{5.13}$$

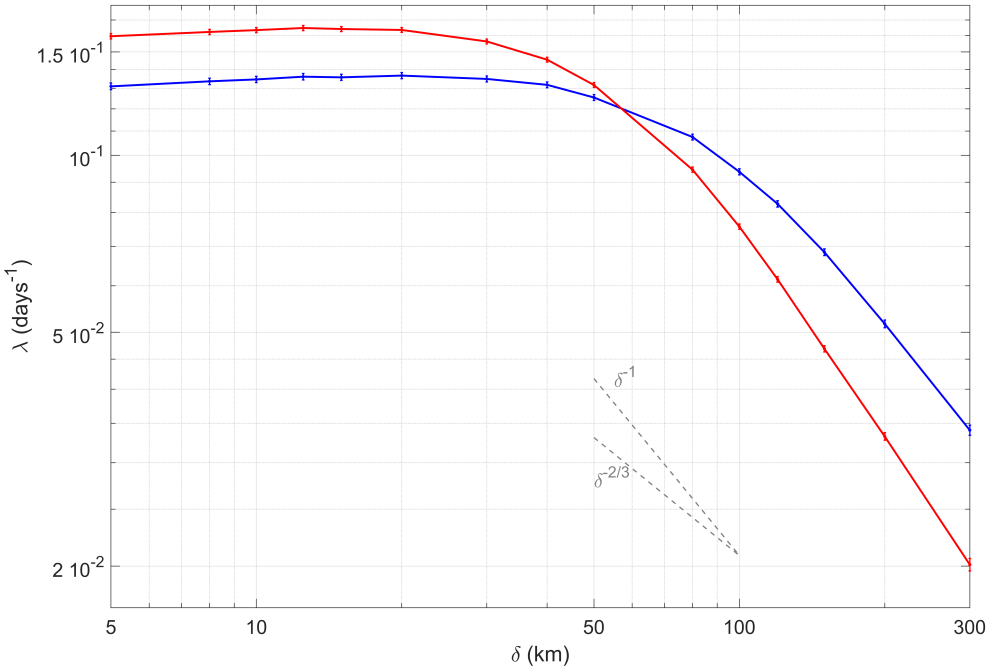

Figure 5.2 *FSLE spectrum, $\lambda(\delta)$ (in days^{-1}) for different zonal (blue line) and meridional (red line) spatial scales (δ, in km) calculated with virtual drifters advected in the total velocity field U_T and without measuring the total final distance along an specific direction. The scaling exponents associated with ballistic/shear (-1) and Richardson (-2/3) dispersion regimes are included in the plot with dashed grey lines.*

where $\delta_x = \delta_y = \delta$ and α have the same values to calculate $\lambda_x(\delta_x)$ and $\lambda_y(\delta_y)$. This dimensionless index varies between -1 and 1, depending on whether the dispersion is dominated by latitudinal or longitudinal flows, respectively. The perfect isotropy is thus represented by zero value.

5.3.2 Lagrangian Coherent Structures

FSLE can also be used to unveil dynamical flow structures that act as transport barriers (Boffetta et al., 2001; d'Ovidio et al., 2004; Hernández-Carrasco et al., 2011). In this case, the calculation of the LCSs from FSLEs goes through computing the minimum time, τ, required for two fluid particles initially centered in **r** and separated by a distance δ_0 to reach a fixed final separation distance δ_f=α δ_0, with $\alpha \gg 2$. At position **r** and time t, the FSLE, is given by:

$$FSLE(\mathbf{r}, t, \delta_0, \delta_f) = |\tau|^{-1} \ln \frac{\delta_f}{\delta_0}. \tag{5.14}$$

At this point, we remark that averages are not performed in this definition of the FSLE in order to have an explicit space-time dependence, in contrast with the original averaged definition (Eq. 5.10), as well as, that α has to be large enough ($O(10^1)$) to adequately distinguish regions of extrema in the FSLE field. The largest Lyapunov values concentrate along characteristic lines, Lyapunov lines, which can approximate

manifolds of relevant hyperbolic points, the so-called Lagrangian Coherent Structures (LCS) (Shadden et al., 2005; Haller, 2015). Fronts, eddies and filamentary barriers to transport can be identified with these manifolds. Since LCS cannot be crossed by particle trajectories, such lines strongly constrain and determine fluid motion, organizing ocean transport. The minimum time τ is computed by integrating the trajectories of the four neighboring points of the analyzed one located at **r** and by selecting the associated particle that separates faster to a distance δ_f.

In this Chapter, LCS are computed from instantaneous FSLE maps using $\sim 3 \cdot 10^6$ pairs of backward trajectories initialized in a regular grid of $\delta_0 = 1/64°$ over the entire Mediterranean Sea and with a final distance of $10\delta_0$. Each daily FSLE map is computed using 44032 pairs of trajectories located in a regular grid with $1/8°$ of spatial resolution, where the final fixed distance is $1°$. The time averaged values in each grid point are computed only considering the days when the pair of particles trajectories does not reach the beach. In this way, there are some grid points where the time-average value is calculated with less amount of data, such as the points located near the coast of the Alboran Sea.

Similarly to LAI, we compute the Lagrangian Coherent Structure Anisotropy (LCSA), as:

$$LCSA(\mathbf{r}, t, \delta, \alpha) = \frac{FSLE_x(\mathbf{r}, t, \delta_x, \alpha) - FSLE_y(\mathbf{r}, t, \delta_y, \alpha)}{FSLE_x(\mathbf{r}, t, \delta_x, \alpha) + FSLE_y(\mathbf{r}, t, \delta_y, \alpha)}, \tag{5.15}$$

where FSLE$_x$ (FSLE$_y$) are the Finite Size Lyapunov exponent obtained evaluating the pair separation along the longitudinal, δ_x, (latitudinal, δ_y) directions. This expression allows an assessment of the spatial variability of the effect of the flow anisotropy on the LCS. Depending on whether LCSA is positive or negative, the LCS is given by a higher contribution of the longitudinal or latitudinal separation of the trajectories, respectively. Note that to compute the LCSA, we use large values of α ($\gg 2$) as used before for the LCS estimation.

5.4 Results and discussion

5.4.1 Ageostrophic induced leakage across mesoscale LCS

In this section, we analyze how ageostrophic Ekman and Stokes induced currents influence transport pathways in the upper ocean. We first compare the shape of the LCSs derived from the total velocity field (henceforth LCS$_T$) and from the geostrophic velocities (LCS$_g$) at a given time. Fig. 5.3, a and b display an example of instantenous maps of FSLE computed from total velocity (FSLE$_T$) and from the geostrophic velocity field (FSLE$_g$), respectively, for 19 January of 2005 at 12:00 UTM. FSLE$_T$ and FSLE$_g$ values are in the same range, between 0 and 0.6 days^{-1} (mixing time-scales of days/weeks) typical of mesoscale horizontal stirring (Hernández-Carrasco et al., 2012). A similar large scale pattern of intricate Lyapunov lines, associated with fronts and mesoscale eddy-like structures, is exhibited also when including the ageostrophic velocities. However, some discrepancies in the shape and intensity, as well as, in the position of LCS$_T$ with respect to the LCS$_g$, are clearly evident in Fig. 5.3, c where we present the difference between both (FSLE$_T$-FSLE$_g$) maps. Numerous LCS derived from FSLE$_g$ (in blue) are shifted, modified in intensity, or even totally dissipated when considering the total currents (in red).

The impact of the ageostrophic currents on the LCS are evidenced if we zoom in on

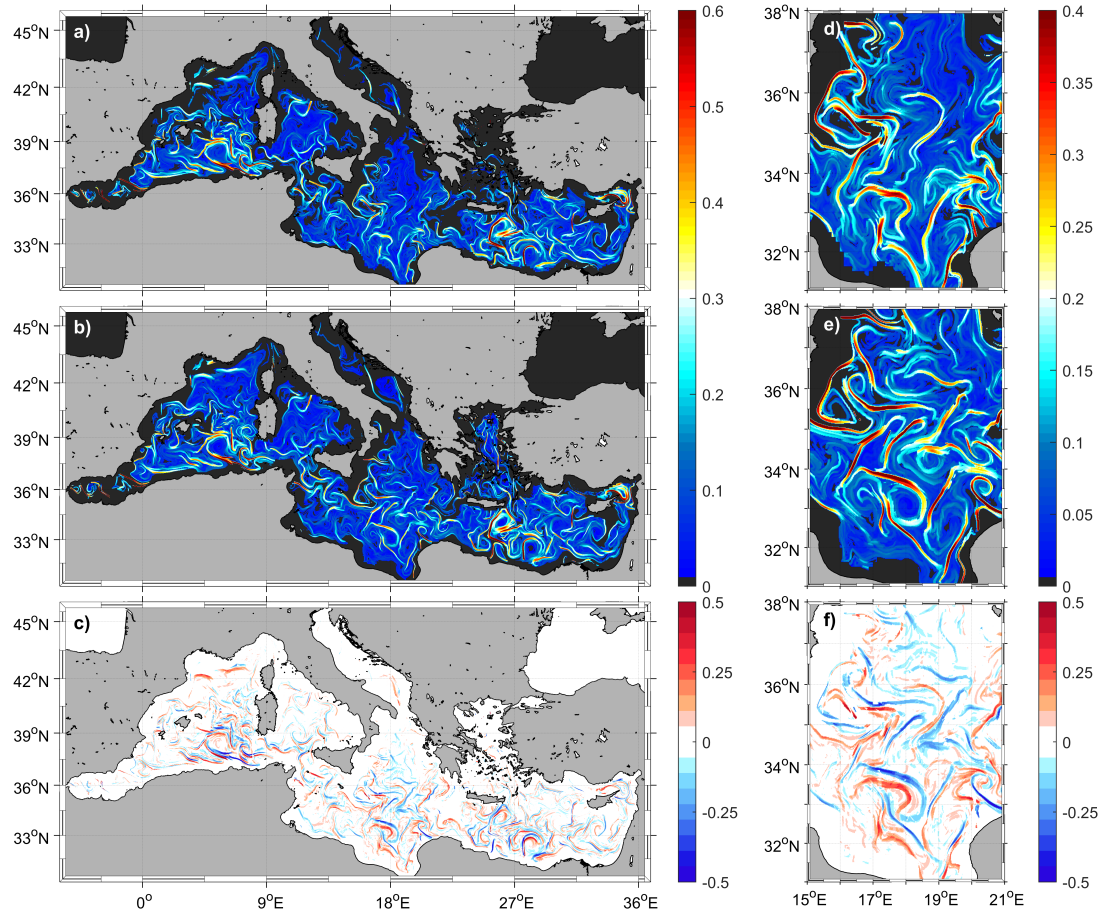

Figure 5.3 *Spatial distribution of backward FSLE (days^{-1}) in the Mediterranean Sea corresponding to January* 19*,* 2005 *at* 12:00 *UTM computed using* 2791665 *pairs of trajectories with a) total velocity fields, U_T, and b) geostrophic velocity fields, U_g. c) Difference between total and geostrophic FSLE fields shown in a) and b) ($FSLE_T$ - $FSLE_g$) (days^{-1}). d), e) and f) are zooms in on the Ionian Sea of the $FSLE_T$, $FSLE_g$ and its difference, respectively (days^{-1}). The initial separation is $\delta_0 = 1/64°$ and the final separation, $\delta_f = 10\delta_0$.*

specific regions. Fig. 5.3, d, e and f show large differences in the Lagrangian transport pattern obtained from both velocity fields in the Ionian Sea. The shape of mesoscale vortices and filaments are drastically altered in the $FSLE_T$ map, as seen in the eddies over the Ionian Sea (e.g., the eddy centered at 18E - 33N), or even suppressed, as in the case of the filament-like LCS located over the northeast and central regions of the Ionian Sea. Additional examples showing that this ageostrophic modification of the LCS is not an isolated event are reported in the Supplementary material (Fig. S.5.12). This suggests that the ageostrophic currents could play an important role in the spreading of tracers in the ocean.

To better illustrate the effect of the wind and waves induced currents on the Lagrangian distribution of transported material, we compare the evolution of a set of passive tracer trajectories advected in U_T with the same set of particles trajectories (released with the same initial conditions), advected in the geostrophic velocity field U_g (Fig. 5.4). While tracers advected in the geostrophic field (cyan points) remain

inside the mesoscale eddy, tracers inside total currents (pink points) leave the eddy, and eventually spread across the southwestern Mediterranean, toward the Alboran Sea. This suggests that wind and waves induced circulation could significantly impact on the permeability of the Lagrangian Coherent Structures (i.e. intense fronts and eddies) obtained from the geostrophic currents. The Ekman and Stokes developed motions permit a leak across the mesoscale transport barriers identified by the geostrophic LCS. It implies that, while the geostrophic transport barrier constrains strongly the motion of the particles inside the eddy when they are advected in the geostrophic flow, it becomes permeable when adding the ageostrophic component to the total currents. This fact could have profound consequences on the connectivity patterns, as well as, the retention capacity of eddies, which can be substantially influenced by the wind and waves conditions.

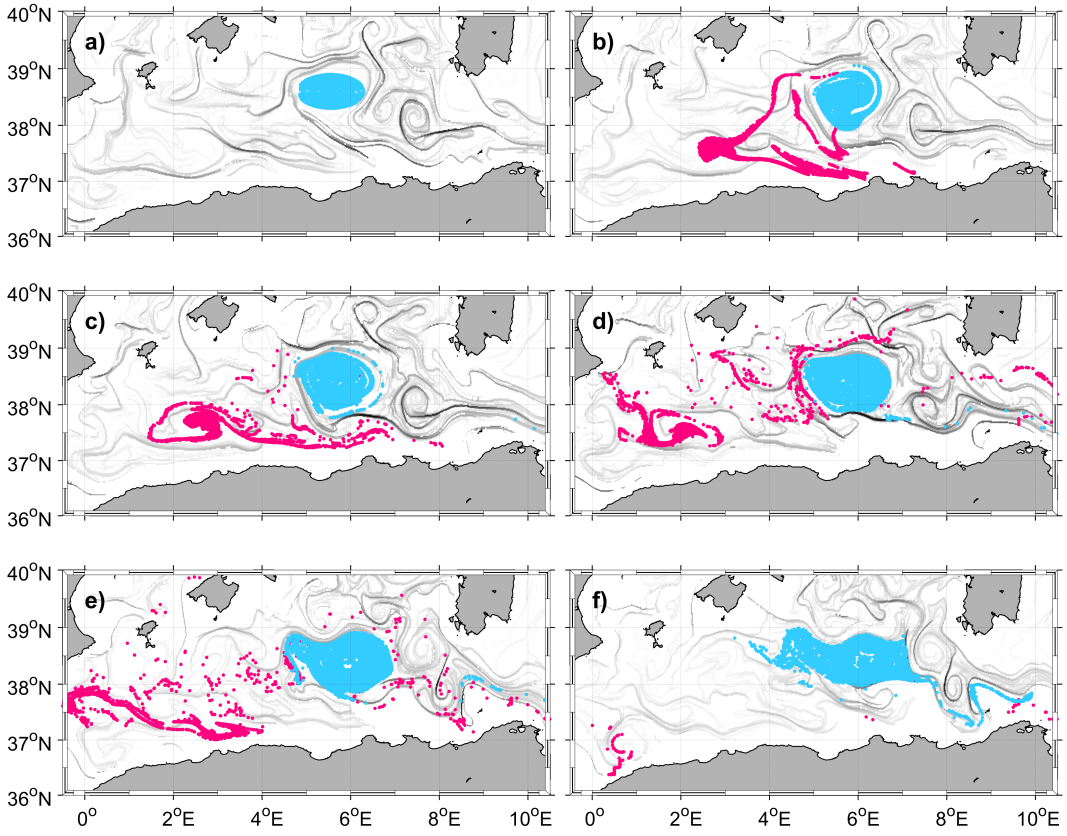

Figure 5.4 *Evolution during one month (a) January* 26*, b) January* 31*, c) February* 5*, d) February* 10*, e) February* 15 *and f) February* 20*,* 2005*) of two sets of 10000 passive tracers launched with the same initial conditions in the interior of a mesoscale eddy. One set is advected by the geostrophic field (in cyan) and the other set is advected by the total velocity field (in pink). The attracting geostrophic LCS are displayed in the background in gray (darker grey for more intense LCS).*

5.4.2 Horizontal stirring variability

We further analyze the low-frequency signature, large-scale signal, of the horizontal stirring by computing the time average of FSLE$_T$ and FSLE$_g$ over the 25-years of data. Areas with large values of averaged FSLE identify zones with more persistent horizontal stirring (d'Ovidio et al., 2004). Fig. 5.5 shows that regions with more mesoscale activity are located in the Alboran Sea (associated with the Alboran gyres variability, with values of FSLE$_T$ around $0.6\ \mathrm{days}^{-1}$), the Gulf of Lion (associated with the Northern current), the Algerian basin (related to the instabilities of the Algerian Current) and the south of Crete in the eastern Mediterranean (associated with the variability of the intense gyres south of Crete, with values around $0.3\ \mathrm{days}^{-1}$). The impact of the ageostrophic component on the horizontal stirring can be inferred by computing the difference between the time average of FSLE$_T$ and FSLE$_g$. The areas of more intense horizontal stirring due to ageostrophic mesoscale activity are characterized by large values of the relative difference between temporal averages of the total and the geostrophic FSLE with respect to the total FSLE, computed for each position (**r**) as:

$$\%FSLE_a(\mathbf{r}) = \frac{1}{\mathrm{T}} \sum_{k=1}^{\mathrm{T}} \frac{FSLE_T(\mathbf{r},k) - FSLE_g(\mathbf{r},k)}{FSLE_T(\mathbf{r},k)} \cdot 100,$$

where T is the time period over which the time series are evaluated, being different in each position (**r**) depending on the simultaneous availability of both FSLE$_T$ and FSLE$_g$ fields (e.g. T = 8927 daily time steps corresponds to 24 years, if there exit values of FSLE$_T$ and FSLE$_g$ fields over the whole period of study at the same pixel). This allows knowing how is the ageostrophic contribution with respect to the total FSLE. Fig. 5.5, b shows that areas where the mesoscale activity is increased by the effect of Ekman and Stokes (in red) are located in the Gulf of Lion and south of Crete. Regions where wind and waves have a suppressing effect on the geostrophic horizontal stirring (in blue) are observed in the western part of the Mediterranean Sea, near Sardinia and west Sicily, as well as, in the middle of the Eastern Mediterranean basin.

The average of FSLE is also calculated seasonally from 1994 to 2018 in order to characterize the regional impact of the intra-annual variability of the wind and waves conditions on the LCS. We only focus on the winter-summer differences (not shown all the seasons). The averaged FSLE$_T$ over winter months (December-January-February-March) is shown in Fig. 5.5, c and over summer (June-July-August) in Fig. 5.5, e. Clear differences between seasons are appreciated in the Gulf of Lion, Alboran Sea, Algerian basin and at the south of Crete, with higher mixing activity during summer. Note that, in winter the mesoscale activity is almost cancelled in the Gulf of Lion. Similarly, we compute the normalized contribution of ageostrophic currents to horizontal mixing for winter (Fig. 5.5, d) and summer (Fig. 5.5, f). In winter, the ageostrophic component mainly exhibits an inhibitory effect of stirring, particularly significant in regions where the intense mistral and tramontane winds develop in winter (Obermann et al., 2018; Soukissian et al., 2018), i.e. west Sicily and Sardinia, and the coastal region of the Gulf of Lion. Conversely, an increase of the mesoscale activity is observed over the south of Crete, the Adriatic and Aegean Sea, and in the south part of the Gulf of Lion. In summer, Ekman and Stokes currents substantially impact on the geostrophic horizontal stirring (with an increase up to 50% of FSLE$_T$) around Crete and the Aegean Sea, likely caused by the persistent northerly etesian winds that prevail over the eastern Mediter-

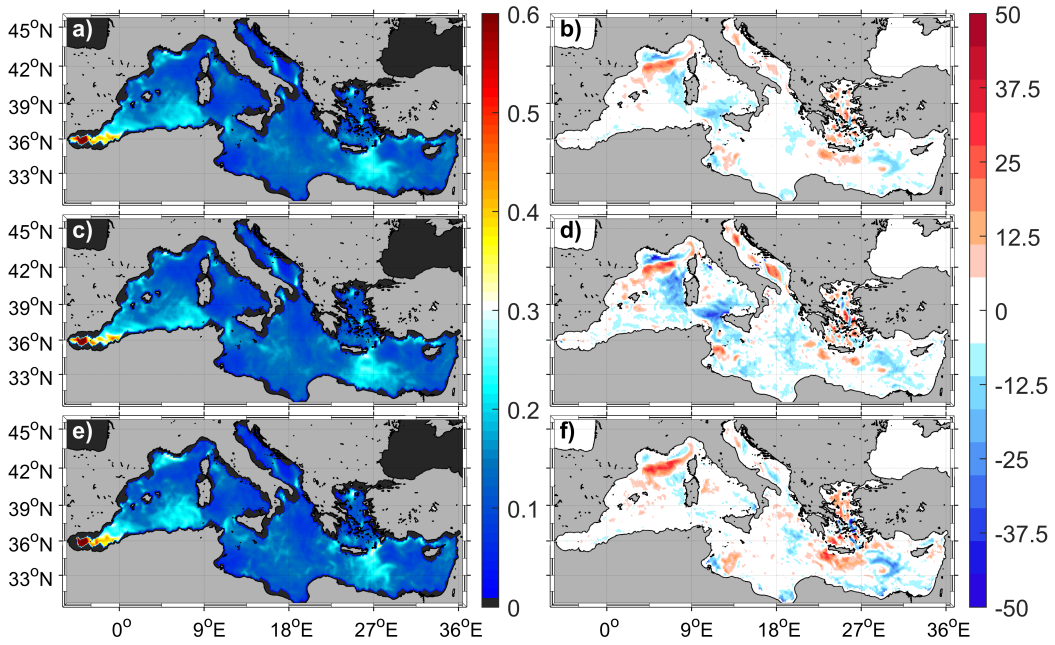

Figure 5.5 *Spatial distribution of the time average of backward FSLE$_T$, in $days^{-1}$, over: a) the 24 years of data (from 1994 to 2018); c) only averaging over winter months (DJFM); and e) only averaging over summer months (JJAS). Contribution of the ageostrophic currents proportional to the total horizontal stirring in % [(FSLE$_T$ - FSLE$_g$)/FSLE$_T$], for b) the total period; d) for winter; and f) for summer. The initial separation is $\delta = 1/8°$ and the final separation, $r\delta = 1°$.*

ranean during summer (Zecchetto and De Biasio, 2007; Soukissian et al., 2018); and in the northwestern Mediterranean where, although characterized by low values of the total mesoscale activity, an increase is observed induced by the ageostrophic currents likely due to occasional intense mistral winds blowing during this season (Small et al., 2012).

A convenient quantity to characterize mixing activity in a specific region, is the spatial average of FSLE at a given time which allows to study the temporal variability over different regions. Here, we are interested in the variability of the horizontal mixing in the SOM-regions shown in Fig. 5.1. The time evolution of the spatial average of the FSLE$_T$ and FSLE$_g$ over the whole Mediterranean Sea is shown in Fig. 5.6, a. Both FSLE$_T$ and FSLE$_g$ show a high temporal variability, with larger values of FSLE$_T$ than FSLE$_g$ most of the time, in particular during the 1997-1999 and 2012-2014 periods, and a global contribution of 6% of the total FSLE coming from the ageostrophic component. As expected (and in agreement with Fig. 5.5), we observe high stirring values (mean FSLE$_T$ of ~ 0.23 days^{-1}) corresponding to regions characterized by the major mesoscale features, such as the persistent intense mesoscale eddies, i.e. Alboran and Crete gyres (R3), and jets, i.e. Algerian Current (R2). Intermediate mixing values correspond to northwestern and eastern basins (R1 and R6) while central basin (R5) and Adriatic and Tyrrhenian Sea (R4) display significantly lower values. While events of maximum ageostrophic contribution (up to 37% of the FSLE$_T$ in Fig. 5.5, d) occur in the northwestern regions (R1), the average contribution is larger ($\sim$9%) in the eastern basin (R6) and north-central basin, including the Adriatic, Tyrrhenian and north Ionian Seas (R4),

and lower ($\sim 3\%$) in the Aegean Sea and the south Ionian Sea (R5). Intermediate mean contributions ($\sim 5\%$) are found in R1, R2 and R3. In contrast to the results obtained in Morales-Márquez et al. (2020a), where it was reported a high ageostrophic impact on the total kinetic energy in R1, we obtain that wind and waves induced currents do not play an important role in the mixing activity in this region. This suggests that mesoscale variability generated by the ageostrophic component is more significant in the eastern basin and in the north and central part of the Mediterranean Sea than in the rest of the regions.

Another interesting feature depicted from the mean FSLE time series is the general positive trend experienced in the Mediterranean basin, suggesting a continuous increase of the global mixing activity. Trends of the horizontal stirring are computed based on a linear regression of the residual component of FSLE time series after it has been decomposed as a seasonal signal plus a residual component. The global linear trend in the Mediterranean basin for the 1994-2018 period is $1.27{\cdot}10^{-3}$ days^{-1}/year for FSLE$_T$ and $1.32{\cdot}10^{-3}$ days^{-1}/year for FSLE$_g$, which is equivalent to a mean mixing increase of 0.8% per year. Regional differences are evident. Higher positive trends of FSLE$_T$ marking the central basin of the Mediterranean, i.e. the south Ionian Sea and the Aegean Sea (R5) with values of $1.67{\cdot}10^{-3}$ days^{-1}/year (equivalent to 1.2% per year), the Algerian basin (R2) with a value of $1.66{\cdot}10^{-3}$ days^{-1}/year (0.8% per year) and the core of the major gyres (R3) with $1.63{\cdot}10^{-3}$ days^{-1}/year (0.7% per year). This implies a substantial FSLE$_T$ increase in these regions that can reach around 0.2 days^{-1} in 100 years (twice the current mixing level). Slightly lower positive signal is found in the eastern basin (R6) with a value of $1.33{\cdot}10^{-3}$ days^{-1}/year (0.7% per year), and the lowest interannual variations are located in the northwestern Mediterranean, and in the Tyrrhenian and Adriatic Sea (R1 and R4) with an increase of (0.78-0.82)$\cdot 10^{-3}$ days^{-1}/year (0.4-0.5% per year). FSLE$_T$ shows a trend slightly higher than FSLE$_g$ in R1, R2 and R5, suggesting an increase of the mixing activity induced by the ageostrophic component in these regions. The obtained positive trends are globally less pronounced than those reported in Ser-Giacomi et al. (2020) obtained for future climate projections of mixing.

An additional feature that can be observed is a marked seasonal signal in the time series of both geostrophic and total mixing activity. Further information about this seasonal variability can be obtained by analyzing the mean climatology of FSLE using the 24 years of data. In general over the whole Mediterranean basin, the lower FSLE values are found in summer, being constant along the rest of the year, and with the larger difference between FSLE$_T$ and FSLE$_g$ in the Autumn-Winter period (Fig. 5.7, a), likely induced by the intense wave and wind conditions developed during autumn and winter. However, as evidenced in Fig. 5.7 (panels R1-R6), each SOM-region shows different seasonal behavior. While minimum values are reached in summer in all the regions, maximum mixing are found in different months. Regions where the mixing activity is more intense, e.g. Alboran Sea and south Crete (R3), exhibit the highest seasonal variability. The northwestern Mediterranean (R1), associated with the Northern Current, shows maximum values in the mixing activity during spring and autumn and minimum values during summer and winter. This fact is closely associated with the main wind climate of the Mediterranean Sea exposed in Soukissian et al. (2018), since even if the windiest season is winter, the ageostrophic component has opposite direction than geostrophy in this region (R1), removing part of the mixing activity there. The most active currents, in terms of mixing, identified by R2 and R3 present only one maximum in spring and autumn, respectively; and practically constant values during the rest of

the year. The eastern basin, mostly identified by R6, presents constant values except in summer. The north of the central basin and the Adriatic Sea (R4) present maximum values in autumn, while the south of the central basin and the Aegean Sea (R5) show two peaks during winter and spring. R2, R3 and R5 barely show a seasonal impact of the ageostrophic component in the total mixing. It is worth noting that, while region R1 exhibits an important ageostrophic contribution to mixing in autumn and spring, in R4 and R6 this occurs in autumn and summer, coinciding with the presence of the persistent and intense regional winds (tramontane in R1 and etesian winds in R6).

5.4.3 Dispersion properties

We further analyze the effect of wind and waves induced current on the surface dispersion properties over different regions of the Mediterranean Sea. Following other authors (Corrado et al., 2017; Lacorata et al., 2019), we evaluate the dynamical importance of the ageostrophic currents in particle dispersion by computing the averaged FSLE (λ) at different spatial scales using Eq. (5.10) (see section 5.3.1). Unlike Bouzaiene et al. (2020), we perform the average of λ not over the conventional Mediterranean subbasins, but over the dynamically coherent SOM-regions shown in Fig. 5.1. In Fig. 5.8, a, we show the FSLE analysis averaging only over the pair of particles launched during the same period when the pair of real drifters are available in each SOM-region, and being advected by the total velocity field (solid lines) and geostrophic velocity field (dashed lines). The FSLE curves show that the exponential separation rate ($\lambda(\delta) \sim$ constant) denoted by λ_M (maximum mesoscale Lyapunov exponent) varies for the different regions (see Table 5.1). The largest λ_M values are found for R2 and R3, regions characterized by the major Mediterranean mesoscale features: gyres, fronts and jets (Algerian current, Alboran gyres, etc.) with a value around $1.8 \cdot 10^{-1}\mathrm{days}^{-1}$, followed by R1 and R6 (regions experiencing a significant impact of wind stress) with $\lambda_M \sim 1.35 \cdot 10^{-1}\mathrm{days}^{-1}$, and the lowest λ_M corresponding to R4 and R5 with $1 \cdot 10^{-1}\mathrm{days}^{-1}$. Similar values (same order of magnitude) were reported in Lacorata et al. (2019), where $\lambda(\delta)$ was computed averaging for the whole Mediterranean Sea. The same ranking in the λ values is observed using real drifters (see Fig. 5.8, b).

Comparing the FSLE curves obtained from geostrophic currents with the obtained for total currents, we observe that both λ_M are rather similar over R5 and R6 and slightly higher as computed from the total velocities in regions R1, R2, R3 and R4. This suggests that wind and waves induced currents have more impact on the dispersion of tracers over these Mediterranean Sea regions, being less pronounced in the eastern subregions.

The spatial scale identifying the transition between the exponential and the power law separation rate, denoted as δ_M, is different in each region. This scale could give some insight about the minimum size of the mesoscale structures governing the relative dispersion. In R1, δ_M is around $36\mathrm{km}$, followed by R4 $\delta_M \sim 41\mathrm{km}$, R6 $\sim 54\mathrm{km}$, R5 $\sim 60\mathrm{km}$ and R2 $\sim 62\mathrm{km}$, and finally in R3 $\sim 69\mathrm{km}$.

The best-fitting of the regional FSLE$_T$ and FSLE$_g$ curves (λ-U$_T$ and λ-U$_g$, respectively) at larger scales return values of the slopes spanning from -0.97 to -0.66 (see Table 5.1). In all the regions the relative dispersion obtained from both U$_T$ and U$_g$ is associated with a Richardson's turbulent diffusion (scaling rate of $-2/3$), except for R3, R5 and R6 obtained from U$_g$ and for R5 obtained from U$_T$, where the scaling law is rather related to a ballistic or shear dispersion (scaling rate of -1). It means that in R1,

Table 5.1 *Values of λ_M ($\cdot$ 10^{-1} $days^{-1}$), δ_M (in km) and the slopes (μ) resulting from the best fitting of the FSLE curves obtained using pairs of virtual drifters advected in U_g (referred as to λ-$\mathrm{U_g}$), U_T (λ-$\mathrm{U_T}$) and pairs of real drifters (λ-Drifters), and of their corresponding zonal and meridional component (λ_x and λ_y), computed for each SOM-region of the Mediterranean Sea. In all cases the obtained correlation coefficients (R^2) are larger than 0.95 except for the fit of λ-Drifters in R1 (R^2 = 0.89) and λ_y-U_T and λ_x-Drifters in region R2 (R^2 = 0.90 and 0.92, respectively). Slopes associated with Richardson (shear) [standard] turbulent dispersion are indicated in bold black (in red) [in blue].*

		λ - $\mathrm{U_g}$	λ - $\mathrm{U_T}$	λ_x - $\mathrm{U_T}$	λ_y - $\mathrm{U_T}$	λ - Drifters	λ_x - Drifters	λ_y - Drifters
R1	λ_M	1.30	1.36	1.22	1.11	7.96	18.33	14.21
	μ	**-0.72**	**-0.67**	-0.99	**-0.79**	**-0.65**	-0.56	-0.97
	δ_M	40.48	35.88	80.01	50.54			
R2	λ_M	1.73	1.79	1.64	1.56	10.49	21.50	23.27
	μ	**-0.72**	**-0.74**	**-0.67**	-0.91	**-0.77**	**-0.82**	-1.37
	δ_M	61.48	61.73	72.32	60.03			
R3	λ_M	1.77	1.85	1.66	1.56	20.38	29.72	24.20
	μ	-0.96	**-0.66**	-0.43	-0.87	-1.47	-1.26	N/A
	δ_M	83.95	69.05	80.94	85.13			
R4	λ_M	1.00	1.03	0.82	0.74	6.91	15.94	12.34
	μ	**-0.66**	**-0.70**	-0.89	-1.42	**-0.82**	-0.91	-0.84
	δ_M	38.79	41.06	73.28	80.69			
R5	λ_M	1.01	1.01	0.88	0.77	10.24	23.13	18.04
	μ	-0.97	-0.92	**-0.75**	**-0.63**	-0.99	-1.02	-1.03
	δ_M	60.92	59.85	68.99	49.52			
R6	λ_M	1.29	1.30	1.28	0.99	7.72	22.50	32.95
	μ	-0.86	**-0.73**	-0.50	-1.09	-1.36	-1.31	-2.10
	δ_M	57.92	54.03	45.05	66.83			

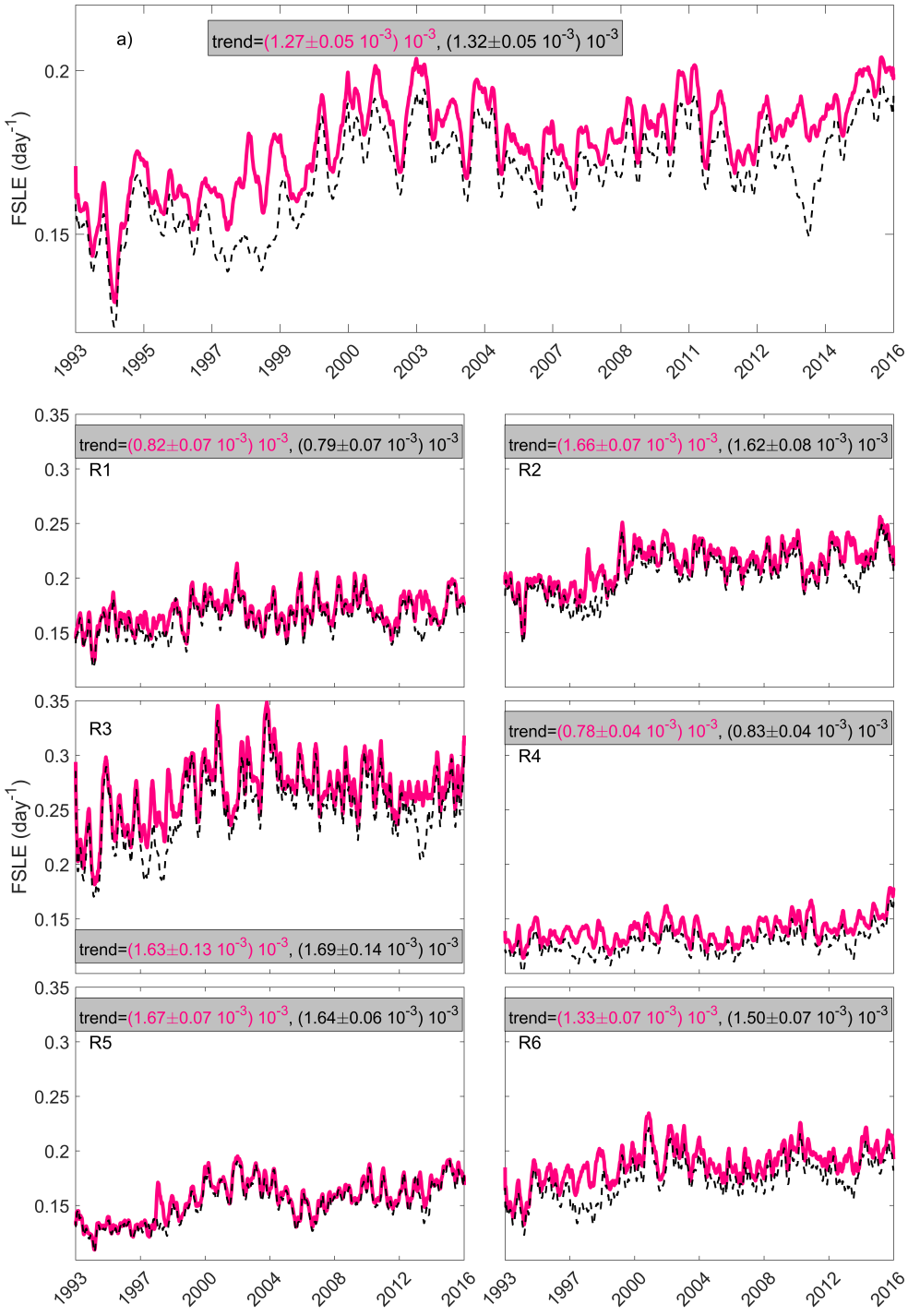

Figure 5.6 *Time evolution, from* 1994 *to* 2018*, of the spatial average of daily* $FSLE_T$ *(bold pink lines) and* $FSLE_g$ *(dashed black lines), in days*$^{-1}$*, over the whole Mediterranean Sea (panel a); and over the SOM-regions (panels R1-R6) shown in Fig. 5.1. The linear trends of the FSLE time series, expressed in days*$^{-1}$*/year, are included in each plot. Only trends with a significance* $p \leq 0.01$ *are included. FSLE is computed using* $\delta_0 = 1/8°$ *and* $\delta_f = 1°$*.*

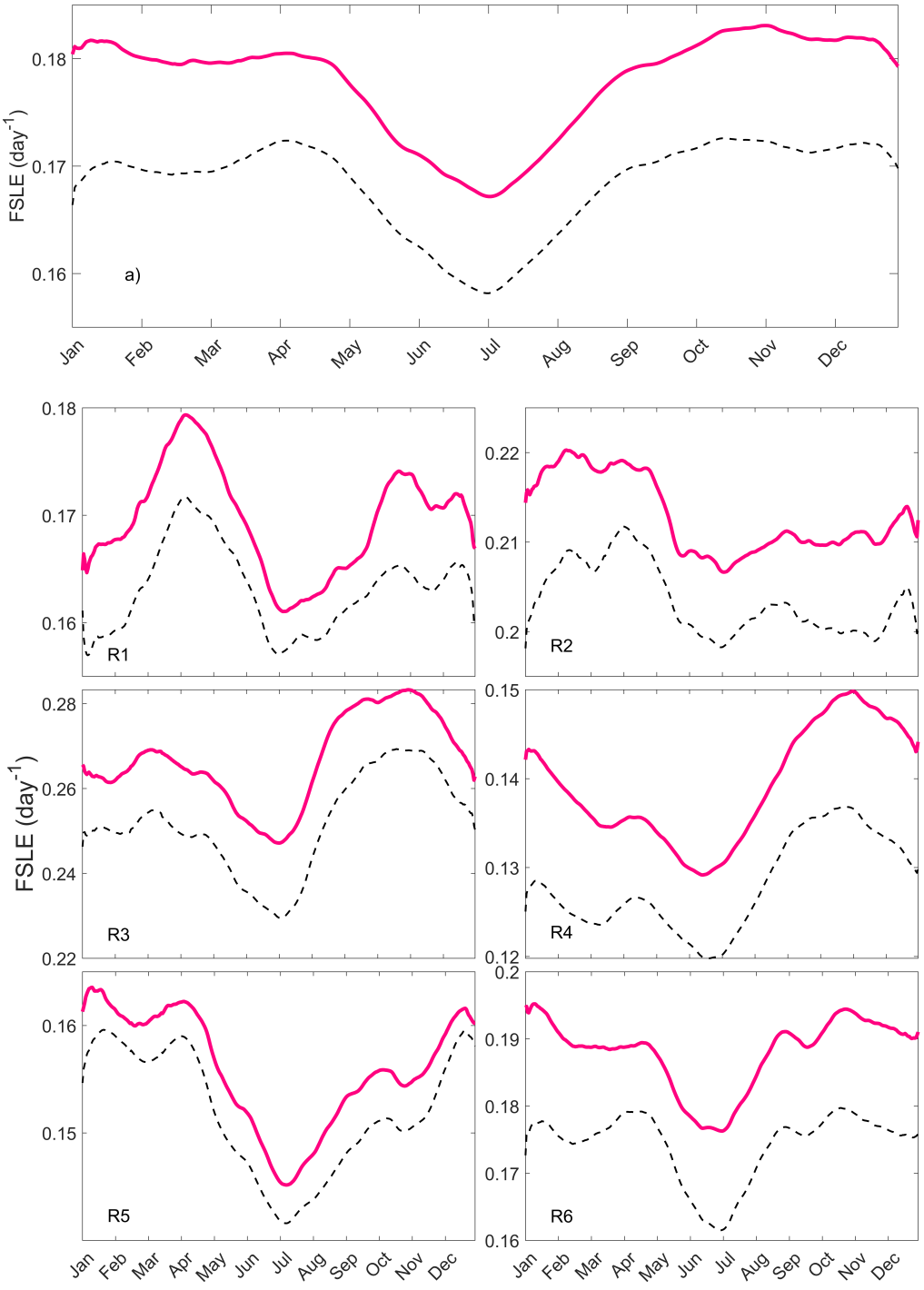

Figure 5.7 *Mean annual cycle of daily FSLE in days*$^{-1}$ *(climatological daily mean over* 24 *years of data): a) for the whole Mediterranean Sea; R1-R6) for the SOM-region (bold pink lines correspond to FSLE*$_T$*, and black-dashed lines to FSLE*$_g$*). FSLE is computed using the* $\delta_0 = 1/8°$ *and* $\delta_f = 1°$.

R2 and R4 the main contributors to the separation rate at these large scales are structures with size comparable with the separation itself. Note that, in general, the obtained slope is slightly steeper for λ-U$_g$ than for λ-U$_T$, particularly lager over R3, where the

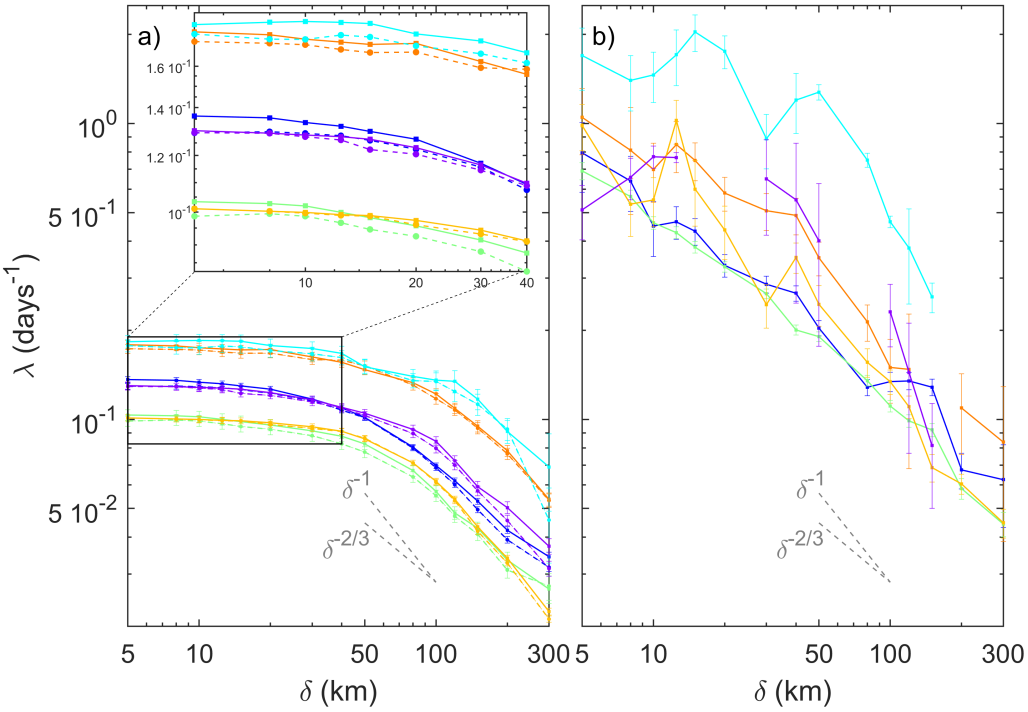

Figure 5.8 *FSLE curves ($\lambda(\delta)$), in days^{-1}, at different spatial scales, in km, (δ) calculated with a) virtual drifters advected in the total velocity field (solid line) and in the geostrophic field (dashed line); b) with the real drifters. Each color corresponds to the averaged FSLE value over all the pairs of virtual drifters homogeneously launched in the SOM-regions identified in Fig. 5.1, and deployed at the same time period of the available pairs of real drifters in the corresponding SOM-region. The scaling exponents associated with ballistic/shear (-1) and Richardson (-2/3) dispersion regimes are included in the plot with dashed grey lines.*

regime dispersion at large scales moves from being associated with a Richardson turbulent dispersion in the total field to a shear dispersion in the geostrophic velocity field.

The relative dispersion for the real drifters is calculated selecting all the simultaneously available drifters in each SOM-region at least during 2 consecutive days. In Fig. S.5.13 in the Supplementary material is shown the number of drifter pairs transects available for each scale and region. Similarly to the obtained for virtual drifters, R3 shows the higher value of λ_M, followed by R2 and R5; and finally R1, R6 and R4, although all the λ curves converge at large scales. The FSLE spectrum in regions R2, R3 and R6 suggest a plateau between 5 and 20 km (Fig. 5.8, b), associated with a mesoscale exponential separation, and a ballistic/shear dispersion at scales larger than 20 km, although this has been taken with caution due to the small number of pairs used in the average, particularly in R3 and R6 (Fig. S.5.13 of Supplementary material). This FSLE plateau at small scales observed in regions R2 and R3 reflects the absence of relevant submesoscale features and the dominance of the mesoscale structures in the dispersion, i.e. the major Mediterranean mesoscale eddies and the intense jets, such as the Algerian current and its propagation toward the Ionian Sea. The other regions, R1 and R4 present a relative dispersion behavior associated with a Richardson scaling and, R5 associated with shear dispersion, in agreement with the results obtained in Lacorata

et al. (2019) for the global Mediterranean analysis (see Table 5.1). Comparing these results with the obtained from virtual drifters, we observe that, as expected, the coupled geostrophic and Ekman-Stokes model underestimates relative dispersion at small scales (range $\sim [1-80]$) km as reported in Lacorata et al. (2019).

5.4.4 Anisotropy of the Mediterranean Sea flow

In this section, we study the anisotropy of the flow in the different regions of the Mediterranean Sea based on the analysis of the relative dispersion along orthogonal flow components. In particular, we compute the longitudinal and latitudinal FSLE given by Eqs. (5.11) and (5.12) where the initial and final separations of the trajectory pairs are evaluated exclusively along one of the orthogonal components. This allows to assess the contribution of the zonal and meridional separation rate to the total dispersion.

We start analyzing the scaling properties of the dispersion for total velocity field U_T in both directions. In Fig. 5.9, blue and red lines show the zonal and meridional FSLE spectrum ($\lambda_x(\delta_x)$ and $\lambda_y(\delta_y)$), respectively, calculated with U_T for each SOM-region (R1-R6). Anisotropy of the flow is reflected in the different behavior of the zonal and meridional components of the relative dispersion. In all regions, values of λ_M are larger for the zonal component than for the meridional (up to 20% greater). Values of λ_M range between $(0.82\text{-}1.66)\cdot 10^{-1}\mathrm{days}^{-1}$ for the zonal FSLE curves and between $(0.74\text{-}1.56)\cdot 10^{-1}\mathrm{days}^{-1}$ for the meridional FSLE (see Table 5.1 and Fig. 5.9). Note that λ_M values are larger when considering the total separation distance than only considering the separation along one of the orthogonal directions (see Table 5.1). This shows that while the leading expansion direction of the separation vector is not only aligned along one exclusive orthogonal direction but a combination of both. In general, the zonal component of the flow has a higher impact on the relative dispersion than the meridional, being more significant at larger scales. As a consequence, the spreading of tracers is more oriented along the zonal direction than along the meridional.

Regions R1, R2 and R5 show a δ_M significantly greater for the zonal than for the meridional FSLE, up to 30 km of difference in R1. This suggests that in these regions the coherent structures governing the zonal dispersion are larger than the meridional structures. In fact, these regions are dominated by intense and large currents flowing zonally, e.g., Northern Current, Algerian Current, etc. While the slopes obtained from the best-fitting of the λ_x is closer to a Richardson dispersion type slope, λ_y curves show a slope associated with shear dispersion, except for R1, where we find the opposite behavior, and for R5 where both components follow the Richardson's law. This slight departure from the Richardson-like dispersion in the latitudinal FSLE suggests that particles are dispersed in this direction due to the effect of a latitudinal shear produced by separated currents along the latitude, e.g. in R2 the Algerian Current and its associated re-circulation sub-currents.

Next, we compute the LAI for each scale and region to further characterize the difference between the zonal and meridional FSLE and to identify the characteristic scales of the flow anisotropy. We report in Fig. 5.10 the scale dependence of LAI obtained for the FSLE of the total velocity field U_T. While each region shows a different degree of anisotropy, over the small-scales range, in general, LAI is constant with relatively small positive values, and over large-scales LAI increases as the separation distance grows. This confirms that at large scales the longitudinal flows have more impact on the dispersion processes than the latitudinal component, in particular in regions R1, R2, R4 and

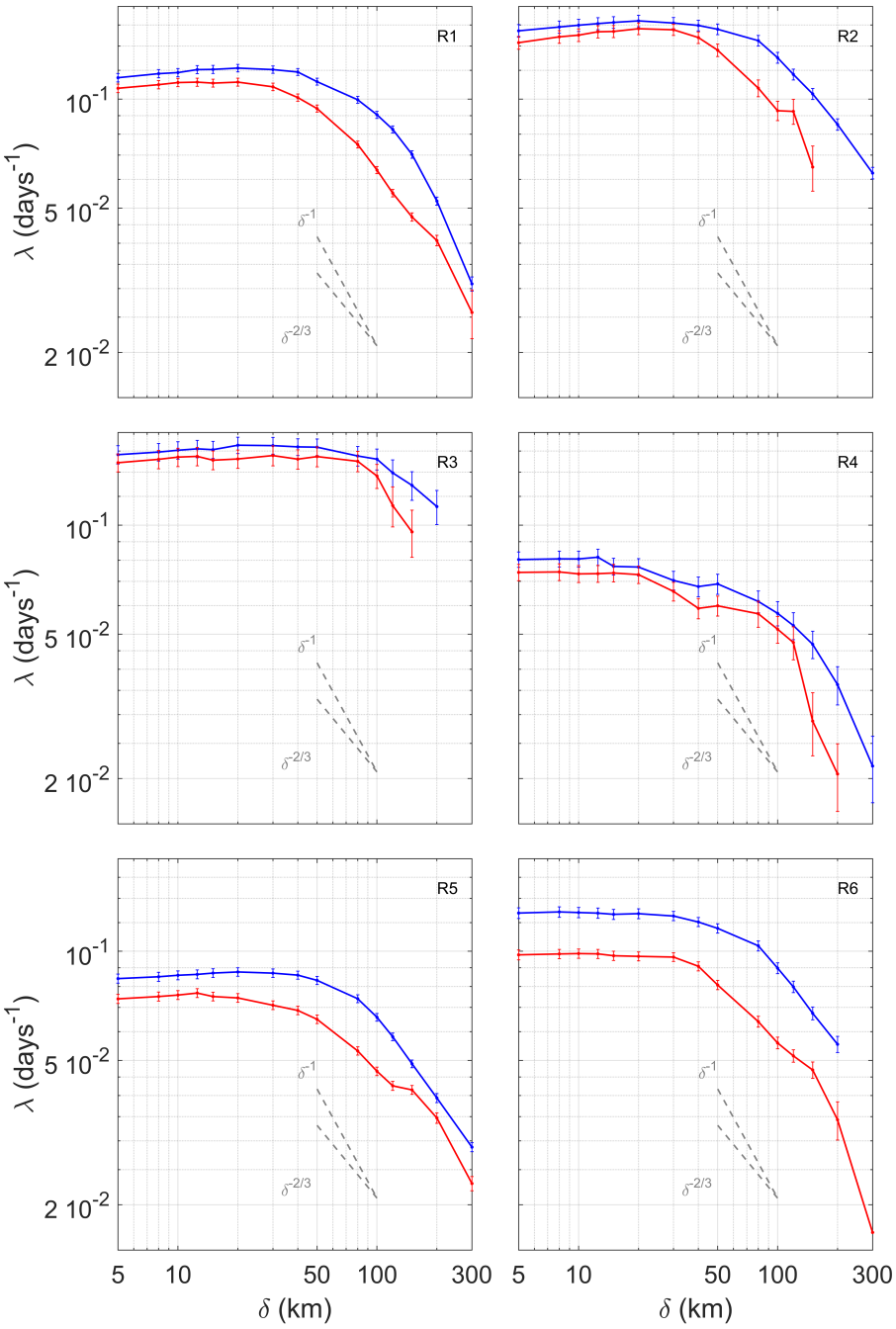

Figure 5.9 *Zonal (blue lines) and meridional (red lines) FSLE curves (in days^{-1}) given by $\lambda_x(\delta_x)$ and $\lambda_y(\delta_y)$, respectively (see Eqs.* (5.11) *and* (5.12)*), at different spatial scales (δ_x and δ_y, in km) calculated for pairs of virtual drifters advected in the total velocity field U_T. Each subplot (R1-R6) corresponds to the averaged FSLE values over all the pairs of virtual drifters launched in the SOM-regions identified in Fig. 5.1, and deployed at the same time period of the available pairs of real drifters in the corresponding SOM-region. The scaling exponents associated with ballistic/shear (-1) and Richardson (-2/3) dispersion regimes are included in the plot with dashed grey lines.*

R6. Regions where the flow anisotropy is weaker are R3 and R5. To identify the threshold scales δ_A at which the presence of anisotropy becomes relevant in the dispersion processes we use the following criteria: we consider the spatial scale at which the LAI departures from the constant range values. We found different δ_A values depending on the region. The regions more affected by the Ekman and Stokes induced currents (R1 and R5) present small δ_A values ($\sim$ 15 km), while the region R6, regions where geostrophic dynamics is dominant (R2 and R3) and R4 are characterized with large values of δ_A ($\sim$ 40, 30, 80 and 120 km, respectively). Fig. S.5.15 of Supplementary material shows the LAI obtained for the available real drifters in each region. It should be noted that the scarcity of drifters trajectories contributes to the existence of large uncertainties, practically over all the separation scales, and a robust characterization of the scale dependence of LAI cannot be properly addressed (see Fig. S.5.16 in the Supplementary material for more details about the number of available pairs of real drifters used in these computations).

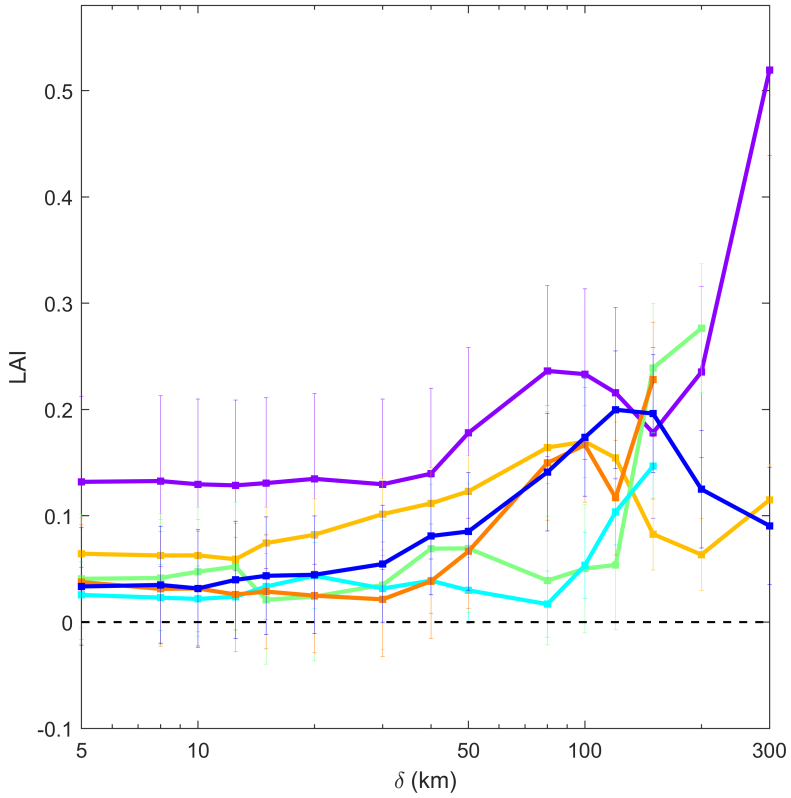

Figure 5.10 *Scale dependence of LAI computed with virtual drifters advected in the total velocity field for each SOM-region of the Mediterranean Sea. Colors correspond to SOM-regions identified in Fig. 5.1. The dashed black line represents the isotropy (LAI=0).*

We finally study the effect of the flow anisotropy on the Lagrangian Coherent Structures given by LCSA, and on the mixing activity obtained from $<\text{LCSA}>_T$, where the brackets represent a temporal average over the time period T. To focus the analysis on the typical size of the mesoscale structures, LCSA is computed for final separation

scales of 1°. In Fig. 5.11, a, the spatial distribution of $<\text{LCSA}>_T$ averaged over the 24 years of U_T data is depicted. Positive values (in red) indicates that the mixing activity is dominated by the longitudinal FSLE and negative $<\text{LCSA}>_T$ (in blue), by the latitudinal FSLE. In general, we find that, across the Mediterranean basin, the zonal FSLE are more significant than the meridional, in particular in the Eastern basin and the Adriatic Sea where $<\text{LCSA}>_T$ reaches values up to 0.5. This suggests that the zonal flow plays an important role in the mixing activity in Mediterranean Sea. The meridional FSLE dominates in specific regions, such as the northwestern basin and the south of Sicily, with the highest negative $<\text{LCSA}>_T$ located along the Northern current, with values around -0.5. This implies that while in the eastern basin there are more transport barriers meridionally oriented, in the northwestern basin prevail zonally oriented transport barriers. In the central basin (Ionian Sea) the flow is more isotropic. To identify regions showing seasonal variability of the anisotropy, we compute the average of the LCSA over the winter months (Fig. 5.11, c) and over the summer period (Fig. 5.11, e) across the 24 years of data. Slight seasonal differences are found in specific locations, such as along the Adriatic Sea and the Balearic Sea with an intensification of the longitudinal mesoscale mixing, and a weakening at the sourrondings of Create in summer, because this is time when etesian wind is stronger there.

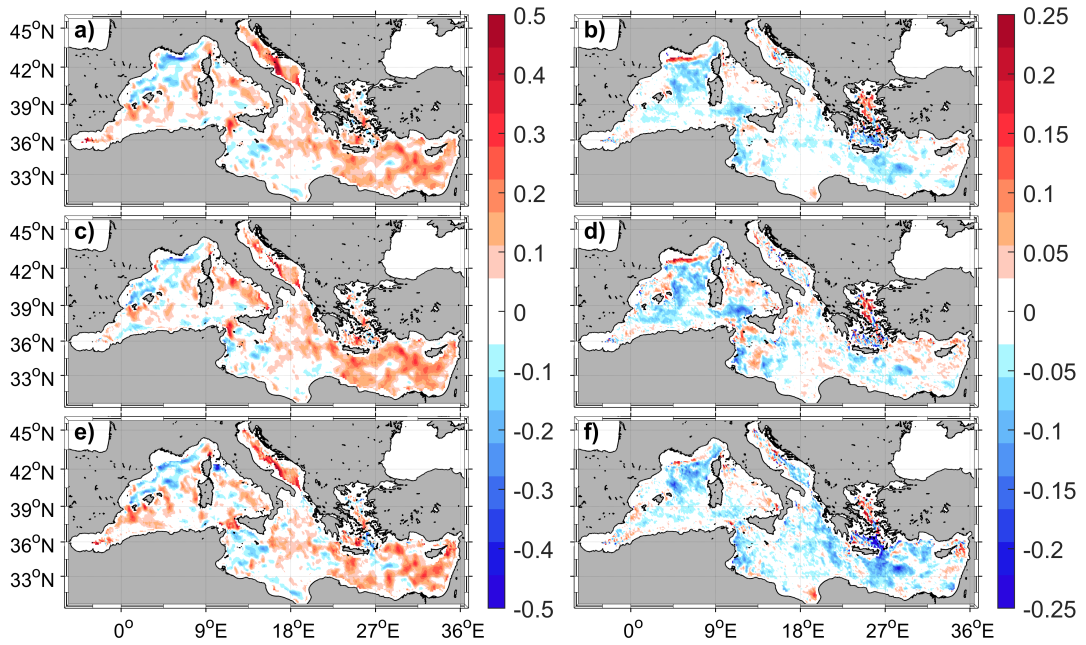

Figure 5.11 *Maps of the time average of LCSA computed over the 24 years of data (from* 1994 *to* 2018*) for the a)* U_T *and b) the difference between the LCSA obtained for* U_T *and for* U_g*. c) and d) are the same as a) and b) but only averaged over winter; and e) and f), the same as a) and b) but only averaged over summer. The initial resolution is* $\delta = 1/8^{\circ}$ *and the final resolution,* $r\delta = 1^{\circ}$.

In order to further study, the anisotropy of the flow associated with ageostrophic component, we compute the difference of the $<\text{LCSA}>$ obtained for U_T with the $<\text{LCSA}>$ for U_g. The spatial distribution of the 24 years average of this difference is plotted in Fig. 5.11, b. We observe that while the ageostrophic FSLE are rather isotropic ($<\text{LCSA}>$ = 0) in the Ionian Sea, the Algerian basin and the most easterly

part; significant negative <LCSA> values are located over the northwestern basin, north of Sicily and south of Crete. In these regions, the wind and waves main direction is North-South, which explains the ageostrophic contribution to the latitudinal mixing (Zecchetto and De Biasio, 2007; Obermann et al., 2018). Positive ageostrophic contribution to <LCSA> are concentrated along the Northern current and the Aegean Sea, suggesting that Ekman currents and Stokes drift induce a zonal flow which has a large impact on the mixing properties in these regions. Furthermore, this ageostrophic meridional increase (zonal increase) of mixing is more intense during winter over the Strait of Sicily (Norther current) (see Fig. 5.11, d), and more intense at the south of Crete in summer (Fig. 5.11, f). This seasonal variability is in agreement with the seasonal intensification of the corresponding regional winds (Zecchetto and De Biasio, 2007; Obermann et al., 2018).

5.5 Conclusions

With this work, we have analyzed the horizontal mixing and transport properties at the upper layer of the Mediterranean Sea associated with the wind and waves generated fluid particle motions. We have combined data from real drifters trajectories and the output of an Ekman modified model applied to 24 years of satellite altimetry observations and winds and waves derived from the ERA-interim reanalysis data. Although we have used data from drifters, in the present work we are not interested in reproducing the submesoscale dispersion, but large-scale features of the flow.

We have found that the ageostrophic component not only can drastically modify the mesoscale LCS, but also the direction of the tracer spreading and the retention capacity of geostrophic eddies. Consequently, this fact makes us also question about the classical view of the role of some oceanographic features, such as geostrophic transport barriers identified through LCS, in governing the spreading of particles or even in controlling the connectivity of the flow across different oceanic regions.

FSLEs strongly vary depending on the region. The main hot spots of horizontal mixing in the Mediterranean Sea are associated with the major Mediterranean mesoscale features. The horizontal mixing is not very intense in the majority of the Mediterranean basin, but it concentrates at some specific locations, such as inside the main mesoscale gyres (e.g. in the Alboran and Crete gyres) and other mesoscale features active enough to produce high stirring as the topographic generated eddies originated from the interaction of boundary geostrophic flows (e.g. the Algerian and Northern boundary currents) with steep topographic slopes. Wind and wave induced mixing is significant in the northwestern basin and the south of Crete with a contribution up to 40%, but also showing a suppressing effect of mixing activity in the north part of the Algerian basin and Sicily.

As depicted from our results, the sub-regions unveiled from the SOM analysis of the total kinetic energy exhibit a different annual cycle of the horizontal mixing, as measured by averaged FSLEs. While all regions show minimum values in summer time, maximum mixing activity occurs in different months depending on the region. The strongest seasonal variability is identified in the northwestern basin and the Ionian and Aegean Seas. Regions characterized by high intensity of horizontal mixing, i.e. Alboran Sea, Algerian and Eastern basin, also present the lowest seasonal variability, due to the presence of quasi-permanent mesoscale features. The wind and waves induced mixing is also reflected in the seasonal variation of the ageostrophic contribution to the FSLE,

clearly appreciated in the western basin and in the Aegean Sea during the periods of mistral, tramontane and etesian winds intensification.

We have found important interannual variations (positive trends) in the mixing activity, that can reach values up to 1.07% year^{-1} in regions such as the Alboran, Algerian basin and the south of the Ionian Sea. Otherwise, northwestern basin, the Tyrrhenian, Adriatic and the north of the Ionian Sea experience a lower, 0.5%, mixing interannual increase. The global linear trend of FSLE$_g$ is higher than FSLE$_T$, suggesting a decline of mixing induced by wind and wave currents. FSLE trends could be explained by the relatively larger interannual intensification of the eddy amplitude and higher variability, relative to a smaller contribution from the wind and wave stress. Note that, the intensity of geostrophic velocities is associated with larger SSH gradients of eddies with a large increase in amplitude. The FSLE trend could have significant consequences in the transport of essential oceanic variables, such as heat, carbon, etc., with climatic implications. Consequently, determining changes to the FSLE field is fundamental to our understanding of the Mediterranean Sea and its potential response to climate change. Further studies should be performed in order to unravel the physical mechanism and forcing leading this mixing activity variation, for instance analyzing correlations with the regional wind stress and their long-term variability.

The Lagrangian dispersion in each region has been characterized from virtual and real pairs of trajectories. The scale-dependence property of λ allowed us to estimate the maximum dispersion value and the scaling exponents of the pair dispersion spectrum, useful to determine the physical processes controlling the dispersion. The provided information was used to infer the typical scales of the flow structures governing the dispersion in each region. The obtained results from the synthetic trajectories show an exponential regimen at small-scales associated with chaotic advection in all the regions (as expected because of the coarser resolution of the gridded data), followed by a Richardson like dispersion regime (consistent with a 2D inverse cascade) at large scale also in all the Mediterranean, except for the south of Ionian and the Aegean Sea, which are characterized by a shear turbulent diffusion due to separation of particles by uncorrelated currents. Regions with the higher dispersion level are those dominated by the major mesoscale features, in agreement with the regions of high mixing activity. The same regional pair dispersion hierarchy is found for the real drifter trajectories confirming the results obtained from the virtual trajectories. Additionally, we have found similar dispersion regimes, except for the region dominated by the major mesoscale features where the low number of drifters produces a large standard error in the fitting of the slope.

The anisotropy analysis of the relative dispersion reveals the existence of higher contribution of the zonal flow to the dispersion properties in the Mediterranean basin, except for the surroundings of the Gulf of Lion and Sicily, which are characterized by a higher meridional dispersion. As shown in the results the mesoscale coherent structures are larger along the zonal direction than in the meridional. The temporal averaged mixing anisotropy in the Mediterranean Sea is broadly longitudinal (positive LCSA values), revealing that the zonal flow dominates the mesoscale mixing activity. However, there is a central region that can be considered isotropic regarding mixing properties. During winter seasons, the anisotropy at the western basin is intensified, while for summer periods is higher in the eastern; being crucial the ageostrophic component contribution. In general, the ageostrophic component induces an increase of the meridional mixing, likely due to the north-south wind and wave intensification.

These transport properties have profound consequences on the regional distribution of quantities of biological or physical interest, providing novel insights on the distribution of drifting organisms, pollutants and, more generally, any tracer that is transported by the flow.

Supplementary material

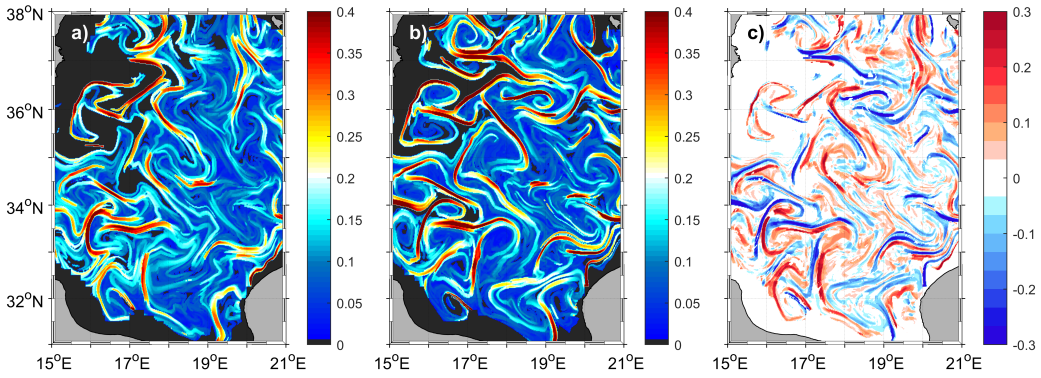

Figure S.5.12 *Spatial distribution of backward FSLE (days^{-1}) in the Ionian Sea corresponding to February* 5, 2014 *at* 6:00 *UTM, computed from a) total velocity field, U_T, and b) geostrophic velocity field, U_g. c) Difference between maps a) and b) (days^{-1}). The initial separation is $\delta_0 = 1/64°$ and the final separation, $\delta_f = 10\delta_0$.*

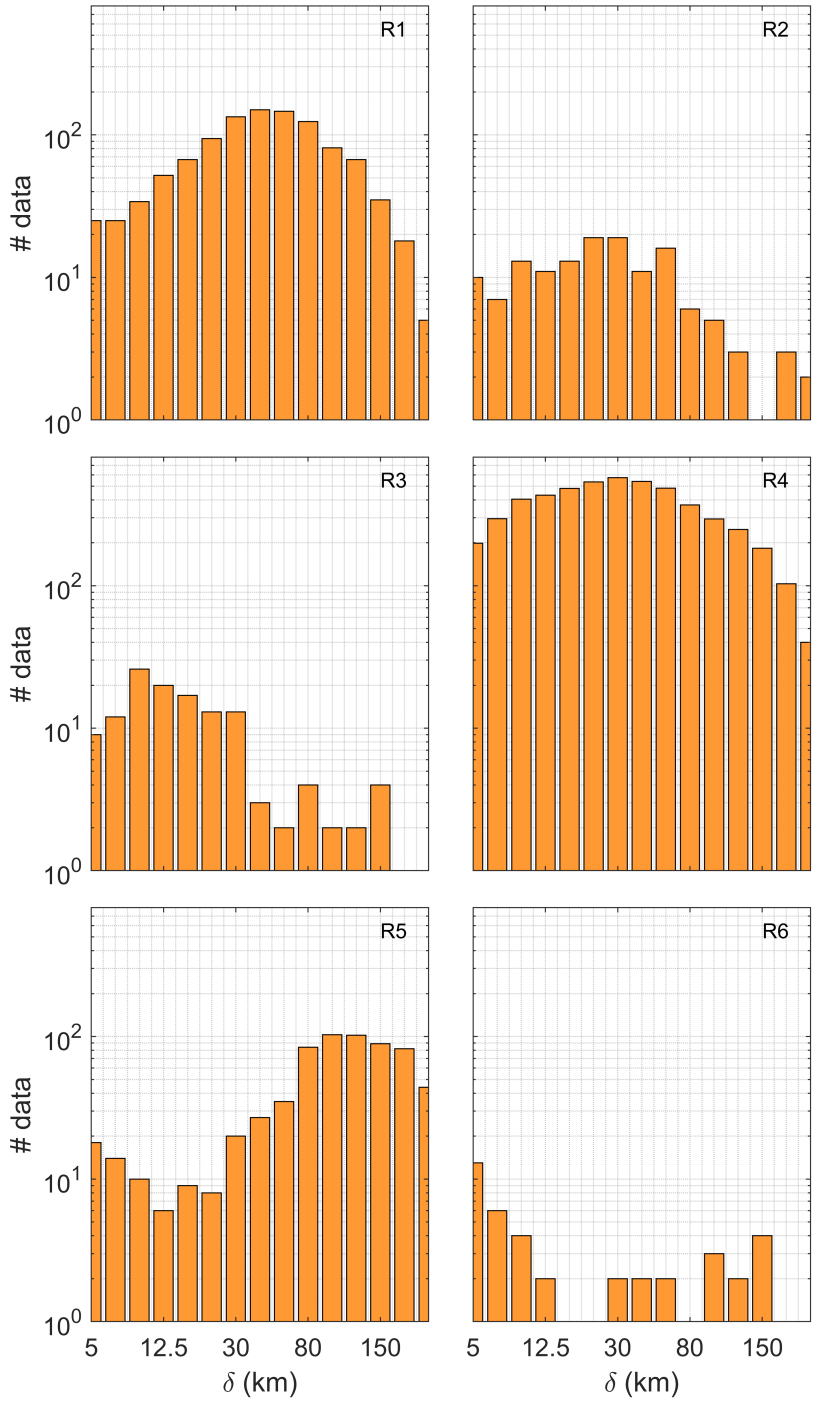

Figure S.5.13 *Number of tracks of pairs of real drifters that are inside each region at least during* 2 *days used in the regional dispersion analysis shown in Fig. 5.8, b.*

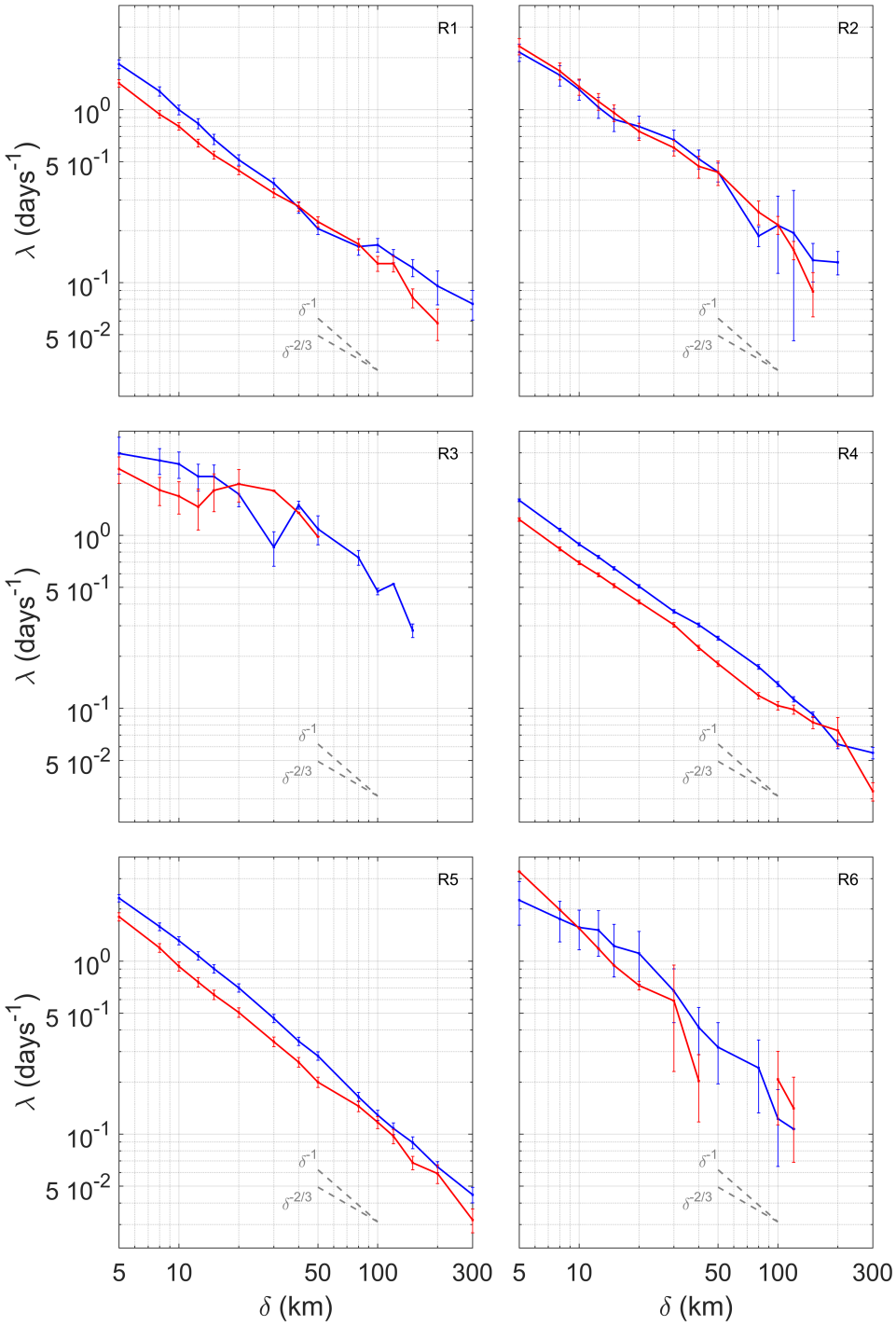

Figure S.5.14 *Zonal (blue lines) and meridional (red lines) FSLE curves (in days^{-1}) given by $\lambda_x(\delta_x)$ and $\lambda_y(\delta_y)$, respectively (see Eqs. 5.11 and 5.12), at different spatial scales (δ_x and δ_y, in km) calculated for pairs of real drifters. Each subplot (R1-R6) corresponds to the averaged FSLE values over all the pairs of real drifters available in the SOM-regions identified in Fig. 5.1. The scaling exponents associated with ballistic/shear (-1) and Richardson (-2/3) dispersion regimes are included in the plot with dashed grey lines.*

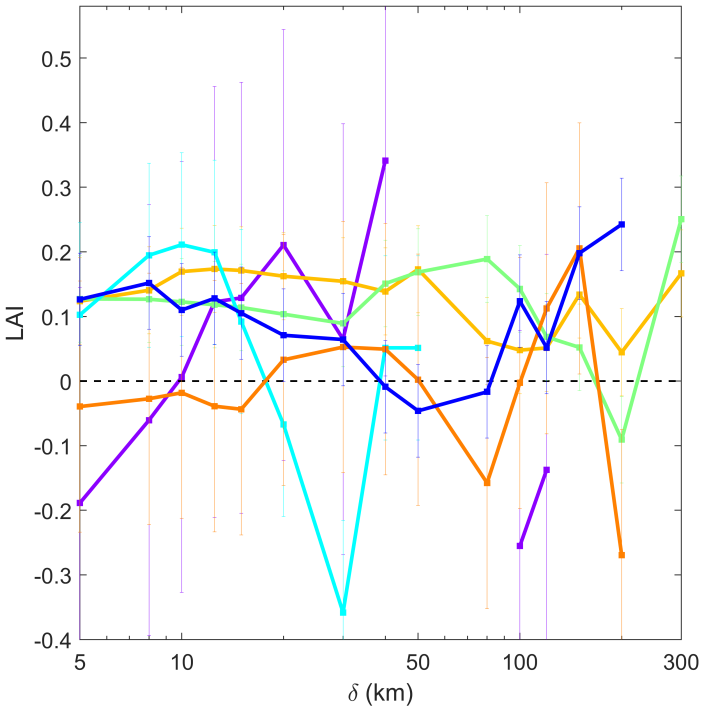

Figure S.5.15 *Scale dependence of LAI computed with drifters for each SOM-region of the Mediterranean Sea. Colors correspond to SOM-regions identified in Fig. 5.1. The dashed black line represents the isotropy (LAI=0).*

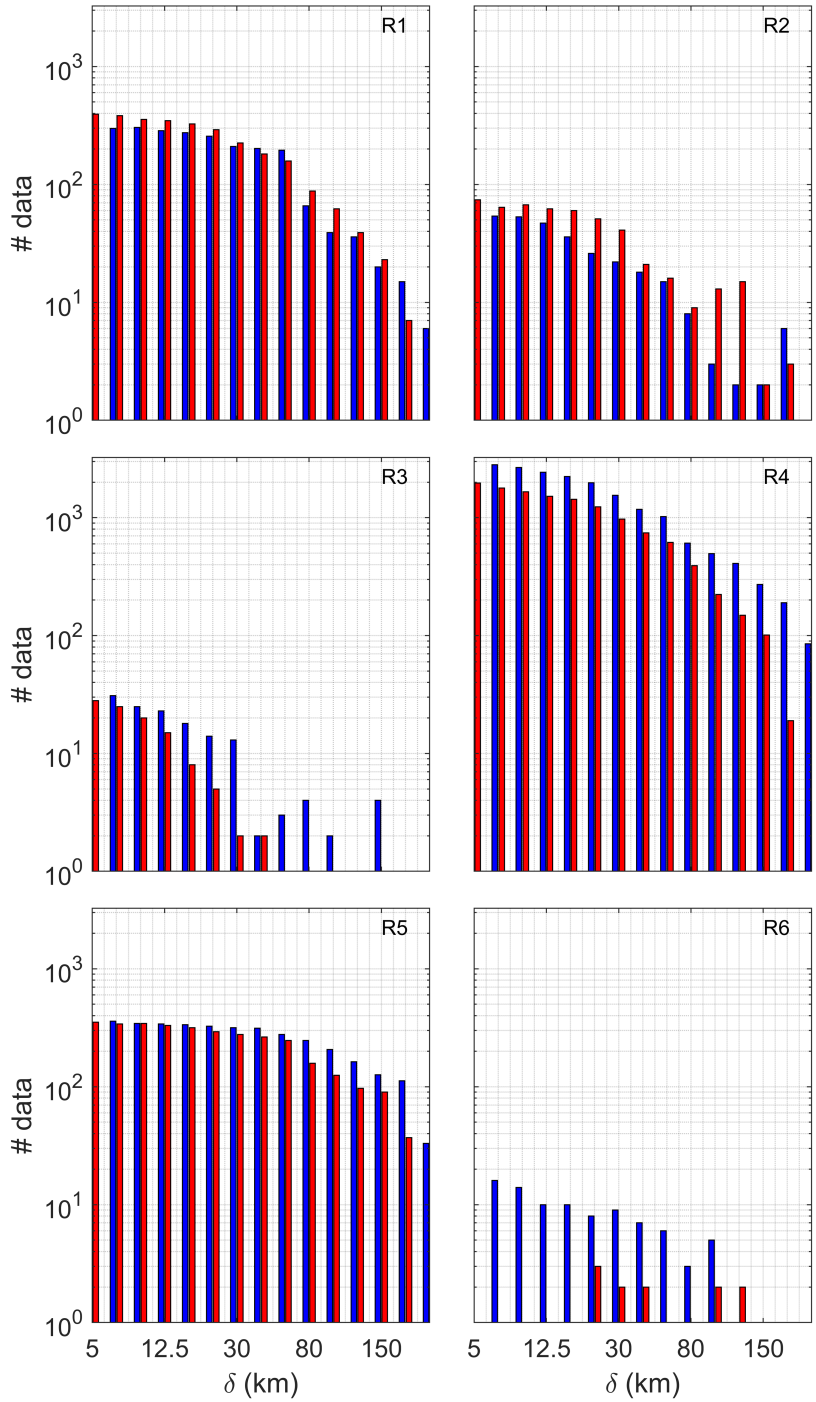

Figure S.5.16 *Number of tracks of pairs of drifters that are inside each SOM-regions identified in Fig. 5.1 at least during 2 days used for making Fig. S.5.14 for zonal (in blue) and meridional (in red) FSLE.*

Chapter 6

Numerical and remote techniques for operational beach management under storm group forcing

This chapter has been published as:

Morales-Márquez, V., Orfila, A., Simarro, G., Gómez-Pujol, L., Álvarez-Ellacuría, A., Conti, D., Galán, Á., Osorio, A., and Marcos, M. (2018). Numerical and remote techniques for operational beach management under storm group forcing. *Natural Hazards and Earth System Sciences*, 18(12): 3211-3223. doi: https://doi.org/10.5194/nhess-18-3211-2018.

Abstract

The morphodynamic response of a microtidal beach under a storm group is analyzed, and the effects of each individual event are inferred from a numerical model, in situ measurements and video imaging. The combination of these approaches represents a multiplatform tool for beach management, especially during adverse conditions. Here, the morphodynamic response is examined during a period with a group of three storms. The first storm, with moderate conditions (Significant Wave Height (SWH)$\sim 1\,\mathrm{m}$ during 6 hours), eroded the aerial beach and generated a submerged sandbar in the breaking zone. The bar was further directed offshore during the more energetic second event (SWH$= 3.5\,\mathrm{m}$ and 53 hours). The third storm, similar to the first one, hardly affected the beach morphology, which stresses the importance of the beach configuration previous to a storm. The volume of sand mobilized during the storm group is around $17.65\ \mathrm{m}^3/\mathrm{m}$. During the following months, which are characterized by mild wave conditions, the aerial beach recovered half of the volume of sand that is transported offshore during the storm group ($\sim 9.27\ \mathrm{m}^3/\mathrm{m}$). The analysis of beach evolution shows two different characteristic timescales for the erosion and recovery processes associated with the storm and mild conditions, respectively. In addition, the response depends largely on the previous beach morphological state. The work also stresses the importance of using different tools (video monitoring, modeling, and field campaign) to analyze beach morphodynamics.

6.1 Introduction

Evolution of sandy coasts at temporal scales (from minutes to years) has been a topic of wide interest over the past decades since sandy beaches and dune systems are the first natural lines of coastal defense against flooding and erosion hazards (Callaghan and Roshanka, 2009; Hallegatte et al., 2013), while at the same time being attractive environments in terms of leisure activities and tourism economy (Bosello et al., 2012; Jiménez et al., 2011; Luijendijk et al., 2018). The maintenance of these areas is crucial for coastal defense and, at the same time, coastal tourism seems to be one main target for beach erosion management (Semeoshenkova and Newton, 2015). For instance, in Spain, beaches represent only the 0.01% of the land surface, producing up to 10% of its gross domestic product (Yepes and Medina, 2005). Beach management tends to be reactive rather than proactive, solving the problems as they appear and without a long term planning.

Mitigation of coastal erosion and preservation of coastal areas represent essential aspects of the Protocol on Integrated Coastal Zone Management in the Mediterranean and are included in the objectives of most countries' national regulations and policies in Europe (Semeoshenkova and Newton, 2015). It is already known that decisions concerning coastal management actions should be made using the best available science, and new tools that take into account physical, natural and socioeconomic characteristics of beaches should be developed (Ariza, 2011; Tintoré et al., 2009). This makes it necessary to transfer the knowledge from scientists to managers in an effective way, which is a challenge today.

For coastal management it is crucial to have continuous measurements of waves and shoreline (Ferreira et al., 2018). One of the main issues in coastal erosion is the response of coastlines to both individual storms and storm groups since the behaviors are quite different (Loureiro et al., 2012; Vousdoukas et al., 2012; Houser, 2013; Coco et al., 2014; Masselink and van Heteren, 2014; Senechal et al., 2015; Masselink et al., 2016, i.e.). Single storms can result in significant beach erosion within a few hours, whereas a sequence of storms can have a large and complex impact on beach morphology, the final effects of which remain difficult to quantify and to predict (Ferreira, 2005; Frazer et al., 2009).

Storm waves and their associated water-level conditions are key drivers in shoreline dynamics. Shoreline response to successive storms can be dependent on storm energy thresholds, as well as, on the feedback mechanisms associated with the beach morphology and the presence or absence of former impacts (Ciavola and Stive, 2012). There are many examples that have shown that shorelines can recover relatively well from erosion triggered by storms and that this recovery can be quick, from a few days or weeks (Birkemeier and WA, 1979; Vousdoukas et al., 2012) to a couple of months (Wang et al., 2006). Therefore, the resilience of beaches, understood as their capacity to recover from a major storm, is related to the combination of sediment reservoirs, arrangement of three-dimensional beach morphology (i.e., sand bar type and location, beach slope) and the beach memory (Jara et al., 2015).

Recent works, such as the study by Vousdoukas et al. (2012), have shown that the observed morphological change during consecutive storms has a strong dependence on the initial beach morphology. These authors, departing from field experiments in southern Portugal, stated that beach recovery did not maintain pace with storm frequency and that storms can have a dramatic impact on erosion if they occur in groups. In addition,

other works dealing with storm impact on shoreline dynamics in the Bay of Biscay (SE France) have suggested that energetic events are probably not the only drivers of erosion processes since significant beach erosion has been characterized under very calm conditions following energetic events (Senechal et al., 2015). In a similar way, observations from a detailed field campaign involving daily beach surveys at Truc Vert beach (Bordeaux, France) during a sequence of storms demonstrated that a sequence of extreme storms does not necessarily result in cumulative erosion, possibly because of the interplay among water levels, the angle of wave approach and the preexisting beach face conditions (Coco et al., 2014).

The goal of this contribution is to study the effect of a storm group on the morphology of a beach system and to advance a multiplatform methodology for effective decision-making regarding beach erosion management according to the available data and numerical models. Here, we present the explanation of temporal patterns of beach accretion and erosion under consecutive storm events at an intermediate microtidal carbonate beach by using the dataset available on the studied beach, high-frequency data on shoreline positions and cross-shore profiles extracted from coastal video monitoring techniques, real-time kinematic (RTK) and echo sounding surveys, concurrent hydrodynamic measurements, and the use of numerical models widely validated in order to fill gaps in the dataset.

6.2 Study area

Cala Millor is a semi embayed beach $1.7\,\mathrm{km}$ in length and ranging between 15 and $30\,\mathrm{m}$ in beach width. It is located on the northeastern coast of Mallorca (western Mediterranean Sea, Fig. 6.1). Sediments are mainly composed of well-sorted medium to coarse biogenic carbonate sand with a grain diameter D_{50} between 0.3 and $0.6\,\mathrm{mm}$ changing along the cross-shore distance, according to the depth (Gómez-Pujol et al., 2011). The beach area is around $1.4\,\mathrm{km}^2$ with a bottom colonized by the endemic *Posidonia oceanica* meadow at depths from 6 to $35\,\mathrm{m}$ (Infantes et al., 2009). This meadow increases bottom roughness, reducing near-bed velocity and thus modifying the sediment transport (Infantes et al., 2009, 2012; Koch et al., 2007) and increasing wave attenuation (Luhar et al., 2013).

From a morphodynamic point of view, Cala Millor is an intermediate beach with a highly dynamic configuration of longitudinal sinuous-parallel bars and troughs, presenting intense variations in the bathymetry related to sandbar movement (Alvarez-Ellacuria et al., 2011; Gómez-Pujol et al., 2011).

Tides are negligible (the tidal amplitude is less than $0.25\,\mathrm{m}$) although other surge components such as those induced by wind or atmospheric pressure can increase the sea level by up to $1\,\mathrm{m}$ (Orfila et al., 2005). The beach is open to the east and, due to the semi-enclosed configuration, is well exposed to waves from the NNE to the SE (Enríquez et al., 2017). Significant wave height (SWH) at deep waters is usually bellow $0.9\,\mathrm{m}$ with a peak period (T_p) between $4\,\mathrm{s}$ and $7\,\mathrm{s}$, although frequent storms account for 2% of time increase SWH up to $5\,\mathrm{m}$ with a T_p higher than $10\,\mathrm{s}$, with a return period of 1.5 years (Tintoré et al., 2009).

Cala Millor is one of the most important tourist resorts created on the eastern coast of Mallorca – more than $60,000$ visitors during the summer period – and has a long history of sand nourishment and coastal management approaches (Tintoré et al., 2009).

Since November 2010 the Balearic Islands Coastal Observing and Forecasting Sys-

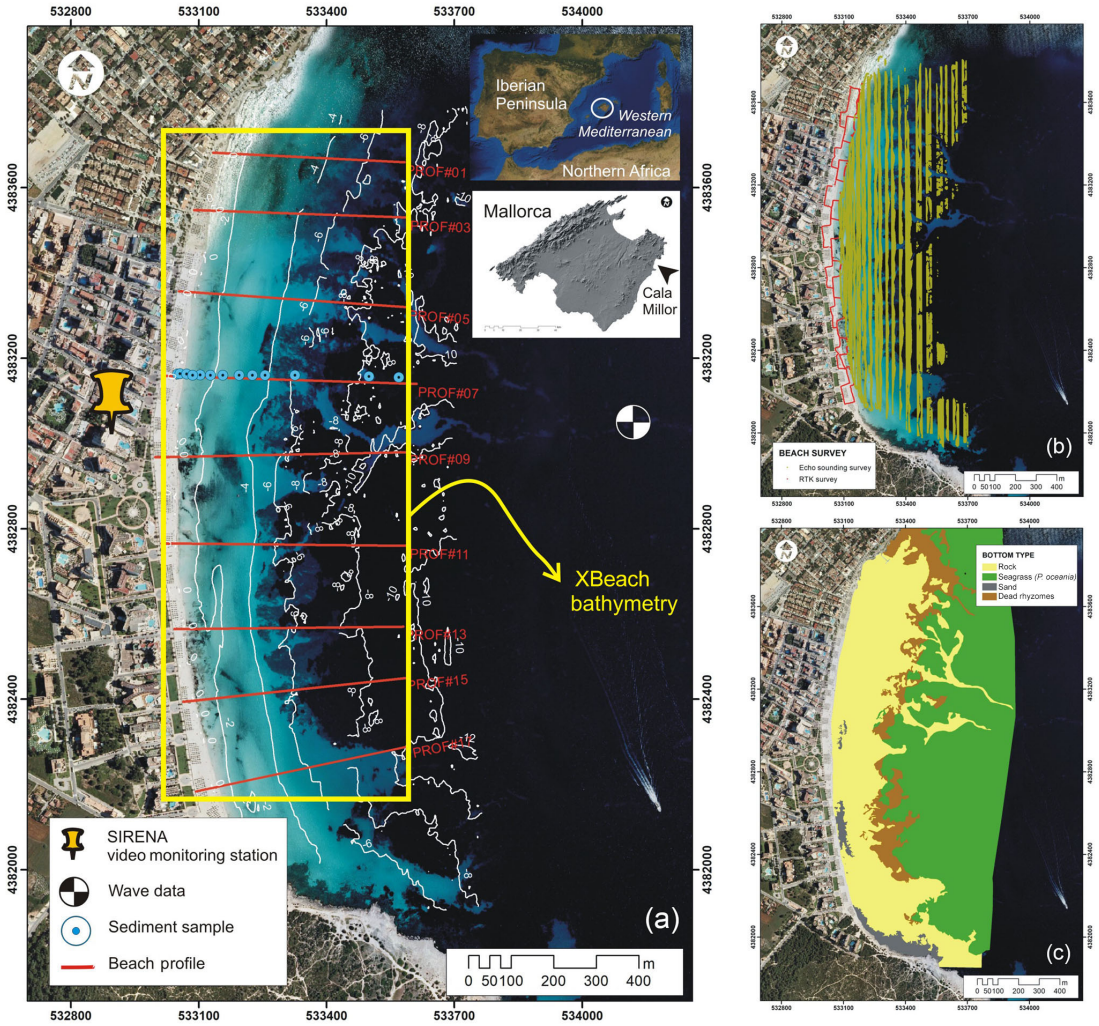

Figure 6.1 *Study site location (a) and major features of Cala Millor. (b, c) White dashed lines correspond to the bathymetric survey (isoline equal distance of* 2 m*); the yellow frame covers the bathymetry area obtained by means of XBeach, and red lines correspond to the beach profile described in text. The bottom orthophoto is provided by the Govern de les Illes Balears-SITIBSA (June* 2008*). Panel (b) shows the combination of multibeam bathymetric survey (green points) and RTK–GPS survey for dry beach and very shallow submerged beach (red points). (c) Bottom type at Cala Millor.*

tem (SOCIB) has been monitoring Cala Millor by means of coastal video monitoring, moored instruments and a periodic program of beach profile and sediment characterization (Tintoré et al., 2013). Along Cala Millor beach, over short temporal scales, shoreline position changes are not always homogeneous (Fig. 6.2, a) and it is possible to appreciate some different behaviors and responses to the wave climate. Cala Millor has experienced at least 19 events with significant wave height at 25 m in depth of over 2 m between November 2010 and January 2017 (Fig. 6.2, b). Some of these events are isolated storms (e.g., April 2013) while others act in groups (e.g., January 2015). Fig. 6.2, a shows the alongshore anomaly of shoreline distances for the period between November 2010 and January 2017. The correlation between beach face response and sea conditions is not clear: there are storms that, even though Cala Millor is not a pocket beach, give rise to apparent temporary rotation, whereas others appear as a gen-

eral shoreline advance or retreat. Nevertheless, from the averaged alongshore shoreline width anomaly (Fig. 6.2, c) a clear change in beach behavior since April 2014, just after a group of storm events that will be analyzed below, can be inferred. Despite that the beach eventually recovers the former alongshore width, a net shoreline recession is observed.

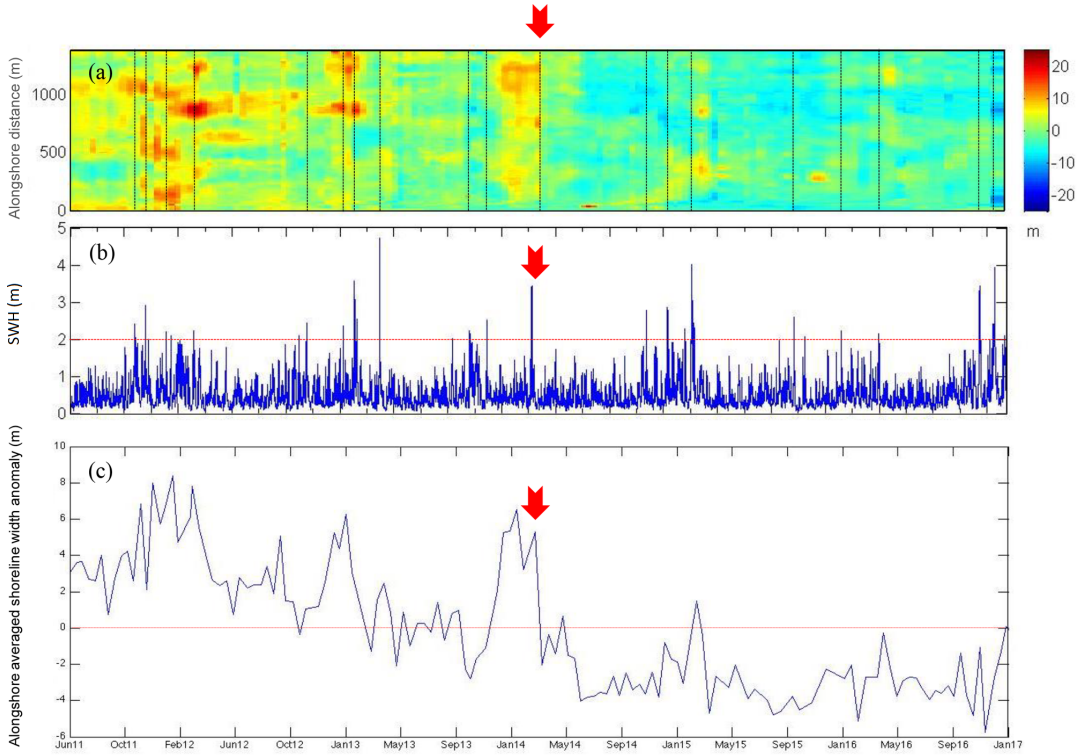

Figure 6.2 *(a) Alongshore shoreline width anomaly (in m) at Cala Millor from November* 2010 *to January* 2017. *Red colors indicate shoreline advance, whereas blue ones indicate shoreline recession. The dashed black lines show the sea storm events larger than* 2 m. *(b) Wave significant height (in m) from a wave recorder located at* -17 m *in the middle of the Cala Millor embayment. (c) Alongshore averaged shoreline width anomaly (in m) at Cala Millor. The red arrows highlight the storm group event at April* 2014.

In March 2014, just a few days before the storm group event, a field experiment was carried out in Cala Millor in order to characterize the beach morphology. This experiment produced detailed bathymetries, and beach profiles were measured before the storms and wave recorders were also installed at different depths. Later, in June 2014, another detailed beach survey and bathymetry belonging to the SOCIB's periodic beach monitoring program were carried out (Tintoré et al., 2013). Unfortunately, even though the April 2014 storm group seems to be critical for the beach width evolution, there are no bathymetric data available immediately after the storms. Nevertheless, the number of available data before and after the storm group impacts makes this an opportunity to validate and generate numerical proxies that contribute to unraveling the beach response to the storm group.

6.3 Data and Methods

This Chapter partially deals with datasets produced during the Riskbeach experiment, performed by the SOCIB, the Mediterranean Institute for Advanced Studies (IMEDEA) and the Institute of Marine Sciences (ICM-CSIC) in Cala Millor from 17^{th} to 26^{th} March 2014. This experiment was designed to study the response and recovery of an intermediate beach to usual (1-year return period) storm conditions and the related sediment transport processes and morphological changes. During the experiment, some instruments, detailed in Fig. 6.1, are installed in a central section of the beach to obtain high-resolution sediment and hydrodynamical data. In this Chapter we employ the wave and current recorder data (acoustic wave and current meter, AWAC) moored at $25\,\text{m}$ depth. Measurements are completed with bathymetric surveys, sediment samples and video monitoring products. After the experiment (just from 26^{th} March) large waves resulted in a significant morphological change of the beach, once the field survey was finished and the echo sounding equipment was dismantled. To assess the effects of these storms we combine numerical modeling with video monitoring techniques to infer the beach profiles that help us to understand the changes in the beach morphology before and after the storm group.

Figures 6.1 and 6.3 summarize the approach developed in this study, showing which data are from different instrumental approaches (i.e., direct measurements from bathymetric and differential GPS–real-time kinematic (DGPS–RTK) surveys) and which ones are inferred from numerical modeling and video images (indirect measurements). According to Fig. 6.3, field wave, sediment and beach morphology data, before the storm event, are required in order to start up numerical model tools. The obtained results when field campaign data are available have to be validated with field bathymetric data. The numerical model validation ensures that the results obtained during the storm period are accurate. In addition, the product acquired by video monitoring, once the cameras have been calibrated with field bathymetric data, will provide the "proxy" of the measured data. Results will be organized in two sections: first, profiles obtained by direct methods and, second, the results related to the use of these data sources for unraveling the beach erosion and recovery timescales.

We have wave mooring data that we use, through statistical analyses, in order to describe the wave climate and the storms that occurred in Cala Millor. We also have bathymetric data, obtained with DGPS–RTK and echo sounding beach surveys. With the wave climate parameters, the bathymetric initial data of the beach and the grain size distribution (taken with sediment sampling), we can simulate the situation of the Cala Millor beach in the XBeach (eXtreme Beach behavior) model. The obtained results must be validated with field bathymetric data during the period of time that we can recollect them. When the field campaign is impossible, we will be able to know the conditions of the beach thanks to the simulation of XBeach (once it has been validated). In addition, we can have another source of data, the video monitoring. Through image analysis we can obtain the beach profile. Once this tool is calibrated and validated against the model and field data, it will act as an independent technique in order to know the state of the beach.

In this way, we can obtain an approximation of the sediment mass balance and the erosion and recovery timescales of the beach.

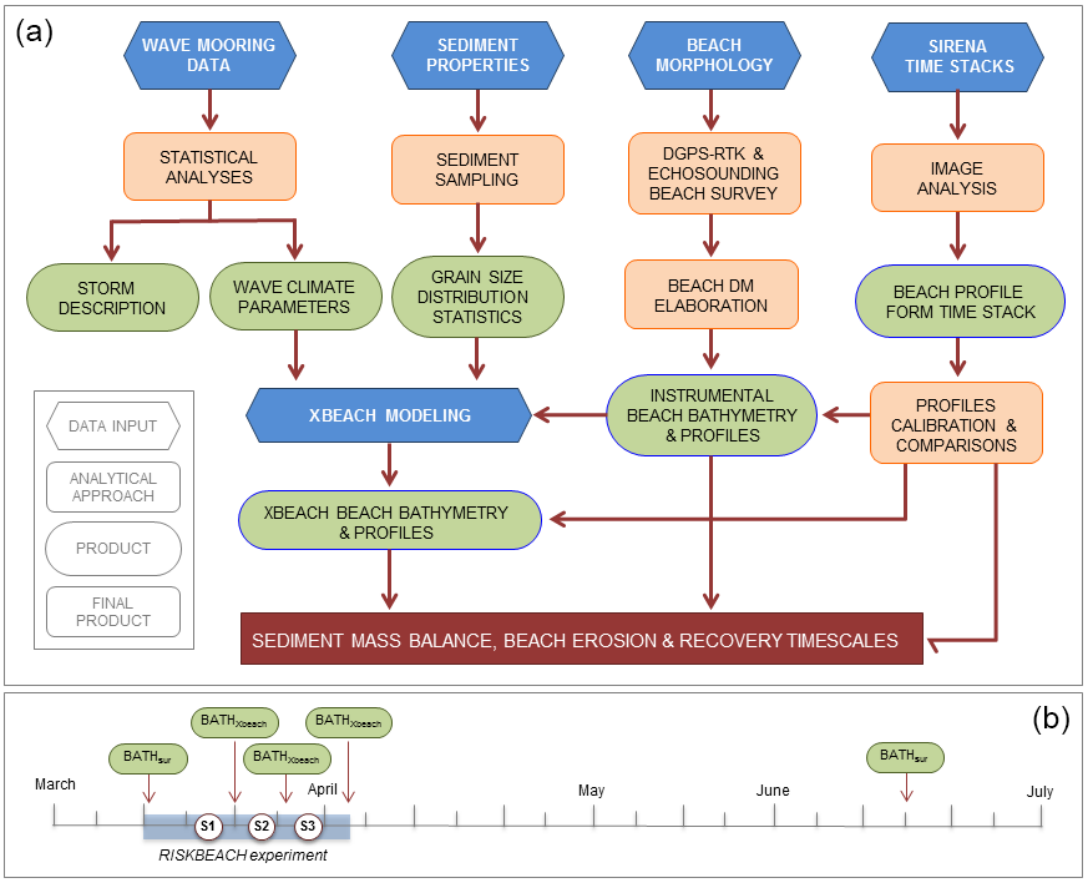

Figure 6.3 *(a) Workflow of the approach followed in the study. (b) Calendar showing the date for the samples used in the study.*

6.3.1 Wave conditions

Offshore wave conditions (significant wave height, SWH, peak period T_p and wave direction at $50\,\mathrm{m}$ in depth every 3 h) are obtained from a reanalysis of a 60-year wave model output produced by the Spanish Harbor Authority (http://www.puertos.es/es-es/oceanografia/Paginas/portus.aspx, last access: 29 November 2018). The mean SWH for the period of study is $0.9\,\mathrm{m}$ with a mean peak period (T_p) of $6\,\mathrm{s}$. During the experiment (17 to 26 March 2014), wave conditions were measured with an AWAC system moored at deep waters ($25\,\mathrm{m}$ in depth) in the central part of the beach.

Deep water wave conditions show three storms during the period of study (Fig. 6.4). Here we define storm as sustained wave conditions during at least 6 hours with SWH$>$ $1\,\mathrm{m}$. Gómez-Pujol et al. (2011) suggested this threshold as the condition required to generate a significant impact along beach morphology and sediment properties. When such an event is not isolated but becomes a succession of events, we refer to it as a group of storms. These episodes can cause larger damage on the beach with smaller wave heights since the beach does not have enough time to recover its initial morphodynamic state. The experiment started on 17 March after a period of moderate conditions with SWH close to $1\,\mathrm{m}$ that did not result in significant morphological changes. The first storm, S1 (see Fig. 6.4, a), occurred on 26 March, just after the instruments were moved away, with a maximum significant wave height SWH$=1.5\,\mathrm{m}$ and $T_p = 9.9\,\mathrm{s}$ from the SE (Fig. 6.4, c) and a duration of $7\,\mathrm{h}$. The second storm, S2, beginning on

28 March, lasted 53 h and peaked during the evening of 29 March with a maximum SWH of 3.4 m and T_p of 10.4 s. The estimated return period for the S2 storm is around 1.2 years. Nevertheless, the return period just refers to the significant wave height threshold, despite that the storm duration and persistence of wave height was 38 h with SWH$>$ 2 m which is unusual. Wave conditions started to build up again on 2 April 2014 after a short period of relatively small waves (SWH$<$ 1 m). The third storm, S3, from 2 to 3 April, peaked 4 days after the former storm with maximum SWH of 1.3 m m and T_p of 7.8 s (Fig. 6.4, a and b) during 48 h. The following 2 months were characterized by mild conditions, which will be used to study the beach recovery after the storm groups.

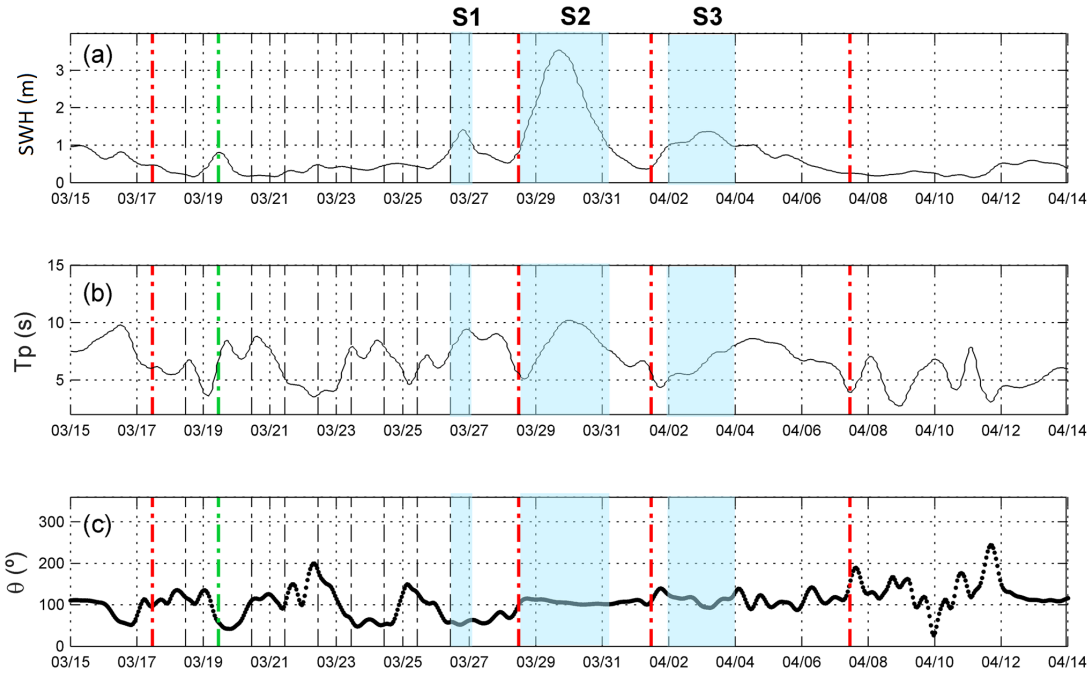

Figure 6.4 *(a) SWH (m) at* 25 m *depth in Cala Millor between* 15 *March and* 14 *April* 2014*. (b)* T_p *(s). (c) Wave direction (*^{circ}*). The blue shading shows the period corresponding to the storms. Vertical red dotted lines indicate the initial bathymetry obtained while dashed dotted lines indicate the dates when cross-shore profiles were measured. Vertical green dotted lines state the day when the model was validated using the corresponding shore profiles. Vertical red lines show the date when bathymetry inferred from XBeach was used for comparison among storms.*

6.3.2 Beach Morphology

The topographic surveys were performed from 17 to 26 March using a DGPS–RTK with submetrical resolution (having a horizontal accuracy of around 8 mm and a vertical accuracy of around 15 mm) for both the aerial (the area located over the mean sea level) and the submerged beach (from deep waters up to 1 m in depth). Additionally, for submerged beach, bathymetric data were obtained using a Biosonics DE-4000 echo sounder with a DGPS, which allowed dense mapping from 0.5 to 10 m in depth. On 17 March, an initial bathymetry was acquired. In addition, nine cross-shore profiles were taken daily between 18 and 26 March (see Fig. 6.1). An additional bathymetry was performed on 12 June for control purposes. Elevations were referenced to the Balearic

Islands ordinance survey mean sea level and the horizontal position referenced to the UTM coordinate system (Gómez-Pujol et al., 2011). These data cover the area between the boulevard sea wall and the lower shoreface (ca. $8\,\mathrm{m}$ in depth).

6.3.3 Sediment characteristics

Sediment samples were collected from aerial beach ($+2\,\mathrm{m}$) to $6\,\mathrm{m}$ in depth at one of the central cross-shore transects (profile 07, Fig. 6.1). Sediments in the aerial beach and up to $1\,\mathrm{m}$ in depth were collected by dragging a plastic bag inserted in an oval metallic frame on the bottom with a vertical penetration of about $2-4\,\mathrm{cm}$, and for greater depths we threw a clamshell bucket from a boat. The weight of samples ranged from 200 to $500\,\mathrm{g}$. After collection, samples were soaked in fresh water for $4\,\mathrm{h}$ and drained before being dried for $24\,\mathrm{h}$. Sediment was analyzed using a laser granulometer and grain size obtained through the method described by Folk and Ward (1957) using GRADISTAT software (Blott and Pye, 2001).

6.3.4 Video monitoring

Coastal monitoring using video images is a practical and widely used technique since the advent of Argus (Holland et al., 1997). Since then, several systems (Cam-era, Horus, Cosmos, Beachkeeper, Ulises, etc.) mimic the Argus philosophy with the objective of providing continuous measurements of coastal processes in an unsupervised and autonomous procedure. Here, we use one such approach, SIRENA/Ulises (Nieto et al., 2010; Simarro et al., 2017), which has been operating since 2009 in Cala Millor. The system is composed of five charge-coupled device (CCD) cameras connected to a server acquiring daily images (Gómez-Pujol et al., 2013). The five cameras encompass an alongshore distance of around $1.7\,\mathrm{km}$, largely including the monitored area. We use the time stacks, consisting of pseudo-images built with all pixel observation taken at $7.5\,\mathrm{Hz}$ at a predefined cross-shore transect during the first $10\,\mathrm{min}$ of each hour, to infer the beach profile with the inversion of the wave dispersion relationship. The underlying idea in the inversion method is that the wave speed for progressive waves can be measured from its visible signature at consecutive snapshots to estimate the bathymetry using linear wave theory at the observed cross-shore transect (Stockdon and Holman, 2000).

Adopting the linear wave theory, the wave celerity c for shallow water waves ($kh < \pi/10$ where k is the wave number and h the local water depth) is

$$c^2 = g \cdot h, \tag{6.1}$$

where g is the gravitational acceleration.

Time stack images (Fig. 6.5, a) are preprocessed to convert the RGB data to a tractable intensity matrix. First, original time stacks, with spatial and temporal dimensions $(n_x, n_t) = (650, 4500)$, are resampled by removing pixels at the aerial beach as well as at the outer domain (intermediate waters) where each pixel corresponds to large distances that are not useful for measuring hydrodynamic processes. Final images have spatial and temporal dimensions of $(\hat{n}_x, n_t) = (460, 4500)$. A quadratic filter with a time window of $3\,\mathrm{s}$ is applied to smooth the intensity timewise, and for each cross-shore position the temporal mean is subtracted. From the intensity matrix $I(x,t)$, the wave frequency is obtained as the main component of the fast Fourier transform (FFT)

in the time domain, which is constant along the cross-shore dimension. A FFT is performed for each of the 460 cross-shore time series and the wave frequency, f, found as the mode of all resulting peaks (Fig. 6.5, b).

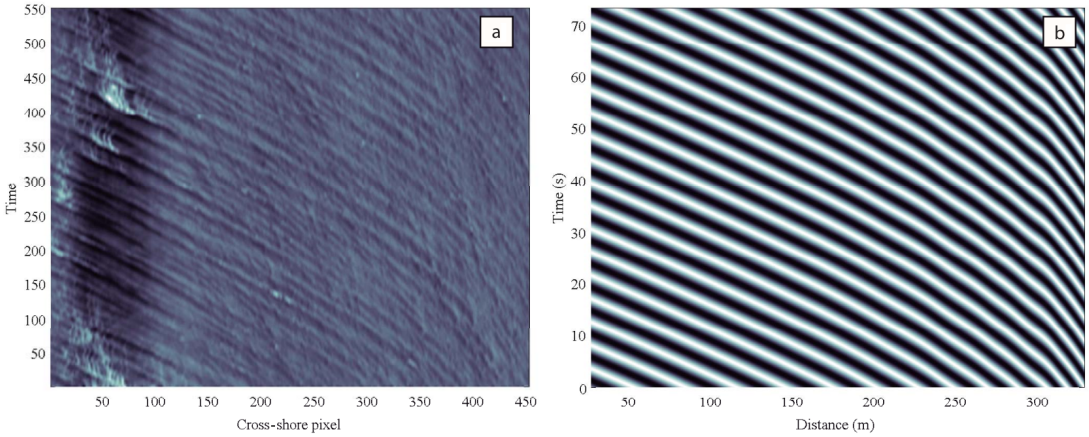

Figure 6.5 *(a) Time stack image for* 19 *March at* $09{:}00$ *UTC* + 1 *for the central camera. The abscissa corresponds to the cross-shore direction and the ordinate for the time. (b) Reconstruction for the same date assuming a constant wave height using the Fourier mode of the detected period (i.e.,* $\cos\left(\phi(x, f_w) - 2\pi\, f_w\right)$*).*

Once f is known, the spatial component of the wave phase function (Fig. 6.5, b), is evaluated following (Stockdon and Holman, 2000) as,

$$\phi = \arctan\left\{\frac{\mathrm{Im(I(x,\omega))}}{\mathrm{Re(I(x,\omega)}}\right\}, \tag{6.2}$$

and the wave celerity obtained as,

$$c = \frac{2\pi f}{\partial\phi/\partial x}. \tag{6.3}$$

The beach profile is finally obtained from Eq. (6.1).

6.3.5 Numerical modelling

Morphological evolution is assessed using the XBeach model (Roelvink et al., 2009), which resolves the hydrodynamic processes of both the short waves (refraction, shoaling and breaking) and the long waves (generation, propagation and dissipation). We use version 4920 for 64 bits. The model has been extensively validated with laboratory data as well as with field observations to study the morphological response of beach and sandy dunes, mostly under storm conditions. Here, we apply the model to analyze the storm group period with the surf beat mode that resolves the 2-D averaged equations.

The initial bathymetry (of 17 March) is discretized in an orthogonal rectangular grid evenly spaced with a resolution of $\Delta x = 7.44\,\mathrm{m}$ in the cross-shore direction and with $\Delta y = 15.86\,\mathrm{m}$ in the alongshore direction. Hourly JONSWAP spectra, generated through the measured data with the AWAC at $25\,\mathrm{m}$ in depth, are propagated from the seaward boundary to the coast for the period of 17 March to 8 April, after S3 (summing up 528 runs of $1\,\mathrm{h}$ of real time). The seaward boundary is imposed as the absorbing–generating (weakly reflective) boundary condition and the lateral boundaries as

Neumann type, for which the alongshore gradients are set to zero. The incoming wave directions in almost all simulations come from the east perpendicular to the shoreline (Fig. 6.4, c).

Sediment characteristics measured before the experiment (D_{50} and D_{90}) are interpolated along the sampled profile and then they are extrapolated alongshore according to the depth of each grid point. The dimensionless porosity of the sediment is set to $30\,\%$ and the density considered to be $2650\,\mathrm{kg/m^3}$.

6.4 Results and Discussion

6.4.1 Bathymetry extraction from model and video images

The analyses based on XBeach and on time stacks are used to obtain the bathymetry and beach profiles to address changes in sediment mass balance. The initial bathymetry was measured before the storms (17 March). The numerical model is run for the period between 7 March and 8 April, as stated. For each day a model-derived bathymetry is obtained and nine profiles are extracted at the same locations of the measured cross-shore profiles. Table 6.1 shows the error parameters between measured profiles and the XBeach modeled profiles from 17 to 26 March. The computed error parameters are the correlation coefficient (R^2), the scatter index (SCI) normalized with the maximum of the RMS of the data and the absolute value of the mean of the data, and the relative bias (RB) normalized in the same way as the scatter index, used in Roelvink et al. (2009):

$$R^2 = \frac{\mathrm{Cov(m,c)}}{\sigma_\mathrm{m}\sigma_\mathrm{c}}, \tag{6.4}$$

$$SCI = \frac{\mathrm{rms_{c-m}}}{\max(\mathrm{rms_m}, |\langle \mathrm{m} \rangle|)}, \tag{6.5}$$

$$RB = \frac{\langle \mathrm{c-m} \rangle}{\max(\mathrm{rms_m}, |\langle \mathrm{m} \rangle|)}, \tag{6.6}$$

being m the field data and c the modeled results.

The profiles derived from the model compare well with the measured ones from the aerial beach ($h = 2\,\mathrm{m}$) to the depth of closure ($h = -7\,\mathrm{m}$, according to the Hallermeier (1981), formulation). The minimum R^2 is 99.31%, the maximum SCI is 0.11 and the maximum RB is 0.03 in the central profile. Therefore, the modeled bathymetries (XBeach) can be considered an efficient and reliable tool for unraveling the beach storm effects.

As an additional source of data, a cross-shore seabed profile in the SIRENA/Ulises central camera (Fig. 6.6) is obtained following the above-described methodology. Table 6.2 compares the cross-shore profiles derived from time stacks against the instrumental measured profiles for the period between 19 March and 26 April (there are not time stacks available for 17 and 18 March). Since the time stack is defined in a cross-shore transect located between profiles 07 and 09, in situ measurements are interpolated daily to the time stack transect for comparison purposes. Error parameters from in situ measurements and from video images are shown in Table 6.2, with a R^2 value of 97.95%, SCI of 0.14 and RB of 0.04. The largest differences tend to be located at deep profile positions where the model is known to perform worse since the accepted assumption on Eq. (6.1) is only valid for shallow waters. In general, there is a good agreement

Table 6.1 *Error statistics for the simulated profiles by XBeach compared with the measured profiles during Riskbeach.*

Profile #	$R^2(\%)$	SCI	Relative bias
01	99.79 ± 0.08	0.07 ± 0.03	0.02 ± 0.04
03	99.77 ± 0.09	0.07 ± 0.03	-0.02 ± 0.03
05	99.48 ± 0.13	0.08 ± 0.01	0.01 ± 0.01
07	99.53 ± 0.08	0.09 ± 0.01	0.00 ± 0.03
09	99.31 ± 0.21	0.11 ± 0.02	0.03 ± 0.01
11	99.73 ± 0.18	0.06 ± 0.02	0.00 ± 0.01
13	99.72 ± 0.03	0.07 ± 0.01	0.02 ± 0.03
15	99.59 ± 0.49	0.08 ± 0.03	-0.03 ± 0.02
17	99.90 ± 0.04	0.04 ± 0.01	0.03 ± 0.02

between both sets of data.

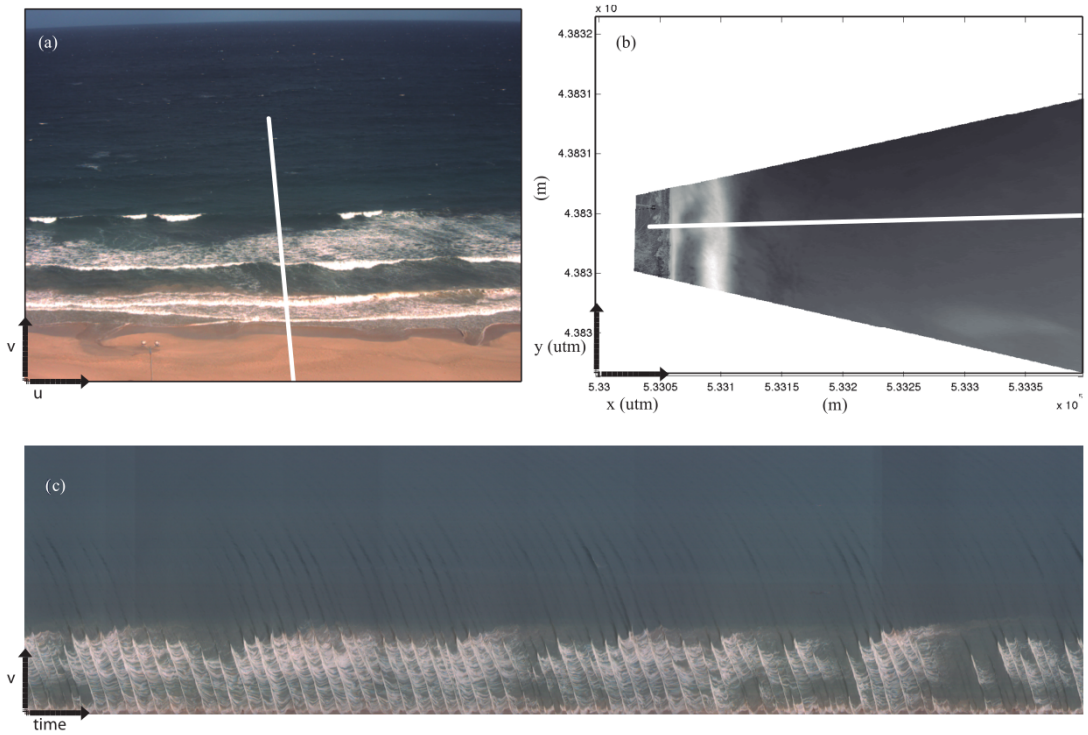

Figure 6.6 *(a) Cross-shore transect defined for the time stack image on camera no.* 3*. The figure shows the original image in the (u,v) ≡ pixel coordinate system. (b) The same after rectification in the (x,y) ≡ UTM coordinate system. (c) Resulting time stack for* 19 *March at* 10:00 *UTC* + 1*.*

Both comparisons, XBeach vs. instrumental and time stack vs. instrumental, present the same order of magnitude as that obtained in Roelvink et al. (2009). This allows us to compare beach sediment mass balance before and after the storm group as well as

during the longer period of calm after the storms using different datasets and different techniques. This would allow a correct management of the beach, avoiding unnecessary engineering works between tourist seasons.

Table 6.2 *Error statistics for the estimated profile from time-stacks compared with the measured profiles during Riskbeach.*

$R^2(\%)$	SCI	Relative bias
97.95 ± 1.4	0.14 ± 0.07	0.04 ± 0.06

6.4.2 Beach morphological response to storms and recovery

Although the individual storms are not exceptional in terms of intensity, their occurrence as a storm group has a significant imprint on the beach morphology. The initial bathymetry, performed before the storm group (on 17 March 2014), shows a sinuous-parallel and patchy bar at $-1\,\mathrm{m}$ and a cross-shore profile with attenuated secondary forms with a mean slope of 2.6%, whereas the bathymetry obtained for 8 April 2014 from XBeach shows a marked dissipative configuration. This is consistent with the obtained timex images through the SIRENA video monitoring station (see Fig. 6.7). The

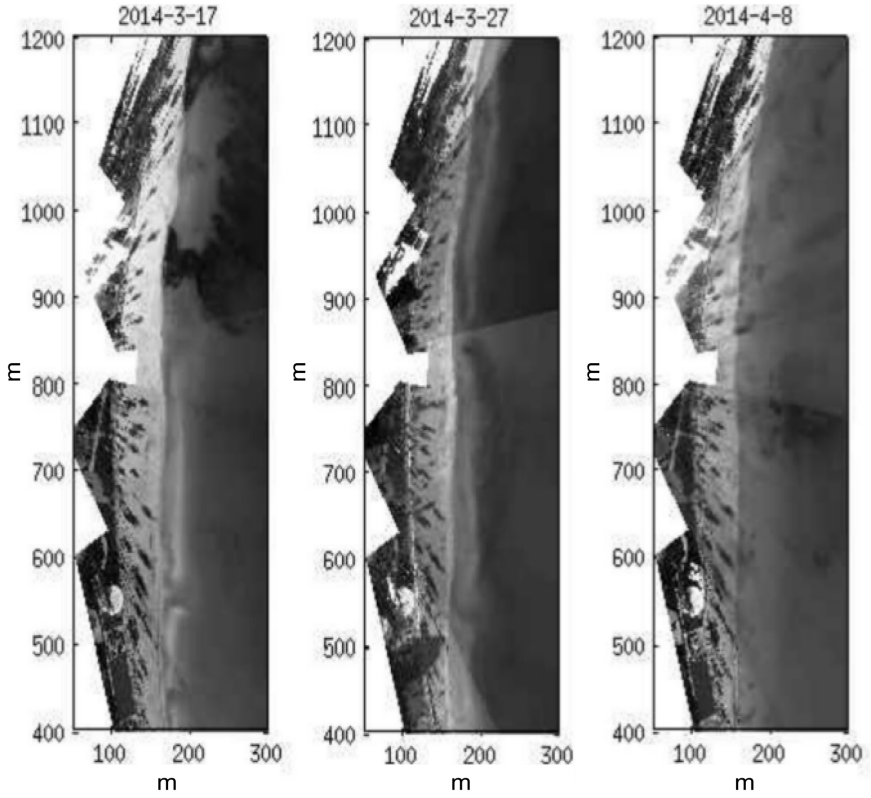

Figure 6.7 *Timex images with dates referred to in each image. Notice the intermediate configuration with a sinuous parallel bar along the coast (ca.* $180\,\mathrm{m}$*) for* 17 *and* 27 *March and the dissipative scenario without a bar for* 8 *April.*

seabed variation after the storm group (S1, S2 and S3, in Fig. 6.4, a) is presented in Fig. 6.8, a. This morphological change is obtained as the difference between the bathymetry

obtained with XBeach after storm S3 (8 April) and the initial bathymetry. The effect of consecutive storms is to mainly erode the aerial beach, mobilizing the sediment from the berm to depths of between $-1\,\mathrm{m}$ and $-5\,\mathrm{m}$, forming a bar (around $100\,\mathrm{m}$ from the shoreline, Fig. 6.8, a). The sediment mobilized to the bar is around $2.69\mathrm{x}10^4\ \mathrm{m}^3$ and comes from the aerial beach, where the volume loss is estimated as $3.01\mathrm{x}10^4\ \mathrm{m}^3$. This approximation of the sediment transport is calculated as the variation in depth at each spatial grid point between the initial bathymetry on 17 March and the simulated bathymetry for 8 April. All grid points are finally summed to obtain an approximated value of the sediment transport. The same methodology is applied to determine the sediment volume during the recovery period, but in this case the initial bathymetry is simulated by XBeach on 8 April and the final one is the one measured during 12 June. The redistribution can also be examined by analyzing the profile at the center of the beach using video images. Figure 6.9, a shows the beach profile change using video images from 19 March (the selection of 19 March is made since no images are available for the previous days) to 8 April (after S3).

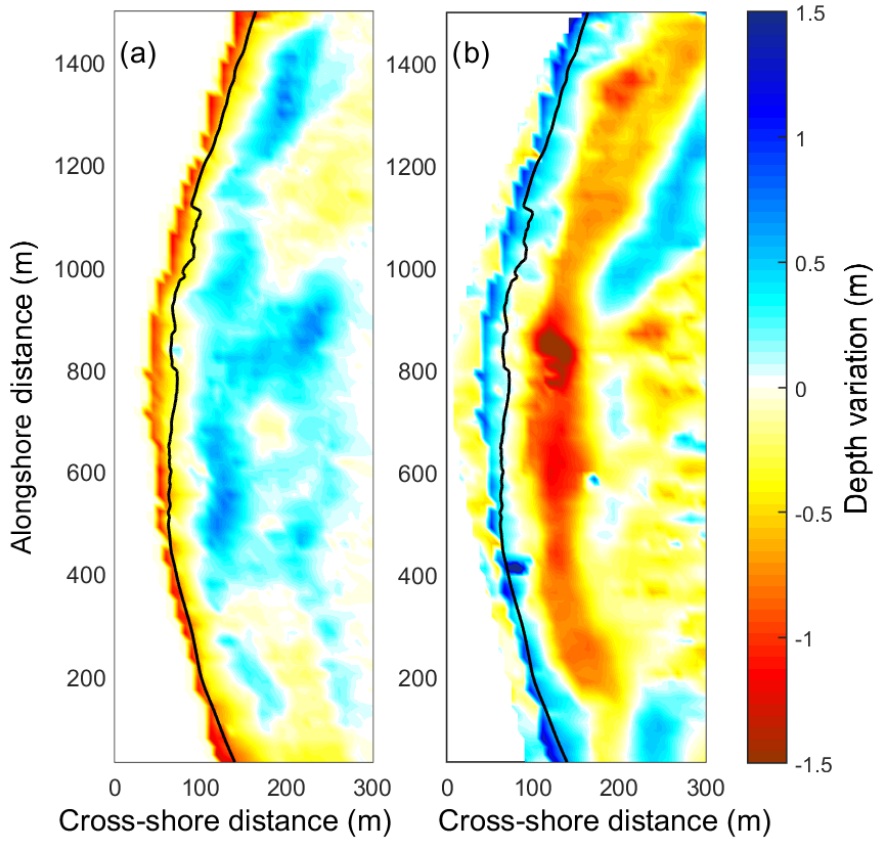

Figure 6.8 *Depth variation (in m) estimated from XBeach and from measurements. (a) Bottom variation (in m) during the storm group (17 March to 8 April). (b) Bottom variation (in m) for the period of calms (8 April to 12 June).*

We analyze the differences between the initial bathymetry (17 March 2014, preceding S1) and the bathymetries after storms S1, S2 and S3 (28 March, 1 and 8 April, respectively) obtained from XBeach. Figure 6.10 shows the differences, i.e., the impact of each of the storms. The first storm, S1, with moderate SWH and short duration, produces erosion at the beach face (volume loss of $1.18\mathrm{x}10^4\ \mathrm{m}^3$), accumulating large volumes of sand between $-1\,\mathrm{m}$ and $-2\,\mathrm{m}$ (not shown in Fig. 6.10). During the sec-

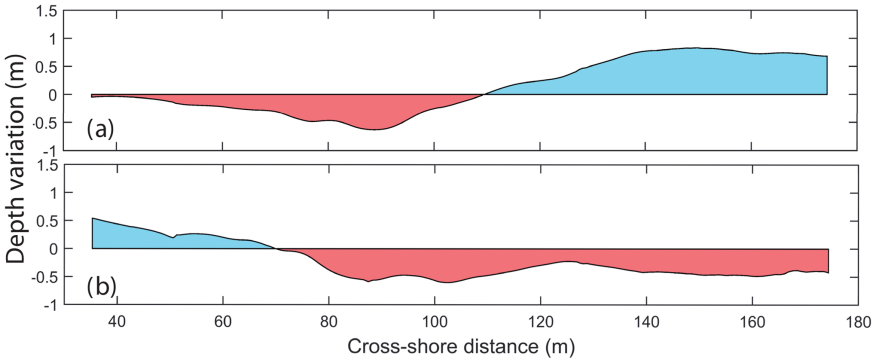

Figure 6.9 *Depth variation (in m) estimated from bathymetry inversion of the time stack during storm conditions; (a) between* 8 *April and* 20 *March (storm conditions); (b) between* 12 *June and* 8 *April (calm conditions).*

ond storm, S2, which is the most energetic, the beach face suffers a new episode of intense erosion, with depth variations between $1\,\mathrm{m}$ and $1.5\,\mathrm{m}$ and movement of the bar offshore (Fig. 6.10, b). The gain in volume in the bar zone is around $1.51\mathrm{x}10^4\ \mathrm{m}^3$. Finally, the third storm (S3), with moderate wave heights but with long duration, continues eroding the aerial beach with little change in the submerged beach (Fig. 6.10, c). This indicates that a sequence of storms does not necessarily result in cumulative erosion, supporting previous findings by Birkemeier (1999) and Coco et al. (2014). The eroded sediment that is transported offshore but not lost has the capacity to modify the cross-shore morphology and promote the wave attenuation contributing to the sediment transport feedback.

The three-dimensional beach response to three successive storms highlights the importance of the storm duration in the sedimentary budget. This has been recently addressed in different studies (De Alegria-Arzaburu and Masselink, 2010; Vousdoukas et al., 2012; Coco et al., 2014; Senechal et al., 2015) and particularly for the Mediterranean by Jiménez et al. (2008). This scenario fits with the usual "storm–post storm" behavior model (Stive et al., 2002; Archetti et al., 2016) and highlights the need for more research, especially in the physical description and numerical modeling, in order to improve our knowledge of the characterization of the temporal scales associated with the beach sedimentary budget. Here, we found evidence that recovery times, jointly with antecedent morphology, play a crucial role in shoreline and beach dynamics as stated by Senechal et al. (2015) or Jara et al. (2015).

After the S3 storm the beach experienced relatively calm conditions. A new bathymetry was performed on 12 June 2014, allowing us to address the behavior of the beach during this period. Figure 6.8, b shows the differences between the bathymetry on 12 June and the post-storm bathymetry obtained with numerical modeling for 8 April 2014. As can be seen, 2 months after the storm group, there is an opposite scenario. The sand reservoir below feeds up the shoreface again but also redistributes sediment along the beach at different depths. The sand volume recovered at the aerial beach during this period is $1.58\mathrm{x}10^4\ \mathrm{m}^3$, which is half of the volume lost during the storm period. This behavior is confirmed from the analysis of the beach cross-shore profile obtained from the time-stack video image. Fig. 6.9, b shows the difference between the summer profile (12 June 2014) and the beach profile after S3 (8 April 2014), supporting a recovery of the upper part of the beach.

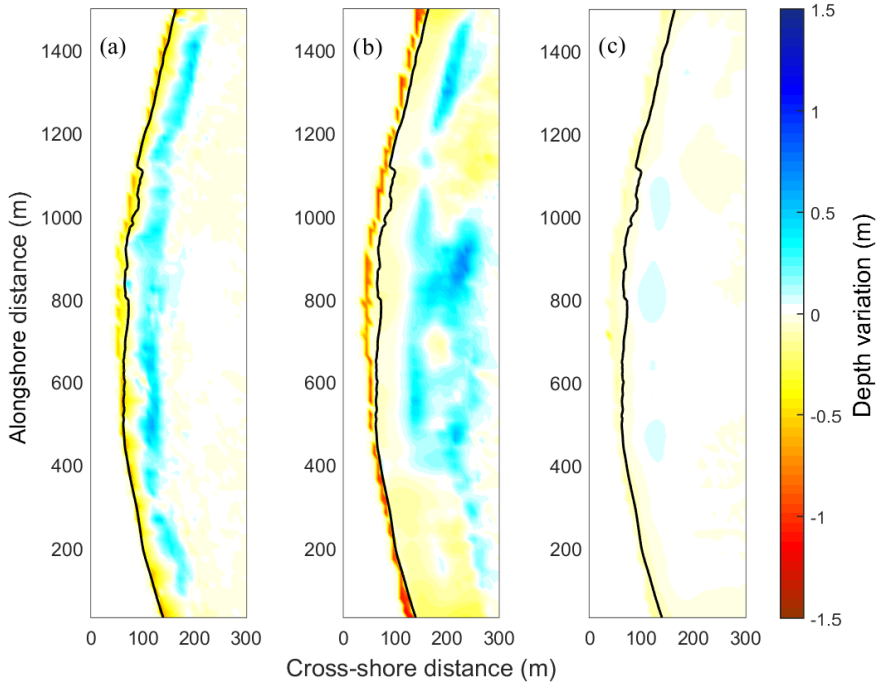

Figure 6.10 *Depth variation (in m) estimated from XBeach and from measurements. (a) Bottom variation (in m) between* 17 *and* 28 *March (storm S1). (b) Depth variation (in m) between* 28 *March and* 1 *April (storm S2). (c) Depth variation (in m) between* 1 *and* 8 *April (storm S3).*

The proposed approach aims to be a tool to assist in beach management, especially during adverse conditions when field surveys are not possible. The combination of numerical models, video monitoring and in situ data provides alternatives for the lack of data, especially during adverse conditions. This approach follows the change in the paradigm in ocean studies in which multiplatform approaches are being developed across the globe in order to fill spatial and temporal gaps in the measured time series.

On the studied beach, the results show that the beach is able to recover the lost sediment on a larger scale than the erosion and that it is crucial to know the beach configuration at any time in order to know its evolution in front-specific wave climate episodes.

6.5 Conclusions

The response of a low-energy microtidal beach in front of storm groups on timescales related to processes of beach erosion and accretion is studied. For this purpose, different techniques and approaches including DGPS–RTK and bathymetry surveys, modeling, and video monitoring are combined. The observations confirm that the previous morphological conditions are crucial for controlling the sediment exchange and the morphological response of the beach.

Focusing on the effect of individual storms, the first storm mobilizes sand mostly from the aerial area, generating a parallel bar at depths of $\sim 1\,\mathrm{m}$ and modifying the beach profile from near reflective to more dissipative. The effect of S2, lasting for more than $30\,\mathrm{h}$, is to mobilize a large volume of sediment, redistributing the profile along the whole beach and generating a large submerged sandbar at depths of $\sim -2.5\,\mathrm{m}$ ($\sim$

$100\,\mathrm{m}$ from the shoreline). This profile is very efficient in protecting the beach from the third storm, which has a duration of $48\,\mathrm{h}$, with the sediment mobilized during this event being almost negligible. The largest changes in sediment mobilization occur in the transition from the reflective to the dissipative states, when the beach adjusts its profile to the incoming wave conditions. The combined effects of this storm group confirm that in low-energy systems such as the one analyzed here, it is necessary to know the previous morphological state in order to properly assess the new beach conditions.

Results highlight the different well-known temporal scales for erosion and accretion in low-energy systems. While offshore sand migration is produced at storm timescales, the onshore sediment transport has a much slower characteristic timescale. In particular, a group of relatively energetic storms has the capacity to generate significant erosion in 3 days. Despite the moderate conditions and the lack of storms during the next 2 months, only half of the sediment is recovered. In this study the recovery of the beach is not documented, either in sediment mass balance or in shoreline width. Nevertheless, from Fig. 6.2, a, it can be seen that the aerial beach remains relatively stable and the beach width slightly increases at the end of 2014. Then in December 2014 and early January 2015, a new set of storm group events affect the beach, and since then the beach shoreline width has not recovered to former conditions, despite some advance in shoreline position.

Time recovery after storms is a key issue for local beach managers who are pressed by tourism stakeholders to nourish the beach after energetic processes in order to reach the quality standards required by beach users. The combined use of remote-sensing data, in situ observations and numerical models should already be integrated into management tools to make short-term decisions, such as those concerning beach nourishment, based on reliable physical data.

Chapter 7

Conclusions

This Thesis dealt with the analysis, at several scales, of wind waves variability. First, we analyzed the extreme wave climate in the Mediterranean Sea and the North Atlantic Ocean. The analysis was based on a 3-hour wave hindcast of 31 years, from 1979 to 2009. This hindcast was performed forcing a wave averaging model with NCEP-CFSR wind reanalysis. From these data, we computed the monthly extreme waves (99-th percentile) and their interannual variability was assessed. At the regional scale, the 6 hour wind and wave field in the Mediterranean Sea using ERA-Interim reanalysis from 1993 to 2018 was assessed. A novel approach was presented to compute the Ekman and Stokes velocity components that allowed us to study the importance of the ageostrophic dynamics at the different sub-basins under both Eulerian and Lagrangian standpoint. At the coastal scale, we studied the effect of a group of storms in the bathymetric evolution of a beach. We performed hourly simulations during 22 days of the wave climate arriving to the beach obtaining the wave induced bottom sediment transport and the consequent bottom variation.

In Chapter 3, we presented a new methodology in order to study the extreme wave climate and the atmospheric synoptic conditions responsible for this extreme wave in the North Atlantic Ocean and in the Mediterranean Sea. We obtained wind and pressure patterns computing the composites corresponding to the monthly values of the 99^{th} percentile of the significant wave height. We found that the extreme wave climate has a large seasonal signal in both, the North Atlantic Ocean and the Mediterranean Sea, although in the latter we observed different degrees of seasonality depending on the main mesoscale meteorological features of the locations analyzed, being higher in the central Mediterranean and lower in the Alboran and Ligurian sub-basins. The long-term trend of extreme waves is predominantly negative, although there are some areas, such as in the central North Atlantic Ocean and in the Aegean Sea, where we obtained a positive trend. In addition, the interannual variability of extreme wave climate has been analyzed using empirical orthogonal functions, which have been correlated against the four main climate indices of variability in the area, i.e., NAO, EA, EA/WR and SCAND. For the winter season (DJFM), the North Atlantic Oscillation and the Scandinavian modes are the dominant large-scale atmospheric patterns that control the interannual variability of extreme waves in the North Atlantic Ocean; to a lesser extent, the East Atlantic Oscillation also modulates extreme waves in the central part of the basin. In the Mediterranean Sea, the dominant modes explaining the variability of extreme waves during winter season are the East Atlantic and East Atlantic/Western Russia modes which act strongly during their negative phases. Since the periodicity of the large scale climatic modes of variability are a widely studied topic, the results of this work can

be used to prognostic severe waves conditions in the Atlantic and Mediterranean basin. This knowledge is crucial to manage maritime routes and to anticipate the mitigation strategies for reducing the coastal hazards resulting from extreme waves.

In Chapter 4, at regional scale, the effect of Ekman currents and wave-induced Stokes drift on the total kinetic energy at the upper layer of Mediterranean Sea was analyzed. We included the interaction between Ekman currents and Stokes drift with the geostrophic velocity in the momentum equation. The regional relevance of each velocity component was evaluated through a SOM decomposition, and their variability through wavelet analysis. We obtained that the Mediterranean basin can be classified in 6 different regions according to their similarity regarding the dynamical behavior measured by the total kinetic energy. We found that the effects of wind and waves are more prominent in the northwestern Mediterranean (where there is large fetch, allowing the development of large swells), while the southwestern and eastern basins are mainly dominated by geostrophy. There are two regions where the geostrophy modulates the total kinetic energy related with the main Mediterranean gyres and the Algerian current. These regions present a positive trend of the geostrophic velocity module of 0.14 $\pm 2.15\ 10^{-5}\ \mathrm{cm/s}$ per year during the 25 analyzed years, with stronger increments during 1993-2002. The trend in the total velocity module for the whole Mediterranean Sea is slightly lower, with a value of $0.058 \pm 1.43\ 10^{-5}\ \mathrm{cm/s}$ per year. Ekman currents contribute to the short-term variability (seasonal, semi-seasonal and smaller time scales) of the surface circulation in the whole Mediterranean Sea, especially during winter when the Ekman component occasionally exceeds geostrophy due to strong regional winds. The total kinetic energy was mainly characterized with a characteristic period at 5-6 years strongly related to the EA mode of variability. These results can be relevant to understand the regional interactions between physical and biogeochemical processes occurring at the upper layers of the Mediterranean Sea. Since the proposed method was based on observations, operational applications, such as search and rescue operations and predicting, mitigating the spread of oil spill or other pollutants at the ocean surface can be directly implemented from the presented results.

In Chapter 5, we analyzed the horizontal mixing and transport properties at the upper layer of the Mediterranean Sea associated with the wind and waves generated fluid particle motions. We found that the ageostrophic component not only can drastically modify the mesoscale LCS, but also the direction of the tracer spreading and the retention capacity of geostrophic eddies. The main hot spots of horizontal mixing in the Mediterranean Sea were associated with the major mesoscale features, such as inside the main mesoscale gyres (e.g. in the Alboran and Crete gyres) and other mesoscale features active (e.g. the Algerian and Northern boundary currents). Wind and wave induced mixing was significant in the northwestern basin and the south of Crete with a contribution up to 40%, but also showing a suppressing effect of mixing activity in the north part of the Algerian basin and Sicily. Regarding the seasonal cycle of the horizontal mixing, the whole Mediterranean Sea exhibited minimum values in summer time, while maximum mixing activity occurred in different months depending on the region. The wind and waves induced mixing was also reflected in the seasonal variation of the ageostrophic contribution, clearly appreciated in the western basin and in the Aegean Sea during the periods of mistral, tramontane and etesian winds intensification. We found important interannual variations (positive trends) in the mixing activity, being smoother when we considered the ageostrophic induced mixing. This trend could have significant consequences in the transport of essential oceanic variables, such as

heat, carbon, etc., with climatic implications. We obtained that the exponential regime (associated with chaotic advection) dominated at small-scales in whole Mediterranean Sea, followed by a Richardson-like dispersion regime at large scale, except for the south of Ionian and the Aegean Sea, which were characterized by a shear turbulent diffusion due to separation of particles by uncorrelated currents. In addition, we found a higher contribution of the zonal flow to the dispersion and mixing properties in the Mediterranean basin, except for the surroundings of the Gulf of Lion and Sicily, which were characterized by a higher meridional dispersion. In general, the ageostrophic component induced an increase of the meridional mixing, likely due to the north-south wind and wave intensification. This work disclosed that there is a need for an improved drifter database covering the whole Mediterranean Sea to obtain robust results on the Lagrangian dispersion properties. Future work is devoted to analyze the impact of wind and wave on the connectivity patterns between different sub-basins. These results can be used to further understand the spatial distribution and dynamics of any transported passive particle or organism (including fish larvae, jellyfish, etc.), to eventually provide the tools to mitigate hazardous effects on ecosystems.

Evolution of sandy coasts at temporal scales (from minutes to years) has been a topic of wide interest over the past decades since sandy beaches and dune systems are the first natural lines of coastal defense against flooding and erosion hazards. In Chapter 6, we presented a multi-platform approach combining remote, *in situ* data and numerical techniques to analyze the morphodynamical response of sandy beaches to extreme waves impact. Analyzing a concatenated group of storms, we found that (i) the time scale for the eroding processes is of hours (storm scale), while the time scale for the accretion processes is of months, and (ii) the morphological evolution of the beach depends, not only on the incoming waves, but also on its history. We analyzed the response of a beach during three different storm configurations. The first one, with moderate conditions, eroded the aerial beach and generated a submerged sandbar in the breaking zone. The bar was further directed offshore during the more energetic second event. The third storm, similar to the first one, hardly affected the beach morphology, which stresses the importance of the beach configuration previous to a storm. During the following 2 months, characterized by mild wave conditions, the aerial beach recovered half of the volume of lost sand. Results indicated the different time scales of sandy systems for the erosion and accretion periods associated to storms and mild conditions respectively. Thus, the proposed multi-platform can be an effective tool to make short-term decisions for beach management, knowing that the beach can be recovered after storms without carrying out any external action.

Bibliography

Abascal, A. J., Castanedo, S., Mendez, F. J., Medina, R., and Losada, I. J. (2009). Calibration of a Lagrangian transport model using drifting buoys deployed during the Prestige oil spill. *Journal of Coastal Research*, 25(1 (251)):80–90.

Alvarez-Ellacuria, A., Orfila, A., Gómez-Pujol, L., Simarro, G., and Obregon, N. (2011). Decoupling spatial and temporal patterns in short-term beach shoreline response to wave climate. *Geomorphology*, 128(3-4):199–208.

Amante, C. and Eakins, B. (2009). ETOPO1 Arc-minute Global Relief Model: procedures, data sources and analysis. NOAA Technical Memorandum NESDIS NGDC-24. *National Geophysical Data Center, NOAA*, 10:V5C8276M.

Archetti, R., Paci, A., Carniel, S., and Bonaldo, D. (2016). Optimal index related to the shoreline dynamics during a storm: the case of Jesolo beach. *Natural Hazards and Earth System Sciences*, 16(5).

Ardhuin, F., Aksenov, Y., Benetazzo, A., Bertino, L., Brandt, P., Caubet, E., Chapron, B., Collard, F., Cravatte, S., Delouis, J.-M., Dias, F., Dibarboure, G., Gaultier, L., Johannessen, J., Korosov, A., Manucharyan, G., Menemenlis, D., Menendez, M., Monnier, G., Mouche, A., Nouguier, F., Nurser, G., Rampal, P., Reniers, A., Rodriguez, E., Stopa, J., Tison, C., Ubelmann, C., Van Sebille, E., and Xie, J. (2018). Measuring currents, ice drift, and waves from space: the Sea surface KInematics Multiscale monitoring (SKIM) concept. *Ocean Science*, 14(3):337–354.

Ardhuin, F., Marié, L., Rascle, N., Forget, P., and Roland, A. (2009). Observation and estimation of Lagrangian, Stokes, and Eulerian currents induced by wind and waves at the sea surface. *Journal of Physical Oceanography*, 39(11):2820–2838.

Ardhuin, F. and Orfila, A. (2018). Wind waves. *New Frontiers in Operational Oceanography*, pages 393–422.

Ardhuin, F., Rogers, E., Babanin, A. V., Filipot, J.-F., Magne, R., Roland, A., Van Der Westhuysen, A., Queffeulou, P., Lefevre, J.-M., Aouf, L., and Collard, F. (2010). Semiempirical dissipation source functions for ocean waves. Part I: Definition, calibration, and validation. *Journal of Physical Oceanography*, 40(9):1917–1941.

Ariza, E. (2011). An analysis of beach management framework in Spain. Study case: the Catalonian coast. *Journal of Coastal Conservation*, 15(4):445–455.

Artale, V., Boffetta, G., Celani, A., Cencini, M., and Vulpiani, A. (1997). Dispersion of passive tracers in closed basins: Beyond the diffusion coefficient. *Physics of Fluids*, 9(11):3162–3171.

Aurell, E., Boffetta, G., Crisanti, A., Paladin, G., and Vulpiani, A. (1997). Predictability in the large: an extension of the concept of Lyapunov exponent. *Journal of Physics A: Mathematical and General*, 30(1):1.

Ayata, S.-D., Irisson, J.-O., Aubert, A., Berline, L., Dutay, J.-C., Mayot, N., Nieblas, A.-E., d'Ortenzio, F., Palmiéri, J., Reygondeau, G., Rossi, V., and Guineu, C. (2018). Regionalisation of the Mediterranean basin, a MERMEX synthesis. *Progress in Oceanography*, 163:7–20.

Babanin, A. (2006). On a wave-induced turbulence and a wave-mixed upper ocean layer. *Geophysical Research Letters*, 33(20).

Babanin, A. (2011). *Breaking and dissipation of ocean surface waves*. Cambridge University Press.

Babanin, A. V., Ganopolski, A., and Phillips, W. R. (2009). Wave-induced upper-ocean mixing in a climate model of intermediate complexity. *Ocean Modelling*, 29(3):189–197.

Barnston, A. G. and Livezey, R. E. (1987). Classification, seasonality and persistence of low-frequency atmospheric circulation patterns. *Monthly Weather Review*, 115(6):1083–1126.

Berrisford, P., Dee, D., Poli, P., Brugge, R., Fielding, K., Fuentes, M., Kallberg, P., Kobayashi, S., Uppala, S., and Simmons, A. (2011). The ERA-Interim archive, version 2.0. Technical report, ECMWF.

Bettencourt, J. H., López, C., Hernández-García, E., Montes, I., Sudre, J., Dewitte, B., Paulmier, A., and Garçon, V. (2015). Boundaries of the Peruvian oxygen minimum zone shaped by coherent mesoscale dynamics. *Nature Geoscience*, 8(12):937–940.

Birkemeier, W. A. (1999). Storms, storm groups and nearshore morphologic change. *Proc. Coastal Sed. 99*, pages 1109–1122.

Birkemeier, W. A. and WA, B. (1979). The effects of the 19 December 1977 coastal storm on beaches in North Carolina and New Jersey. *Shore and Beach*, 47:7–15.

Blott, S. J. and Pye, K. (2001). GRADISTAT: a grain size distribution and statistics package for the analysis of unconsolidated sediments. *Earth surface processes and Landforms*, 26(11):1237–1248.

Boffetta, G., Celani, A., and Vergassola, M. (2000). Inverse energy cascade in two-dimensional turbulence: Deviations from Gaussian behavior. *Physical Review E*, 61(1):R29.

Boffetta, G., Lacorata, G., Redaelli, G., and Vulpiani, A. (2001). Detecting barriers to transport: a review of different techniques. *Physica D: Nonlinear Phenomena*, 159(1-2):58–70.

Bosello, F., Nicholls, R. J., Richards, J., Roson, R., and Tol, R. S. (2012). Economic impacts of climate change in Europe: sea-level rise. *Climatic change*, 112(1):63–81.

Bourassa, M. A., Meissner, T., Cerovecki, I., Chang, P., Dong, X., De Chiara, G., Donlon, C., Dukhovskoy, D., Elya, J., Fore, A., et al. (2019). Remotely sensed winds and wind stresses for marine forecasting and ocean modeling. *Frontiers in Marine Science*, 6:443.

Bouzaiene, M., Menna, M., Poulain, P.-M., Bussani, A., and Elhmaidi, D. (2020). Analysis of the surface dispersion in the Mediterranean sub-basins. *Frontiers in Marine Science*.

Breivik, Ø., Bidlot, J.-R., and Janssen, P. A. (2016). A Stokes drift approximation based on the Phillips spectrum. *Ocean Modelling*, 100:49–56.

Bronselaer, B. and Zanna, L. (2020). Heat and carbon coupling reveals ocean warming due to circulation changes. *Nature*, 584(7820):227–233.

Buesseler, K. O. (1998). The decoupling of production and particulate export in the surface ocean. *Global Biogeochemical Cycles*, 12(2):297–310.

Cacho, I., Grimalt, J. O., Sierro, F. J., Shackleton, N., and Canals, M. (2000). Evidence for enhanced Mediterranean thermohaline circulation during rapid climatic coolings. *Earth and Planetary Science Letters*, 183(3-4):417–429.

Caires, S., Swail, V. R., and Wang, X. L. (2006). Projection and analysis of extreme wave climate. *Journal of Climate*, 19(21):5581–5605.

Callaghan, D. P. and Roshanka, R. (2009). Quantifying the storm erosion hazard for coastal planning. *Coastal Engineering*, 56(1):90–93.

Castelle, B., Dodet, G., Masselink, G., and Scott, T. (2018). Increased winter-mean wave height, variability, and periodicity in the Northeast Atlantic over 1949–2017. *Geophysical Research Letters*, 45(8):3586–3596.

Chawla, A., Spindler, D., and Tolman, H. (2012). 30 Year Wave Hindcasts using WAVEWATCH III with CFSR winds-Phase I. MMAB Contribution No. 302: NCEP/NOAA, 12p., College Park, MD, United States of America.

Chawla, A., Spindler, D., and Tolman, H. L. (2011). A thirty year wave hindcast using the latest NCEP Climate Forecast System Reanalysis winds. In *Proc. 12th Int. Workshop on Wave Hindcasting and Forecasting*.

Chawla, A., Spindler, D. M., and Tolman, H. L. (2013). Validation of a thirty year wave hindcast using the Climate Forecast System Reanalysis winds. *Ocean Modelling*, 70:189–206.

Chelliah, M. and Bell, G. D. (2004). Tropical multidecadal and interannual climate variability in the NCEP–NCAR reanalysis. *Journal of Climate*, 17(9):1777–1803.

Ciavola, P. and Stive, M. (2012). Thresholds for storm impacts along European coastlines: Introduction. *Geomorphology*, 143:1–2.

Coco, G., Senechal, N., Rejas, A., Bryan, K. R., Capo, S., Parisot, J., Brown, J. A., and MacMahan, J. H. (2014). Beach response to a sequence of extreme storms. *Geomorphology*, 204:493–501.

Corrado, R., Lacorata, G., Palatella, L., Santoleri, R., and Zambianchi, E. (2017). General characteristics of relative dispersion in the ocean. *Scientific Reports*, 7(1):1–11.

Covey, C. and Barron, E. (1988). The role of ocean heat transport in climatic change. *Earth-Science Reviews*, 24(6):429–445.

Daubechies, I. (1990). The wavelet transform, time-frequency localization and signal analysis. *IEEE transactions on information theory*, 36(5):961–1005.

Davis, R. E. (1985). Drifter observations of coastal surface currents during CODE: The method and descriptive view. *Journal of Geophysical Research: Oceans*, 90(C3):4741–4755.

De Alegria-Arzaburu, A. R. and Masselink, G. (2010). Storm response and beach rotation on a gravel beach, Slapton Sands, UK. *Marine Geology*, 278(1-4):77–99.

Dee, D. P., Uppala, S. M., Simmons, A., Berrisford, P., Poli, P., Kobayashi, S., Andrae, U., Balmaseda, M., Balsamo, G., Bauer, d. P., et al. (2011). The ERA-Interim reanalysis: Configuration and performance of the data assimilation system. *Quarterly Journal of the royal meteorological society*, 137(656):553–597.

Dibarboure, G., Lauret, O., Mertz, F., Rosmorduc, V., and Maheu, C. (2008). SSALTO/DUACS user handbook:(M) SLA and (M) ADT near-real time and delayed time products. *Rep. CLS-DOS-NT*, 6:39.

Dobler, D., Huck, T., Maes, C., Grima, N., Blanke, B., Martinez, E., and Ardhuin, F. (2019). Large impact of Stokes drift on the fate of surface floating debris in the South Indian Basin. *Marine pollution bulletin*, 148:202–209.

d'Ortenzio, F. and d'Alcalà, M. R. (2009). On the trophic regimes of the Mediterranean Sea: a satellite analysis. *Biogeosciences*, 6(2).

d'Ovidio, F., Fernández, V., Hernández-García, E., and López, C. (2004). Mixing structures in the Mediterranean Sea from finite-size Lyapunov exponents. *Geophysical Research Letters*, 31(17).

Dubois, M., Rossi, V., Ser-Giacomi, E., Arnaud-Haond, S., López, C., and Hernández-García, E. (2016). Linking basin-scale connectivity, oceanography and population dynamics for the conservation and management of marine ecosystems. *Global Ecology and Biogeography*, 25(5):503–515.

Eichentopf, S., Karunarathna, H., and Alsina, J. M. (2019). Morphodynamics of sandy beaches under the influence of storm sequences: Current research status and future needs. *Water Science and Engineering*, 12(3):221–234.

Eichentopf, S., Van der Zanden, J., Cáceres, I., Baldock, T. E., and Alsina, J. M. (2020). Influence of storm sequencing on breaker bar and shoreline evolution in large-scale experiments. *Coastal Engineering*, 157:103659.

Ekman, V. W. (1905). On the influence of the Earth's rotation on ocean-currents. *Arkiv for Matematik, Astronomi, och Fysik*, 2(11):1–53.

Enríquez, A. R., Marcos, M., Álvarez-Ellacuría, A., Orfila, A., and Gomis, D. (2017). Changes in beach shoreline due to sea level rise and waves under climate change scenarios: application to the Balearic Islands (western Mediterranean). *Natural Hazards and Earth System Sciences*, 17(7):1075–1089.

Espa, S., Lacorata, G., and Di Nitto, G. (2014). Anisotropic Lagrangian dispersion in rotating flows with a β effect. *Journal of physical oceanography*, 44(2):632–643.

Faltinsen, D. (1990). Wave loads on offshore structures. *Annual Review of Fluid Mechanics;(USA)*, 22.

Ferreira, Ó. (2005). Storm groups versus extreme single storms: predicted erosion and management consequences. *Journal of Coastal Research*, pages 221–227.

Ferreira, Ó., Viavattene, C., Jiménez, J., Bolle, A., Das Neves, L., Plomaritis, T., McCall, R., and Van Dongeren, A. (2018). Storm-induced risk assessment: Evaluation of two tools at the regional and hotspot scale. *Coastal Engineering*, 134:241–253.

Folk, R. L. and Ward, W. C. (1957). Brazos River bar [Texas]; a study in the significance of grain size parameters. *Journal of Sedimentary Research*, 27(1):3–26.

Fraser, C. I., Morrison, A. K., Hogg, A. M., Macaya, E. C., van Sebille, E., Ryan, P. G., Padovan, A., Jack, C., Valdivia, N., and Waters, J. M. (2018). Antarctica's ecological isolation will be broken by storm-driven dispersal and warming. *Nature climate change*, 8(8):704–708.

Frazer, L. N., Anderson, T. R., and Fletcher, C. H. (2009). Modeling storms improves estimates of long-term shoreline change. *Geophysical Research Letters*, 36(20).

Frisch, U. and Kolmogorov, A. N. (1995). *Turbulence: the legacy of AN Kolmogorov*. Cambridge University Press.

Futch, V. C. and Allen, A. (2019). Search and rescue applications: on the need to improve ocean observing data systems in offshore or remote locations. *Frontiers in Marine Science*, 6:301.

Gallagher, S., Gleeson, E., Tiron, R., McGrath, R., and Dias, F. (2016). Twenty-first century wave climate projections for Ireland and surface winds in the North Atlantic Ocean. *Advances in Science and Research*, 13:75–80.

Gallagher, S., Tiron, R., and Dias, F. (2014). A long-term nearshore wave hindcast for Ireland: Atlantic and Irish Sea coasts (1979–2012). *Ocean Dynamics*, 64(8):1163–1180.

Gleeson, E., Clancy, C., Zubiate, L., Janjić, J., Gallagher, S., and Dias, F. (2019). Teleconnections and Extreme Ocean States in the Northeast Atlantic Ocean. *Advances in Science and Research*, 16:11–29.

Gleeson, E., Gallagher, S., Clancy, C., and Dias, F. (2017). NAO and extreme ocean states in the Northeast Atlantic Ocean. *Advances in Science and Research*, 14:23–33.

Gómez-Pujol, L., Orfila, A., Álvarez-Ellacuría, A., Terrados, J., and Tintoré, J. (2013). *Posidonia oceanica* beach-cast litter in Mediterranean beaches: a coastal videomonitoring study. *Journal of Coastal Research*, 65:1768–1773.

Gómez-Pujol, L., Orfila, A., Álvarez-Ellacuría, A., and Tintoré, J. (2011). Controls on sediment dynamics and medium-term morphological change in a barred microtidal beach (Cala Millor, Mallorca, Western Mediterranean). *Geomorphology*, 132(3-4):87–98.

Grinsted, A., Moore, J. C., and Jevrejeva, S. (2004). Application of the cross wavelet transform and wavelet coherence to geophysical time series. *Nonlinear Processes Geophysics*, 11:561–566.

Group, T. W. (1988). The WAM model—A third generation ocean wave prediction model. *Journal of Physical Oceanography*, 18(12):1775–1810.

Hallegatte, S., Green, C., Nicholls, R. J., and Corfee-Morlot, J. (2013). Future flood losses in major coastal cities. *Nature climate change*, 3(9):802–806.

Haller, G. (2001). Lagrangian structures and the rate of strain in a partition of two-dimensional turbulence. *Physics of Fluids*, 13(11):3365–3385.

Haller, G. (2015). Lagrangian coherent structures. *Annual Review of Fluid Mechanics*, 47:137–162.

Haller, G. and Yuan, G. (2000). Lagrangian coherent structures and mixing in two-dimensional turbulence. *Physica D: Nonlinear Phenomena*, 147(3-4):352–370.

Hallermeier, R. J. (1981). Terminal settling velocity of commonly occurring sand grains. *Sedimentology*, 28(6):859–865.

Hansen, D. V. and Poulain, P.-M. (1996). Quality control and interpolations of WOCE-TOGA drifter data. *Journal of Atmospheric and Oceanic Technology*, 13(4):900–909.

Hasselmann, K., Barnett, T. P., Bouws, E., Carlson, H., Cartwright, D. E., Enke, K., Ewing, J., Gienapp, H., Hasselmann, D., Kruseman, P., et al. (1973). Measurements of wind-wave growth and swell decay during the Joint North Sea Wave Project (JONSWAP). *Ergänzungsheft 8-12*.

Haza, A. C., Poje, A. C., Özgökmen, T. M., and Martin, P. (2008). Relative dispersion from a high-resolution coastal model of the Adriatic Sea. *Ocean Modelling*, 22(1-2):48–65.

Herbers, T. and Burton, M. (1997). Nonlinear shoaling of directionally spread waves on a beach. *Journal of Geophysical Research: Oceans*, 102(C9):21101–21114.

Hernández-Carrasco, I., Alou-Font, E., Dumont, P.-A., Cabornero, A., Allen, J., and Orfila, A. (2020). Lagrangian flow effects on phytoplankton abundance and composition along filament-like structures. *Progress in Oceanography*, 189:102469.

Hernández-Carrasco, I., López, C., Hernández-García, E., and Turiel, A. (2011). How reliable are finite-size Lyapunov exponents for the assessment of ocean dynamics? *Ocean Modelling*, 36(3-4):208–218.

Hernández-Carrasco, I., López, C., Hernández-García, E., and Turiel, A. (2012). Seasonal and regional characterization of horizontal stirring in the global ocean. *Journal of Geophysical Research: Oceans*, 117(C10).

Hernández-Carrasco, I. and Orfila, A. (2018). The Role of an Intense Front on the Connectivity of the Western Mediterranean Sea: The Cartagena-Tenes Front. *Journal of Geophysical Research: Oceans*, 123(6):4398–4422.

Hernández-Carrasco, I., Orfila, A., Rossi, V., and Garçon, V. (2018). Effect of small scale transport processes on phytoplankton distribution in coastal seas. *Scientific reports*, 8(1):1–13.

Hernández-Carrasco, I., Rossi, V., Hernández-García, E., Garçon, V., and López, C. (2014). The reduction of plankton biomass induced by mesoscale stirring: A modeling study in the Benguela upwelling. *Deep Sea Research Part I: Oceanographic Research Papers*, 83:65–80.

Herrmann, M., Somot, S., Calmanti, S., Dubois, C., and Sevault, F. (2011). Representation of spatial and temporal variability of daily wind speed and of intense wind events over the Mediterranean Sea using dynamical downscaling: impact of the regional climate model configuration. *Natural Hazards and Earth System Sciences*, 11:1983–2001.

Holland, K. T., Holman, R. A., Lippmann, T. C., Stanley, J., and Plant, N. (1997). Practical use of video imagery in nearshore oceanographic field studies. *IEEE Journal of oceanic engineering*, 22(1):81–92.

Holthuijsen, L. (2007). Linear wave theory (oceanic waters). *Waves in oceanic and coastal waters*, pages 106–142.

Houser, C. (2013). Alongshore variation in the morphology of coastal dunes: Implications for storm response. *Geomorphology*, 199:48–61.

Huang, N. E. (1979). On surface drift currents in the ocean. *Journal of Fluid Mechanics*, 91(1):191–208.

Hui, Z. and Xu, Y. (2016). The impact of wave-induced Coriolis-Stokes forcing on satellite-derived ocean surface currents. *Journal of Geophysical Research: Oceans*, 121(1):410–426.

Hulme, M., Barrow, E. M., Arnell, N. W., Harrison, P. A., Johns, T. C., and Downing, T. E. (1999). Relative impacts of human-induced climate change and natural climate variability. *Nature*, 397(6721):688–691.

Hurrell, J. W. (1995). Decadal trends in the North Atlantic Oscillation: regional temperatures and precipitation. *Science*, 269(5224):676–679.

Hurrell, J. W., Kushnir, Y., Ottersen, G., and Visbeck, M. (2003). An overview of the North Atlantic Oscillation. *Geophysical Monograph-American Geophysical Union*, pages 1–35.

Infantes, E., Orfila, A., Simarro, G., Terrados, J., Luhar, M., and Nepf, H. (2012). Effect of a seagrass (*Posidonia oceanica*) meadow on wave propagation. *Marine Ecology Progress Series*, 456:63–72.

Infantes, E., Terrados, J., Orfila, A., Canellas, B., and Alvarez-Ellacuria, A. (2009). Wave energy and the upper depth limit distribution of *Posidonia oceanica*. *Botanica Marina*, 52(5):419–427.

Izaguirre, C., Méndez, F. J., Menendez, M., Luceño, A., and Losada, I. J. (2010). Extreme wave climate variability in southern Europe using satellite data. *Journal of Geophysical Research: Oceans*, 115(C4).

Izaguirre, C., Menéndez, M., Camus, P., Méndez, F. J., Mínguez, R., and Losada, I. J. (2012). Exploring the interannual variability of extreme wave climate in the Northeast Atlantic Ocean. *Ocean modelling*, 59:31–40.

Janssen, P. A. (2008). Progress in ocean wave forecasting. *Journal of Computational Physics*, 227(7):3572–3594.

Janssen, P. A., Hansen, B., and Bidlot, J.-R. (1997). Verification of the ECMWF wave forecasting system against buoy and altimeter data. *Weather and Forecasting*, 12(4):763–784.

Jara, M., González, M., and Medina, R. (2015). Beach memory related to cross-shore processes. In *The Proceedings of the Coastal Sediments 2015*. World Scientific.

Jiménez, J. A., Gracia, V., Valdemoro, H. I., Mendoza, E. T., and Sánchez-Arcilla, A. (2011). Managing erosion-induced problems in NW Mediterranean urban beaches. *Ocean and Coastal Management*, 54(12):907–918.

Jiménez, J. A., Guillén, J., and Falqués, A. (2008). Comment on the article "Morphodynamic classification of sandy beaches in low energetic marine environment" by Gómez-Pujol, L., Orfila, A., Cañellas, B., Alvarez-Ellacuria, A., Méndez, FJ, Medina, R. and Tintoré, J. Marine Geology, 242, pp. 235–246, 2007. *Marine Geology*, 255(1-2):96–101.

Jones, S. D., Le Quéré, C., Rödenbeck, C., Manning, A. C., and Olsen, A. (2015). A statistical gap-filling method to interpolate global monthly surface ocean carbon dioxide data. *Journal of Advances in Modeling Earth Systems*, 7(4):1554–1575.

Kai, E. T., Rossi, V., Sudre, J., Weimerskirch, H., Lopez, C., Hernandez-Garcia, E., Marsac, F., and Garçon, V. (2009). Top marine predators track Lagrangian coherent structures. *Proceedings of the National Academy of Sciences*, 106(20):8245–8250.

Kaihatu, J. M., Handler, R. A., Marmorino, G. O., and Shay, L. K. (1998). Empirical orthogonal function analysis of ocean surface currents using complex and real-vector methods. *Journal of atmospheric and oceanic technology*, 15(4):927–941.

Kaiser, G. (1994). A Friendly guide to wavelets: Basic wavelet analysis, physical wavelets. *Birkhauser*, page 300.

Kinsman, B. (1984). *Wind waves: their generation and propagation on the ocean surface*. Courier Corporation.

Koch, E. W., Ackerman, J. D., Verduin, J., and van Keulen, M. (2007). Fluid dynamics in seagrass ecology—from molecules to ecosystems. In *Seagrasses: biology, ecologyand conservation*, pages 193–225. Springer.

Kohonen, T. (1982). Self-organized formation of topologically correct feature maps. *Biological Cybernetics*, 43(1):59–69.

Lacorata, G., Aurell, E., and Vulpiani, A. (2001). Drifter dispersion in the Adriatic Sea: Lagrangian data and chaotic model. *Annales Geophysicae*, 19(1):121–129.

Lacorata, G., Corrado, R., Falcini, F., and Santoleri, R. (2019). FSLE analysis and validation of Lagrangian simulations based on satellite-derived GlobCurrent velocity data. *Remote sensing of environment*, 221:136–143.

Laplace, P. S. (1776). Suite des recherches sur plusieurs points du systeme du monde (XXV–XXVII). Mém. Présentés Acad. R. *Sci. Inst. France*, pages 542–552.

Large, W. G., McWilliams, J. C., and Doney, S. C. (1994). Oceanic vertical mixing: A review and a model with a nonlocal boundary layer parameterization. *Reviews of Geophysics*, 32(4):363–403.

LeBlond, P. H. and Mysak, L. A. (1981). *Waves in the Ocean*. Elsevier.

Legrand, T., Di Franco, A., Ser-Giacomi, E., Calo, A., and Rossi, V. (2019). A multidisciplinary analytical framework to delineate spawning areas and quantify larval dispersal in coastal fish. *Marine environmental research*, 151:104761.

Lehahn, Y., d'Ovidio, F., Lévy, M., and Heifetz, E. (2007). Stirring of the northeast Atlantic spring bloom: A Lagrangian analysis based on multisatellite data. *Journal of Geophysical Research: Oceans*, 112(C8).

Lévy, M., Franks, P. J., and Smith, K. S. (2018). The role of submesoscale currents in structuring marine ecosystems. *Nature communications*, 9(1):1–16.

Lewis, D. and Belcher, S. (2004). Time-dependent, coupled, Ekman boundary layer solutions incorporating Stokes drift. *Dynamics of atmospheres and oceans*, 37(4):313–351.

Lin, Y., Oey, L.-Y., and Orfila, A. (2019). Two 'faces' of ENSO-induced surface waves during the tropical cyclone season. *Progress in Oceanography*, 175:40 – 54.

Lionello, P., Cogo, S., Galati, M., and Sanna, A. (2008). The Mediterranean surface wave climate inferred from future scenario simulations. *Global and Planetary Change*, 63(2-3):152–162.

Lionello, P., Malanotte-Rizzoli, P., Boscolo, R., Alpert, P., Artale, V., Li, L., Luterbacher, J., May, W., Trigo, R., Tsimplis, M., et al. (2006). The Mediterranean climate: an overview of the main characteristics and issues.

Lionello, P. and Sanna, A. (2005). Mediterranean wave climate variability and its links with NAO and Indian Monsoon. *Climate Dynamics*, 25(6):611–623.

Liu, Y., Weisberg, R. H., and Mooers, C. N. (2006). Performance evaluation of the self-organizing map for feature extraction. *Journal of Geophysical Research: Oceans*, 111(C5).

Loureiro, C., Ferreira, Ó., and Cooper, J. A. G. (2012). Extreme erosion on high-energy embayed beaches: influence of megarips and storm grouping. *Geomorphology*, 139:155–171.

Luhar, M., Infantes, E., Orfila, A., Terrados, J., and Nepf, H. M. (2013). Field observations of wave-induced streaming through a submerged seagrass (*Posidonia oceanica*) meadow. *Journal of Geophysical Research: Oceans*, 118(4):1955–1968.

Luijendijk, A., Hagenaars, G., Ranasinghe, R., Baart, F., Donchyts, G., and Aarninkhof, S. (2018). The state of the world's beaches. *Scientific reports*, 8(1):1–11.

Malanotte-Rizzoli, P., Artale, V., Borzelli-Eusebi, G., Brenner, S., Crise, A., Gacic, M., Kress, N., Marullo, S., Ribera d'Alcalà, M., Sofianos, S., et al. (2014). Physical forcing and physical/biochemical variability of the Mediterranean Sea: a review of unresolved issues and directions for future research. *Ocean Science*, 10(3):281–322.

Mao, Y. and Heron, M. L. (2008). The influence of fetch on the response of surface currents to wind studied by HF ocean surface radar. *Journal of physical oceanography*, 38(5):1107–1121.

Marshall, J., Kushnir, Y., Battisti, D., Chang, P., Czaja, A., Dickson, R., Hurrell, J., McCartney, M., Saravanan, R., and Visbeck, M. (2001). North Atlantic climate variability: phenomena, impacts and mechanisms. *International Journal of Climatology*, 21(15):1863–1898.

Martínez-Asensio, A., Tsimplis, M. N., Marcos, M., Feng, X., Gomis, D., Jordà, G., and Josey, S. A. (2016). Response of the North Atlantic wave climate to atmospheric modes of variability. *International Journal of Climatology*, 36(3):1210–1225.

Massel, S. R. (2017). *Ocean surface waves: their physics and prediction*, volume 45. World scientific.

Masselink, G., Scott, T., Poate, T., Russell, P., Davidson, M., and Conley, D. (2016). The extreme 2013/2014 winter storms: hydrodynamic forcing and coastal response along the southwest coast of England. *Earth Surface Processes and Landforms*, 41(3):378–391.

Masselink, G. and van Heteren, S. (2014). Response of wave-dominated and mixed-energy barriers to storms. *Marine Geology*, 352:321–347.

Matteoda, A. M. and Glenn, S. M. (1996). Observations of recurrent mesoscale eddies in the eastern Mediterranean. *Journal of Geophysical Research: Oceans*, 101(C9):20687–20709.

McWilliams, J. C., Gula, J., Molemaker, M. J., Renault, L., and Shchepetkin, A. F. (2015). Filament frontogenesis by boundary layer turbulence. *Journal of Physical Oceanography*, 45(8):1988–2005.

McWilliams, J. C., Huckle, E., and Shchepetkin, A. F. (2009). Buoyancy effects in a stratified Ekman layer. *Journal of Physical Oceanography*, 39:2581–2599.

McWilliams, J. C. and Restrepo, J. M. (1999). The wave-driven ocean circulation. *Journal of Physical Oceanography*, 29(10):2523–2540.

McWilliams, J. C., Sullivan, P. P., and Moeng, C.-H. (1997). Langmuir turbulence in the ocean. *Journal of Fluid Mechanics*, 334:1–30.

Méndez, F. J., Menéndez, M., Luceño, A., and Losada, I. J. (2006). Estimation of the long-term variability of extreme significant wave height using a time-dependent peak over threshold (pot) model. *Journal of Geophysical Research: Oceans*, 111(C7).

Menéndez, M., Méndez, F. J., Izaguirre, C., Luceño, A., and Losada, I. J. (2009). The influence of seasonality on estimating return values of significant wave height. *Coastal Engineering*, 56(3):211–219.

Menéndez, M., Méndez, F. J., Losada, I. J., and Graham, N. E. (2008). Variability of extreme wave heights in the northeast Pacific Ocean based on buoy measurements. *Geophysical Research Letters*, 35(22).

Menna, M., Gerin, R., Bussani, A., and Poulain, P.-M. (2017). The OGS Mediterranean Drifter Dataset: 1986-2016. *Rel. OGS*, 92.

Millot, C. (2005). Circulation in the Mediterranean Sea: evidences, debates and unanswered questions. *Scientia marina*, 69(S1):5–21.

Morales-Márquez, V., Hernández-Carrasco, I., Simarro, G., Rossi, V., and Orfila, A. (2020a). Regionalizing the impacts of wind and wave-induced currents on surface ocean dynamics: a long-term variability analysis in the Mediterranean Sea. *Essoar*.

Morales-Márquez, V., Orfila, A., Simarro, G., Gómez-Pujol, L., Álvarez-Ellacuría, A., Conti, D., Osorio, A., and Marcos, M. (2018). Numerical and remote techniques for operational beach management under storm group forcing. *Natural Hazards and Earth System Sciences*.

Morales-Márquez, V., Orfila, A., Simarro, G., and Marcos, M. (2020b). Extreme waves and climatic patterns of variability in the Eastern North Atlantic and Mediterranean basins. *Ocean Science*, 16:1385—-1398.

Munk, W. H. (1950). On the wind-driven ocean circulation. *Journal of meteorology*, 7(2):80–93.

Nieblas, A.-E., Drushka, K., Reygondeau, G., Rossi, V., Demarcq, H., Dubroca, L., and Bonhommeau, S. (2014). Defining Mediterranean and Black Sea biogeochemical subprovinces and synthetic ocean indicators using mesoscale oceanographic features. *PloS one*, 9(10):e111251.

Nieto, M. A., Garau, B., Balle, S., Simarro, G., Zarruk, G. A., Ortiz, A., Tintoré, J., Álvarez-Ellacuría, A., Gómez-Pujol, L., and Orfila, A. (2010). An open source, low cost video-based coastal monitoring system. *Earth Surface Processes and Landforms*, 35(14):1712–1719.

Obermann, A., Bastin, S., Belamari, S., Conte, D., Gaertner, M. A., Li, L., and Ahrens, B. (2018). Mistral and Tramontane wind speed and wind direction patterns in regional climate simulations. *Climate Dynamics*, 51(3):1059–1076.

Onink, V., Wichmann, D., Delandmeter, P., and Van Sebille, E. (2019). The role of Ekman currents, geostrophy, and Stokes drift in the accumulation of floating microplastic. *Journal of Geophysical Research: Oceans*, 124(3):1474–1490.

Orejarena-Rondón, A. F., Sayol, J. M., Marcos, M., Otero, L., Restrepo, J. C., Hernández-Carrasco, I., and Orfila, A. (2019). Coastal impacts driven by sea-level rise in Cartagena de Indias. *Frontiers in Marine Science*, 6:614.

Orfila, A., Jordi, A., Basterretxea, G., Vizoso, G., Marbà, N., Duarte, C. M., Werner, F., and Tintoré, J. (2005). Residence time and *Posidonia oceanica* in Cabrera Archipelago National Park, Spain. *Continental Shelf Research*, 25(11):1339–1352.

Pastor, F., Valiente, J. A., and Palau, J. L. (2018). Sea surface temperature in the Mediterranean: Trends and spatial patterns (1982–2016). *Pure and Applied Geophysics*, 175:4017—-4029.

Pearson, B. (2018). Turbulence-induced anti-Stokes flow and the resulting limitations of Large-Eddy simulation. *Journal of Physical Oceanography*, 48(1):117–122.

Phillips, O. M. (1966). *The dynamics of the upper ocean*. Cambridge university press.

Polton, J. A., Lewis, D. M., and Belcher, S. E. (2005). The role of wave-induced Coriolis–Stokes forcing on the wind-driven mixed layer. *Journal of Physical Oceanography*, 35(4):444–457.

Ponce de León, S., Orfila, A., and Simarro, G. (2016). Wave energy in the Balearic Sea. Evolution from a 29 year spectral wave hindcast. *Renewable Energy*, 85:1192–1200.

Poulain, P.-M., Menna, M., and Mauri, E. (2012). Surface geostrophic circulation of the Mediterranean Sea derived from drifter and satellite altimeter data. *Journal of Physical Oceanography*, 42(6):973–990.

Price, J. F., Weller, R. A., and Schudlich, R. R. (1987). Wind-Driven Ocean Currents and Ekman Transport. *Science*, 238(4833):1534–1538.

Priestley, M. B. (1965). Evolutionary spectra and non-stationary processes. *Journal of the Royal Statistical Society: Series B (Methodological)*, 27(2):204–229.

Pujol, M.-I., Faugère, Y., Taburet, G., Dupuy, S., Pelloquin, C., Ablain, M., and Picot, N. (2016). DUACS DT2014: the new multi-mission altimeter data set reprocessed over 20 years. *Ocean Sci*, 12(5):1067–1090.

Pujol, M.-I. and Larnicol, G. (2005). Mediterranean Sea eddy kinetic energy variability from 11 years of altimetric data. *Journal of Marine Systems*, 58(3-4):121–142.

Reygondeau, G., Guieu, C., Benedetti, F., Irisson, J.-O., Ayata, S.-D., Gasparini, S., and Koubbi, P. (2017). Biogeochemical regions of the Mediterranean Sea: an objective multidimensional and multivariate environmental approach. *Progress in oceanography*, 151:138–148.

Richardson, L. F. (1926). Atmospheric diffusion shown on a distance-neighbour graph. *Proceedings of the Royal Society of London. Series A, Containing Papers of a Mathematical and Physical Character*, 110(756):709–737.

Rio, M.-H., Mulet, S., and Picot, N. (2014). Beyond GOCE for the ocean circulation estimate: Synergetic use of altimetry, gravimetry, and in situ data provides new insight into geostrophic and Ekman currents. *Geophysical Research Letters*, 41(24):8918–8925.

Robinson, A. R., Leslie, W. G., Theocharis, A., and Lascaratos, A. (2001). Mediterranean sea circulation. *Ocean currents*, 1:19.

Roelvink, D., Reniers, A., Van Dongeren, A., De Vries, J. V. T., McCall, R., and Lescinski, J. (2009). Modelling storm impacts on beaches, dunes and barrier islands. *Coastal engineering*, 56(11-12):1133–1152.

Rossi, V., Ser-Giacomi, E., López, C., and Hernández-García, E. (2014). Hydrodynamic provinces and oceanic connectivity from a transport network help designing marine reserves. *Geophysical Research Letters*, 41(8):2883–2891.

Saha, S. (2009). Documentation of the Hourly Time Series from the NCEP Climate Forecast System Reanalysis (1979-2009). *EMC/NCEP/NOAA*.

Saha, S., Moorthi, S., Pan, H.-L., Wu, X., Wang, J., Nadiga, S., Tripp, P., Kistler, R., Woollen, J., Behringer, D., et al. (2010). The NCEP climate forecast system reanalysis. *Bulletin of the American Meteorological Society*, 91(8):1015–1058.

Santiago-Mandujano, F. and Firing, E. (1990). Mixed-layer shear generated by wind stress in the central equatorial Pacific. *Journal of Physical Oceanography*, 20(10):1576–1582.

Sartini, L., Besio, G., and Cassola, F. (2017). Spatio-temporal modelling of extreme wave heights in the Mediterranean Sea. *Ocean Modelling*, 117:52–69.

Sayol, J. M., Orfila, A., and Oey, L.-Y. (2016). Wind induced energy–momentum distribution along the Ekman–Stokes layer. Application to the Western Mediterranean Sea climate. *Deep Sea Research Part I: Oceanographic Research Papers*, 111:34–49.

Sayol, J. M., Orfila, A., Simarro, G., Conti, D., Renault, L., and Molcard, A. (2014). A Lagrangian model for tracking surface spills and SaR operations in the ocean. *Environmental Modelling and Software*, 52:74–82.

Semeoshenkova, V. and Newton, A. (2015). Overview of erosion and beach quality issues in three Southern European countries: Portugal, Spain and Italy. *Ocean and Coastal Management*, 118:12–21.

Senechal, N., Coco, G., Castelle, B., and Marieu, V. (2015). Storm impact on the seasonal shoreline dynamics of a meso-to macrotidal open sandy beach (Biscarrosse, France). *Geomorphology*, 228:448–461.

Ser-Giacomi, E., Legrand, T., Hernández-Carrasco, I., and Rossi, V. (2021). Explicit and implicit network connectivity: Analytical formulation and application to transport processes. *Phys. Rev. E*, 103:042309.

Ser-Giacomi, E., Sánchez, G. J., Soto-Navarro, J., Thomsen, S., Mignot, J., Sevault, F., and Rossi, V. (2020). Impact of climate change on surface stirring and transport in the Mediterranean Sea. *Geophysical Research Letters*, page e2020GL089941.

Shadden, S. C., Lekien, F., and Marsden, J. E. (2005). Definition and properties of Lagrangian coherent structures from finite-time Lyapunov exponents in two-dimensional aperiodic flows. *Physica D: Nonlinear Phenomena*, 212(3-4):271–304.

Shrira, V. I. and Almelah, R. B. (2020). Upper-ocean Ekman current dynamics: a new perspective. *Journal of Fluid Mechanics*, 887.

Simarro, G., Ribas, F., Álvarez, A., Guillén, J., Chic, Ò., and Orfila, A. (2017). ULISES: An open source code for extrinsic calibrations and planview generations in coastal video monitoring systems. *Journal of Coastal Research*, 33(5):1217–1227.

Small, R., Carniel, S., Campbell, T., Teixeira, J., and Allard, R. (2012). The response of the Ligurian and Tyrrhenian Seas to a summer Mistral event: A coupled atmosphere–ocean approach. *Ocean Modelling*, 48:30–44.

Soto-Navarro, J., Criado-Aldeanueva, F., García-Lafuente, J., and Sánchez-Román, A. (2010). Estimation of the Atlantic inflow through the Strait of Gibraltar from climatological and in situ data. *Journal of Geophysical Research: Oceans*, 115(C10).

Soukissian, T., Karathanasi, F., Axaopoulos, P., Voukouvalas, E., and Kotroni, V. (2018). Offshore wind climate analysis and variability in the Mediterranean Sea. *International Journal of Climatology*, 38(1):384–402.

Stive, M. J., Aarninkhof, S. G., Hamm, L., Hanson, H., Larson, M., Wijnberg, K. M., Nicholls, R. J., and Capobianco, M. (2002). Variability of shore and shoreline evolution. *Coastal engineering*, 47(2):211–235.

Stockdon, H. F. and Holman, R. A. (2000). Estimation of wave phase speed and nearshore bathymetry from video imagery. *Journal of Geophysical Research: Oceans*, 105(C9):22015–22033.

Stokes, G. G. (1880). On the theory of oscillatory waves. *Transactions of the Cambridge philosophical society*.

Sudre, J., Maes, C., and Garçon, V. (2013). On the global estimates of geostrophic and Ekman surface currents. *Limnology and Oceanography: Fluids and Environments*, 3(1):1–20.

Sybrandy, A. L. (1991). The WOCE/TOGASVP Lagrangian drifter construction manual. *WOCE Rep.*, 63:58.

Taylor, G. I. (1921). Experiments with rotating fluids. *Proceedings of the Royal Society of London. Series A, Containing Papers of a Mathematical and Physical Character*, 100(703):114–121.

Thomson, R. E. and Emery, W. J. (2014). *Data analysis methods in physical oceanography*. Newnes.

Tintoré, J., Medina, R., Gómez-Pujol, L., Orfila, A., and Vizoso, G. (2009). Integrated and interdisciplinary scientific approach to coastal management. *Ocean and Coastal Management*, 52(10):493–505.

Tintoré, J., Vizoso, G., Casas, B., Heslop, E., Pascual, A., Orfila, A., Ruiz, S., Martínez-Ledesma, M., Torner, M., Cusí, S., et al. (2013). SOCIB: the Balearic Islands coastal ocean observing and forecasting system responding to science, technology and society needs. *Marine Technology Society Journal*, 47(1):101–117.

Toffoli, A. and Bitner-Gregersen, E. M. (2017). Types of ocean surface waves, wave classification. *Encyclopedia of Maritime and Offshore Engineering*, pages 1–8.

Tolman, H. L. (2009). User manual and system documentation of WAVEWATCH III TM version 3.14. *MMAB Contribution, College Park, MD, U.S.A.*

Torrence, C. and Compo, G. P. (1998). A practical guide to wavelet analysis. *Bulletin of the American Meteorological society*, 79(1):61–78.

Trigo, I. F., Bigg, G. R., and Davies, T. D. (2002). Climatology of cyclogenesis mechanisms in the Mediterranean. *Monthly Weather Review*, 130(3):549–569.

Trigo, I. F., Davies, T. D., and Bigg, G. R. (1999). Objective climatology of cyclones in the Mediterranean region. *Journal of Climate*, 12(6):1685–1696.

Tsinker, G. P. (2004). *Port engineering: planning, construction, maintenance, and security*. John Wiley and Sons.

Ulbrich, U., Lionello, P., Belusic, D., Jacobeit, J., Knippertz, P., Kuglitsch, F. G., Leckebusch, G. C., Luterbacher, J., Maugeri, M., Maheras, P., et al. (2012). Climate of the Mediterranean: Synoptic patterns, temperature, precipitation, winds and their extremes. In *Climate of the Mediterranean Region-From the Past to the Future*, pages 301–346. Elsevier.

Van Loon, H. and Rogers, J. C. (1978). The seesaw in winter temperatures between Greenland and northern Europe. Part I: General description. *Monthly Weather Review*, 106(3):296–310.

Van Sebille, E., Griffies, S. M., Abernathey, R., Adams, T. P., Berloff, P., Biastoch, A., Blanke, B., Chassignet, E. P., Cheng, Y., Cotter, C. J., et al. (2018). Lagrangian ocean analysis: Fundamentals and practices. *Ocean Modelling*, 121:49–75.

Van Sebille, E., Wilcox, C., Lebreton, L., Maximenko, N., Hardesty, B. D., Van Franeker, J. A., Eriksen, M., Siegel, D., Galgani, F., and Law, K. L. (2015). A global inventory of small floating plastic debris. *Environmental Research Letters*, 10(12):124006.

Villarino, E., Watson, J. R., Jönsson, B., Gasol, J. M., Salazar, G., Acinas, S. G., Estrada, M., Massana, R., Logares, R., Giner, C. R., et al. (2018). Large-scale ocean connectivity and planktonic body size. *Nature communications*, 9(1):1–13.

Vinoth, J. and Young, I. (2011). Global estimates of extreme wind speed and wave height. *Journal of Climate*, 24(6):1647–1665.

Vousdoukas, M. I., Almeida, L. P. M., and Ferreira, Ó. (2012). Beach erosion and recovery during consecutive storms at a steep-sloping, meso-tidal beach. *Earth Surface Processes and Landforms*, 37(6):583–593.

Wallace, J. M. and Gutzler, D. S. (1981). Teleconnections in the Geopotential Height Field during the Northern Hemisphere Winter. *Monthly Weather Review*, 109(4):784–812.

Wang, P., Kirby, J. H., Haber, J. D., Horwitz, M. H., Knorr, P. O., and Krock, J. R. (2006). Morphological and sedimentological impacts of Hurricane Ivan and immediate poststorm beach recovery along the northwestern Florida barrier-island coasts. *Journal of Coastal Research*, 22(6 (226)):1382–1402.

Wang, X. L. and Swail, V. R. (2001). Changes of extreme wave heights in Northern Hemisphere oceans and related atmospheric circulation regimes. *Journal of Climate*, 14(10):2204–2221.

Wang, X. L. and Swail, V. R. (2002). Trends of Atlantic wave extremes as simulated in a 40-yr wave hindcast using kinematically reanalyzed wind fields. *Journal of climate*, 15(9):1020–1035.

Weare, B. C. and Nasstrom, J. S. (1982). Examples of extended empirical orthogonal function analyses. *Monthly Weather Review*, 110(6):481–485.

Weiss, J., Bernardara, P., and Benoit, M. (2014). Formation of homogeneous regions for regional frequency analysis of extreme significant wave heights. *Journal of Geophysical Research: Oceans*, 119(5):2906–2922.

Welander, P. (1957). Wind Action on a Shallow Sea: Some Generalizations of Ekman's Theory. *Tellus*, 9(1):45–52.

Wenegrat, J. O. and McPhaden, M. J. (2016). Wind, waves, and fronts: Frictional effects in a generalized Ekman model. *Journal of Physical Oceanography*, 46(2):371–394.

Wolf, J. and Woolf, D. K. (2006). Waves and climate change in the north-east Atlantic. *Geophysical Research Letters*, 33(6).

Woolf, D. K., Challenor, P., and Cotton, P. (2002). Variability and predictability of the North Atlantic wave climate. *Journal of Geophysical Research: Oceans*, 107(C10).

Yepes, V. and Medina, J. R. (2005). Land use tourism models in Spanish coastal areas. A case study of the Valencia region. *Journal of Coastal Research*, pages 83–88.

Young, I., Vinoth, J., Zieger, S., and Babanin, A. V. (2012). Investigation of trends in extreme value wave height and wind speed. *Journal of Geophysical Research: Oceans*, 117(C11).

Young, I., Zieger, S., and Babanin, A. V. (2011). Global trends in wind speed and wave height. *Science*, 332(6028):451–455.

Young, I. R. and Ribal, A. (2019). Multiplatform evaluation of global trends in wind speed and wave height. *Science*, 364(6440):548–552.

Zecchetto, S. and De Biasio, F. (2007). Sea surface winds over the Mediterranean basin from satellite data (2000–04): Meso-and local-scale features on annual and seasonal time scales. *Journal of Applied Meteorology and Climatology*, 46(6):814–827.

List of Figures

1.1 Frequency and period ranges of ocean waves. The order of magnitude of the relative energy power is indicated by the curve (adapted from Munk, 1950). The shaded area represents the range of wave periods in which this Thesis focuses. 2

1.2 Scheme of wind-driven surface waves generation. 3

1.3 Scheme of Stokes drift. 7

1.4 Temporal correlation between monthly NAO index values and the monthly standardized 500-mb geopotential height anomalies from 1950 to 2020 for a) January, b) April, c) July and d) October. 9

1.5 Temporal correlation between the monthly EA index values and the monthly standardized 500-mb geopotential height anomalies from 1950 to 2020 for a) January, b) April, c) July and d) October. 9

1.6 Temporal correlation between the monthly EA/WR index values and the monthly standardized 500-mb geopotential height anomalies from 1950 to 2020 for a) January, b) April, c) July and d) October. 10

1.7 Temporal correlation between the monthly SCAND index values and the monthly standardized 500-mb geopotential height anomalies from 1950 to 2020 for a) January, b) April, c) July and d) October. 10

1.8 Mediterranean Sea. Color indicates the bathymetry from deep (dark) to shallow (light) blue. Red arrows represent the main wind directions. 11

1.9 Surface circulation scheme at the Mediterranean Sea. Source: GRID Arendal www.grida.no/resources/5915. 12

3.1 Location of the study zones. a) Eastern North Atlantic Ocean. b) Mediterranean Sea. The yellow points are the locations of the buoys used in the comparison with the modeled data by WAVEWATCH III 30-year Hindcast Phase 2. Panels 1 and 2: SWH series of hindcast (black line) and a representative buoy (dashed blue line) for the North Atlantic Ocean and Mediterranean Sea, respectively. The red points are the locations of the representative buoys. 25

3.2 Maximum value of monthly 99^{th} percentile SWH in meters for a) the North Atlantic Ocean and b) Mediterranean Sea, as well as the month of the year [from January (1) to December (12)] when there is the maximum value of the 99^{th} percentile SWH for c) the North Atlantic Ocean and d) Mediterranean Sea. 26

3.3 Variance reduction in percentage if the seasonality is removed from the monthly 99^{th} percentile SWH series for the a) North Atlantic Ocean and b) Mediterranean Sea. Panels 1 and 2: monthly 99^{th} percentile SWH series (black line) and monthly 99^{th} percentile SWH series without seasonality (blue line) for a point in the North Atlantic Ocean and Mediterranean Sea, respectively. 27

3.4 Trend of the monthly 99^{th} percentile SWH during winters (DJFM) in centimeters per year. Dotting indicates no significant values at the 90% confidence interval. 28

3.5 a) Mean field of winter SWH 99^{th} percentile in meters over the North Atlantic. EOF analysis of SWH_{99} anomalies, showing the explained variance of the first three EOFs, b-d) spatial patterns of EOFs 1-3, and 1-3) principal components of the EOFs above. 30

3.6 a) Mean field of winter SWH 99^{th} percentile in meters over the Mediterranean Sea. EOF analysis of SWH_{99} anomalies, showing the explained variance of the first three EOFs, b-d) spatial patterns of the EOFs 1-3, and 1-3) principal components of the EOFs above. 31

3.7 Pearson correlation coefficient of winter mean 99^{th} percentile SWH North Atlantic series and a) NAO, b) EA, c) EA-WR and d) SCAND winter mean indices. Dotting indicates no significant values at the 90% confidence interval. The white points show $1)$ the maximum positive and $2)$ the maximum negative value of the correlation coefficient. 32

3.8 Pearson correlation coefficient of winter mean 99^{th} percentile SWH Mediterranean Sea series and a) NAO, b) EA, c) EA-WR and d) SCAND winter mean indices. Dotting indicates no significant values at the 90% confidence interval. The white points show $1)$ the maximum positive and $2)$ the maximum negative value of the correlation coefficient. 33

3.9 Winter atmospheric situations for the positive phase of a) NAO, b) EA, c) EA-WR and d) SCAND indices in the North Atlantic Ocean. The vectors represent the 10 m wind speed in meters per second; the contours represent the sea level pressure (Pa) and the color range is the mean value of SWH in meters. The red left bottom arrow represents the wind scale. 35

3.10 Winter atmospheric situations for the negative phase of a) NAO, b) EA, c) EA-WR and d) SCAND indices in the North Atlantic Ocean. The vectors represent the 10 m wind speed in meters per second; the contours represent the sea level pressure (Pa) and the color range is the mean value of SWH in meters. The red left bottom arrow represents the wind scale. 36

3.11 Winter atmospheric situations for the positive phase of a) NAO, b) EA, c) EA-WR and d) SCAND indices in the Mediterranean Sea. The vectors represent the 10 m wind speed in meters per second; the contours represent the sea level pressure (Pa) and the color range is the mean value of SWH in meters. The red left bottom arrow represents the wind scale. 37

3.12 Winter atmospheric situations for the negative phase of a) NAO, b) EA, c) EA-WR and d) SCAND indices in the Mediterranean Sea. The vectors represent the 10 m wind speed in meters per second; the contours represent the sea level pressure (Pa) and the color range is the mean value of SWH in meters. The red left bottom arrow represents the wind scale. 38

4.1 Ekman (blue arrows), Stokes (red arrows) and ageostrophic (black arrows) velocity profiles (in cm/s) at spatial point 6ºE, 38.5ºN corresponding to the 5^{th} of February 2014 at $6{:}00$ UTC. 46

4.2 Topography of the Mediterranean basin and naming convention of the main geographical locations used in the Chapter. 48

4.3 a) Total, b) Geostrophic, c) Ekman, d) Stokes and e) Ekman-Stokes velocity fields for January, 19^{th} of 2005 at $12{:}00$ UTC. The magnitudes (module, in cm/s) of each velocity component are displayed as background colors according to the color-scale. The black arrows represent the direction of the velocity fields. Only 1 of each 5 data points have been plotted for clarity. 52

4.4 a) Total, b) Geostrophic, c) Ekman, d) Stokes and e) Ekman-Stokes velocity fields for February the 5^{th} of 2014 at $6{:}00$ UTC. The magnitudes (module, in cm/s) of each velocity component are displayed as background colors according to the color-scale. The black arrows represent the direction of the velocity fields. Only 1 of each 5 data points have been plotted for clarity. 53

4.5 Zoom at the Liguro-Provençal current for a) Geostrophic, b) Ekman and c) Total velocity fields for February the 5^{th} of 2014 at $6{:}00$ UTC. The magnitudes (module, in cm/s) of each velocity component are displayed as background colors according to the color-scale. The black arrows represent the direction of the velocity fields. 54

4.6 Temporal patterns of the absolute value of the total (black line), geostrophic (cyan line), Ekman (blue line) and Stokes (red line) velocity component fields (in cm/s) extracted from the coupled SOMs technique for 2005. Patterns have been smoothed using a moving window of 3.5 days in order to facilitate comparison. The means and the standard deviations (in cm/s) of each temporal pattern are reported within each panel. 55

4.7 Regions unveiled from the SOM analysis according to the coupled variability of the absolute value of each velocity field component for 2005. R1 is dominated by the ageostrophic component; R2/ R3, by the geostrophic one and R4/ R5/ R6 are intermediate patterns. 56

4.8 Time series of the spatially-averaged total (black line), geostrophic (cyan line), Ekman (blue line) and Stokes (red line) velocity component module fields (in cm/s) from 1993 to 2018 in the regions of the temporal SOMs of 2005. 58

4.9 Wavelet power spectrum of the 6-hours time series of the spatially-averaged (over the SOM regions shown in Fig. 4.8) Total, Geostrophic and Ageostrophic velocity components from 1993 to 2018. Contours in black indicates the 95% significant levels. Lighter shades show the cone of influence (COI) where the edge effects may distort the Fourier analysis. 59

4.10 Wavelet coherence between the 6-hours time series of the spatially-averaged total velocity module (over the SOM regions shown in Fig. 4.8) and the monthly values of NAO, EA, EA/WR and SCAND climatic indices from 1993 to 2018. The arrows determine the phase between both series. Arrows pointing to the right represent positive correlation (signals in phase) and when they point to the left, anti-correlation (signals in anti-phase). Contours indicate wavelet squared coherence. 61

4.11 Trend in cm/s per year of the a) Total velocity module and b) Geostrophic component module from 1993 to 2018. c) Difference between a) and b) in cm/s per year. No significant values at the 90% confidence interval are dotted (with Mann Kendall method). 63

4.12 Trend in cm/s per year of the a) Total velocity module and b) Geostrophic component module from 1993 to 2002. c) Difference between a) and b) in cm/s per year. No significant values at the 90% confidence interval are dotted (with Mann Kendall method). 64

S.4.13 Temporal patterns of the absolute value of the total (black line), geostrophic (cyan line), Ekman (blue line) and Stokes (red line) velocity component fields (in cm/s) extracted from the coupled SOMs technique for 2005 with 9 neurons. Patterns have been smoothed using a moving window of 3.5 days in order to facilitate comparison. The means and the standard deviations (in cm/s) of each temporal pattern are reported within each panel. 66

S.4.14 Regions unveiled from the SOM analysis for 2005 with 9 neurons, according to the coupled variability of the absolute value of each velocity field component. 67

5.1 Map of the Mediterranean Sea showing the main oceanographic features and the regions extracted through the SOM analysis applied to the total kinetic energy computed from the coupled geostrophic and ageostrophic (i.e. Ekman and Stokes induced currents) velocity fields. Figure adapted from Morales-Márquez et al. (2020a). 73

5.2 FSLE spectrum, $\lambda(\delta)$ (in days^{-1}) for different zonal (blue line) and meridional (red line) spatial scales (δ, in km) calculated with virtual drifters advected in the total velocity field U_T and without measuring the total final distance along an specific direction. The scaling exponents associated with ballistic/shear (-1) and Richardson (-2/3) dispersion regimes are included in the plot with dashed grey lines. . . 76

5.3 Spatial distribution of backward FSLE (days^{-1}) in the Mediterranean Sea corresponding to January 19, 2005 at 12:00 UTM computed using 2791665 pairs of trajectories with a) total velocity fields, U_T, and b) geostrophic velocity fields, U_g. c) Difference between total and geostrophic FSLE fields shown in a) and b) ($FSLE_T$ - $FSLE_g$) (days^{-1}). d), e) and f) are zooms in on the Ionian Sea of the $FSLE_T$, $FSLE_g$ and its difference, respectively (days^{-1}). The initial separation is $\delta_0 = 1/64°$ and the final separation, $\delta_f = 10\delta_0$. 78

5.4 Evolution during one month (a) January 26, b) January 31, c) February 5, d) February 10, e) February 15 and f) February 20, 2005) of two sets of 10000 passive tracers launched with the same initial conditions in the interior of a mesoscale eddy. One set is advected by the geostrophic field (in cyan) and the other set is advected by the total velocity field (in pink). The attracting geostrophic LCS are displayed in the background in gray (darker grey for more intense LCS). 79

5.5 Spatial distribution of the time average of backward $FSLE_T$, in $days^{-1}$, over: a) the 24 years of data (from 1994 to 2018); c) only averaging over winter months (DJFM); and e) only averaging over summer months (JJAS). Contribution of the ageostrophic currents proportional to the total horizontal stirring in % [($FSLE_T$ - $FSLE_g$)/$FSLE_T$], for b) the total period; d) for winter; and f) for summer. The initial separation is $\delta = 1/8°$ and the final separation, $r\delta = 1°$. 81

5.6 Time evolution, from 1994 to 2018, of the spatial average of daily $FSLE_T$ (bold pink lines) and $FSLE_g$ (dashed black lines), in days^{-1}, over the whole Mediterranean Sea (panel a); and over the SOM-regions (panels R1-R6) shown in Fig. 5.1. The linear trends of the FSLE time series, expressed in days^{-1}/year, are included in each plot. Only trends with a significance $p \leq 0.01$ are included. FSLE is computed using $\delta_0 = 1/8°$ and $\delta_f = 1°$. 85

5.7 Mean annual cycle of daily FSLE in days^{-1} (climatological daily mean over 24 years of data): a) for the whole Mediterranean Sea; R1-R6) for the SOM-region (bold pink lines correspond to FSLE$_T$, and black-dashed lines to FSLE$_g$). FSLE is computed using the $\delta_0 = 1/8°$ and $\delta_f = 1°$. 86

5.8 FSLE curves ($\lambda(\delta)$), in days^{-1}, at different spatial scales, in km, (δ) calculated with a) virtual drifters advected in the total velocity field (solid line) and in the geostrophic field (dashed line); b) with the real drifters. Each color corresponds to the averaged FSLE value over all the pairs of virtual drifters homogeneously launched in the SOM-regions identified in Fig. 5.1, and deployed at the same time period of the available pairs of real drifters in the corresponding SOM-region. The scaling exponents associated with ballistic/shear (-1) and Richardson (-2/3) dispersion regimes are included in the plot with dashed grey lines. 87

5.9 Zonal (blue lines) and meridional (red lines) FSLE curves (in days^{-1}) given by $\lambda_x(\delta_x)$ and $\lambda_y(\delta_y)$, respectively (see Eqs. (5.11) and (5.12)), at different spatial scales (δ_x and δ_y, in km) calculated for pairs of virtual drifters advected in the total velocity field U$_T$. Each subplot (R1-R6) corresponds to the averaged FSLE values over all the pairs of virtual drifters launched in the SOM-regions identified in Fig. 5.1, and deployed at the same time period of the available pairs of real drifters in the corresponding SOM-region. The scaling exponents associated with ballistic/shear (-1) and Richardson (-2/3) dispersion regimes are included in the plot with dashed grey lines. 89

5.10 Scale dependence of LAI computed with virtual drifters advected in the total velocity field for each SOM-region of the Mediterranean Sea. Colors correspond to SOM-regions identified in Fig. 5.1. The dashed black line represents the isotropy (LAI=0). 90

5.11 Maps of the time average of LCSA computed over the 24 years of data (from 1994 to 2018) for the a) U_T and b) the difference between the LCSA obtained for U_T and for U_g. c) and d) are the same as a) and b) but only averaged over winter; and e) and f), the same as a) and b) but only averaged over summer. The initial resolution is $\delta = 1/8°$ and the final resolution, $r\delta = 1°$. 91

S.5.12 Spatial distribution of backward FSLE (days^{-1}) in the Ionian Sea corresponding to February 5, 2014 at 6:00 UTM, computed from a) total velocity field, U_T, and b) geostrophic velocity field, U_g. c) Difference between maps a) and b) (days^{-1}). The initial separation is $\delta_0 = 1/64°$ and the final separation, $\delta_f = 10\delta_0$. 95

S.5.13 Number of tracks of pairs of real drifters that are inside each region at least during 2 days used in the regional dispersion analysis shown in Fig. 5.8, b. 96

S.5.14 Zonal (blue lines) and meridional (red lines) FSLE curves (in days^{-1}) given by $\lambda_x(\delta_x)$ and $\lambda_y(\delta_y)$, respectively (see Eqs. 5.11 and 5.12), at different spatial scales (δ_x and δ_y, in km) calculated for pairs of real drifters. Each subplot (R1-R6) corresponds to the averaged FSLE values over all the pairs of real drifters available in the SOM-regions identified in Fig. 5.1. The scaling exponents associated with ballistic/shear (-1) and Richardson (-2/3) dispersion regimes are included in the plot with dashed grey lines. 97

S.5.15 Scale dependence of LAI computed with drifters for each SOM-region of the Mediterranean Sea. Colors correspond to SOM-regions identified in Fig. 5.1. The dashed black line represents the isotropy (LAI=0). 98

S.5.16 Number of tracks of pairs of drifters that are inside each SOM-regions identified in Fig. 5.1 at least during 2 days used for making Fig. S.5.14 for zonal (in blue) and meridional (in red) FSLE. 99

6.1 Study site location (a) and major features of Cala Millor. (b, c) White dashed lines correspond to the bathymetric survey (isoline equal distance of $2\,\mathrm{m}$); the yellow frame covers the bathymetry area obtained by means of XBeach, and red lines correspond to the beach profile described in text. The bottom orthophoto is provided by the Govern de les Illes Balears-SITIBSA (June 2008). Panel (b) shows the combination of multibeam bathymetric survey (green points) and RTK–GPS survey for dry beach and very shallow submerged beach (red points). (c) Bottom type at Cala Millor. 104

6.2 (a) Alongshore shoreline width anomaly (in m) at Cala Millor from November 2010 to January 2017. Red colors indicate shoreline advance, whereas blue ones indicate shoreline recession. The dashed black lines show the sea storm events larger than $2\,\mathrm{m}$. (b) Wave significant height (in m) from a wave recorder located at $-17\,\mathrm{m}$ in the middle of the Cala Millor embayment. (c) Alongshore averaged shoreline width anomaly (in m) at Cala Millor. The red arrows highlight the storm group event at April 2014. 105

6.3 (a) Workflow of the approach followed in the study. (b) Calendar showing the date for the samples used in the study. 107

6.4 (a) SWH (m) at $25\,\mathrm{m}$ depth in Cala Millor between 15 March and 14 April 2014. (b) T_p (s). (c) Wave direction (^{circ}). The blue shading shows the period corresponding to the storms. Vertical red dotted lines indicate the initial bathymetry obtained while dashed dotted lines indicate the dates when cross-shore profiles were measured. Vertical green dotted lines state the day when the model was validated using the corresponding shore profiles. Vertical red lines show the date when bathymetry inferred from XBeach was used for comparison among storms. 108

6.5 (a) Time stack image for 19 March at 09:00 UTC + 1 for the central camera. The abscissa corresponds to the cross-shore direction and the ordinate for the time. (b) Reconstruction for the same date assuming a constant wave height using the Fourier mode of the detected period (i.e., $\cos(\phi(x, f_w) - 2\pi f_w)$). 110

6.6 (a) Cross-shore transect defined for the time stack image on camera no. 3. The figure shows the original image in the (u,v) $\equiv$ pixel coordinate system. (b) The same after rectification in the (x,y) $\equiv$ UTM coordinate system. (c) Resulting time stack for 19 March at 10:00 UTC + 1. 112

6.7 Timex images with dates referred to in each image. Notice the intermediate configuration with a sinuous parallel bar along the coast (ca. 180 m) for 17 and 27 March and the dissipative scenario without a bar for 8 April. 113

6.8 Depth variation (in m) estimated from XBeach and from measurements. (a) Bottom variation (in m) during the storm group (17 March to 8 April). (b) Bottom variation (in m) for the period of calms (8 April to 12 June). 114

6.9 Depth variation (in m) estimated from bathymetry inversion of the time stack during storm conditions; (a) between 8 April and 20 March (storm conditions); (b) between 12 June and 8 April (calm conditions). 115

6.10 Depth variation (in m) estimated from XBeach and from measurements. (a) Bottom variation (in m) between 17 and 28 March (storm S1). (b) Depth variation (in m) between 28 March and 1 April (storm S2). (c) Depth variation (in m) between 1 and 8 April (storm S3). . . . 116

List of Tables

3.1 Statistical comparison between SWH data from WAVEWATCH III 30-year Hindcast Phase 2 and CMEMS buoys. 24

3.2 Correlation between main climate indices and the amplitudes of the first three modes of the average monthly SWH_{99} series for the North Atlantic Ocean and the Mediterranean Sea in winter. 31

4.1 Statistical comparison between the ERA-Interim and ERA5 dataset. . . 48

5.1 Values of λ_M ($\cdot$ 10^{-1} days^{-1}), δ_M (in km) and the slopes (μ) resulting from the best fitting of the FSLE curves obtained using pairs of virtual drifters advected in U_g (referred as to λ-$\mathrm{U_g}$), U_T (λ-$\mathrm{U_T}$) and pairs of real drifters (λ-Drifters), and of their corresponding zonal and meridional component (λ_x and λ_y), computed for each SOM-region of the Mediterranean Sea. In all cases the obtained correlation coefficients (R^2) are larger than 0.95 except for the fit of λ-Drifters in R1 (R^2 = 0.89) and λ_y-U_T and λ_x-Drifters in region R2 (R^2 = 0.90 and 0.92, respectively). Slopes associated with Richardson (shear) [standard] turbulent dispersion are indicated in bold black (in red) [in blue]. 84

6.1 Error statistics for the simulated profiles by XBeach compared with the measured profiles during Riskbeach. 112

6.2 Error statistics for the estimated profile from time-stacks compared with the measured profiles during Riskbeach. 113

List of Terms and Abbreviations

λ Averaged Lyapunov exponent

λ_M Maximum mesoscale Lyapunov exponent

δ_M Transition spatial scale between the exponential and the power law separation rate of Lyapunov exponent

ASCAT Advanced Scatterometer

AWAC Acoustic Waves and Current meterAdvanced Scatterometer

CCD Charge-Coupled Device cameras

CFSR Climate Forecast System Reanalysis

CFSRR Climate Forecast System Reanalysis and Reforecast

Chl Chlorophyll

CMEMS Copernicus Marine Environment Monitoring Service

CMOD Compact Meteorological and Oceanographic Drifter

CODE Coastal Ocean Dynamics Experiment drifters

COI Cone Of Influence

CSIC Spanish National Research Council

DGPS-RTK Differential Global Positioning System - Real-Time Kinematic

DJFM December - January - February - March

DUACS Data Unification and Altimeter Combination System

EA East Atlantic climatic index

EA/WR East Atlantic-Western Russian climatic index

ECMWF European Centre for Medium-Range Weather Forecasts

ENVISAT Environmental Satellite

EOF Empirical Orthogonal Functions

ERS1 European Remote Sensing Satellite 1

FFT Fast Fourier Transform

FSLE Finite Size Lyapunov Exponents

FSLE$_T$ Finite Size Lyapunov Exponents calculated with the total velocity field

FSLE$_g$ Finite Size Lyapunov Exponents calculated with the geostrophy velocity field

GDS Global Positioning System

GFO Geodetic satellite Follow-On

GRADISTAT Grain Size Distribution and Statistics

ICM Institute of Marine Sciences

IFREMER French Research Institute for the Oceanic Operation

IMEDEA Mediterranean Institute of Advanced Studies

JONSWAP Joint North Sea Wave Observation Project

KE Kinetic Energy

LAI Lagrangian Anisotropy Index

LCS Lagrangian Coherent Structure

LCS$_T$ Lagrangian Coherent Structure calculated with the total velocity field

LCS$_g$ Lagrangian Coherent Structure calculated with the geostrophy velocity field

LCSA Lagrangian Coherent Structure Anisotropy

MSLP Mean Sea Level Pressure

NAO North Atlantic Oscillation climatic index

NCAR National Center for Atmospheric Research

NCEP National Centers for Environmental Prediction

NDBC-NOAA National Data Buoy Center of National Oceanic and Atmospheric Administration

NOAA National Oceanic and Atmospheric Administration

OGS Italian National Institute of Oceanography and Experimental Geophysics

PC Principal Component

P1-6 Pattern 1-5

R^2 Correlation coefficient

R1-6 Region 1-6

RB Relative Bias

RPCA Rotated Principal Component Analysis

RTK Real-Time Kinematic

RMS Root Mean Square

SCAND Scandinavia climatic index

SCI Scatter Index

SLA Sea Level Anomaly

SLP Sea Level Pressure

SOCIB Balearic Islands Coastal Observing and Forecasting System

SOM Self-Organizing Maps

SSH Sea Surface Height

SVP Surface Velocity Program drifters

SWH Significant wave height

$\mathbf{SWH_{99}}$ Monthly 99^{th} percentile of Significant wave height

$\mathbf{T_p}$ Peak period

T/P TOPEX/Poseidon

$\mathbf{U_{10}}$ 10 m-height wind velocity

UNWTO The United Nations World Tourism Organization

$\mathbf{U_a}$ Ageostrophic velocity currents component

$\mathbf{U_E}$ Ekman velocity currents component

$\mathbf{U_g}$ Geostrophic velocity currents component

$\mathbf{U_S}$ Stokes velocity currents component

$\mathbf{U_T}$ Total velocity currents

UTC Universal Time Coordinated

UTM Universal Transverse Mercator

WCA Wavelet Coherence Analysis

WAM Wave Modeling Project

WH Wave Height

$\mathbf{WH_{RMS}}$ Root Mean Square Wave Height

WEPA Western Europe Pressure Anomaly

XBeach Extreme Beach behavior numerical model

XWT Cross-Wavelet Transform